MECHANICAL PROPERTIES OF TEMPERED MARTENSITE

A Thesis Submitted for the Degree of Doctor of Philosophy

by

LINGYU WANG
B.E. (HON.I), MONASH UNIVERSITY

MAY 2020

Department of Materials Science and Engineering

Monash University

Victoria, Australia

Copyright notice

Abstract

Martensite is a key constituent of almost all high strength steels. The traditional view of the strength of martensite (e.g. 0.2% proof strength) is that it is largely due to solid solution strengthening by carbon. This view has prevailed largely because of the experimentally observed correlation between the 0.2% proof strength and the square root of bulk carbon concentration despite the fact that it is well known that autotempering results in much lower carbon contents being retained in solid solution. New experiments over the past decade have also shown that this simple solid solution strengthening picture is not able to explain well the extended elastic-plastic transition and the high strain hardening rates of martensite. Recent interpretations of the yielding of as-quenched martensite, including the composite models considering mircrostructural constituents with different yield stresses and residual stresses, have shown some success in describing the strength and strain hardening behaviour of as-quenched martensite.

However, commercial martensitic steels are used in the tempered (or heavily auto-tempered) state. The concurrent occurrences of solute segregation, carbide formation, defect recovery and stress relaxation during tempering and their effects on any potential composite strengthening effect of martensite remain to be characterised and understood. In the current study, key hypotheses of the composite models have been tested with experiments. It is found that although the overall hypothesis of composite strengthening is correct, existing models have some limitations in their microstructural origins and resulting flow curves. When martensite is subject to tempering, transformation induced residual stresses can be relaxed at lower temperatures (300 °C and 400 °C) and the composite strengthening response is lowered. At temperatures above 500 °C, the composite strengthening mechanism is no longer operative and new interpretations based on classical dislocation storage based mechanisms need to be considered.

Two different modelling approaches are presented to rationalise the mechanical response of martensite depending on the tempering conditions. For the as-quenched and low temperature (300 °C and 400 °C) tempered conditions, the two composite models are integrated to consider both the variation in intrinsic yield stresses and the relaxation of residual stresses during straining. For high temperature tempered conditions where the strain hardening capability of martensite is recovered ($T \geq 600$ °C) , a combined isotropic and kinematic hardening model is developed. In both cases, the modelled results show good agreement with experimental tension-compression data. However, further works are required to rationalise the strain hardening behaviour of martensite tempered at intermediate temperatures, especially at 500 °C.

Declaration

I hereby declare that except where specific reference is made to the work of others, the contents of this thesis are original and have not been submitted in whole or in part for consideration for any other degree or qualification in this, or any other university. In particular, I independently performed the alloy processing, electron microscopy, simulations, calculations and analysis presented in this thesis. This thesis is my own work and contains nothing which is the outcome of work done in collaboration with others, except as specified in the text and Acknowledgements.

_____

Lingyu Wang

4 May 2020

Acknowledgement

This thesis would not have been possible without the guidance and support of many people, institutions and funding agencies.

First and foremost, I would like to express my sincere gratitude to my supervisors Professor Christopher Hutchinson and Dr. Laurence Brassart for their patience and guidance throughout the project. Thanks Chris for letting me join the martensite project and for his enthusiasm and constant support during my PhD studies. I have learnt a lot from you during my stays at Monash. Thanks Laurence for introducing me to the continuum mechanics community and her help on the setup of the modelling framework in the beginning of the project.

I would like to thank Dr. Artem Arlazarov for managing the project at ArcelorMittal and providing valuable materials for the current study. I also want to thank him for inviting me to visit Maizieres research centre and the stimulating discussions with colleagues in the industry.

I am also deeply indebted to Professor Yves Brechet for his tremendous help on nearly all aspects of the project during his visit to Monash in August 2019. His deep insight into materials science has helped me reconstruct the theoretical framework of the thesis.

Special thanks to Dr. Yuxiang Wu for working on the martensite project and his help on the analyses of powder diffraction experiments. I am also indebted to you for many fruitful discussions during my study.

Many people have helped on the experimental side of this thesis. Many thanks to Dr. Wenwen Sun and Mr. Sam Gao for their help on the TEM experiments during the last few months of the project. Thanks to Dr. Qi Zhang for her help on the DSC measurements. Thanks to Mr. Brett Williams (Monash Instrumentation Facilities, MIF) for his tolerance and great work on sample making. Thanks to Mr. Adrian Ward and Mr. Graeme Burnett for their help on the setup of the MTS machine. Thanks to the staff at Monash X-ray platform (MXP) and Monash Centre for Electron Microscopy (MCEM) for their support on the characterisation facilities used in this project.

I am also grateful to the group members who are not mentioned above, Dr. Shengchao Yang, Mr. Michael Moriarty, Mr. Derui Jiang, Mr. Timothy Murry and Mr. Thang Vu Dinh, for their companion and friendship throughout the years.

This project would not be possible without the financial support from many funding agencies. I would like to thank the support of ArcelorMittal Global Research and Development and the Australian Research Council through the Linkage Grant Scheme (LP150100756). I am also grateful for the support from the Australian government through the Australian Government Research Traning Program (RTP) scholarship.

Finally, I would like to thank the love, encouragement and support from my family throughout my studies in Australia.

Table of contents

List of Figures

List of Tables

Chapter 1

Introduction

1.1 General background

Car manufacturers are in constant search for advanced materials that are able to reduce the weight of vehicles. The goal of the weight reduction is to meet the increasingly strict regulatory and legislative requirements on fuel consumption and greenhouse gas emissions. There are mainly two strategies to achieve this goal: (i) to use stronger steel materials that enable the reduction in design geometries and (ii) to use alternative low density materials such as aluminium, magnesium and composites. At the same time, the reduction in car body weight should never compromise the strength and toughness of the structure that jeopardises the safety of passengers. As a consequence, the target material should also excel in both strength and elongation that improve the anti-intrusion properties and crash-worthiness. Until now, steels play the main role in car manufacturing thanks to the diversity in microstructures that allows a wide combination of mechanical properties at low cost. In light of the requirements in weight reductions, a road map of development of advanced high strength steels (AHSS) is presented in Figure 1.1 [1, 2]. The x-axis represents the ultimate tensile strength of the steels and the y-axis shows the elongation to failure. These parameters are important for steels used in the automobile industry since the manufactured components should provide both high anti-intrusion properties (i.e. high strength) and high crash-worthiness (i.e. combination of high strength and high elongation) [1].

A classic materials problem in conventional high strength steels (HSS) is that increasing the strength is often accompanied by the reduction in elongation. This situation has been improved by the 1st generation AHSS including the TRansformation Induced Plasticity (TRIP) and Dual Phase (DP) steels. However, the average elongation of the 1st generation AHSS is still relatively low. This limitation triggered the investigation of the 2nd generation AHSS including the TWinning Induced Plasticity (TWIP) steels, Al added Low density steels with Induced Plasticity (L-IP) and austenitic stainless steels (AUST. SS).

Although they demonstrate tremendous ultimate tensile strength and elongation combinations, the low yield strengths and high production cost associated with high alloying additions have limited the production of 2nd generation AHSS. As a consequence, the target for the development of the 3rd generation AHSS is to achieve a high yield strength together with a great tensile strength and elongation combination but with lower solute additions than the 2nd generation AHSS and hence lower cost. Many concepts for the 3rd generation AHSS have been proposed recently and Medium Manganese TRIP steel [3] and Quenching and Partitioning (Q&P) steels [4] are the two most promising steel grades to achieve the goal. In both cases, the microstructures contain bainite/martensite constituents that provide the base strength while the remaining austenite constituents transform to martensite during straining that provides extra strain hardening and improves tensile strengths and total elongation. In addition, martensite is also a key constituent in low Mn TRIP steels and DP steels. Therefore, the understanding of the mechanical properties of martensite is a fundamental concern in the development of future AHSS.

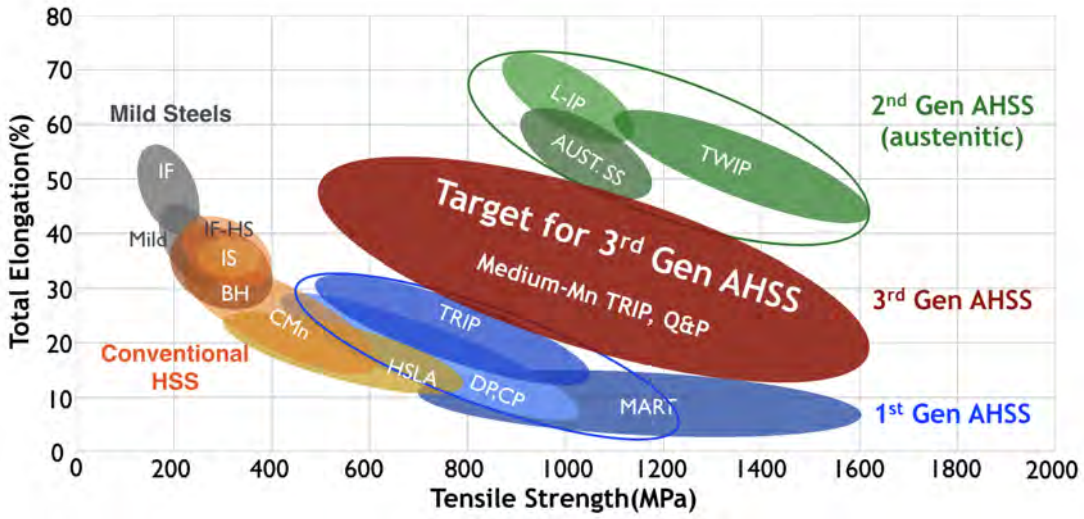

Figure 1.1: *Tensile strengths and total elongation combinations for conventional high strength steels (HSS), existing advanced high strength steels (AHSS) and target generation AHSS, reproduced from [1, 2].*

1.2 Challenges in describing the tensile behaviour of martensite

Historically, martensite is considered as a hard but brittle phase and fully martensitic steels are often used in wear resistant applications such as machine tools, stamping dies and load bearing shafts. The strength of as-quenched martensite is normally attributed to solid solution hardening as the experimental 0.2% proof stress scales with the square root of the carbon content. As the development of AHSS advanced in the last 5-10 years, an increasing number of studies on the strain hardening behaviour of as-quenched martensite have shown that the solid solution strengthening theory can em-

pirically describe the yield strength of martensite but fails to explain the strain hardening behaviour. New interpretations, emphasising the importance of the heterogeneity of martensite structure and the composite effect provided by microstructural elements with different strengths, were proposed recently and demonstrated capabilities in describing both the yield strength and strain hardening of as-quenched martensite [5–7]. Yet the origin of the microstructural elements with different strengths has not been identified and requires in-depth, multi-scale characterisations. In addition, the new interpretations for as-quenched martensite need to be validated and extended to consider tempered martensite since most martensite constituents in AHSS are tempered, or at least heavily auto-tempered. The concurrent occurrences of solute segregation, carbide formation and annealing at elevated temperatures and their effects on the strain hardening of martensite remain to be characterised and understood. This project focuses on the understanding of the strengthening mechanisms of as-quenched and tempered martensite, which includes both experimental and modelling works on the tensile and tension-compression behaviours of the material. The effect of Si and Al on martensite tempering is also studied as they are key alloying elements in the development of 3rd generation AHSS.

Chapter 2

Literature review

In this chapter, literature on the strength of as-quenched and tempered martensite are reviewed. Both topics have been studied extensively in the past but the main focus has been the evolution of yield strengths and the strain hardening properties lack in-depth investigations. In both cases, the review begins with the phase transformations occurred during quenching and tempering followed by discussions on mechanical properties and strain hardening behaviours.

2.1 As-quenched martensite

In Fe-C and Fe-Ni-C systems, martensite adopts a body centre cubic (BCC) or body centre tetragonal (BCT) lattice structure and forms predominantly in two morphologies: lath and plate. The transition between lath morphology to plate morphology in martensite is controlled by the nominal composition, especially the carbon content. Maki *et al.* have produced martensitic steels with carbon contents ranging from 0.1 wt.% to 0.8 wt.% to show the evolution of the substructure evolution of lath martensite (Figure 2.1) [8]. The substructures were refined by an increasing carbon content and a possible transition from lath to plate martensite occurred when the carbon content was greater than 0.6 wt.%. Similar contribution of Ni has been documented by Magee and Davies [9] and Sherman *et al.* [10]. In this review, the emphasis is mainly on lath martensite with low to medium carbon contents and low alloying element contents.

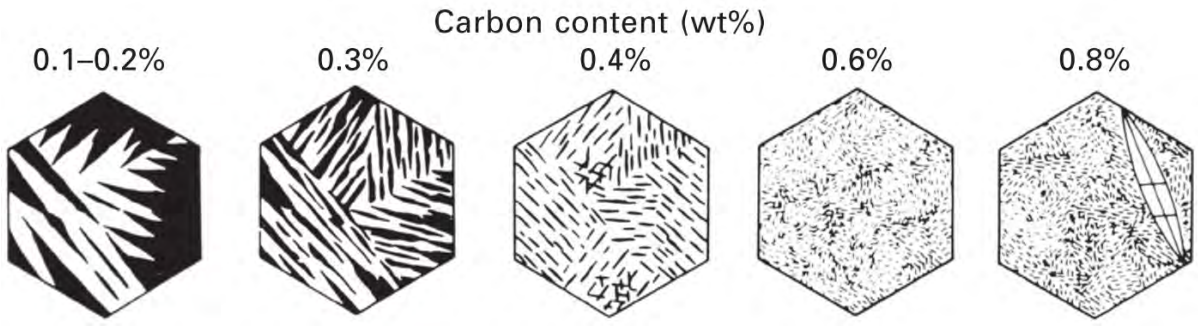

Figure 2.1: *Schematics showing the evolution of martensite morphology with respect to carbon content. The black and white contrasts in the two left-most figures demonstrate the lath morphology of low carbon martensite. Figure adapted from [8].*

2.1.1 Thermodynamics and crystallography of as-quenched martensite

2.1.1.1 Thermodynamics of martensitic transformation

Ferrous martensite is obtained by a displacive and diffusionless transformation of the parent austenite when sufficient undercooling is provided to avoid diffusional transformations such as ferrite and pearlite [11]. Figure 2.2 shows the change in the Gibbs free energies of austenite and martensite as a function of temperature [12]. It demonstrates that the austenite-martensite transformation does not occur spontaneously when the free energy of the two phases are equal (at T_0 temperature) but rather at a lower temperature designated as the martensite start temperature M_s. The reasons for the observed undercooling is attributed to the extra driving force required to accommodate the increase in strain energy during transformation [12].

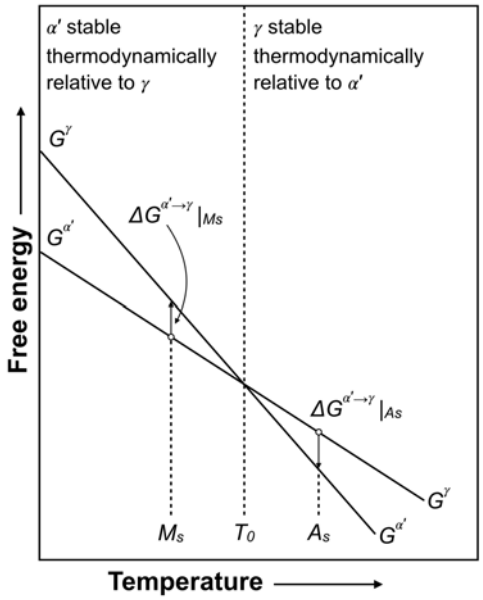

Figure 2.2: *Gibbs free energies of austenite and martensite as a function of temperature. Figure reproduced from [12].*

A common way to estimate M_s for a multicomponent alloy is to use its dependence on alloying elements. While factors such as the prior austenite grain size and external stress affect the onset of martensitic transformation, the M_s temperature is controlled largely by the chemical composition of the steel. Van Bohemen recently studied the measured M_s for multiple steels and proposed an empirical equation (x_i represents the weight percentage of each element) [13]:

$$M_s = 565 - \sum_i K_i x_i - 600\left[1 - \exp\left(-0.96 x_C\right)\right] \tag{2.1}$$

and

$$\sum_i K_i x_i = 31 \cdot x_{Mn} + 13 \cdot x_{Si} + 10 \cdot x_{Cr} + 18 \cdot x_{Ni} + 12 \cdot x_{Mo} \tag{2.2}$$

The effect of carbon is the largest and enters the exponential term while substitutional elements have less effect with Mn being the greatest contributor. While this equation is derived based on the bulk chemical content, the true composition of the untransformed austenite will vary from region to region due to chemical inhomogeneities (e.g. Mn banding) and may be subject to dynamic changes as the transformation proceeds. Experimentally, the start (M_s) and the finish (M_f) of martensitic transformation can be measured by dilatometry.

The martensitic transformation is athermal and the volume fraction of martensite is a function of the quenching temperature T_q. Koistinen and Marbuger have described the transformation with an empirical equation [14]:

$$V_{\alpha'}\left(T_q\right) = 1 - \exp\left[\alpha_T\left(M_s - T_q\right)\right] \tag{2.3}$$

where $V_{\alpha'}$ is the martensite volume fraction at a given quenching temperature (T_q) and α_T is a constant. In most scenarios, the constant α_T is identified as $-0.011\,\mathrm{K}^{-1}$. Van Bohemen has also demonstrated the effect of alloy composition on the change of this constant [13]:

$$\alpha_T\left(10^{-3}\,\mathrm{K}^{-1}\right) = 27.2 - \sum_i S_i x_i - 19.8\left[1 - \exp\left(-1.56 x_C\right)\right] \tag{2.4}$$

and

$$\sum_i S_i x_i = 0.14 \cdot x_{Mn} + 0.21 \cdot x_{Si} + 0.11 \cdot x_{Cr} + 0.08 \cdot x_{Ni} + 0.05 \cdot x_{Mo} \tag{2.5}$$

2.1.1.2 Crystallography and orientation relationship of lath martensite

Bain first demonstrated the lattice correspondence between the face centred cubic (FCC) austenite and the BCC/BCT martensite [15]. It can be seen in Figure 2.3a that a BCT cell can be identified in the superlattice consisting of two FCC cells when $(001)_{\alpha'} \parallel (001)_{\gamma}$. During the transformation, the BCT lattice contracts along $[001]_{\gamma}$ and expands along $[110]_{\gamma}$ and $\left[\bar{1}10\right]_{\gamma}$ to achieve the BCC lattice structure (Figure 2.3b). The full orientation relationship (OR) according to the Bain correspondence is:

$$(001)_{\alpha'} \parallel (001)_{\gamma}$$
$$[100]_{\alpha'} \parallel [110]_{\gamma}$$

Carbon atoms in the octahedral sites of the FCC lattice are retained in the BCC octahedral sites since the martensitic transformation does not involve diffusion. However, the carbon atoms in BCC preferably occupy one of the three groups of octahedral sites which can lead to a tetragonal distortion of BCC to a BCT structure [16]. The tetragonality of the martensite lattice is predominantly controlled by the carbon content and is often used to estimate the carbon content in solid solution [17].

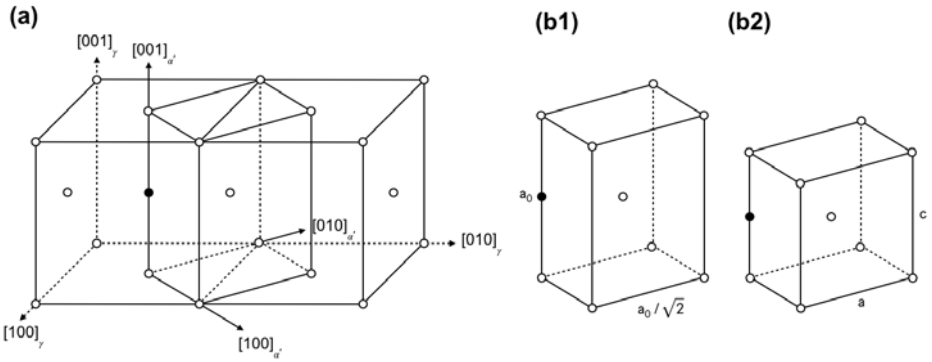

Figure 2.3: *Transformation of parent austenite to martensite according to the Bain correspondence. (a) BCT lattice can be identified in two adjacent FCC cells (b) The BCT cell before (b1) and after (b2) the lattice deformation due to transformation. Figures reproduced from [18].*

Experimentally, the Kurdjumov-Sachs (K-S) OR is the most commonly observed OR [19], which can be described as follows:

$$(110)_{\alpha'} \parallel (111)_{\gamma}$$
$$\left[\bar{1}\bar{1}1\right]_{\alpha'} \parallel \left[\bar{1}01\right]_{\gamma}$$

Other ORs observed in ferrous martensite include the Nishiyama-Wasserman (N-W) OR [20, 21] and the Greninger-Troiano (G-T) OR [22]. It has been observed that the Bain OR is more than 10° from the experimental OR thus the Bain correspondence is insufficient in describing the full crystallographic change during FCC to BCC/BCT transformation. To incorporate the observed high coherency at the austenite-martensite interface, the phenomenological theory of martensite crystallography (PTMC) was proposed and it describes the crystallography change in two steps [16]. The first step is the same as the Bain correspondence that involves the homogeneous distortion of the lattice to achieve the BCC/BCT cell structure. The second step is considered to be the inhomogeneous lattice-invariant deformation that brings the austenite and martensite lattice together on the same invariant shear plane which is the martensite habit plane. As a result, a large strain energy increase must be accommodated by the system during the martensitic transformation, resulting in the extra undercooling required to initiate the martensitic transformation (Figure 2.2).

2.1.2 Phase transformation induced microstructural heterogeneities

2.1.2.1 Hierarchical microstructures due to the effect of the transformation sequence

In lath martensite with low carbon contents, the final transformation product usualy adopts a hierarchical microstructure. A prior austenite grain can be divided into several packets and laths within the same packet share the same habit plane. Laths growing in the same direction then aggregate and form blocks. Both blocks and packets are separated by high angle grain boundaries while laths are usually separated by low angle grain boundaries [23]. A typical schematic of these substructures can be found in Figure 2.4. As a result of this hierarchical microstructure, a variety of constituents with heterogeneous properties may be found in as-quenched martensite.

The overall heterogeneity of martensite can be captured nicely by the schematic proposed by Morsdorf *et al.* (Figure 2.4) [24, 25]. The transformation starts with nucleation of martensite laths at the prior austenite grain boundaries when the temperature drops below M_s. The first laths formed do so in an effectively 'strain-free' austenite and their formation results in a three-dimensional strain on the prior austenite grain which is accommodated by plastic deformation, represented by the darkened colour in Figure 2.4. As the temperature decreases, the austenite-martensite transformation becomes more favourable but the laths transformed at lower temperatures grow into a successively hardened austenite matrix, which may hinder the growth of the laths and reduce the final dimensions of blocks. The block dimensions can also be limited by geometrical constraints as the martensite crystals transformed at early

stages will take up more space in the austenite grain. The transformed martensite should inherit both the dislocation density and the carbon content of the parent austenite that it replaces which means there will also be differences in the mechanical properties of the different laths formed at different temperatures.

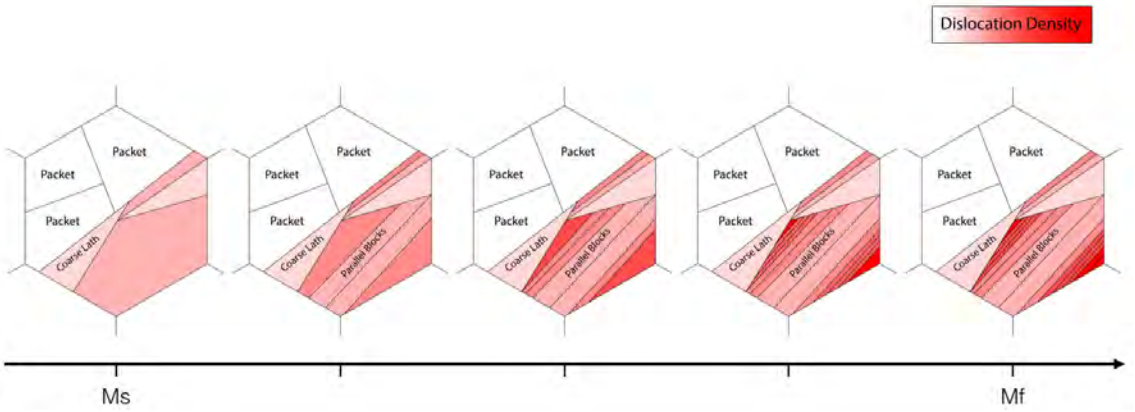

Figure 2.4: *Transformation sequence of a modelled austenite grain showing the heterogeneity in product martensite laths. Figure reproduced from [25].*

2.1.2.2 Retained austenite

As suggested by the K-M equation (Eq. 2.3), the fraction of austenite transformed is a function of quenching temperature and the transformation may not be complete for some steels even at room temperature. Experimental observations are often made using dark-field transmission electron microscopy (DF-TEM) with the austenite diffraction spots. An example of inter-lath retained austenite is shown in Figure 2.5 [26]. Laths of martensite are surrounded by retained austenite thin films. Morito *et al.* studied the composition of the retained austenite and found an enrichment of carbon, which suggests the carbon atoms can move from the martensite to the untransformed austenite during the quench and the stabilisation behaviour could be attributed to carbon enrichment [27]. The segregation behaviour can also occur within the martensite lath and will be discussed in the next subsection.

2.1.2.3 Segregation of carbon to defects (auto-tempering)

Since carbon occupies the interstitial sites in the BCC martensite, it has significant mobility even at room temperature. The effect of carbon segregation to defects in plain carbon ferritic steels has been proposed by Cottrell and co-workers as reviewed by Baird [28]. In the case of martensite, the numerous substructure boundaries as well as the high dislocation density makes it naturally prone to carbon segregation. One specific aspect that can lead to microstructural heterogeneity is the segregation occurring concomitantly with martensite formation in high M_s steels, known as *auto-tempering*.

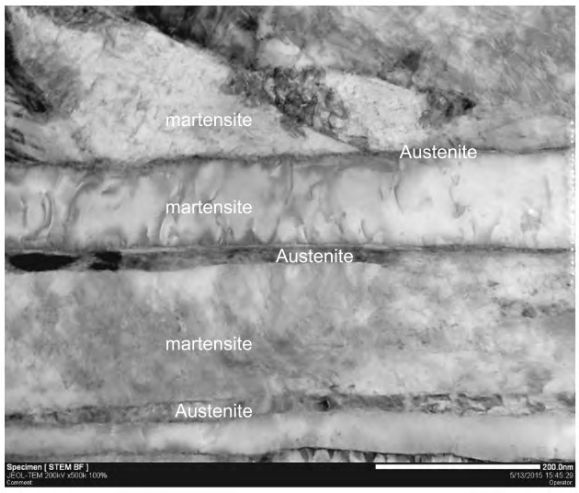

Figure 2.5: *Retained austenite thin film in as-quenched martensite, shown in an Fe-0.25C-2Mn-1.5Al (wt.%) steel. Figure adapted from [26].*

Speich has performed electrical resistivity measurements that probed the carbon content sensitivity of auto-tempering (Figure 2.6) [29]. In this case, although no carbide precipitation was observed due to the fast cooling rate, the trend of increasing resistivity was marked with two distinct regimes. The first regime showed that for martensite with less than 0.2 wt.% carbon, almost all carbon atoms were segregated to lattice defects as compared with the complete segregation master line. The slope of the second regime, on the other hand, was in between the no segregation and complete segregation lines so it appears that carbon segregation cannot be avoided even at high carbon contents.

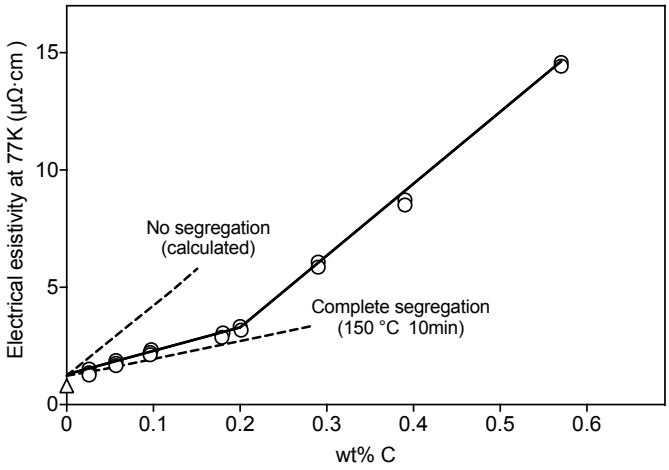

Figure 2.6: *Electrical resistivity of martensitic steels plotted against the carbon contests to show the evolution of segregation behaviour. Figure reproduced from [29].*

Calculations on carbon diffusion below the M_s temperature have be performed by several authors. Morsdorf *et al.* [24] and Hutchinson *et al.* [30] have constructed a simple integration scheme over the mean diffusion distance $2\sqrt{Dt}$ using a diffusion coefficient $D = 0.02\exp\left(-\frac{109600}{RT}\right)$ in $\mathrm{cm^2 s^{-1}}$ ($R = 8.314$ J/(mol · K), and T is the temperature) [30]. Figure 2.7 shows the calculation for an Fe-

0.13C-5Ni (wt.%) steel that forms martensite during cooling from 423 °C [24]. It demonstrates that for martensite crystals formed at temperatures greater than 400 °C, the diffusion distance of carbon in the BCC lattice could be 1.5 μm even at a 1000 K/s cooling rate. For lower cooling rates, the diffusion distance could exceed 10 μm. The diffusion distances in both cases are in the range of block and packet or even prior austenite grain sizes. When the cooling rate is sufficiently high and the martensite forms below 300 °C, the distance can be lowered to nanometres but this still resembles the size of laths. Takaki *et al.* also demonstrated the possibility to form transition η-carbide during auto-tempering when an intermediate cooling rate was used [31].

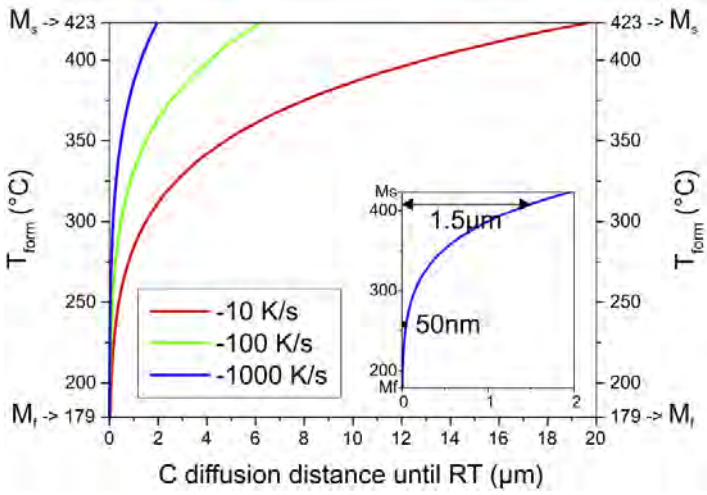

Figure 2.7: *Diffusion distance of carbon from the M_s temperature to the room temperature. Figure adapted from [24].*

The work of Morsdorf *et al.* and Hutchinson *et al.* also included atom probe tomography (APT) results that studied the local enrichment of carbon at lattice defects [24, 30]. In Figure 2.8a, three lath boundaries enriched with carbon are observed with two of them spaced very closely. A carbide particle can also be seen at the right of the tip. Other features in the tomograph that had darker contrast were characterised as dislocations. With a higher carbon content, carbon segregated to dislocations was also apparent in Figure 2.8b but more carbon atoms could also be found randomly distributed in the solid solution. Morsdorf *et al.* showed that the segregation could be vastly different in adjacent fine and coarse laths probably due to the effect of transformation sequences [24], with the coarse laths formed at high temperatures and the fine laths formed at lower temperatures (Figure 2.4). Nevertheless, it should be noted that although APT can give very nice description of the segregation behaviour, its limited sampling volume makes it difficult for the studies of prolonged tempering effect when the size and spacing of cementite particles are of the order of tens of nanometres.

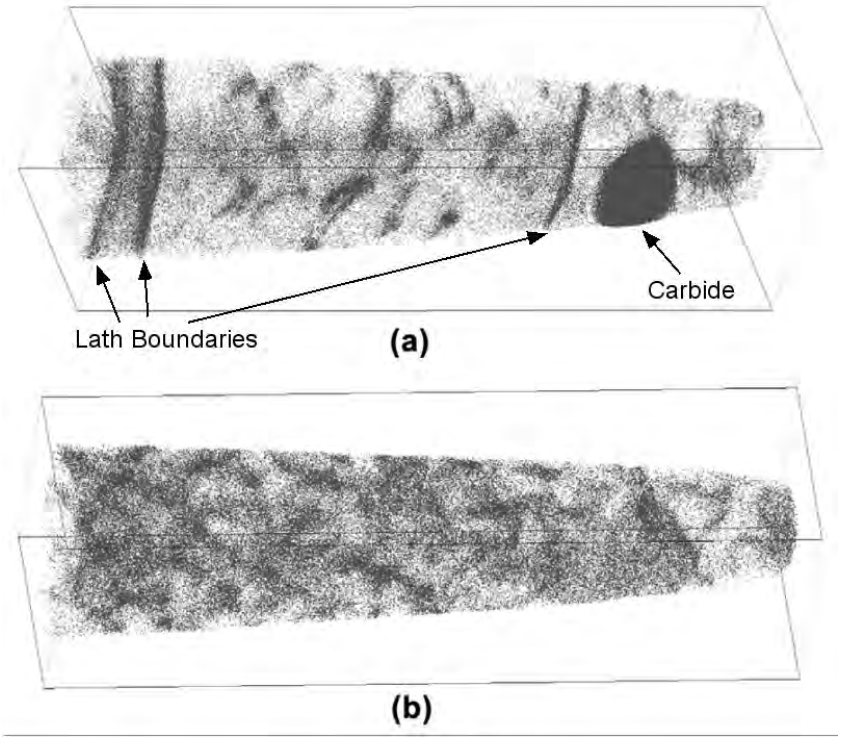

Figure 2.8: *APT results of carbon segregation at lattice defects (a) Fe-0.23C (wt.%) steel, tip length 210 nm, 17×106 atoms (b) Fe-0.48C (wt.%) steel, tip length 220 nm, 17×106 atoms. Figures adapted from [30].*

2.2 Mechanical properties of as-quenched martensite

In the majority of studies of martensite strength, the 0.2% proof stress is often regarded as the approximation of the yield strength [32]. However, the true stress-strain response of as-quenched martensite does not always show a clear yield point and is usually characterised by an extended elastic-plastic transition. As a consequence, the 0.2% proof stress and the ultimate tensile strength (UTS) of martensite are strongly influenced by the strain hardening behaviour. This section is thus divided into three parts: the first part shows experimental findings on the unique tensile behaviour of as-quenched martensite; the second part reviews classic strengthening theories which focus on the high yield strength of as-quenched martensite whilst the third part discusses the descriptions developed to explain the high strain hardening behaviour of as-quenched martensite.

2.2.1 Characteristics of the tensile behaviour of as-quenched martensite

Muir *et al.* first studied systematically the change in the elastic limit of martensite as a function of carbon content and tempering temperature [33]. It was interesting to find that for martensite with low carbon contents (0.2 wt.% and 0.4 wt.%), the measured elastic limits in the as-quenched state were almost the same and approximately one tenth of the ultimate tensile strength. As tempering proceeded, the elastic limit increased to a peak between 205 °C to 370 °C and then further decreased with higher tempering temperatures. Allain *et al.* recently summarised experimental results from Fe-C and Fe-Mn-C systems and plotted the true stress-strain and strain hardening behaviours of as-quenched martensite (Figure 2.9) [5]. The stress-strain plots show the low elastic limit and extended elastic-plastic transition (Figure 2.9a).

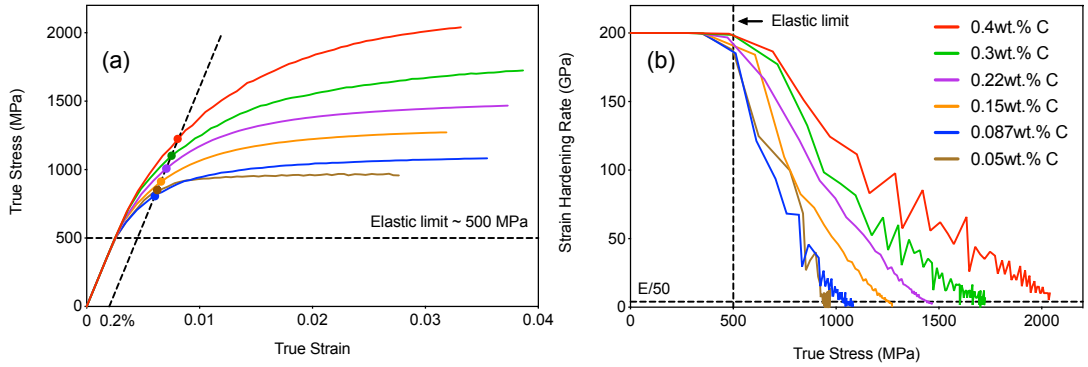

Figure 2.9: *True stress-true strain (a) and strain hardening (b) behaviours of selected as-quenched martensite. Figures reproduced from [5].*

Further interpretation can be made from the strain hardening rate versus true stress plot (Figure 2.9b, proposed by Kocks and Mecking [34]). The curves show three distinct regimes; the first stage corresponds to elastic loading and the strain hardening rates are constant at 200 GPa, the second regime marks a linear decrease in the hardening rate followed by the third exponential decay regime. All curves deviate from the elastic regime at approximately the same value (300 - 500MPa) independent of carbon content. Regime 2 and 3, however, show a clear dependency on the carbon content until the onset of necking, which suggests the 0.2% proof stress observed in previous studies is a result of considerable strain hardening at the early stage of plasticity. The third feature highlighted by Allain *et al.* is that the extremely high strain hardening rate cannot be justified using the classical model of dislocation storage [5]. According to Kocks and Mecking, the maximum contribution of dislocation storage in FCC or BCC crystals is around E/50 (4 GPa) to E/100 (2 GPa) [34]. This value is significantly

lower than the observed hardening rates in as-quenched martensite (50 GPa - 150 GPa in Figure 2.9b). Swarr and Krauss demonstrated that the low elastic limit and high initial strain hardening rate could be diminished by fast tempering of the specimen at 400 °C for 1 minute [35], which further illustrates the uniqueness of this phenomenon in as-quenched martensite.

2.2.2 Classic strengthening theories of as-quenched martensite

2.2.2.1 Solid solution strengthening

Solid solution strengthening is usually considered as the most important strengthening mechanism for martensite in the literature [32]. As martensite inherits the chemical composition from the parent austenite, it is natural to consider that the supersaturated solute atoms (both substitutional and interstitial) interact strongly with dislocations and provide substantial strengthening. However, it is difficult to study the contribution of substitutional and interstitial atoms separately as the atomic percentage of interstitial atoms (mostly carbon) is much higher compared to substitutional atoms and the individual effect of an interstitial atom is much larger than a substitutional atom because of the much larger strain field associated with the interstitial size misfit. This means strengthening by substitutional elements less effective than carbon/nitrogen. As a result, the studies reviewed in this section are predominantly on the effect of carbon. The effect of substitutional atoms can be estimated using the relationship found by Pickering and Gladman in ferritic alloy steels [36].

In the Fe-C system, Speich and Warlimont [37] studied the 0.2% yield strength of martensite as a function of carbon content ranging from 0.0004 wt.% to 0.18 wt.%. Due to the lack of hardenability in the steels with less than 0.013 wt.% carbon, it was not possible for the them to obtain fully martensitic structures. Figure 2.10 shows that for materials with more than 0.013 wt.% carbon, the 0.2% proof stress increases linearly with the square root of the carbon content. According to Fleischer's theory of solid solution strengthening [38], Speich and Warlimont found the dependency of the 0.2% yield strength (MPa) on carbon concentration could be estimated by:

$$\sigma_y\,(0.2\%) = 414 + 1724\,(\text{wt\% C})^{1/2} \tag{2.6}$$

where the first term on the right-hand side of the equation considered the contribution of the frictional stress of pure iron and the extra stress needed for dislocations to propagate through dislocation cell walls (lath boundaries) with a constant spacing (250 nm) [37]. Moreover, Speich and Warlimont discussed that the carbon atoms in the studied steels would easily segregate to substructure boundaries and dislocations due to the high M_s temperature [29, 37]. Segregated carbon at dislocations may further hinder the movement of dislocations and contribute to hardening.

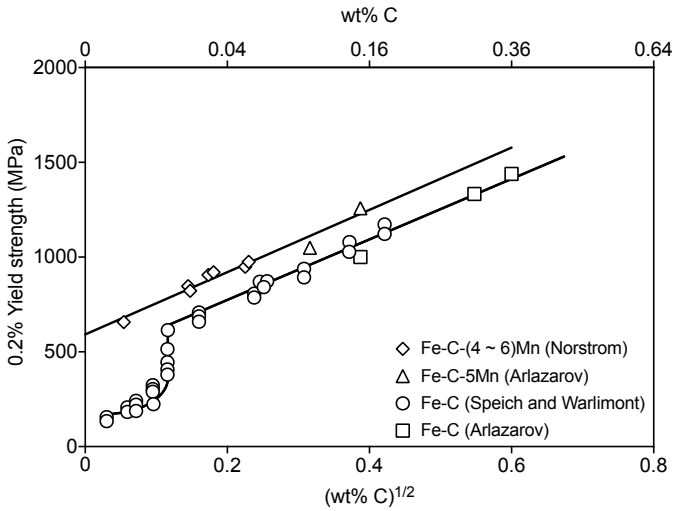

Figure 2.10: *0.2% yield strength as a function of the square root of the carbon content. Figure reproduced using data from [7, 37, 39].*

A more recent study by Hutchinson *et al.* [30] investigated the hardness of as-quenched martensite with carbon contents ranging from 0.1 wt.% to 0.5 wt.%. After converting the hardness values to yield strengths and subtracting contributions from the base strength, substructure boundary hardening and dislocation hardening, they found the unaccounted strengths were also proportional to the square root of the carbon content. In this case, APT experiments were conducted to show that while the test specimens were quenched into brine directly after austenitisation, significant segregation of carbon to dislocations and lath boundaries could still be observed (Figure 2.8) [30]. Since there was limited evidence to suggest other strengthening mechanisms in as-quenched martensite, the authors reached the conclusion that although carbon atoms were not fully located at interstitial positions, lath boundaries and dislocations enriched with carbon played a more important role in resisting the dislocation motion. Since the observed linearity is obtained using the 0.2% proof stress which is significantly affected by strain hardening (Figure 2.9a), the $C^{1/2}$ dependence may also be a result of the increase in strain hardening capabilities as a function of carbon content, even though carbon is not fully in solid solution.

In an attempt to study the strength of the ultra-low carbon martensite, Nörstrom [39] used Mn additions to improve the hardenability of the studied steels with 0.022wt.% to 0.058wt.% carbon. Nörstrom also plotted the 0.2% proof stress against the square root of carbon content in order to compare with Speich and Warlimont's results (Figure 2.10). It was found that two extrapolated lines shared virtually the same slope despite the increase of proof stresses in Mn containing martensite. If Pickering and Gladman's Mn solid solution hardening coefficient ($\sim$32 MPa per wt.% of Mn) is considered [36], the 175 MPa strength increase is justifiable. However, Arlazarov *et al.* showed in Fe-Mn-C steels that although the correlation between the yield strength and the C/Mn content can be extrapolated to higher carbon contents (Figure

2.10), it fails to describe the higher UTS in the steels with 5 wt.% Mn. The solid solution strengthening from Mn is only able to rationalise the yield strength but not the strain hardening behaviour [7]. They suggested that carbon and manganese can work in synergy during strain hardening of as-quenched martensite.

2.2.2.2 Substructure boundary strengthening

In many preceding studies on the effect of carbon content, the size of substructures (lath thicknesses, block widths, packet and prior austenite grain sizes) was either ignored or identified to be the same [37]. In reality, the hierarchical substructures resulting from the sequence of martensite transformation as a function of temperatures (Figure 2.4) can provide substantial strengthening to the material via boundary strengthening. According to the classic Hall-Petch relationship [40, 41], the contribution from substructure boundaries can be estimated by:

$$\Delta\sigma_{gb} = k_{gb} D_g^{-\frac{1}{2}} \tag{2.7}$$

where k_{gb} represents the potency of the substructure boundary in resisting dislocation motion and D_g is the effective grain size. In martensitic structures, prior austenite grain boundaries, packet boundaries and most block boundaries can all be classified as high angle grain boundaries (grain misorientations greater than 15°) that contribute to boundary strengthening [23, 35, 42–44]. It is thus insufficient to study only the effect of prior austenite grain boundaries as substructure morphologies can also be altered via different thermal mechanical processing routes [45].

Figure 2.11a shows a summarised plot of 0.2% proof stresses against packet sizes. Roberts first studied this effect in the Fe-Mn system and found a linear correlation when the Mn additions were high enough to produce fully martensitic structures [43]. The increase from 5 wt.% Mn to 9 wt.% Mn did not result in a change in the slope of the correlation. Krauss and his collaborators followed this study in the Fe-C system and showed a much steeper slope with 0.2 wt.% carbon [35, 44]. They have attributed this steep increase to the interaction between carbon and packet boundaries. More recently, Morito *et al*. performed similar experiments on Fe-Mn-C steels with the same carbon content but with Mn additions [42]. The results showed a much decreased slope that contradicts the prediction in Krauss' and Roberts' studies. Morito *et al.* suggested the discrepancy could be alleviated by considering block widths as the effective grain size since the block widths were found to be finer after adding 2 wt.% Mn. Figure 2.11b shows the correlations between the 0.2% proof stress and the block width from the works of Morito

et al. and Swarr and Krauss. It should be noted that the block width values for the Fe-0.2C (wt.%) steel were calculated by Morito *et al.* with the correlation between the packet size and the block width determined in their work [42]. In this situation, the addition of Mn showed no significant effect on the slope of the correlation, which suggests the block width may be considered as the effective grain size.

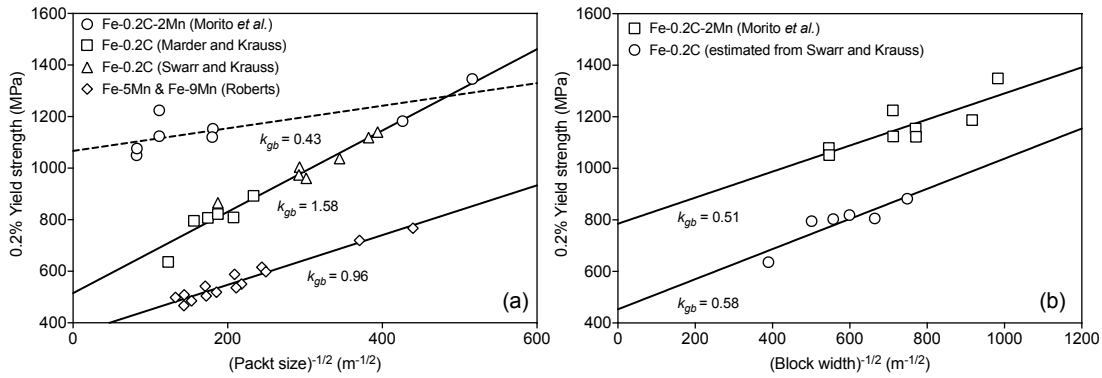

Figure 2.11: *0.2% yield strengths of martensitic steels with different compositions plotted against the inverse square root of measured packet (a) and block (b) sizes. k_{gb} represents the effectiveness of packet boundaries in resisting dislocation motion. Figure reproduced from [46], original data from [35, 42–44].*

Thanks to the recent advances in micro-mechanical testing, many researchers have shown that the presence of block boundaries indeed strengthens as-quenched martensite [47, 48]. Figure 2.12a shows the results of micro-bending tests on samples with and without a block boundary performed by Shibata *et al.* in a Fe-23Ni (wt.%) steel [47]. It is obvious to see the increase of the onset of the micro-yielding by introducing the block boundary. The strain hardening behaviour was also seen to be greater when the block boundary is present. Further imaging of the specimen surface showed dislocation slip cannot be easily transmitted through the high angle block boundary thus confirming the contribution of the block size. More evidence can be found in the work of Du *et al.* in which the critical resolved shear stress required to activate slip increases linearly with the square root of the number of block boundaries in microscopic tensile samples [48]. Du *et al.* also found the same correlation in the number of sub-block boundaries (misorientations around 10° between two K-S variants [23]) but with a slightly lower slope (Figure 2.12b). With the help of fracture surface analysis, they concluded that block and sub-block boundaries can both serve as barriers for dislocation motion but the sub-block boundary has a lower potency to resist dislocation transmission.

2.2.2.3 Dislocation strengthening

As a result of the accommodation of transformation induced strain (Figure 2.4), high dislocation densities are found in as-quenched martensite. Morito *et al.* summarised the TEM measurements from other authors and plotted the dislocation densities as a function of nominal carbon content (Figure 2.13a) [49]. At low carbon contents, results from both Kehoe and Kelly [50] and Nörstrom [39] show an

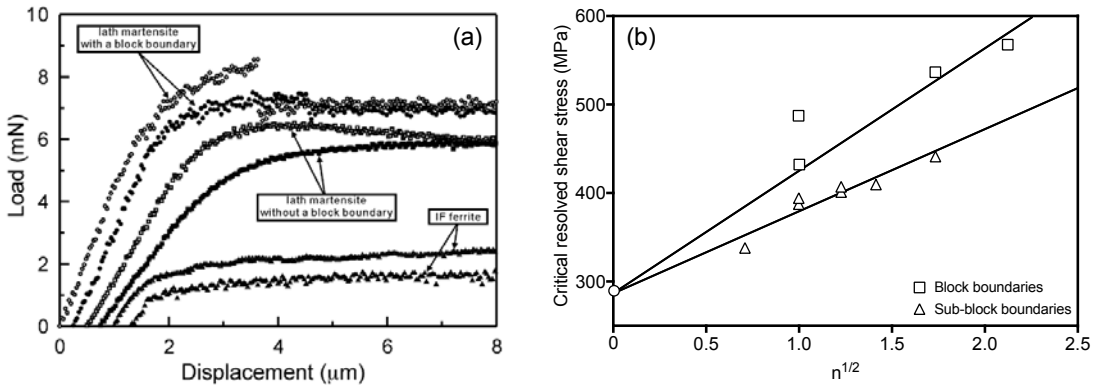

Figure 2.12: *Effect of block boundary on the strengthening of as-quenched martensite. (a) Load-displacement curves of micro-bending tests conducted on samples with and without a block boundary. Figure adapted from [47]. (b) Critical resolved shear stress as a function of number of block/sub-block boundaries. Figure reproduced from [48].*

almost linear correlation between dislocation densities and carbon contents. Mn addition seemed to reduce the overall dislocation density. In the study of Morito *et al*. the increasing trend persisted until 0.6 wt.% carbon but decreased at 0.8 wt.% carbon. Based on the study of Maki *et al.* the transition from dislocated lath martensite to internally twinned plate martensite could be the reason [8]. Nevertheless, there appears to be a sharp increase in dislocation densities when the carbon content is raised from 0.4 wt.% to 0.6 wt.%. It should also be noted that high standard deviations seen in the high carbon region illustrates the high uncertainty in the measurement using TEM.

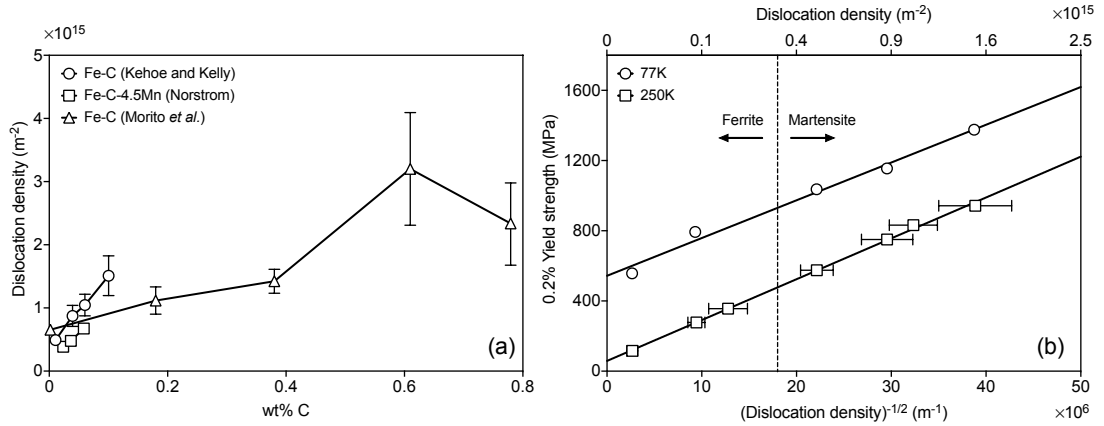

Figure 2.13: *Effect of dislocation density on the strength of as-quenched martensite. (a) Evolution of dislocation density as a function of carbon content. Figure reproduced from [49]. (b) Evolution of 0.2% yield strength as a function of dislocation density. Figure reproduced from [50].*

The contribution of dislocation strengthening to the flow stress can be described with Taylor's equation [51]:

$$\Delta\sigma_f = \alpha M \mu b \rho^{1/2} \tag{2.8}$$

where α is a constant related to the efficiency of the obstacles, M is the constant considering the polycrystalline effect (i.e. the Taylor factor), μ is the shear modulus, b is the Burger's vector and ρ is the dislocation density. Kehoe and Kelly performed tensile tests to evaluate the strengthening effect of dislocations in as-quenched martensite with carbon contents from 0.01 wt.% to 0.1 wt.% (Figure 2.13b) [50]. When the measured 0.2% yield strengths were plotted against the square root of dislocation densities, the relationship could be described well with a linear regression as suggested by the Taylor's equation. Despite the drastically different nominal carbon contents, the carbon contents in solid solution for all steels were found to be very similar using internal friction experiments. Therefore, Kehoe and Kelly concluded that the solid solution strengthening contribution observed by Speich and Warlimont (Figure 2.10, [37]) was actually an indirect effect of the increase of dislocation density as the carbon content was raised. Furthermore, since the carbon contents investigated by Kehoe and Kelly were all below 0.2 wt.%, it is likely that dislocations were segregated by carbon [29] and the strengthening effect was actually due to the complicated interaction between carbon clusters and dislocations, as suggested by Hutchinson *et al.* [30].

2.2.3 Early yielding and strain hardening of as-quenched martensite

While the traditional views on the strengthening of as-quenched martensite could explain the high hardness and strength of the material, they have difficulties addressing the extended elastic-plastic transition and the extremely high strain hardening rate found in as quenched martensite (Figure 2.9). In this section, theories on the early yielding and strain hardening of as-quenched martensite are reviewed.

2.2.3.1 Mobile dislocations and formation of dislocation cells

In an early investigation by McEvily *et al.* in the Fe-Ni-C system, they attributed the low elastic limit of the as-quenched martensite to the movement of free dislocations [52]. It was argued that as the martensitic transformation proceeds with decreasing temperatures, there would be constituents in the final microstructure that inherit the high dislocation density of the strained austenite. When martensite is strained, these dislocations are free to move until being pinned by carbon atoms. To test this hypothesis, specially designed Fe-Ni-C alloys with $M_s \approx -35\,^{\circ}\mathrm{C}$ were transformed and tested at $-196\,^{\circ}\mathrm{C}$ to demonstrate the low elastic limit. After ageing the transformed sample at room temperature for 4 hours and tested at $-196\,^{\circ}\mathrm{C}$, there was a significant increase in the elastic limit of the aged sample. It was argued that the ageing treatment introduced segregation of carbon and increased the elastic limit.

To avoid the complication with low M_s plate martensite and retained austenite, Takaki and co-workers used Fe-Ni alloys with ultra-low carbon content to test this hypothesis [53, 54]. While the as-quenched martensite shows a low elastic limit and extended elastic-plastic transition, samples after 5% cold rolling show a much longer elastic region (Figure 2.14). TEM investigations (Figure 2.15) showed that dislocations were randomly distributed in the as-quenched martensite but were re-arranged into cell structures after 2% deformation which resembled the results of Swarr and Krauss in an Fe-0.2C (wt.%) steel [35]. Line profile analyses by the same group suggested that while there was limited change in the dislocation density before and after cold rolling, there was an increase in the fraction of edge dislocations [54]. Based on the experimental results, they suggested that cold working broke the initial lath boundaries and provided more edge dislocations to construct dislocation cell walls [55]. A stable dislocation cell structure requires much larger stress to be exerted in order to deform the material. This is similar to the theory proposed by Swarr and Krauss in which the strain hardening of as-quenched martensite was attributed to the decrease in the average free dislocation length as dislocation cell structures developed during straining [35].

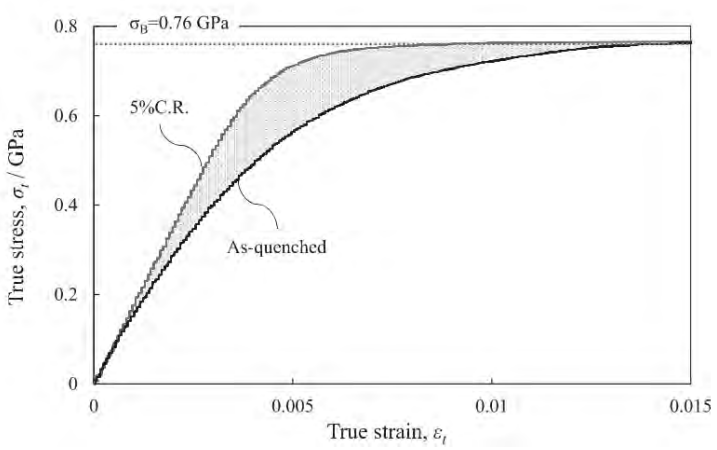

Figure 2.14: *The true stress-true strain curves of an as-quenched Fe-18Ni (wt.%) steel before and after cold rolling. Figure adapted from[54].*

However, it has been emphasised with experimental results that there is a high chance that the majority of carbon atoms are trapped by lattice defects during normal quenching [29, 30]. It is then difficult to quantify the number density of mobile dislocations and their contributions to strain hardening in traditional Fe-C martensite. On the other hand, it may not be possible that the mobile dislocations account for all of the unusually high strain hardening during loading. Consider a martensitic steel with a mobile dislocation density $\rho_m = 1 \times 10^{15}$ m^{-2} and uniaxial tensile loading is exerted to move the dislocations. The linear strain associated with the dislocation motion can be estimated as $\varepsilon = \rho_m bL/M \approx 1.8\%$, where $b = 0.248$ nm, $M = 2.75$ and L, the distance dislocations travel, is estimated as the typical lath thickness of 200 nm. Hence the mobile dislocations that might move freely and

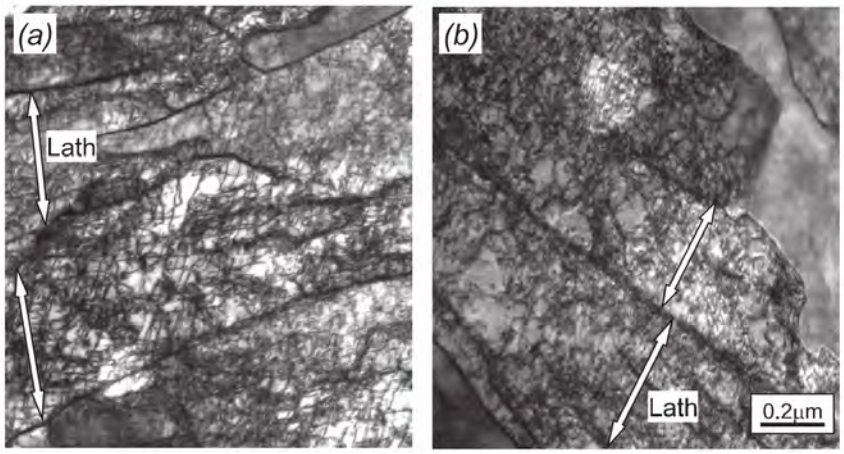

Figure 2.15: *Dislocation substructures in martensite. (a) Dislocations are randomly distributed in the as-quenched Fe-18Ni (wt.%) martensite. (b) Entangled dislocation network formed after 2% deformation. Figure adapted from [54].*

cause the low elastic limit will be exhausted at the early stage of straining of 1.8%. Although one may argue that the magnitude of ρ_m in this approximation may be too small, the mean free path of mobile dislocations scales with $1/\sqrt{\rho_m}$ which means the effective glide distance of dislocations will only be smaller than 200 nm if ρ_m is large. Theoretical treatments are lacking to rationalise the extremely high strain hardening rate of as-quenched martensite based on the dislocation cell mechanism.

2.2.3.2 Retained austenite and the TRIP effect

As shown in previous sections, it is not always possible to transform all the austenite to martensite. Usually there will be a fraction of retained austenite located in between martensite laths. Retained austenite can be softer than the surrounding martensite matrix and may further contribute to strain hardening due to the TRIP effect. Magee and Paxton have demonstrated using three-point bending tests that retained austenite in Fe-Ni martensite could lead to an early yielding of the bulk specimen and provide extra hardening via austenite-martensite transformation [56]. Zaccone and Krauss found in a series of slightly tempered AISI 41xx steels that the elastic limit decreases as a function of increasing carbon content up to 0.8 wt.% while the volume fractions of retained austenite varied from 1.4% to 22% [57]. During straining of the AISI 4150 sample quenched and tempered at 200 °C, the retained austenite fraction dropped from 5.9% to 3.8% at 0.002% true strain, suggesting the stress-assisted austenite transformation contributed to the early yielding. However, the effect of low temperature tempering on the stability of retained austenite was not fully discussed in their work. Further explanation on this issue will be given in a later section. In another study conducted by Morsdorf *et al.* [25] on an as-quenched Fe-0.3C-5Ni (wt.%) steel, synchrotron XRD was used to study the evolution of retained austenite as a

function of accumulated strain. It was found that the 1% retained austenite in the undeformed, as-quenched martensite disappeared at approximately 4% strain. Hence the retained austenite might not contribute to the plasticity at higher strains and the full strain hardening behaviour could be a result of a combination of TRIP effect and dislocation slip.

Recent theoretical treatments on this assumption focused mainly on the thin-film retained austenite at substructure boundaries [27, 58]. By carefully orientating lath, blocks and sub-block boundaries to the loading direction, Du *et al.* showed in micro-tensile tests that when the substructure boundaries were at 45° to the tensile axis, sliding of the boundaries was more favourable than dislocation slip. It was proposed that the $(111)_\gamma$ habit plane for laths and blocks (also the favourable slip plane in FCC systems) acted as a 'greasy' plane for substructure boundary sliding [59]. The hypothesis was pursued by Maresca *et al.* within a crystal plasticity model [58]. The model constructed an interconnected retained austenite network (average width about 10 nm, volume fraction at 5%) in martensite which demonstrated that the incorporation of 5% retained austenite can indeed decrease the yield stress (blue and green curves in Figure 2.16c) of the material regardless of the morphology of austenite films (Figure 2.16a - b). However, the model does not include the implementation of the TRIP effect which leads to low strain hardening of the material with 5% retained austenite as seen in the slope of the red and the blue/green curves in Figure 2.16c, which is not consistent with the high strain hardening rate found in as-quenched martensite (Figure 2.9). Furthermore, the retained austenite is not stable at high tempering temperatures which should not contribute much to the strain hardening of tempered martensite.

2.2.3.3 Mechanical heterogeneity

As shown schematically in Figure 2.4, the microstructure of as-quenched martensite is not only hierarchical but also heterogeneous. Due to the athermal nature of the transformation, substructures formed at temperatures just below M_s will experience more relaxation in transformation stress and dislocation re-arrangements [24]. At temperatures near M_f, the last formed substructures will have less chance to be auto-tempered. As a consequence, it is reasonable to imagine that the substructures inherit a large distribution of intrinsic strengths and the martensite behaves like a composite material. This assumption was first proposed by Ansell and Arott in 1963 [60], which considered the 'stronger' substructures as finely dispersed reinforcement embedded in a soft matrix. However, it did not attract much attention at that time. Allain *et al.* [5] revisited this explanation with a "continuous composite approach" (CCA) which generalised the discrete Masing model [61] to a continuous distribution of intrinsic yield strengths.

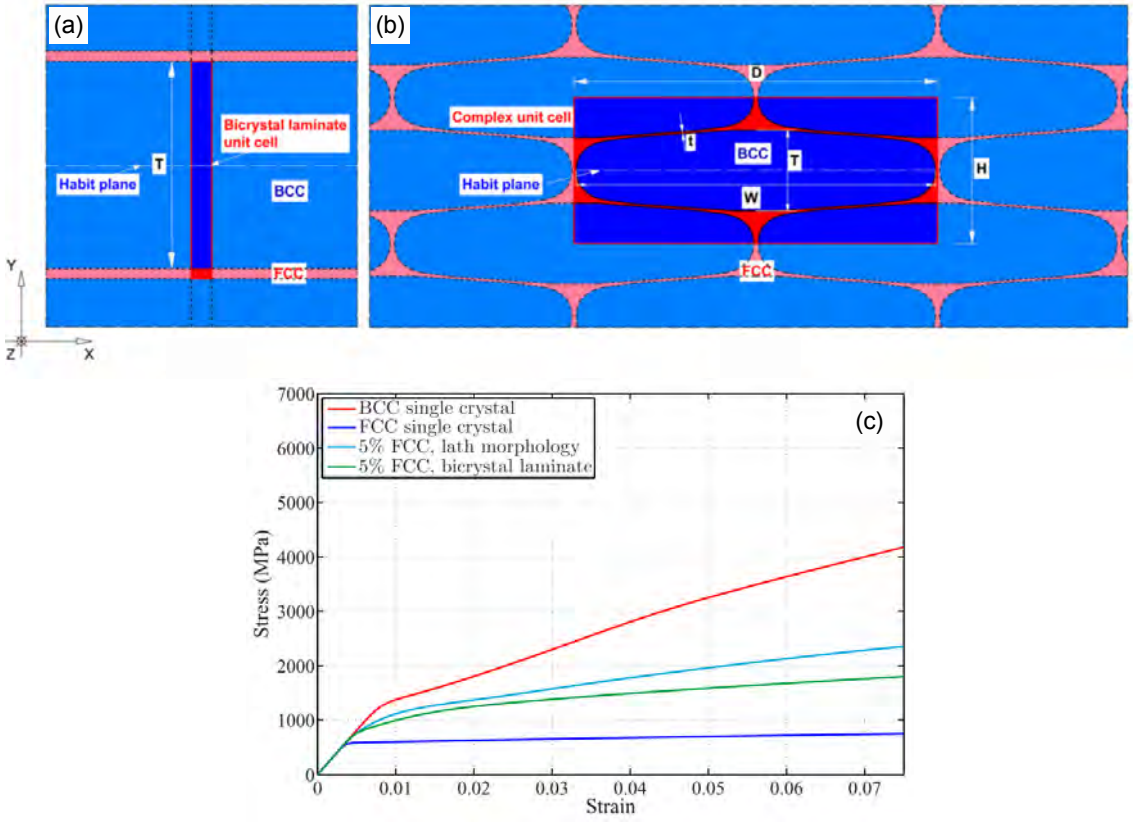

Figure 2.16: *Effect of austenite thin films in the ferrite matrix on the mechanical properties of the bulk material. (a) A simple bicrystal laminate morphology. (b) The lath morphology that mimics the true microstructure of as-quenched martensite. (c) Equivalent Piola–Kirchhoff stress plotted against equivalent Green–Lagrange strain calculated based on BCC/FCC single crystals and the mixed BCC/FCC composite structures. Figure adapted from [58].*

The distribution started at a relatively low value corresponding to the softest constituents in the matrix and extended to very high yield stresses around 4000 to 5000 MPa (Figure 2.17a). The widths of extracted yield stress spectra showed a power law dependence on the carbon content (Figure 2.17b), which implies martensitic steels become mechanically more heterogeneous when more carbon is present [5]. During straining, elements with lower strengths would yield first, leading to the low elastic limit; the extended elastic-plastic transition could also be reproduced when constituents with higher strengths yielded successively (Figure 2.17c). The variation in the local yield stress also results in kinematic hardening due to strain partitioning [62] which allows the model to reproduce the large Bauschinger in as-quenched martensite (Figure 2.17d). Arlazarov *et al.* have also used this model to demonstrate that the effect of Mn addition could be incorporated in order to describe the synergetic strengthening effect by Mn and C [7].

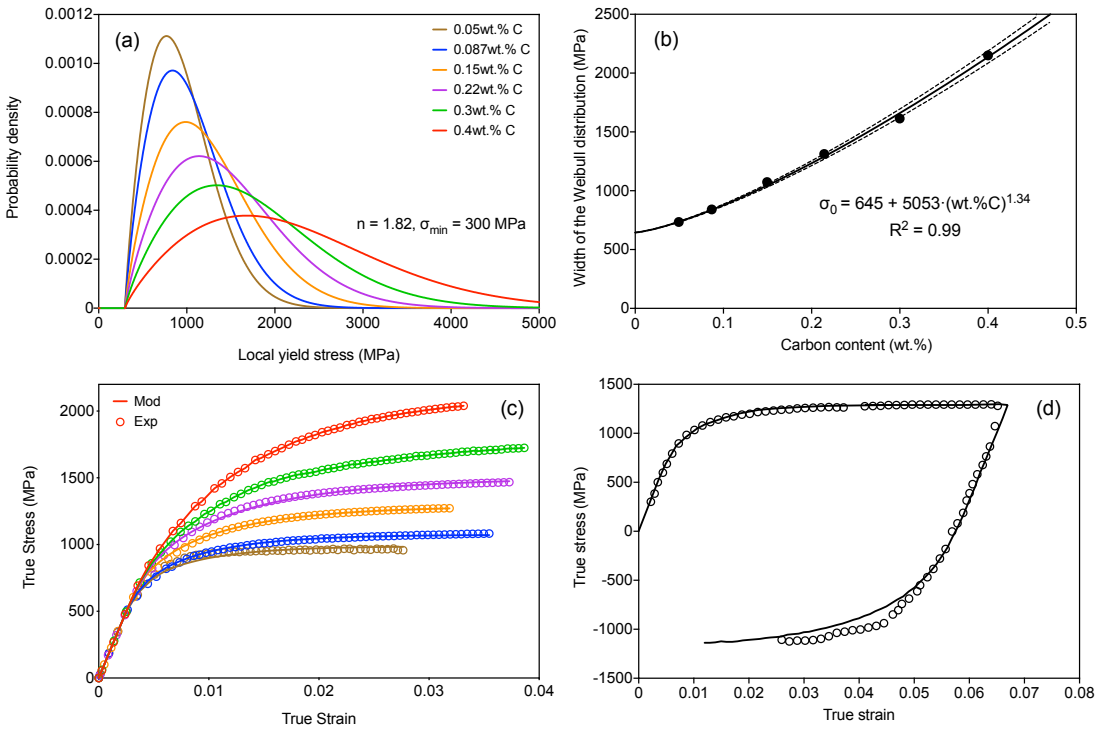

Figure 2.17: *Implementation of the continuous composite hypothesis in steels with various carbon contents. (a) Extracted local yield stress spectra for steels studied in Allain et al. (b) The extracted widths of spectra follows a power low relationship with the carbon content. (c) Comparison between modelled and experimental tensile curves. (d) Comparison between modelled and experimental tension-compression curves in an Fe-0.1C-2.3Mn-0.3Si-0.8Cr (wt.%) as-quenched steel. Figures reproduced from [5].*

Although the continuous composite approach is able to simultaneously describe both the monotonic and the tension-compression behaviour of as-quenched martensite, it is difficult to quantify the mechanical heterogeneity in fine microstructures like martensite. Morsdorf *et al.* [24] and He and Huang [63] showed nanohardnesses in fine laths/blocks were higher than their coarse counterparts. However, Zhang *et al.* suggested that the nanohardness was stable across many laths/blocks [64]. Nevertheless, no authors have reported a mechanical heterogeneity as large as the continuous composite model predicted in as-quenched martensite (Figure 2.17a). In order to justify the validity of the large strength distribution, Scott *et al.* measured nanohardnesses of martensite in two DP steels and compared them with the yield strength spectra of martensite that could best describe the tensile behaviour of the two DP steels [65]. The authors also performed electron energy loss spectroscopy (EELS) experiments to measure the carbon variations in martensite islands and estimated the nanohardness with an empirical correlation between nanohardness and carbon content. Figure 2.18 (a) and (b) show the nanohardness results of martensite in both DP steels using the above experimental/modelling techniques. It can be seen that the agreement between the experimental results and the prediction of the continuous composite model is good in DP-Ref$_{59}$ but the model significantly overestimates the average and the spread of the nanohardness in DP-V$_{52}$. Moreover, the variations of carbon content in martensite

islands could only explain 25% of the modelled spread of nanohardness in DP-Ref$_{59}$ and accounted for an even smaller fraction in DP-V$_{52}$. The authors suggested that other sources of heterogeneities such as the size difference in martensite crystals and residual stresses may explain the remaining stress spectrum. However, Scott *et al.* did not provide detailed explanations for the discrepancies in DP-V$_{52}$ or why martensite islands in two DP steels have drastically different spreads in nanohardness. More systematic studies on the spread of localised mechanical properties need to be performed to test the validity of the continuous composite spectrum.

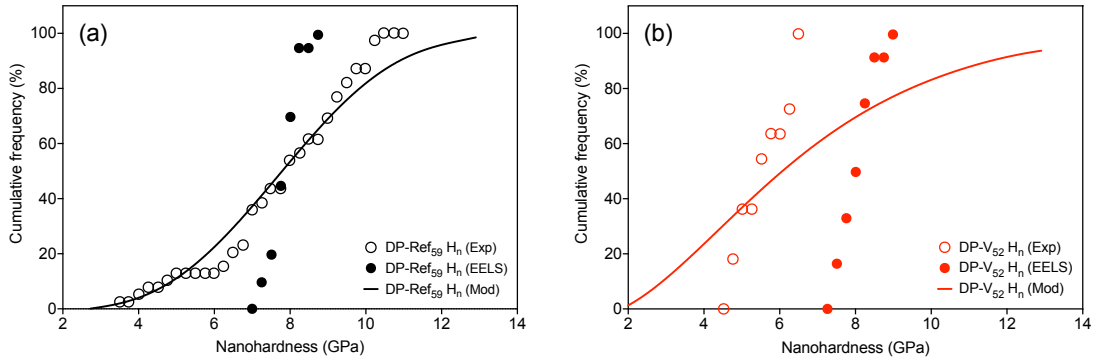

Figure 2.18: *Distribution of nanohardnesses of martensite islands in two DP steels measured/estimated using nanoindentation (Exp), EELS and continuous composite modelling (Mod). (a) DP-Ref$_{59}$ with a composition of Fe-0.186C-1.6Mn (wt.%) and (b) DP-V$_{52}$ with a composition of Fe-0.182C-1.7Mn-0.14V (wt.%). Figures reproduced from [65].*

Ungár *et al.* have also reported a composite-like behaviour of martensite upon straining but interpreted the deformation processes quite differently [66]. Based on neutron diffraction experiments and line profile analyses, the authors showed that the original symmetrical BCC peak before straining became asymmetrical upon straining, which could be fitted with two sub-profiles with increasing or decreasing dislocation densities during deformation. This disruption in the originally quasi-homogeneous dislocation density distribution produced a composite microstructure that could lead to further strain partitioning and internal stress development which affected the overall tensile behaviour of as-quenched martensite. However, the initially quasi-homogeneous dislocation density distribution is hard to justify based solely on the neutron diffraction results as many other factors can contribute to the symmetrical peak such as the self-accommodation of strain in lath martensite [67]. Therefore, although the idea of strain partitioning during deformation bears similarities with the model proposed by Allain *et al.*, more specific multi-scale characterisation experiments are required to justify this assumption.

2.2.3.4 Residual stresses

Muir *et al.* proposed that the low elastic limit exhibited by as-quenched martensite was caused by a series of residual stresses from quenching and the martensitic transformation itself [33]. When residual stresses were oriented towards or against the uniaxial tensile direction, they could either facilitate or resist the onset of plasticity. The authors interpreted the increase of elastic limit after low temperature tempering as an effective way to relax the internal stresses. Leslie and Sober also remarked the apparently high strain hardening rate at the initial stage of plasticity was a result of residual stress relaxation rather than a true dislocation storage response [68]. In support of this argument, Magee and Paxton performed reversible three point bending experiments to show that when the initial loading was relaxed and reversed, there was an appreciable increase in elastic limit [69]. Unfortunately, since the material they examined could have around 10% retained austenite, it was difficult to differentiate the true contribution of residual stresses as well as the origin of the increased elastic limit in the reverse direction.

Recently, Hutchinson and co-workers developed a similar composite model based on a distribution of small scale, Type II residual stresses remaining from the martensitic transformation [6, 70]. They proposed that the extended elastic-plastic transition can be regarded as gradual yielding of constituents with residual stresses of different orientations and magnitudes. If the constituents have the same yield stress, the residual stresses can be homogenised during plastic loading until the ultimate tensile strength is reached. As a result, the reported peak narrowing [53, 71, 72] and peak asymmetry [66, 73] in diffraction experiments after deformation were not caused by a reduction in dislocation densities but were results of residual stress homogenisation and heterogeneous elastic strain development within individual constituents in the material (Figure 2.19a and b). By introducing a distribution of residual stresses in a crystal plasticity finite element model (CPFEM), Hutchinson *et al.* have successfully reproduced the tensile curve of as-quenched martensite without taking into account any other sources of mechanical heterogeneities or strain hardening (Figure 2.19c and d [70]).

While this hypothesis seems promising in describing the monotonic tensile behaviour of as-quenched martensite, it may not work as well when the tension-compression behaviour of martensite is taken into account. Consider a sample that is divided into many constituents with the same yield strength but each constituent has a different residual stress (constituents are assumed to be elastically perfect plastic, the same assumption was made in the work of Allain *et al.* [5] and Hutchinson *et al.* [70]). During forward straining, the residual stresses will be nearly homogenised when the macroscopic stress approaches the bulk UTS. If the sample is then unloaded and further loaded in the reverse direction, all constituents should now yield at the same stress level and produce a narrower elastic-plastic transition compared with the one during forward straining. This contradicts the strain reversal test results where

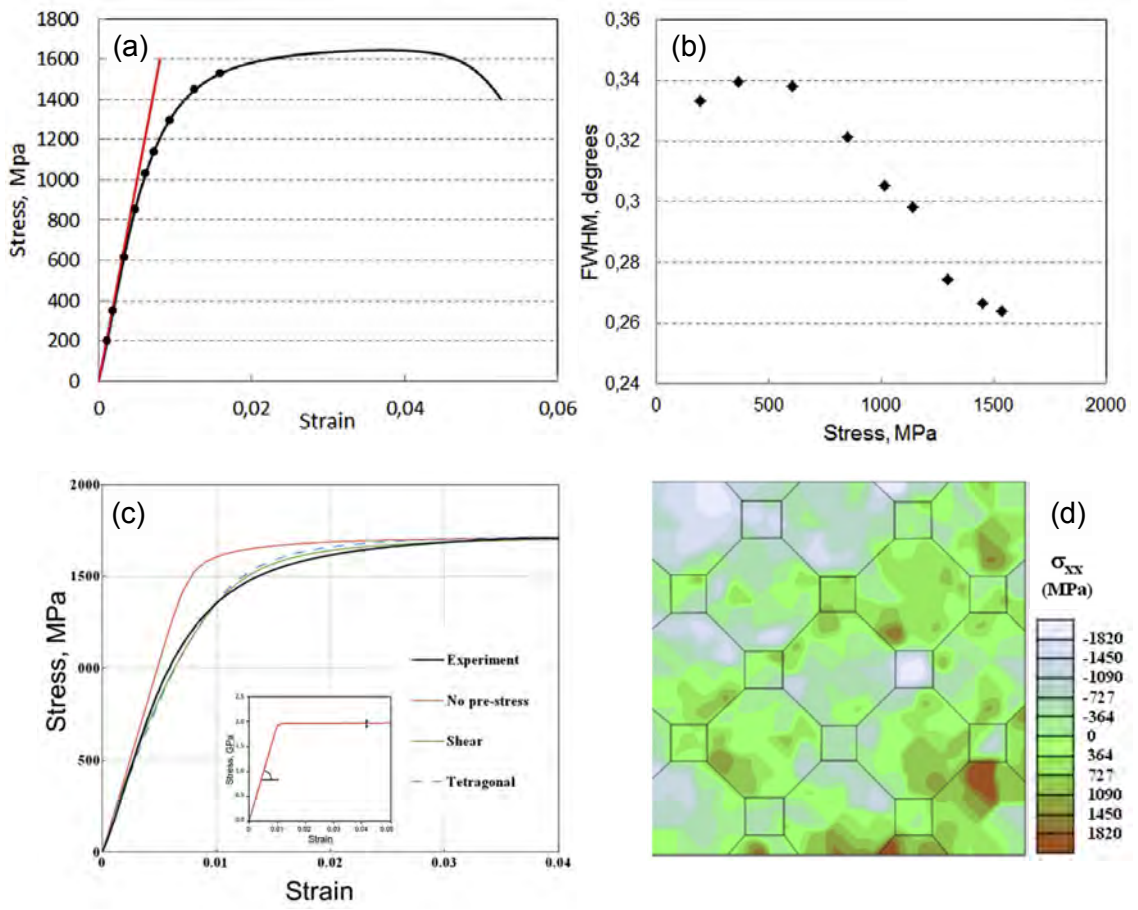

Figure 2.19: *Physical origin and implementation of the residual stress spectrum model. (a) Experimental tensile curve of the as-quenched Fe-0.2C-0.98Mn (wt.%) steel, black dots represent the points where synchrotron XRD patterns were collected* in-situ. *(b) Evolution of FWHM of the (002) ferrite peak during* in-situ *deformation. (c) Comparison between experimental and modelled tensile curves using the residual stress spectrum model, the initial residual stress spectrum can be found in (d). Figures adapted from [70].*

as-quenched and tempered martensite show a broad elastic-plastic transition in both forward and reverse loading directions (Figure 2.17d, see also Ref [5, 74, 75]). Other hardening contributions need to be taken into account in order to properly describe both the forward and the reverse flow behaviours simultaneously. Furthermore, this residual stress should be able to relax significantly upon tempering and may not contribute as much to the strain hardening of tempered martensite. Indeed, Kennett has shown in a low carbon martensite that while peak narrowing was seen in as-quenched tensile samples unloaded during the elastic-plastic transition, peak broadening was observed in the case of 600 °C tempered samples [46]. Similar results were also reported by Morooka *et al.* on a Fe-0.4C (wt.%) steel tempered at 550 °C using *in-situ* neutron diffraction [71]. However, systematic studies on the transition from peak narrowing to peak broadening during deformation as a function of tempering are not found in the literature.

Another complication associated with the residual stress hypothesis is the magnitude and the length scale of such stresses. Type II residual stresses considered in this model originate from local distortions as a result of the martensitic transformation. Therefore, the length scale of such stresses are likely to be similar to the dimension of small martensite constituents (e.g. laths or blocks). Hutchinson and Brask recently investigated this issue using specially designed samples [76]. The samples were electropolished by dipping the samples in and out of the solution which produces a tapered lens shape at the far end of the samples. The samples were then examined by X-ray diffraction in transmission mode. In the case of as-quenched martensite, a decrease in the full width at half maximum (FWHM) was observed when the incident beam was moved to regions with thicknesses below 5 μm (Figure 2.20). No change in FWHM was observed in the specimen tempered at 650 °C for 1 hour. This indicates that the length scale of the residual stresses should be around 5 μm and the stresses could be relaxed when the sample thickness got smaller. The length scale also corresponded well with the intercept length of grains separated by high angle grain boundaries, which suggests that sub-blocks and blocks are the dominant constituents that defines the wavelength of residual stresses. Using the difference in FWHM before and after relaxation, the residual stress was estimated to be around 300 MPa. The authors argued that the stress could be underestimated as FWHM gave an averaged response of the examined volume and further relaxation may occur if thinner regions were examined (the original test was only conducted down to 1 μm in sample thickness, Figure 2.20).

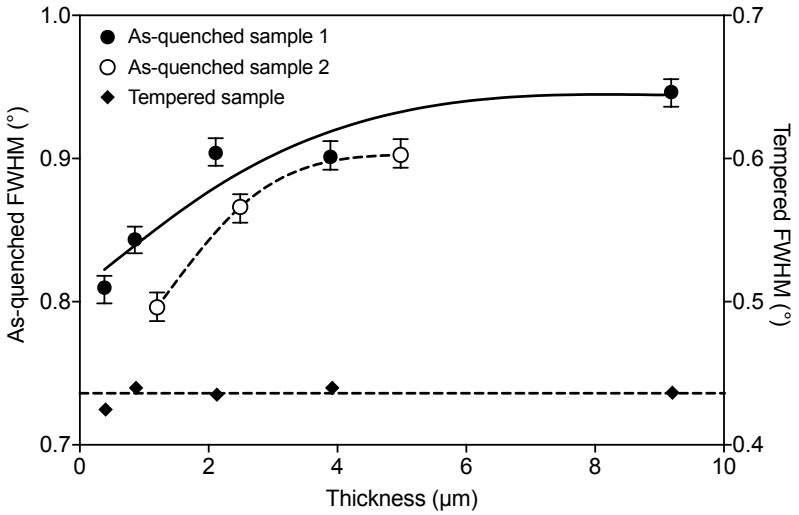

Figure 2.20: *Evolution of FWHM as a function of sample thickness in the as-quenched and tempered states. Figure reproduced from [76].*

While the lateral resolution of the diffraction technique is limited by the beam size and the related interaction volume, micro-scale experiments have been explored to resolve the residual stress of individual martensite crystals. Archie *et al.* used the micro-meter ring-core milling method to estimate the stress relaxation of the isolated micro-pillar [77] (Figure 2.21a - d). In this case, the micro-pillar

consisted of mainly one martensite variant (Figure 2.21f - g) and the milling process (up to 5 μm in depth) caused anisotropic relaxation of the pillar with a maximum relaxation strain of -0.18% along the vertical direction (Figure 2.21e). Further analyses on the 2-D relaxation strain field revealed the maximum relaxation strain along the radial direction could be as large as -0.3%, which corresponded to a principle stress of -388 MPa in a non-biaxial stress state. Although this value seems to agree well with the magnitude found in the work of Hutchinson and Brask, Archie *et al.* also showed that the magnitude of the stress relaxation depends on the variant of the martensite block and the size of the micro-pillar milled. If the micro-pillar encloses many variants within a parent austenite or a prior austenite grain boundary, the variant selection during martensitic transformation may reduce the stress that can be relaxed by ring-core milling. Nevertheless, it is proposed that the diameter of the micro-pillar could be reduced to $\sim$1 μm, which can help develop understandings on the distribution of residual stresses in as-quenched martensite.

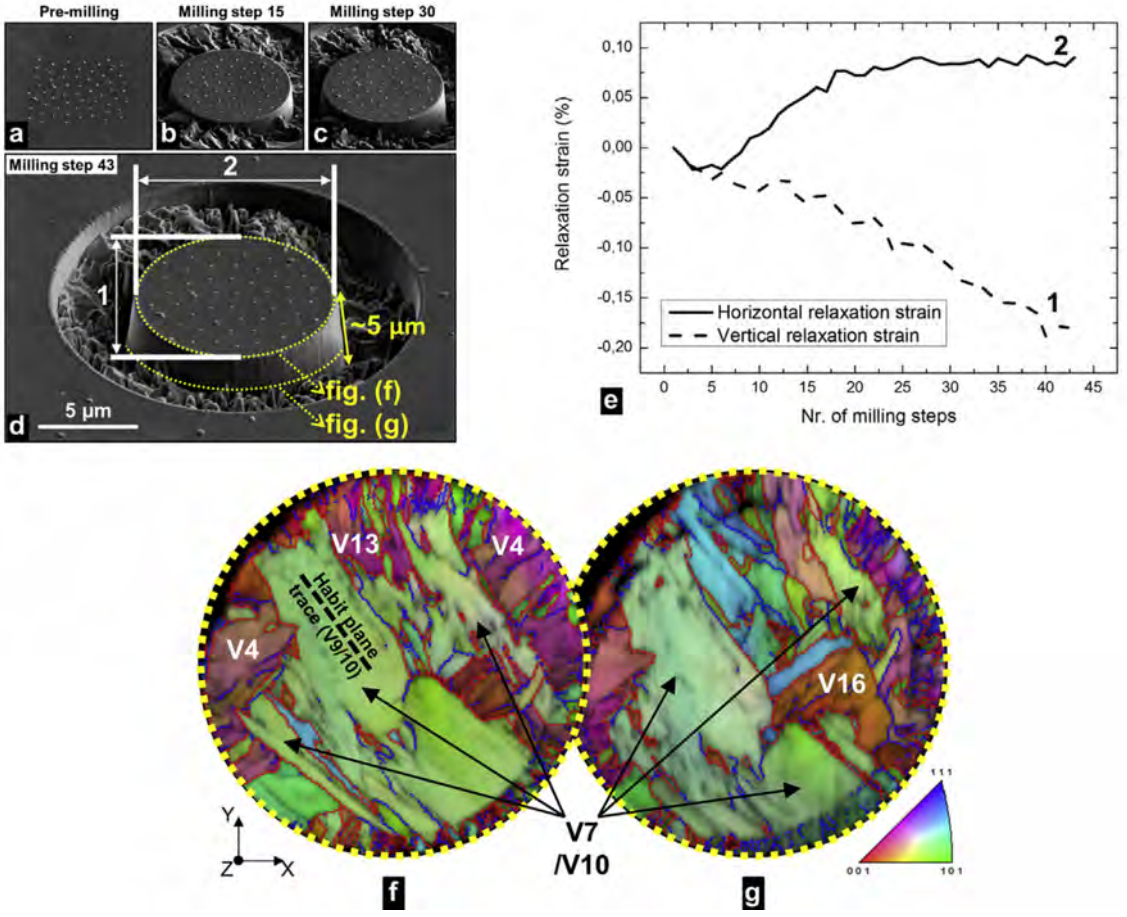

Figure 2.21: *Residual stress relaxation studied by the micro-meter ring-core milling method. (a) - (d) SEM images showing the milling process. (e) Relaxation strain along the horizontal and the vertical direction of the pillar diameter. (f) - (g) EBSD IPF-Z maps of the pillar cross-section at different depth showing the variants included in the pillar. Figures adapted from [77].*

2.3 Tempered martensite

In practical applications, martensitic steels are always tempered before use as the brittleness of the as-quenched martensite can lead to catastrophic failure [78]. Numerous structural heterogeneities in the as-quenched state also provide a substantial driving force for precipitation, recovery and recrystallisation during tempering treatments. Tempering of martensite is often classified into ageing and tempering. Ageing of martensite is defined at very low temperatures from -60 °C to 100 °C focusing on the carbon atom ordering and segregation to lattice defects or retained austenite [10, 79–81]. Martensite tempering is often referred to temperatures above 100 °C when carbon atoms gain sufficient mobility to form carbides [79, 81, 82]. The precipitation reaction can be sustained to temperatures up to 700 °C and overlaps with other structural changes such as transformation of retained austenite, recovery and recrystallisation [83]. Table 2.1 shows the various tempering stages and corresponding temperature ranges, which presents a guideline for the current review. This section focuses on the tempering behaviour starting from the precipitation of transition carbide. A detailed review on the low temperature ageing behaviour of martensite can be found in the work of Badinier *et al.* [84].

Table 2.1: *Tempering stages in ferrous martensite. It is worth noting that the temperature range for each tempering stage is subject to change in the presence of alloying elements.*

Tempering stage	Tempering process	Temperature range
I	Precipitation of transition carbides	60 °C - 200 °C
II	Decomposition of retained austenite	150 °C - 250 °C
III	Precipitation of cementite	150 °C - 700 °C
IV	Recovery and recrystallisation	400 °C - 700 °C

2.3.1 Transition carbides formed at low temperatures

Temperatures ranging from 60 °C to 200 °C mark the first stage of tempering as the formation of transition carbides. The often observed ε and η carbides distribute uniformly in the martensite matrix (Figure 2.22). Upon further tempering at temperatures above 200 °C, transition carbides transform to θ cementite, which signifies the third stage of tempering. Jack first proposed the hexagonal structured ε carbide with the help of X-ray diffraction and identified the orientation relationship between the carbide and the matrix as [85]:

$$(0001)_{\varepsilon} \parallel (011)_{\alpha'}$$

$$\left(10\bar{1}1\right)_{\varepsilon} \parallel (101)_{\alpha'}$$

This was experimentally supported by Wells [86]. Jack also suggested the stoichiometry of ε carbide should be between Fe_2C and Fe_3C and was refined by theoretical calculations and atom probe experiments as $Fe_{2.4}C$. Hirotsu and Nagakura, on the other hand, investigated the electron diffraction pattern of a low temperature tempered high carbon steel and found the symmetry of the transition carbide could be reduced to orthorhombic and designated it as η-carbide [87]. The orientation relationship of the η carbide was measured as:

$$(110)_\eta \parallel (010)_{\alpha'}$$

$$[001]_\eta \parallel [100]_{\alpha'}$$

and the determined stoichiometry was Fe_2C. Electron diffraction studies by Williamson *et al.* showed that the diffraction spots from precipitates could be indexed interchangeably with orientation relationships from either ε or η carbides [88]. Taylor *et al.* have also suggested it might be appropriate to reassign it as ε' carbide [80].

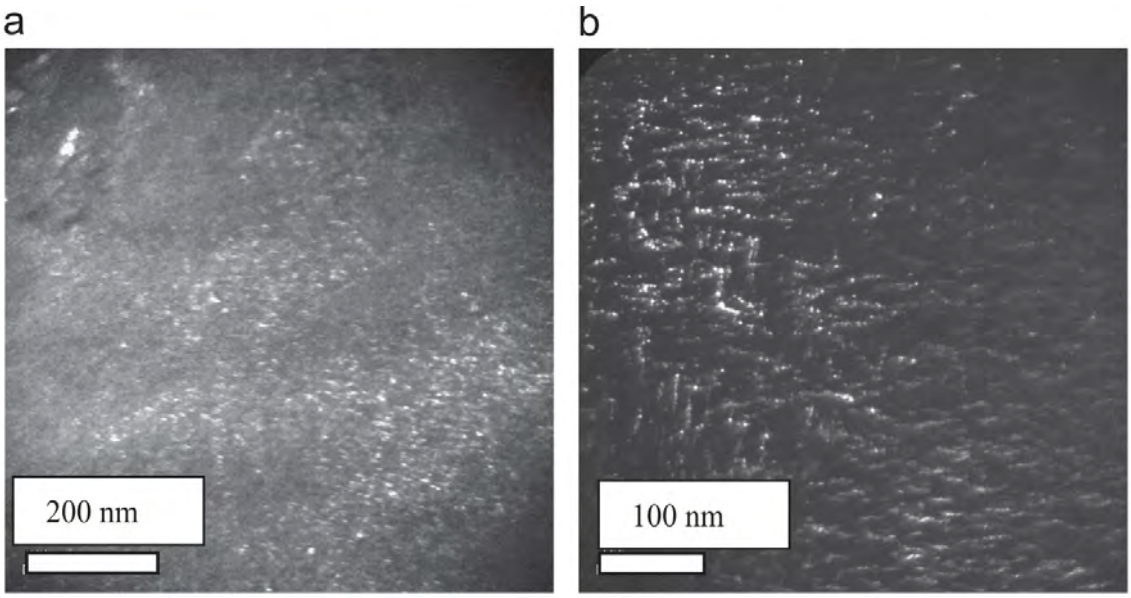

Figure 2.22: *DF-TEM images showing η carbides in 300M steel tempered at 120 °C (a) and 150 °C (b) for 1 hour [89].*

2.3.2 Decomposition of retained austenite

Previous sections have shown that austenite can be retained in the martensitic matrix as a result of incomplete transformation. The second stage of tempering involves the decomposition of retained austenite into ferrite and cementite. Figure 2.23 shows a study from Williamson *et al.* illustrating the evolution of austenite and cementite fraction as a function of tempering temperature [90]. The starting fraction of retained austenite was already low and started to decrease further as soon as the

temperature reached above 200 °C. The transformation ends above 300 °C while the volume fraction of cementite starts to rise, suggesting an overlap between austenite decomposition and cementite precipitation. Horn and Ritchie have demonstrated in similar steels that it is possible to reduce the mechanical stability of retained austenite after tempering in this temperature range [91]. It was suggested that the decomposition would inevitably lead to a depletion of carbon in the austenite and in turn makes the austenite more favourable to transform upon straining. Zaccone and Krauss' experimental results using low temperature tempered martensite could be affected by this phenomenon [57] (Section 2.2.3.2).

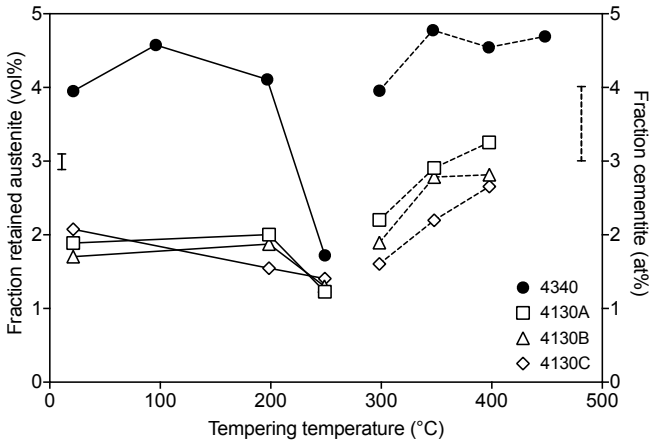

Figure 2.23: *Volume fraction of austenite (solid lines, left y-axis) and atomic fraction of cementite (dashed lines, right y-axis) of one type of AISI 4340 and three types of AISI 4130 steels as a function of tempering temperature. Phase fractions were obtained by Mössbauer spectroscopy and relative errors in measurements can be found next to the y-axes. Figure reproduced from [90].*

2.3.3 Cementite precipitation at intermediate and high temperatures

The third stage of martensite tempering is the precipitation of cementite [81, 83]. Cementite has an orthorhombic lattice structure and a stoichiometry of Fe_3C [92]. At lower tempering temperatures, cementite particles will adopt a needle-shaped morphology similar to transition carbides and grow on $\{011\}_{\alpha'}$ habit planes. The orientation relationship was first proposed by Bagaryatsky as [85, 93]:

$$(100)_\theta \parallel (101)_{\alpha'}$$

$$[010]_\theta \parallel \left[\bar{1}11\right]_{\alpha'}$$

$$[001]_\theta \parallel \left[\bar{1}\bar{2}1\right]_{\alpha'}$$

Several other orientation variants can be also found in the martensite matrix which makes the differentiation between tempered martensite and lower bainite easy under high magnification microscopy. Figure 2.24a shows the needle-shaped arrangement of cementite particles oriented to different directions while cementite in lower bainite shares the same orientation with the ferrite phase. At higher tempering temperatures, cementite particles spheroidise and coarsen (Figure 2.24b).

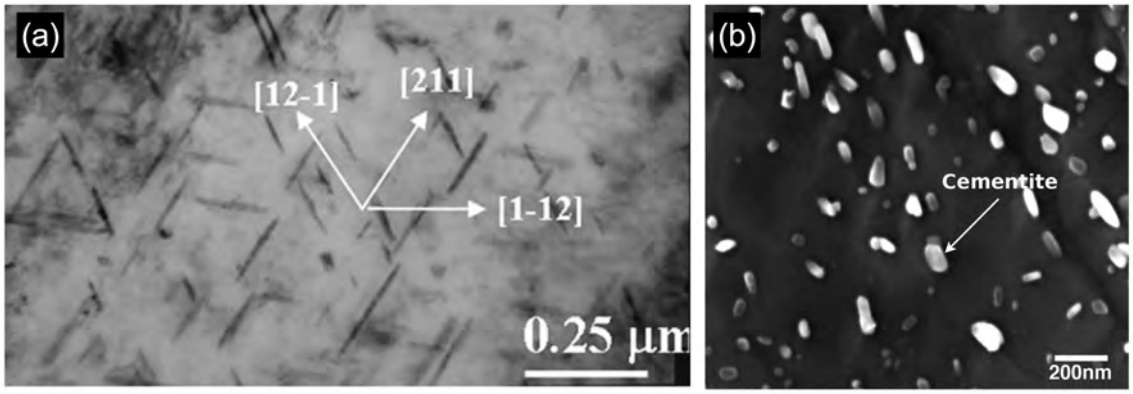

Figure 2.24: *Typical morphologies of cementite precipitates tempered at different temperatures. (a) TEM micrograph of needle-shaped cementite in an Fe-0.15C-1.97Mn (wt.%) steel rapidly tempered at 400 °C for about 3 seconds. Figure adapted from [94]. (b) SEM micrograph of spheroidised cementite in an Fe-0.1C-2Mn (wt.%) steel tempered at 600 °C for 30 minutes. Figure adapted from [95].*

Substitutional elements can affect the kinetics of cementite precipitation by partitioning. First principle calculations have shown that Si, Al, Ni, Co, Cu and P tend to partition away from cementite to ferrite while Cr, Mo, Mn, V and W tend to partition into cementite [96]. Miyamoto *et al.* have shown in the Fe-Mn-C-Si system that both Mn and Si may retard the growth of cementite but in different manners [97]. Cementite may grow initially without Mn partitioning but at later stages requires more Mn in order to approach equilibrium. As Mn is a substitutional element and has a much lower diffusivity than carbon, further growth of cementite would be constrained by Mn partitioning. Wu *et al.* have recently demonstrated that both the cementite growth and the Mn partitioning kinetics can be simultaneously reproduced by considering the composition gradient among precipitates during cementite coarsening [95]. Silicon, on the other hand, slows down cementite precipitation at the early stage since Si has a low solubility in cementite and needs to be rejected from cementite as precipitates grow. Al shares similar properties to Si in slowing down cementite precipitation kinetics [26, 98] and is being trialed to replace Si in the development AHSS since Al can also help expand the temperature window for intercritical annealing [99].

The addition of Si and Al may also affect the transformation sequence during martensite tempering. Figure 2.25 shows the phases present in typical Fe-C-Mn-(Si, Al) steels as a function of tempering temperature using *in situ* synchrotron X-ray diffraction [26]. In the steel with the reference composition (Fe-0.25C-2Mn (wt.%)), precipitation of ε carbides commenced at around 250 °C and the onset of ε

precipitation was not affected significantly by the addition of 1 wt.% Si or Al. However, decomposition of retained austenite showed a large dependence on the Si composition as 1 wt.% of Si postpones the full decomposition of austenite from 320 °C to 440 °C. Cementite precipitation could be found in the Fe-C-Mn reference at 320 °C accompanied with the disappearance of ε carbides. The addition of 1 wt.% Al raised the cementite formation temperature to 350 °C but coexistence of ε carbide and θ cementite can be found up to 430 °C. The coexistence phenomenon was also found in the early work of Leslie and Rauch [98]. The addition of 1 wt.% of Si, on the other hand, could stabilise ε carbide and postpone θ cementite formation up to 450 °C, consistent with the findings of Miyamoto *et al.* in an Fe-0.6C-2Si (wt.%) steel [97].

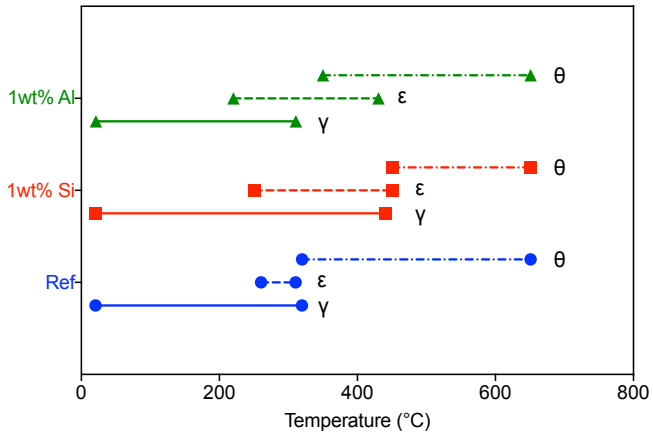

Figure 2.25: *Schematic showing the phases present in Fe-0.25C-2Mn (Ref), Fe-0.25C-2Mn-1Si and Fe-0.25C-2Mn-1Al (wt.%) steels when tempered to 650 °C at a heating rate of 30 °C/min during in situ synchrotron X-ray diffraction experiments. Figure reproduced from [26].*

2.3.4 Recovery and recrystallisation of martensite

Martensite has a hierarchical microstructure separated by numerous substructure boundaries (Figure 2.4). Together with the high dislocation density in the as-quenched martensite, the microstructure should be susceptible to recovery and recrystallisation. Indeed, several authors have used XRD line profile analyses to report that the dislocation density in tempered martensite witnessed an abrupt decrease after short time tempering regardless of composition [2, 100–102]. Apart from the reduction of dislocations within laths, the elimination of low angle grain boundaries upon tempering may also play a significant role [103]. Figure 2.26 shows the evolution of grain boundary densities in tempered martensite as a function of tempering temperatures and times. At all tempering temperatures, there is a sudden drop in the total grain boundary density while the decrease in the high-angle grain boundary density is not as large. This indicates a large number of low angle grain boundaries have been consumed as a consequence of recovery. After the initial drop, both the total and the high angle grain

boundary density gradually decrease at 400 °C and 500 °C and remain relatively constant at 600 °C and 700 °C. It was suggested that short time tempering did not only diminish low angle grain boundaries, but also reduced the intra-lath dislocation density which decreased the strain energy and consequently the driving force for recrystallisation [104].

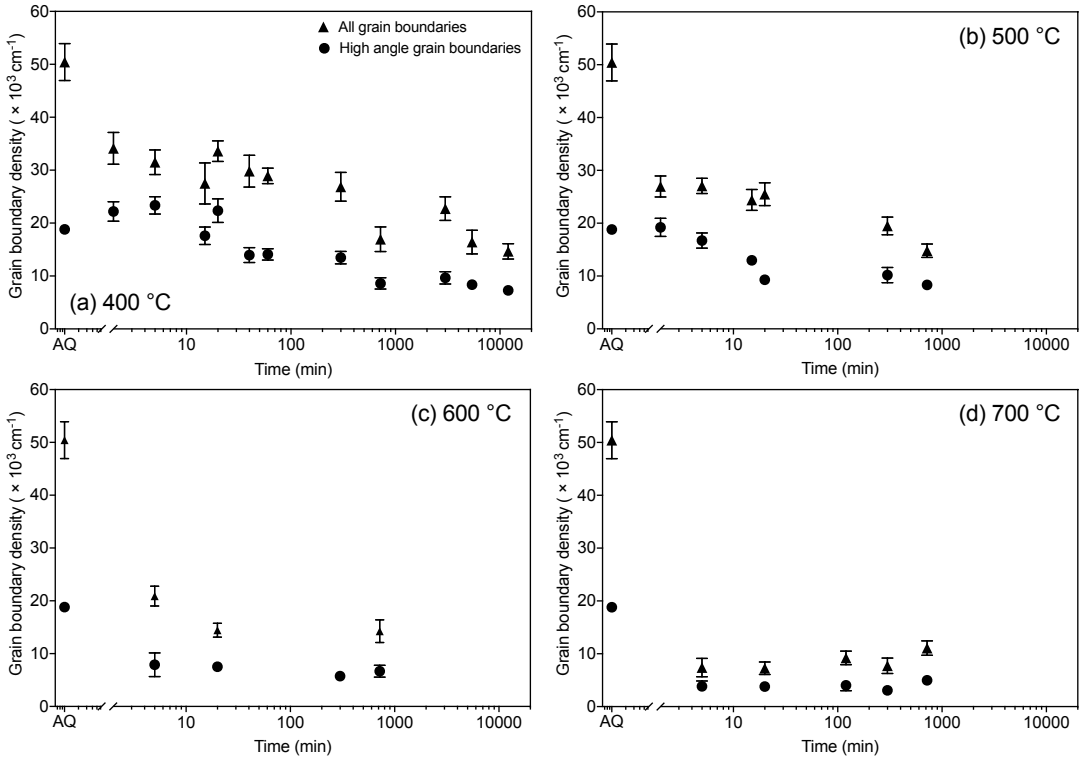

Figure 2.26: *Evolution of grain boundary densities in a Fe-0.2C (wt.%) as a function of temperatures and times. Grain boundary densities were estimated from replica samples lifted from polished and etched bulk samples. Figures reproduced from [103].*

Pronounced recrystallisation of martensite was not observed in the study of Caron and Krauss even after tempering at high temperatures for long times. Instead, the lath structure coarsens during tempering while retaining its elongated shape. At 400 °C, fine carbide particles were found at high-angle block boundaries that might resist boundary migration (Figure 2.27a, carbides are highlighted by red arrows). After tempering at 700 °C, cementite particles spheroidised which allowed faster boundary migration and coarsening of substructures. Fine equiaxed grains were also visible in high temperature tempered samples as a result of localised recrystallisation (Figure 2.27b). Recent studies suggest that the coarsening and recrystallisation of tempered martensite may be further retarded by adding carbide formers (such as Cr) that slow down the coarsening of particles [102, 104].

Tokizane *et al.* have found that compared to undeformed martensite, deformed martensite tended to show recrystallisation more readily at high temperatures [105]. They proposed that cold-work could introduce inhomogeneously deformed regions to the as-quenched martensite, which provided an extra driving force for recrystallisation. However, the assumption of this interpretation is that dislocation density is uniform in the as-quenched martensitic structure. This contradicts the latest results showing the heterogeneity of martensite [24] but some may still argue that the uniform distribution of dislocation could be achieved at the very beginning of tempering during recovery.

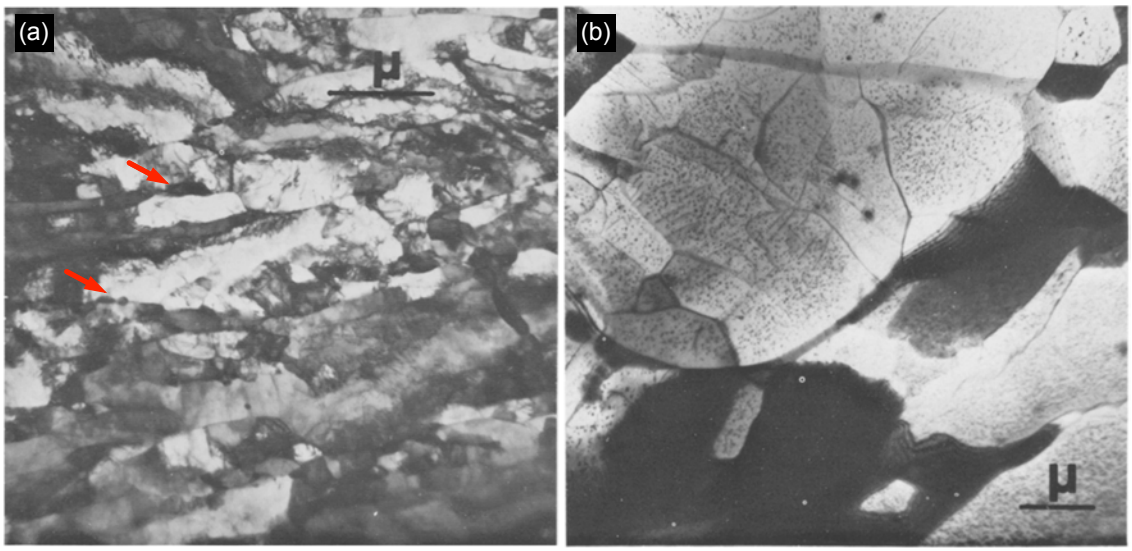

Figure 2.27: *TEM micrographs of an Fe-0.2C (wt.%) steel tempered at 400 °C for 200 hours (a) and tempered at 700 °C for 12 hours. Figures adapted from [103].*

2.4 Mechanical properties of tempered martensite

Speich and Leslie have reviewed major findings on the mechanical properties of martensite before the 1970s [29, 82]. Since then, Krauss and his collaborators have systematically studied the mechanical properties of tempered martensite especially in AISI 41xx and AISI 43xx steels [35, 57, 78, 103, 106, 107]. A summary of their works can be found in several more recent review articles by Krauss [32, 108, 109]. Unfortunately, the studies often focused only on the evolution of the yield strength and seldomly looked at the strain hardening behaviour, mainly because of the limited applications of martensitic steels at that time. Only recently did the community pay more attention to strain hardening and the entire stress-strain curve of tempered martensite as a result of the development of AHSS. In this section, the review starts with a general introduction to the evolution of tensile properties of martensite during

tempering, followed by two sub-sections that look at the evolution of the strain hardening behaviours of tempered martensite during low temperature tempering (LTT) and high temperature tempering (HTT). Modelling of strain hardening behaviour in both temperature regimes are also discussed but reports in the literature are very limited.

2.4.1 Evolution of mechanical properties during tempering

The early work by Hollomon and Jaffe [110] has demonstrated that the evolution of the hardness of tempered martensite as a function of different tempering temperatures and times could be captured by a linear regression between the hardness values and a temperature-time equivalence tempering parameter (TP). TP is often described as:

$$TP = T\,(K) \times [A + \log(t\,(sec))] \tag{2.9}$$

Although the choice of the constant A has been in debate, the temperature-time equivalence approach provides a simplified means to display and evaluate data from different tempering temperatures and times. Figure 2.28(a) shows that the linear regression curves found in AISI 43xx steels are indeed in good agreement with the experimental hardness values using the same constant A regardless of the differences in bulk carbon contents.

Figure 2.28b - d shows the evolution of the yield strength (YS estimated using the 0.2% proof stress), the UTS and the yield strength to ultimate tensile strength ratio (Y-T ratio) as a function of tempering parameters. While the evolution of UTS can also be described by a linear relationship with TP, both YS and Y-T ratio show behaviours that may be more adequately described by a quadratic function (i.e. curves with a maximum). The increase in YS at low tempering parameters (i.e. lower temperatures, shorter times) coincides with the findings by Muir *et al.* that the elastic limit witnesses a peak between 205 °C to 370 °C [33]. Muir *et al.* and Hutchinson *et al.* have attributed the increase in the elastic limit to the reduction of quenched-in residual stresses during tempering [6, 33] while the hypothesis by Allain *et al.* suggests it is due to the homogenisation of local strengths by carbon redistribution or dislocation re-arrangement [5].

Compared to as-quenched martensite, classic strengthening mechanisms such as solid solution strengthening due to carbon and dislocation strengthening should both reduce significantly as a function of tempering due to the microstructural evolutions mentioned earlier. Strengthening due to grain refinement may also reduce but the reduction could be smaller as grain growth may still be suppressed by

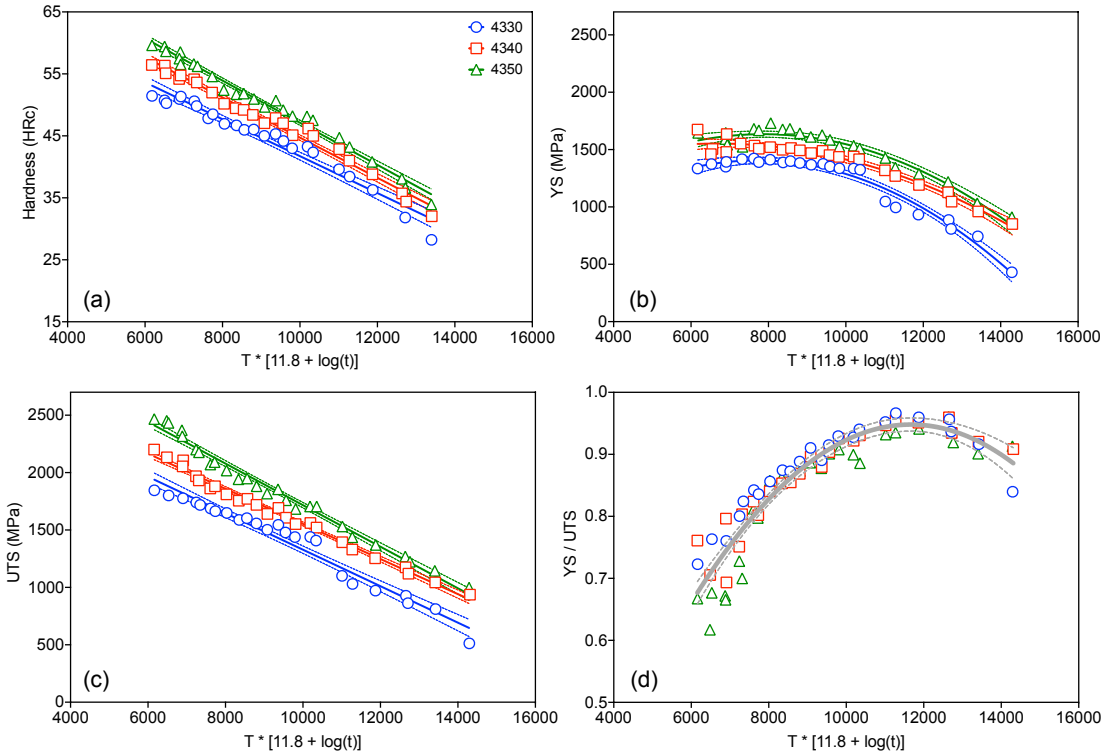

Figure 2.28: *Evolution of key mechanical properties as a function of tempering parameters for the rockwell hardness (a) , the 0.2% yield strength (b), the ultimate tensile strength (c) and the yield strength to ultimate tensile strength ratio (d). Regression lines in (a) and (c) were made based on linear regressions and lines in (b) and (d) were made based on quadratic functions. Dashed lines represent the 95% confidence band of the regression lines. Figures reproduced from [18], original data from the unpublished work of Lee [111].*

cementite particles. Precipitation strengthening from cementite is the only contribution that increases as a function of tempering but the precipitates are also subject to coarsening when tempered at higher temperatures [95]. As a consequence, high temperature and long time tempering of Fe-C martensite always leads to a reduction in yield strength and UTS as shown in Figure 2.28b and c.

The Y-T ratio is used here as a qualitative means to describe the strain hardening capability of the material. A higher Y-T ratio means a smaller increment between YS and UTS, which implies a lower capability for the material to strain harden. A more quantitative measurement, the strain hardening exponent in the Hollomon's equation ($\sigma = K\varepsilon_p^n$), will be used in the following chapters. The evolution of the Y-T ratio is relatively insensitive to carbon content and may be described with a single quadratic function. Tempered martensite first loses its strain hardening capability up to TP ~12000 (equivalent to tempering at 500 °C for 1 hour) and then gradually regains strain hardening capability when tempered at higher temperatures (e.g. above 600 °C). Neither the reduction nor the rejuvenation of the strain hardening behaviour in tempered martensite are fully understood in the literature [109].

2.4.2 Evolution of strain hardening behaviours during low temperature tempering (LTT, $\leq$ 200 °C)

The literature definition of low temperature tempering and high temperature tempering is quite vague. In AISI 41xx and 43xx steels, Krauss and co-workers often regarded LTT as tempering up to 200 °C where cementite was absent or sparsely identified [109]. Saeglitz and Krauss studied the effect of low temperature tempering in 43xx steels [107]. In the engineering stress-strain curves (Figure 2.29a), the same continuous yielding behaviour as as-quenched martensite could be found in the low temperature tempered samples. The strain hardening rates share the same carbon dependence as discussed by Allain *et al.*, which means the mechanical heterogeneity may still be present (Figure 2.29b). They have also demonstrated the increase in YS of martensite during LTT and attributed this increase to the re-configuration of dislocations and transition carbide precipitation.

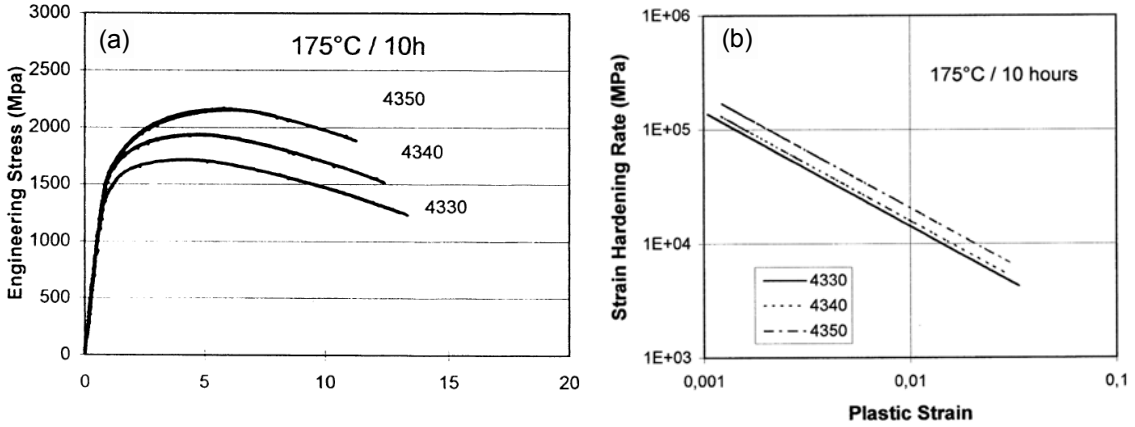

Figure 2.29: *Engineering stress-strain curves (a) and strain hardening rates (b) of 43xx steels tempered for 10 hours at 175 °C [107].*

Badinier *et al.* performed similar experiments on 300M steels (a Si modified 4340 steel) using torsion tests [89]. They found a similar extended elastic-plastic transition during LTT (Figure 2.30a - c) but this effect quickly diminished as the temperature was raised above 300 °C (Figure 2.30d). According to the continuous composite hypothesis, they interpreted the effect of LTT as retainment or further development of mechanical heterogeneity via carbon segregation and transition carbide precipitation. Based on the assumption that the dislocation density would be different between laths formed at different temperatures, Badinier *et al.* demonstrated that laths with low dislocation densities tended to have faster transition carbide transformation kinetics than the ones with high dislocation densities, which retains or even enhances the mechanical heterogeneity of martensite. As a consequence, the continuous composite model was extended to consider measurable physical heterogeneities such as dislocation densities and precipitates. This extended model showed good capability in describing the

strain reversal behaviour of the low temperature tempered martensite as shown by the red curve in Figure 2.30. One disadvantage of the extended model is that it relies on a parameter α' to describe the strength of forest dislocations (i.e. a modified α in the Taylor strengthening equation Eq. 2.8) but attempts to quantify this parameter are not shown.

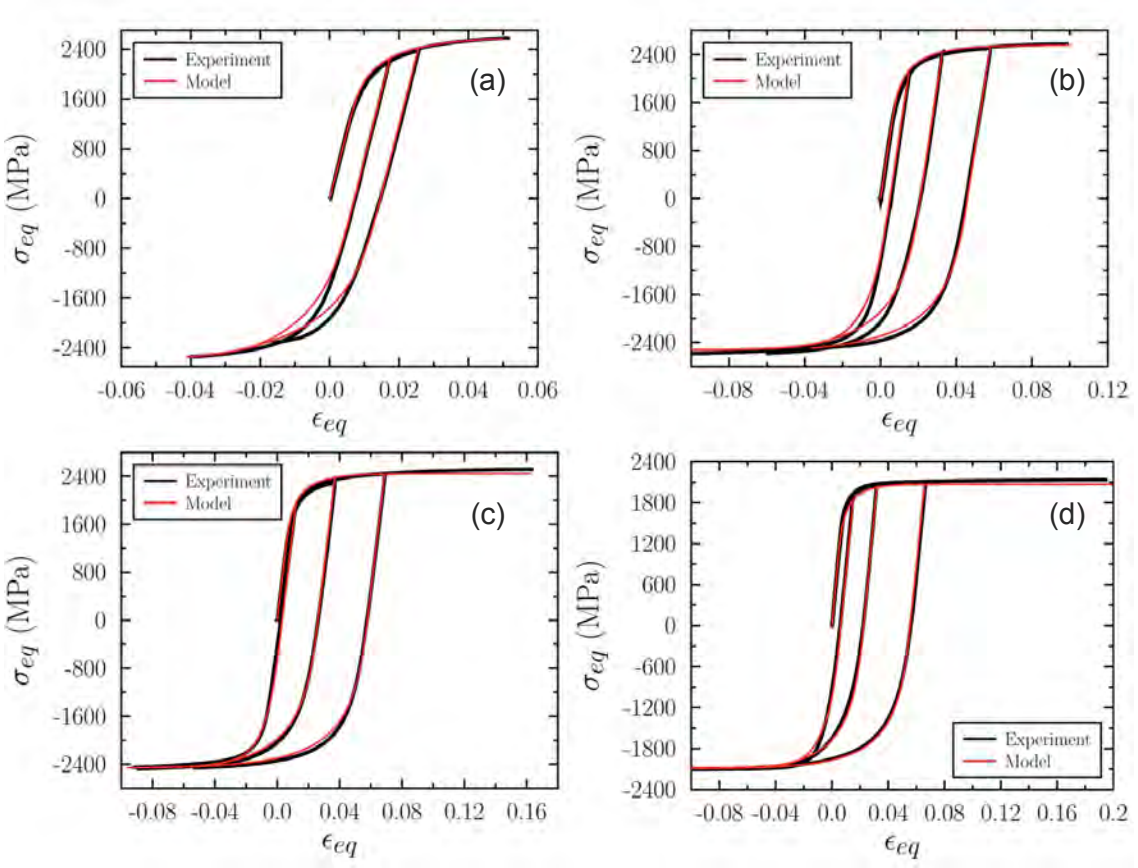

Figure 2.30: *Comparison between modelled and experimental strain reversal curves in a 300M steel for different tempering conditions. (a) 120 °C 3 hours, (b) 120 °C 5 hours, (c) 150 °C 1 hour and (d) 350 °C 1 hour. Experimental results were obtained from torsion reversal tests where the von Mises equivalent stress and strain were converted from shear stress and strain. Figure adapted from [74].*

2.4.3 Evolution of strain hardening behaviours during intermediate and high temperature tempering (HTT, $\geq$ 300 °C)

Figure 2.31a shows tensile curves of a Fe-0.2C-2.2Mn-1.4Si (wt.%) steel tempered up to 500 °C [112]. The strength of the material is decreased by tempering while the elongation is much improved except for the possible tempering-induced embrittlement around 400 °C. At lower temperatures up to 300 °C, the curves show continuous yielding (extended elastic-plastic transition) similar to as-quenched martensite. As the temperature increases above 400 °C, discontinuous yielding and yield point elongations (YPEs) appear and YPEs become longer as tempering temperature increases. After the termination of YPE, samples show very limited strain hardening compared to as-quenched and LTT conditions, which leads

to the low Y-T ratio seen in Figure 2.28. The discontinuous yielding behaviour and low strain hardening rate can also be found in Lee's work on 43xx steels tempered at 500 °C and 600 °C [111] (Figure 2.31b). Therefore, martensite tempered at high temperatures tends to share similar strain hardening behaviours with fine grained, ferrite-cementite steels (Figure 2.31c) as a result of pronounced precipitation and the significant reduction in dislocation densities. Swarr and Krauss proposed that the low strain hardening rate in tempered martensite was due to the presence of fine cementite particles that disrupts dislocation storage and the formation of dislocation cell structures [35]. In the case of ultra-fine grained steels, the low strain hardening rate was often attributed to the presence of grain boundaries as dislocation sinks that increase the rate of dislocation annihilation. This may also be relevant to martensite as the fine laths/blocks are often only a few hundred nanometers in width [35, 89, 102].

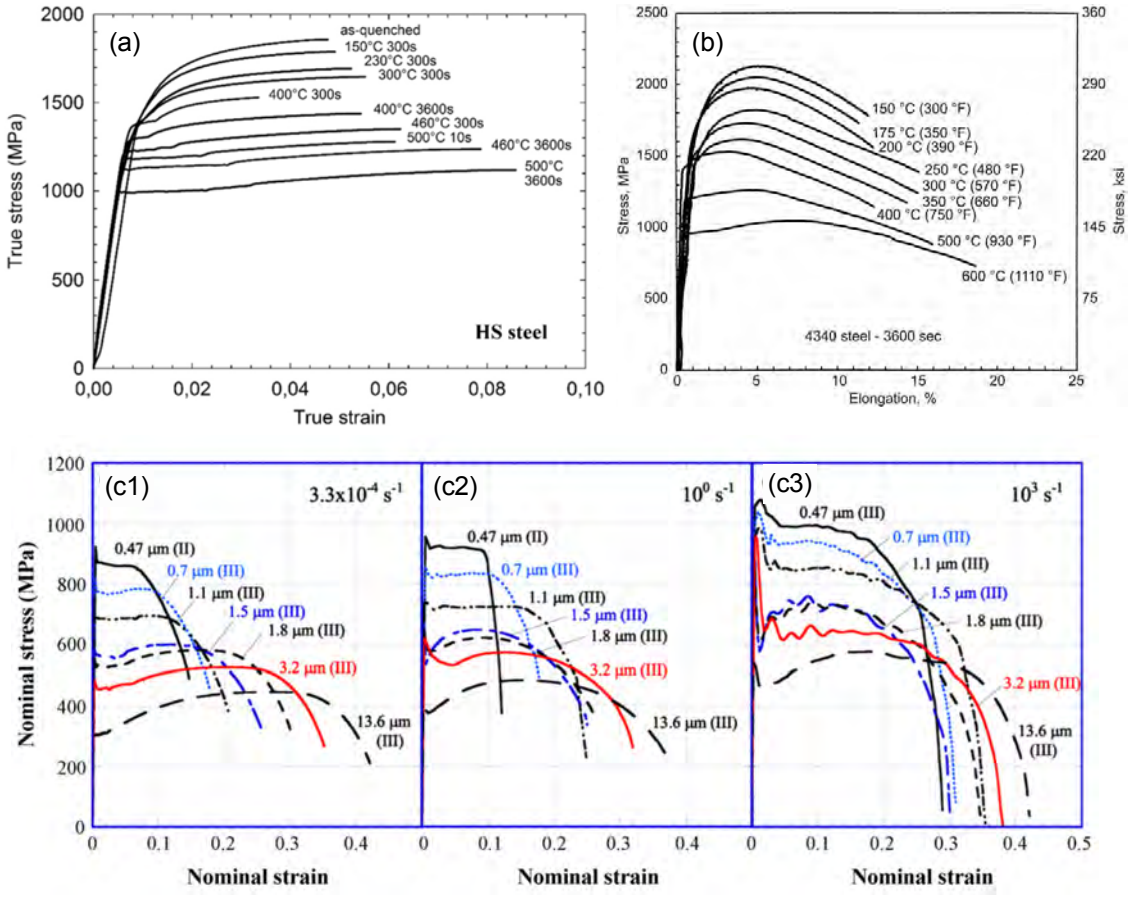

Figure 2.31: *Tensile response of tempered martensite and fine grained ferrite-cementite steels. (a) True stress - true strain curves of a Fe-0.2C-2.2Mn-1.4Si (wt.%) steel as a function of tempering [112]. (b) Engineering stress-strain curves of 4340 steel tempered at different temperatures for 1 hour [18, 111]. (c) Engineering stress-strain curves of a Fe-0.15C-1.5Mn-0.4Si (wt.%) steel ferrite-cementite steel processed to have different ferrite grain sizes [113].*

2.4.4 Modelling the strength of high temperature tempered martensite

Many researchers have attempted to describe the evolution of the strength of tempered martensite as a function of tempering temperatures and times. Wu has found a strong correlation between the hardness and the microstrain (obtained from synchrotron X-ray diffraction line profiles) of tempered martensite (Figure 2.32a and Ref. [2]). Since the microstrain can be assumed to be caused by dislocations in the matrix, Wu explained the softening of tempered martensite using a recovery model considering thermally activated dislocation motion [114]. However, the model only works well when the tempering time is longer than 2 minutes (Figure 2.32b), the significant drop of hardness in the beginning of the tempering reaction is thought to be caused by other mechanisms.

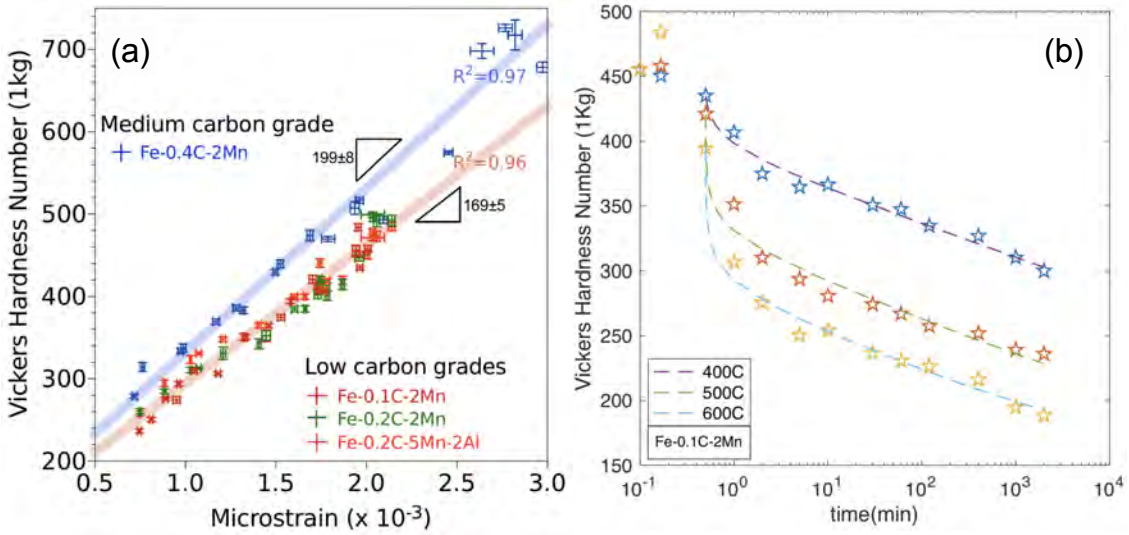

Figure 2.32: *(a) Correlation between the Vickers hardness and the microstrain for steels with a various of compositions. (b) Experimental (stars) and modelled (dashed lines) hardness evolution as a function of tempering time in a Fe-0.1C-2Mn (wt.%) steel. Figures adopted from Wu [2].*

Galindo-Nava and Rivera-Diaz-del-Castillo interpreted the recovery process as a result of carbon diffusing away from dislocation arrays at lath boundaries, which produces dislocation recovery and lath coarsening simultaneously [115]. With an estimation of block size (grain refinement strengthening) and precipitation kinetics (precipitate hardening), the authors were able to predict the yield strength of tempered martensite but many of parameters used in the model need to be further justified. Similar research on the effect of dislocation density and cementite precipitates can also be found in the early work by Malik and Lund [116]. Unfortunately, few modelling works can be found that focused on modelling the strain hardening behaviour of tempered martensite.

One exception is the work of Mahlheiros *et al.* who attempted to use a simplified continuous composite model to fit the tensile curves of tempered martensite [112]. In this case, the width of the spectrum σ_0 can be correlated with the equivalent carbon content in the matrix C_{eq} as $\sigma_0 = 130 + 1997C_{eq}$. Generally, the model could reproduce the tensile behaviour of tempered martensite (Figure 2.33a). The effect of tempering can be quantified as the reduction of C_{eq} after tempering normalised by the initial C_{eq}. This normalised parameter increases linearly as a function of tempering parameters, which indicates the width of the spectrum decreases during tempering (Figure 2.33b). However, detailed experimental results were not given to quantify the depletion of carbon in the matrix and further work needs to be focused on the linkage between modelling parameters and microstructural evolutions.

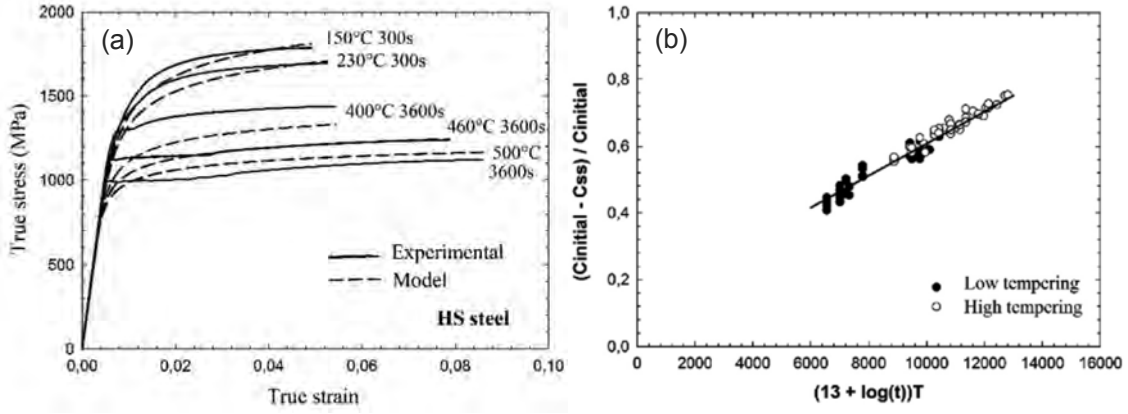

Figure 2.33: *(a) Comparison of modelled and experimental tensile curves in an Fe-0.2C-2.2Mn-1.4Si (wt.%) steel for different tempering conditions. (b) Evolution of the reduction in C_{eq} after tempering normalised by the initial C_{eq}. Figure adapted from [112].*

2.5 Kinematic hardening in martensite

All strengthening mechanisms discussed in the previous sections are isotropic hardening contributions which, in principle, should not change their magnitudes when the loading direction is reversed. However, microstructural features in martensite also suggest that kinematic hardening contributions, the ones that can change signs and magnitudes, may also be relevant to martensite strengthening. Indeed, previous studies have revealed that both as-quenched and tempered martensite show significant reductions in reverse yield strengths after strain reversal tests (Figure 2.34) [5, 74, 75, 117, 118]. It has been demonstrated by Allain *et al.* and Badinier that the phenomenological continuous composite model could provide intrinsic kinematic hardening as strain partitioning occurs among constituents with different yield strengths (Section 2.2.3.3) [5, 74]. Chang and Asaro have attributed the kinematic hardening to the presence of cementite particles [118], which will be further reviewed later. The other two works [75, 117], however, did not discuss about the microstructural origins of the kinematic

hardening. This section reviews two microstructure-based kinematic hardening models in the literature and discusses several implementations of the models in martensite. Unfortunately, tension-compression tests were not included in their implementations to validate not only the forward but also the reverse straining behaviours of the materials.

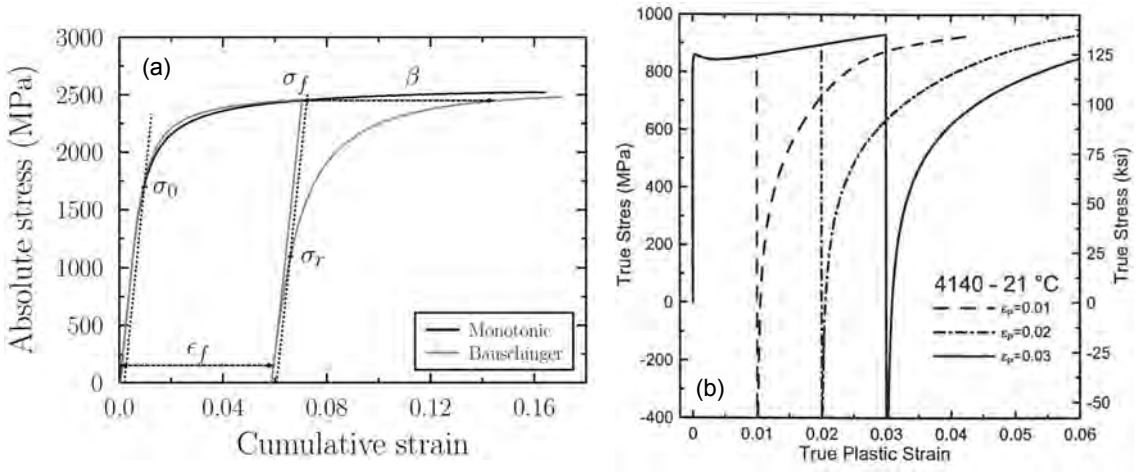

Figure 2.34: *Tension-compression test results of (a) a 300M steel tempered at 150 °C for 1 hour [74] and (b) a 4140 steel induction tempered at 760 °C for less than 1 minute [119]. In both cases, it can be found that reverse yield strengths are much smaller than the forward flow stress at which the loading is reversed, indicating a possible kinematic hardening contribution to strain hardening.*

2.5.1 Isotropic hardening and kinematic hardening

In continuum mechanics, the hardening of a material after macroscopic yielding can be categorised into two types: isotropic hardening and kinematic hardening. During uniaxial loading, pure isotropic hardening leads to isotropic expansion of the yield surface in the stress space and the hardening is the same regardless of loading directions (Figure 2.35a). Pure kinematic hardening, on the other hand, results in translation of the yield surface along the loading direction but no change in the dimension of the yield surface (Figure 2.35b). As the origin of the yield surface moves towards the loading direction, the yield point in the reverse direction will be reduced by the same amount of the lateral translation. In reality, a combined behaviour is more commonly observed which leads to both expansion and translation of the yield surface (Figure 2.35c).

From a materials science point of view, the isotropic hardening of materials can be related to the accumulation and multiplication of dislocations during plastic deformation. Kocks and Mecking have demonstrated that the evolution of dislocation density can be described as a function of plastic strain [34]:

$$\frac{1}{M}\frac{d\rho}{d\varepsilon_p} = k_1\sqrt{\rho} - k_2\rho \tag{2.10}$$

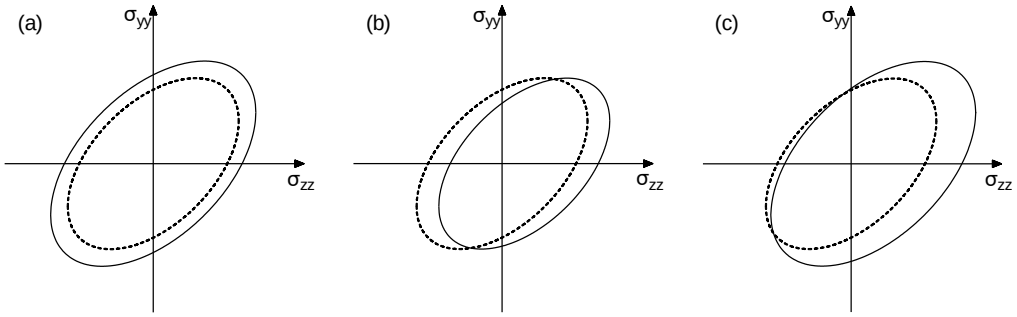

Figure 2.35: *Evolution of the von Mises yield surface during uniaxial pure isotropic hardening (a), pure kinematic hardening (b) and combined isotropic and kinematic hardening (c). The position of the initial yield surface is represented by dashed lines.*

k_1 is a constant that considers the self-trapping efficiency of dislocations and k_2 accounts for the annihilation of dislocations due to dynamic recovery. Integration of Eq. 2.10 and combination with Taylor's equation (Eq. 2.8) leads to a description of isotropic hardening due to dislocation multiplication:

$$\sigma_{iso} = \frac{\theta_0}{\beta_0}\left[1 - \exp\left(\beta_0 \varepsilon_p\right)\right] \tag{2.11}$$

where $\theta_0 = \alpha M^2 \mu b k_1/2$ and $\beta_0 = k_2 M/2$. Eq. 2.11 takes the form of the commonly known Voce law and can be easily implemented in existing continuum mechanics models. Eq. 2.10 and Eq. 2.11 can also be extended to include the effects of grain boundaries [120] and precipitates [121].

There are also many phenomenological models developed for kinematic hardening in continuum mechanics. However, few have attempted to link the phenomenological models to microstructural parameters even though existing models in both fields share the similar formalism [122, 123]. In continuum mechanics, kinematic hardening is often modelled using the Armstrong-Frederick (A-F) type non-linear hardening law [124]. In the case of one-dimensional, uniaxial loading, the kinematic hardening contribution can be written as:

$$\sigma_{kin} = \nu \frac{C_\xi}{\xi} + \left(\sigma^0_{kin} - \nu \frac{C_\xi}{\xi}\right) \exp\left[-\nu\xi\left(\varepsilon_p - \varepsilon^0_p\right)\right] \tag{2.12}$$

$\nu = \pm 1$ represents the loading direction, C_ξ describes the effective hardening modulus of kinematic hardening, ξ takes into account the dynamic recovery of hardening and σ^0_{kin} and ε^0_p are the magnitudes of kinematic hardening and plastic strain at the beginning of each loading cycle. The following sections discuss two microscopic kinematic hardening models that take the same form as Eq. 2.12 but use physical parameters that may be extracted from the microstructure.

2.5.2 Kinematic hardening from dislocation pile-ups at grain boundaries

The first kinematic hardening contribution is considered to be applicable in martensite as it has a fine microstructure. Sinclair *et al.* proposed that grain boundaries can act as perfect obstacles for dislocations at small strains [120]. Dislocations stopped at the grain boundary are able to generate a back stress that resist further dislocation motion towards the boundary. They can also provide extra trapping sites for incoming dislocations and contribute to isotropic hardening. The back stress from dislocation pile-ups at the grain boundary can be estimated as:

$$\langle\sigma\rangle_{gb} = M\frac{\mu b}{D_g}n_{gb} \tag{2.13}$$

D_g is the grain diameter and n_{gb} is the number of dislocations stopped at the grain boundary on a particular slip plane. The maximum back stress is reached when $n_{gb} = n^*_{gb}$, n^*_{gb} is the maximum number of dislocations that can be stored at the boundary before the dislocations are forced to be absorbed by the grain boundary and emitted into the adjacent grain to develop slip. The evolution of n_{gb} as a function of plastic strain can be estimated as:

$$\frac{dn_{gb}}{d\varepsilon_p} = \frac{\lambda}{b}\left(1-\frac{n_{gb}}{n^*_{gb}}\right) \tag{2.14}$$

λ is the mean spacing between slip lines at the grain boundaries. The $\left(1-n_{gb}/n^*_{gb}\right)$ term represents the probability to have sites unoccupied to accommodate an incoming dislocation. Eq. 2.14 can be integrated and combined with Eq. 2.13, which yields the evolution of back stress as a function of plastic strain:

$$\langle\sigma\rangle_{gb} = M\frac{\mu b}{D_g}n^*_{gb}\left[1-\exp\left(-\frac{\lambda\varepsilon_p}{bn^*_{gb}}\right)\right] \tag{2.15}$$

Compared to the phenomenological kinematic hardening model, Eq. 2.15 takes the same form as Eq. 2.12 when $C_\xi = M\mu b\lambda/D_g$ and $\xi = \frac{\lambda}{bn^*_{gb}}$. It is worth noting that Eq. 2.15 only considers the increase of back stress as dislocation pile-ups develop at one side of the grain boundary but does not include the screening effect of dislocations with opposite signs arriving at the grain boundary from the adjacent grain or other slip systems. The screening effect may be accounted for using a similar approach described in Eq. 2.13:

$$\langle\sigma\rangle_{gb} = M\frac{\mu b}{D_g}n^*_{gb}\left[1-\exp\left(-\frac{\lambda\varepsilon_p}{bn^*_{gb}}\right)\right]\left(1-\frac{n_{gb}}{n^*_{gb}}\right) \tag{2.16}$$

Using Eq. 2.16 and a modified Kocks-Mecking equation considering the enhanced dislocation storage at grain boundaries, Sinclair *et al.* successfully reproduced the strain hardening behaviour of copper with grain sizes from $\sim 2\mu$m to $\sim 50\mu$m.

This model has been implemented in the case of as-quenched and tempered martensite by Cobo and Bouaziz [125] and Kim *et al.* [126] respectively. In both implementations, the authors used Eq. 2.15 and the modified Kocks-Mecking equation but did not consider the screening effect by dislocations with opposite signs. While Cobo and Bouaziz used the lath size and Kim *et al.* used the block size as the effective grain size, the n^*_{gb} and D_g ratios n^*_{gb}/D_g were both in the range of 6 μm^{-1} to 10 μm^{-1}, which were able to generate kinematic hardening contributions in the range of 300 MPa to 600 MPa. Modelled stress-strain curves in both works showed reasonably good agreement with experimental curves (Figure 2.36) and substructure size measurements but the physical origin of n^*_{gb} was not discussed in detail and its quantification remains a challenging task for future researchers.

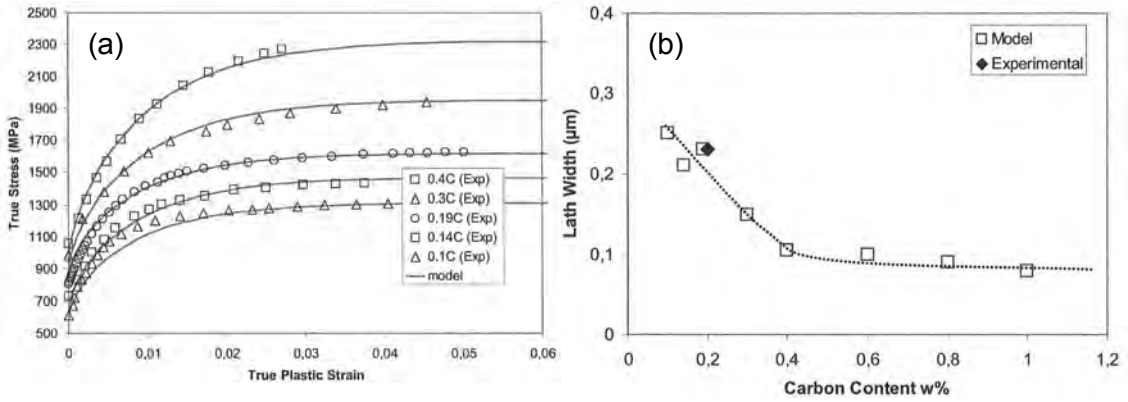

Figure 2.36: *Performance of the kinematic hardening model considering dislocation pile-ups at lath boundaries [125]. (a) Comparison between experimental and modelled tensile curves of as-quenched Fe-C martensite with various carbon contents. (b) Evolution of lath widths that best reproduce tensile curves as a function of carbon content (open squares). The solid diamond represents the lath width measured in the work of Morito et al. [42].*

The model may also have difficulties in describing the low strain hardening capability in tempered martensite. The block width of tempered martensite is usually around a few microns and it does not evolve much as a function of tempering even at high temperatures. As a consequence, the kinematic hardening contribution due to dislocation pile-ups at block boundaries should not change much provided that the value of n^*_{gb} also remains constant throughout tempering. Therefore, it is hard to rationalise the low strain hardening capability of tempered martensite if over 300 MPa strength can be achieved by kinematic hardening by this mechanism. Kim *et al.* argued that a fraction of $\langle\sigma\rangle_{gb}$ contributes to enhance the yield strength and the rest contributes to strain hardening beyond the yield point,

which means Eq. 2.15 can overestimate the kinematic hardening contribution. A low strain hardening capability in tempered martensite implies that most dislocation pile-ups at grain boundaries are caused by microplasticity before the onset of yielding. The screening effect in Eq. 2.16 may also be relevant in reducing the overall kinematic hardening contribution.

2.5.3 Kinematic hardening from Orowan loops around precipitates

A second kinematic hardening contribution that may be found in tempered martensite arises from the plastic incompatibility between the matrix material (ferrite) and secondary particles (cementite). During forward plastic straining, dislocations may encounter secondary particles that are too strong to be sheared along with the matrix and leave Orowan loops on the particles. The Orowan loops exert a long-range back stress opposite to the forward direction and this stress must be overcome for further deformation, which leads to macroscopic strengthening. When the direction of straining is reversed, the directional internal stress can facilitate the development of plasticity in the reverse direction and results in a lower reverse yield strength. As reverse straining proceeds, the internal stress can be fully eliminated and re-develop in the opposite direction (i.e. the direction of forward straining) as a result of removal and re-deposition of Orowan loops.

Brown and Clarke [127] have developed the quantitative description of the internal stress using Eshelby's solutions on elastic inhomogeneity [128]. In polycrystalline materials, the long-range internal stress developed in the material can be written as:

$$\langle \sigma \rangle_{ppt} = M^2 g D \mu V_f \varepsilon_p^* \tag{2.17}$$

g is the accomodation factor, D is the modulus correction factor, μ is the shear modulus of the matrix, V_f is the volume fraction of secondary particles and ε_p^* is the unrelaxed plastic strain. It is important to consider the unrelaxed plastic strain instead of the plastic strain ε_p since plastic relaxation will occur at large plastic strains as a result of localised plasticity in the matrix or plastic deformation of the particle. ε_p^* can be calculated using the number of Orowan loops (n_{ppt}) on a particle with a radius r following the works by Brown and co-workers [127, 129–131]:

$$\varepsilon_p^* = \frac{n_{ppt} b}{2Mr} \tag{2.18}$$

Proudhon *et al.* [132] have derived the evolution of n as a function of plastic strain following the same principle used in the work of Sinclair *et al.* [120]:

$$\frac{dn_{ppt}}{d\varepsilon_p} = \frac{2Mr}{b}\left(1 - \frac{n_{ppt}}{n^*_{ppt}}\right) \tag{2.19}$$

Eq. 2.19 can be integrated and combined with Eq. 2.17 to give the evolution of back stress related to Orowan loops as a function of plastic strain:

$$\langle\sigma\rangle_{ppt} = M^2 g D \mu V_f \varepsilon_p^{*max}\left[1 - \exp\left(-\frac{\varepsilon_p}{\varepsilon_p^{*max}}\right)\right] \tag{2.20}$$

where $\varepsilon_p^{*max} = \frac{n^*_{ppt} b}{2Mr}$. When Eq. 2.20 is compared with Eq. 2.12, it can be found that $C_\xi = M^2 g D \mu V_f$ and $\xi = \frac{2Mr}{n^*_{ppt} b}$.

Quantification of n^*_{ppt} has been demonstrated in the Al-Cu system using diffraction contrast TEM and the n^*_{ppt} to precipitate length ratio is around 0.1 nm^{-1}[121, 133]. As a result, several authors have successfully implemented this model in aluminium alloys [121, 122, 134] but less effort has been made on steels. Chang and Asaro [118], in the case of spheroidised steels (heavily tempered Fe-C martensite), assumed that some of the strain hardening came from the back stress generated at cementite particles due to plastic incompatibility but implemented the idea in a more phenomenological way. They estimated the unrelaxed plastic strain using a plastic strain exponent of 0.3 (i.e. $\varepsilon_p^* \propto \varepsilon_p^{0.3}$). While the estimation of flow curves followed the same trend as experimental results, this treatment clearly lacks physical origins and needs to be amended.

Chapter 3

Gaps in knowledge and thesis structure

Martensite is the strongest phase in steel and its microstructures and mechanical properties have been studied extensively in the literature. Historically, the high strength of as-quenched martensite was attributed to the supersaturated carbon atoms in the matrix that provide solid solution strengthening. However, the stress-strain curve of as-quenched martensite shows a very low elastic limit and the high tensile strength should have been attributed to the high strain hardening rate. Many researches have proposed assumptions to explain the low elastic limit but limited studies were dedicated to the strain hardening of martensite. This could be a result of the applications of martensite being limited to areas such as tool steels that do not face much plasticity. On the other hand, as a key constituent of AHSS, it is essential for martensite to accommodate plastic deformation. Therefore, the plastic behaviour of as-quenched martensite remains a key research problem to be tackled. Although new interpretations showed promising results when considering the as-quenched martensite as a composite material, there are few experimental works that quantitatively assess the mechanical heterogeneities in martensite and link the macroscopic mechanical response to microstructural features.

The story is further complicated by subsequent tempering as the reduction in strength is accompanied by numerous microstructural changes such as carbon redistribution to defects, cementite/alloy carbide precipitation, residual stress relaxation, dislocation recovery and possible recrystallisation of martensite sub- structures. Extensive experimental works were conducted in the low temperature tempering regime whereas limited reports were found at higher tempering temperatures when both the cementite precipitation and recovery kinetics are fast. Many studies have attempted to model the strength of tempered martensite but neglected to address the key changes in strain hardening behaviours. The change

from a broad elastic-plastic transition in as-quenched martensite to the gradually narrowed transitions in tempered martensite as a function of tempering temperatures is not understood. The reduction and then rejuvenation of the strain hardening capability of martensite during tempering has also attracted little attention despite its importance.

The main objective of this project is to develop an understanding of the evolution of strength and strain hardening of tempered martensite. Focus is placed on alloy systems with 3rd generation AHSS alloying elements (C, Mn, Si and Al) at tempering temperatures from 300 °C to 600 °C where understanding from the literature is lacking. To answer the questions mentioned above, the following main results chapters are presented:

- Chapter 5: Recently developed composite models are promising candidates to describe the large strain hardening rate of as-quenched martensite. However, some basic hypotheses and resulting flow curves deviate from experimental results. Before looking deeper into the properties of tempered martensite, a critical analysis of existing models is required. An evaluation framework is developed to compare the hypotheses of composite models and modelled flow curves are compared with experimental results.

- Chapter 6: With a clearer view on the strain hardening mechanisms in as-quenched martensite, we start the investigation on tempered martensite with the objective to see if similar mechanical behaviours can be observed and described with the composite model and to identify if more strengthening mechanisms need to be considered. The effect of Si and Al on the tempering kinetics is also discussed in this chapter.

- Chapter 7: The focus of the final results chapter is to provide a refined physical explanation for the experimental results. Based on the strain hardening behaviours of martensite tempered at different temperatures, the explanation is divided into two parts. The first part concerns the modification and extension of the composite model to tempered martensite since the extended elastic-plastic transition and high strain hardening rate can still be found at lower tempering temperatures (300 °C and 400 °C). The second part tries to explain the strain hardening and the strain reversal behaviours of higher temperature tempered martensite with a model that combines isotropic and kinematic hardening contributions.

Chapter 4

Experimental methodology

4.1 Materials and heat treatments

The materials used in this study were provided by ArcerlorMittal and their compositions from chemical analyses are shown in Table 4.1. The base composition is Fe-0.25C-2.5Mn (wt %) which allows the steel to be water quenched to form a fully martensitic matrix. Si and Al were added to control the kinetics of cementite precipitation. The steels have been provided in two forms, cold rolled (CR) sheets (~1.2 mm thick) and hot rolled (HR) plates (~6 mm thick). The cold rolled sheets were used for tensile tests and microstructural characterisations that ensure a great number of tempering conditions can be covered in the project. After identifying the appropriate tempering conditions, the hot rolled plates were used to perform Bauschinger tests which require the samples to be in larger dimensions to avoid buckling.

Table 4.1: *The chemical composition of the investigated steels (wt.%)*

Designation (reference composition)		Fe	C	Mn	Si	Al	P	S
Base steel (Fe-0.25C-2.5Mn)	CR	Bal.	0.24	2.4	<0.02	0.01	0.01	0.01
	HR	Bal.	0.25	2.43	<0.02	0.01	0.01	0.01
Si steel (Fe-0.25C-2.5Mn-1.4Si)	CR	Bal.	0.25	2.42	1.44	0.01	0.01	0.01
	HR	Bal.	0.24	2.4	1.45	0.01	0.01	0.01
Al steel (Fe-0.25C-2.5Mn-1.4Al)	CR	Bal.	0.27	2.46	0.02	1.38	0.01	0.01
	HR	Bal.	0.26	2.52	0.02	1.42	0.01	0.01

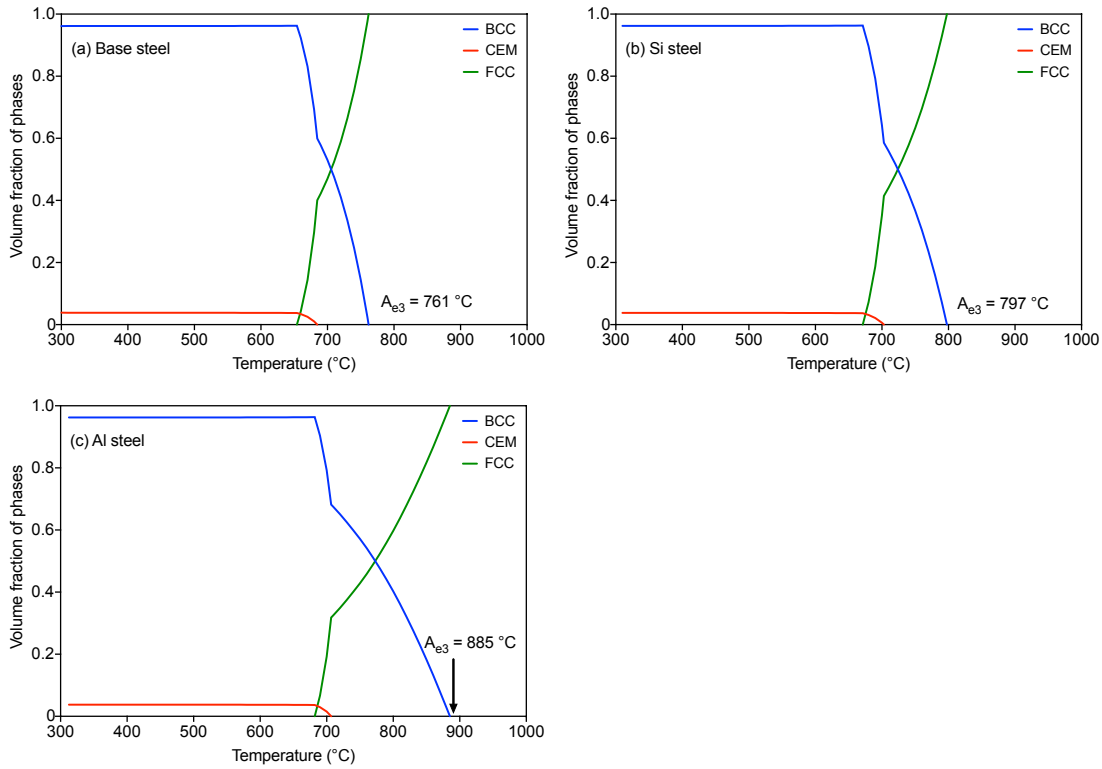

Figure 4.1: *Phase fractions of ferrite, austenite and cementite for the base steel (a), the Si steel (b) and the Al steel (c). Diagrams were calculated using Thermo-Calc and the TCFE9 database with the reference compositions listed in Table 4.1.*

The austenitisation temperature for all alloys was set to be 950 °C which is approximately ~190 °C, ~150 °C and ~65 °C above the A_{e3} temperatures for the base, Si and Al steels (volume fractions of phases are shown in Figure 4.1). The austenitisation experiments were conducted in a horizontal tube furnace with flowing Ar for 10 minutes followed by water quenching. Since the heating rate of the tube furnace is slow, a thermocouple was placed near the samples in the furnace and the timer was set when the readings of the thermocouple reached the desired temperature. The heating time from room temperature to 950 °C was around 7 minutes, corresponding to an average heating rate of ~135 °C/min. As reviewed in the work of Baidnier, quenching from the austenization temperature would result in macroscopic residual stresses across the sample [74]. In this thesis, we have measured the hardness variation across the sample thickness for both CR and HR materials and found the cores of samples (~1 mm for CR samples and ~4.5 mm for HR samples) were hardened to roughly the same hardness values (variation less than 10%). While a more detailed X-ray diffraction analysis is preferred, the hardness results suggest that the influence of macroscopic residual stresses should be small after grinding and final machining of the test samples. The hardness measurements also suggest that decarburisation layer only exists close to the sample surface and can be removed by proper sample preparation.

The tempering experiments were performed in a salt bath at 300 °C, 400 °C, 500 °C and 600 °C for various times and the samples were water quenched after tempering. In the case of salt bath tempering, the timer was set as soon as the samples were immersed into the molten salt. This might lead to some heating rate effect for short time tempering (e.g. <1 minute) but should not affect samples undergoing long time tempering. Two types of salts were used in the current work. For tempering below 600 °C, the salt is a mixture of sodium nitrate and potassium nitrate. For tempering at 600 °C, the salt is a mixture of barium chloride and calcium chloride. It is possible that the nitrate salt leads to nitriding of the samples surface but grinding and machining were conducted for each sample so that the surface effect was eliminated. A test matrix detailing the tempering conditions and characterisation techniques can be found in Table 4.2.

Table 4.2: *Heat treatment and characterisation matrix of the current study.*

Temperature	Time	Bulk mechanical tests			Microstructural characterisations (mostly CR)						
		Tension (CR)	Bauschinger (HR)	strain-rate sensitivity (CR)	Nanoindentation	XRD	XRD (Interrupted)	SEM	EBSD	TEM (HR, Interrupted)	DSC
As-quenched (AQ)	-	✓	✓	✓	✓	✓	✓	✓	✓		✓
300 °C	1 min	✓			✓	✓			✓		
	5 min	✓	✓	✓	✓	✓	✓	✓	✓		
	30 min	✓				✓			✓		
	1 hr		✓	✓			✓				
400 °C	30 sec	✓									
	1 min	✓			✓	✓			✓		
	2 min	✓									
	5 min	✓	✓	✓	✓	✓	✓	✓	✓		
	30 min	✓				✓			✓		
	1 hr		✓	✓			✓				
500 °C	30 sec	✓									
	1 min	✓			✓	✓			✓		
	2 min	✓									
	5 min	✓	✓	✓	✓	✓	✓	✓	✓		
	30 min	✓				✓			✓		
	1 hr		✓	✓							
600 °C	1 min	✓			✓	✓			✓		
	2 min	✓									
	5 min	✓	✓	✓	✓	✓	✓	✓	✓		
	30 min	✓				✓			✓		
	1 hr		✓	✓				✓		✓	
	24 hrs		✓					✓			

4.2 Bulk mechanical properties

4.2.1 Monotonic tensile test with cold rolled sheets

4.2.1.1 Sample design and test parameters

Monotonic tensile tests were conducted on an Instron 4505 screw-driven machine with a 100 kN load capacity and the strain was measured using a clip-on extensometer with a gauge length of 10 mm. The crosshead speed during tensile tests was fixed to be 0.02 mm/s (equivalent strain-rate $\sim 1.67\times10^{-3}$). Samples with a gauge length of 12 mm and a gauge width of 5 mm (Figure 4.2) were electrical discharge machined (EDM'ed) from the cold rolled sheets parallel to the rolling direction. This dimension was selected as the homogeneous heating zone of the horizontal furnace is roughly 60 mm so the entire sample can undergo the same austenitisation treatment. In addition, the recommended gauge length of extensometers should not exceed 85% of the parallel length of the sample according to the ASTM-E8/M standard. In this case, this ratio is ~83%, which is within the tolerance of the standard. The taper radius at the transition between the parallel length and the sample head was also made larger so that strain distribution is uniform. At least three samples were heat treated together and tested to ensure the results are reproducible. It was ensured that the surface hardness after heat treatment and surface grinding matches with the average hardness of the core so that decarburisation and nitriding of the surface would not affect the macroscopic response of the samples.

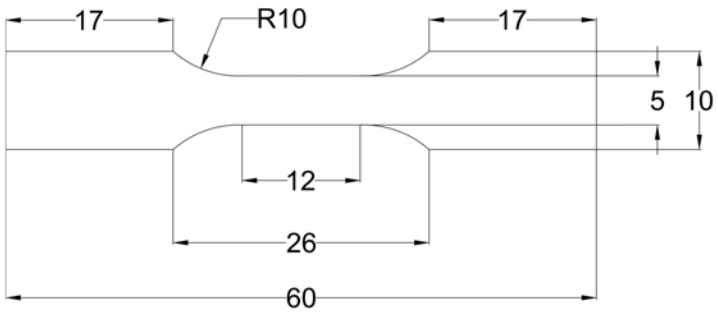

Figure 4.2: *Specimen dimensions of the tensile samples, unit mm.*

4.2.1.2 Determination of mechanical properties

All mechanical properties presented in this work were determined using the true stress-true strain curve. According to the Considère's criterion, the true stress-strain curves were terminated at the onset of necking (i.e. $\frac{d\sigma}{d\epsilon} = \sigma$, Figure 4.3a). The strain hardening rate ($\frac{d\sigma}{d\varepsilon}$) was calculated numerically and smoothed using a Savitzky-Golay filter embedded in MATLAB. Determination of the yield strength (YS, 0.2% proof strength), the ultimate tensile strength (UTS) and the uniform elongation (UE) can also be found in Figure 4.3a.

The strain hardening behaviour of materials were compared using the extracted parameters from the Hollomon's equation:

$$\sigma = K\varepsilon_p^n \tag{4.1}$$

where σ is the true stress, K is the strength coefficient, ε_p is the true plastic strain and n is the strain hardening exponent. Values of K and n were calculated by fitting the $\ln\sigma - \ln\varepsilon_p$ plot with a linear regression. For tensile curves exhibiting continuous yielding, the fitted portion starts from the YS and ends at the UE. For tensile curves exhibiting yield discontinuities and YPE, only the portion after the yield discontinuity was considered. Figure 4.3b shows examples of $\ln\sigma - \ln\varepsilon_p$ curves for the Si steel tempered at different temperatures for 5 minutes. It can be seen that linear regressions can be fitted well to experimental curves except for the as-quenched condition due to its extremely high strain hardening rate.

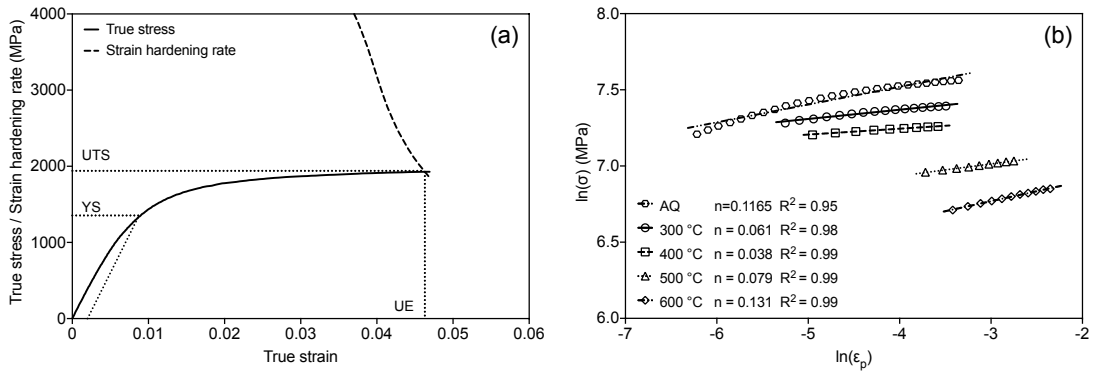

Figure 4.3: *Determination of mechanical properties from the tensile curve of an as-quenched Si steel sample. (a) Determination of YS, UTS and UE. (b) Determination of the strain hardening exponent; open symbols represent experimental* $\ln\sigma - \ln\varepsilon_p$ *curves and lines represent the fitted linear regressions. Number of experimental data points were reduced when producing the graph for clarity.*

4.2.2 Strain-rate sensitivity test with cold rolled sheets

4.2.2.1 Test parameters

Strain-rate sensitivity tests were performed to evaluate the dominant strengthening mechanism in as-quenched and tempered martensite. The same samples shown in Figure 4.2 were loaded with a servo-hydraulic MTS Landmark machine with a 100 kN load capacity. The crosshead speed during the initial ramp was fixed at 0.002 mm/s (equivalent strain-rate $\sim 1.67\times10^{-4}$) until 0.5% total strain was reached. Crosshead speed jumps were then performed every 0.5% between 0.002 mm/s and 0.02 mm/s, which should result in $\dot{\varepsilon}_1/\dot{\varepsilon}_2 = 10$ or 0.1. The exact change in strain-rate was checked with the readings from the clip-on extensometer (10 mm gauge length). The change in flow stress $\Delta\sigma$ after a strain-rate jump event was calculated as the instantaneous change in the true stress during a down-jump (i.e. jump

from high strain-rate to low strain-rate):

$$\Delta\sigma = \sigma_{high\,\dot{\varepsilon}} - \sigma_{low\,\dot{\varepsilon}} \tag{4.2}$$

The values of $\sigma_{high\,\dot{\varepsilon}}$ and $\sigma_{low\,\dot{\varepsilon}}$ were obtained directly from the raw strain-rate jump test data as shown in Figure 4.4a without any data smoothing. The down-jump was chosen since it displays smaller noise compared to the up-jump (i.e. jump from low strain-rate to high strain-rate).

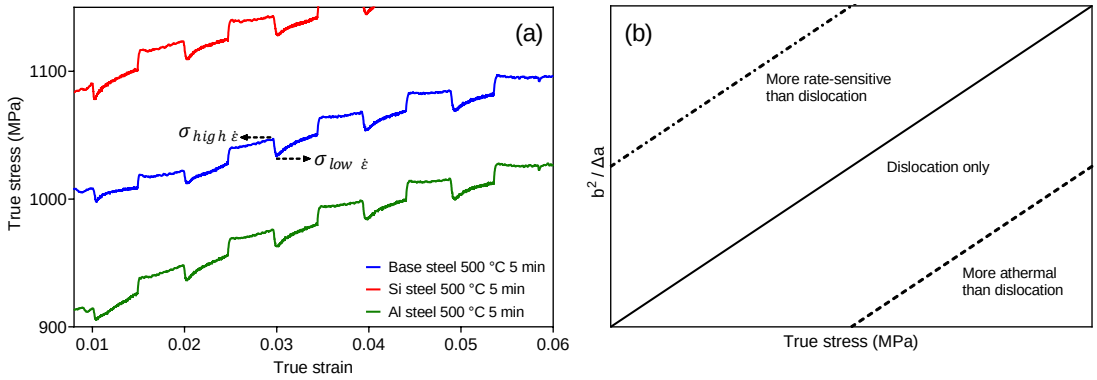

Figure 4.4: *Data analyses of strain-rate sensitivity tests. (a) Determination of stress change $\Delta\sigma$ from backward strain jumps. (b) Schematic showing the effect of dominant strengthening mechanism on the location of the linear regression in a Haasen plot.*

4.2.2.2 Analyses of strain-rate jump data

Analyses of the strain-rate sensitivity test followed the procedures found in the work of Kocks *et al.* [135] and Mulford [136]. The operational activation area Δa during thermally activated dislocation motion can be found as:

$$\Delta a = -\frac{1}{b}\frac{\partial \Delta G}{\partial \sigma} \tag{4.3}$$

where b is the Burgers vector, ΔG is the activation energy and σ is the applied stress. If we define the strain-rate with an Arrhenius behaviour $\dot{\varepsilon} = \dot{\varepsilon}_0 \exp\left(-\frac{\Delta G}{kT}\right)$ and define the strain-rate sensitivity parameter m:

$$m = \frac{\partial \ln \dot{\varepsilon}}{\partial \ln \sigma} \tag{4.4}$$

the activation area can be related to the strain-rate sensitivity by:

$$\Delta a = \frac{MmkT}{b\sigma} \tag{4.5}$$

where M is the Taylor factor. The error in the estimation of $\Delta\sigma$ is around 0.5 - 1 MPa, which results in uncertainties around 5% - 10% in the estimation of Δa. If the material is only strengthened by forest dislocations, the plot of $1/\Delta a$ against the flow stress σ should be linear and can be extrapolated to the origin (i.e. satisfying the Cottrell-Stokes law). However, if the material is strengthened by other types of obstacles, the curve may have a non-zero intercept with the σ or the $1/\Delta a$ axis. For instance, if there is a large athermal contribution σ_{ath} to the flow stress, Eq. 4.5 needs to be modified so that the stress term in the denominator considers only the contribution from dislocations:

$$\Delta a = \frac{MmkT}{b\left(\sigma - \sigma_{ath}\right)} \tag{4.6}$$

In this way, the intercept with the σ axis represents an approximation to σ_{ath}. Likewise, if there is a set of obstacles that are more thermally sensitive than dislocations (e.g. solute atoms), the extrapolated line will have an intercept with the $1/\Delta a$ axis. A graphical representation of the above discussions can be found in Figure 4.4b.

4.2.3 Monotonic and Tension-compression tests with hot rolled plates

4.2.3.1 Sample design and test parameters

Tension - compression Bauschinger tests were performed to quantify the contribution of kinematic hardening. Bauschinger tests were conducted on a servo-hydraulic MTS Landmark machine with a 100 kN load capacity. The alignment of the testing system was calibrated to be close to ASTM E1012 Class 5 (i.e. maximum bending strain smaller than 5% of the total strain) using the MTS 609 alignment fixture and a standard sample with 12 strain gauges. The alignment of the testing system was calibrated every time before a batch of tension-compression tests were conducted. The test frame itself is of high stiffness so the alignment should be good throughout the batch of the samples (typically 10 – 20 samples per batch).

Samples were first EDM'ed into 8.7 mm (diameter) × 6 mm (plate thickness) × 80 mm (length) blocks from the hot rolled plates for heat treatments. The longitudinal direction of the sample is parallel to the rolling direction. Two samples were heat treated together during austenisation and tempering to minimise the sudden temperature decrease upon insertion of samples. Through thickness hardness measurements confirmed the middle 4.5 mm in the gauge section can be fully hardened to the same level of hardness upon quenching and tempering so that the effect of decarburisation and nitriding was removed. The blocks were then machined to the final dimension shown in Figure 4.5. In the case of

as-quenched samples, the samples are too hard for MTS wedge grips so a set of threaded grippers (M6 × 1 mm) were made. The gripping parts of the sample were threaded but the same geometry was maintained in the gauge section. As it is shown in Figure 4.6, the change of gripping method does not affect the forward and reverse behaviour of the material.

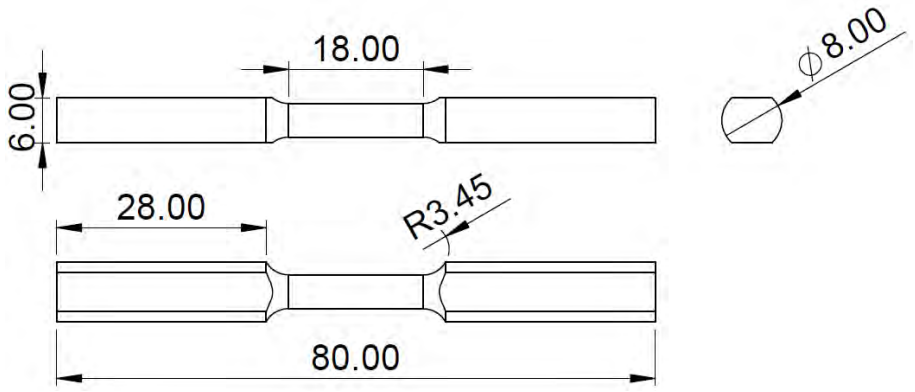

Figure 4.5: *Specimen dimensions of the Bauschinger test samples, unit mm.*

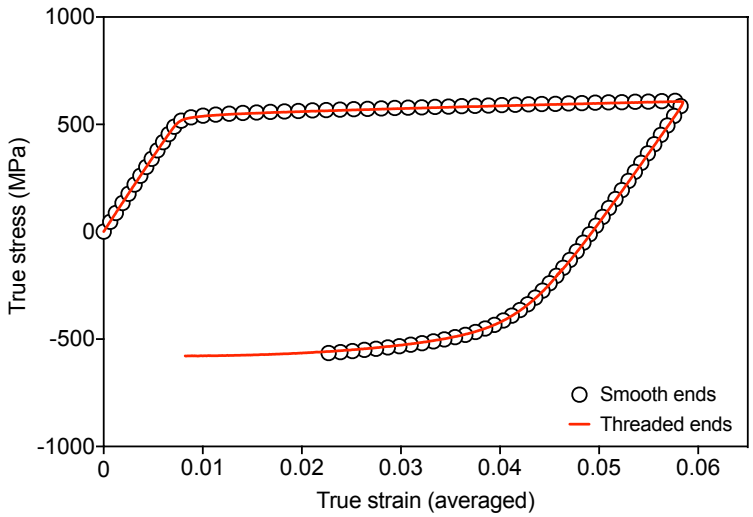

Figure 4.6: *Comparison of flow behaviours between samples with smooth and threaded ends. Test samples were machined from an extruded 7075-T651 aluminium rod.*

Monotonic tension tests were conducted with a constant crosshead speed of 0.03 mm/s (equivalent strain-rate $\sim 1.67 \times 10^{-3}$) and one clip-on extensometer with a gauge length of 10 mm was used to record the strain during monotonic tests. The extensometer was removed during monotonic tests after the engineering UTS to protect the extensometer from damage. Since the true stress-true strain curve is the main interest of this study, the removal of the extensometer should not affect the true flow behaviour before the onset of necking. The tension-compression test consists of two parts, the sample is first loaded in tension to a predefined forward strain followed by unloading to zero force and loaded again in compression until an engineering compressive strain of -5%. Multiple forward strain values were used for each condition to investigate the development of back stress during straining. The maximum

forward strain was selected to be ~ 0.5% to 1% below the uniform elongation which allows the estimation of the maximum back stress and reduce the chance of tension instabilities. Due to the limited amount of the HR materials, only one sample was tested for each forward strain. As will be shown later, the repeatability of the forward loading curves demonstrates that the error associated with sample to sample differences should be small.

One of the difficulties in tension-compression tests is the buckling of the sample during compression. In this study, two clip-on extensometers mounted diametrically opposed to each other were used to monitor the extension of the gauge section during tension-compression tests (Figure 4.7a). The two extensometers were calibrated to have different gauge lengths (GL) to allow easy experimental setup. The dual-extensometer setup has two advantages: (i) the outputs from the two extensometers can be averaged to compensate any bending strain manifested during the test (i.e. $\bar{\varepsilon} = (\varepsilon_1 + \varepsilon_2)/2$); (ii) the difference between extensometer readings can be used to determine the onset of buckling. Figure 4.7b shows the strain from the two extensometers as a function of test running time as well as the averaged output. The readings from the two extensometers show little difference until $t \approx 70$ s where a large deviation starts to develop. The onset of buckling can be more accurately determined using the slopes and the second derivatives of the two strain-time curves.

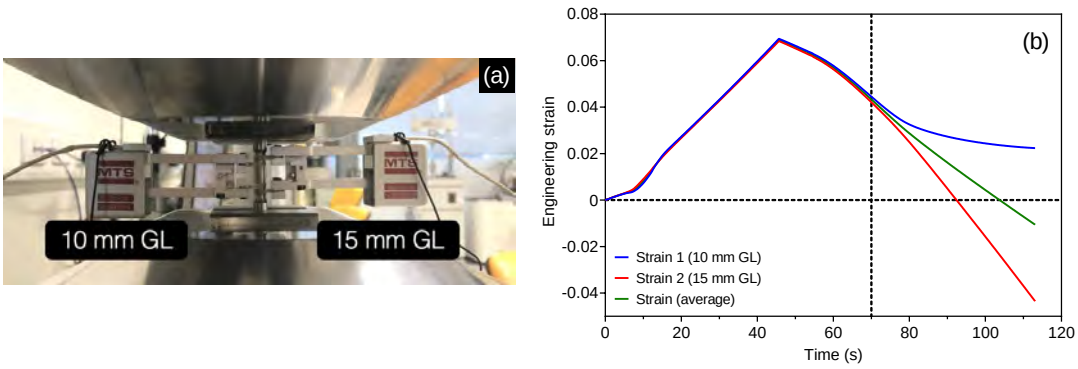

Figure 4.7: *(a) Two extensometers mounted diametrically opposed to each other on the sample. (b) An example of the strain-time evolutions for the two extensometers and the averaged output.*

4.2.3.2 Analyses of tension-compression curves

To conduct the data analysis of tension-compression curves, the raw curve needs to be converted so that the reverse loading part is plotted also in the tensile domain (Figure 4.8a). We can then define the stress at the unloading point as the forward stress σ_f and the intercept with the strain axis after unloading as the forward plastic strain ε_p^f (Figure 4.8b). In the forward direction, the forward flow stress σ_f can be divided into:

$$\sigma_f = \sigma_y + \sigma_d + \langle \sigma_b \rangle \tag{4.7}$$

where σ_y is the yield strength and σ_d is the hardening due to the build-up of forest dislocations during plastic deformation. Both σ_y and σ_d oppose deformation in both forward and reverse directions to the same degree (i.e. non-directional, isotropic hardening). $\langle \sigma_b \rangle$ is the back stress which opposes the deformation in the forward direction but facilitates deformation in the reverse direction (i.e. directional, kinematic hardening).

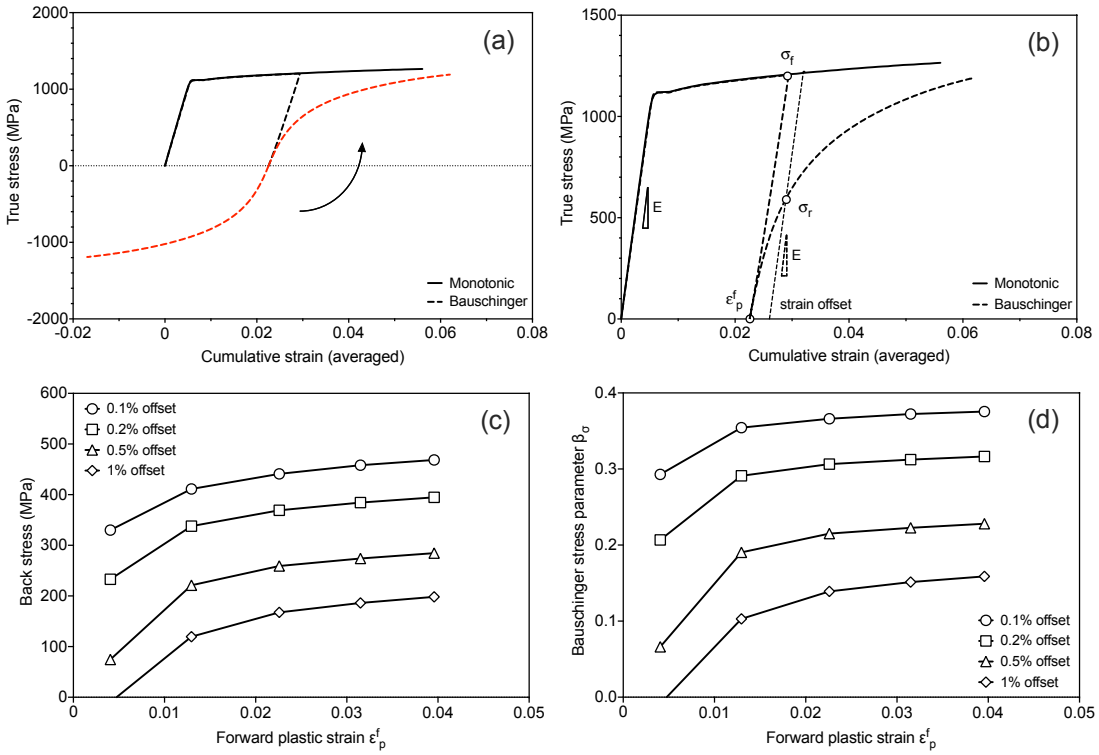

Figure 4.8: *Analysis of the Bauschinger effect using stress based parameters. (a) Conversion of tension-compression curve into the tensile domain. (b) Determination of the reverse yield stress σ_r. (c) Evolution of the back stress as function of forward plastic strain and the effect of the reverse strain offset. (d) Evolution of the Bauschinger stress parameter as a function of forward plastic strain and the effect of the reverse strain offset.*

After the forward loading, the loading direction is reversed. The flow stress in the reverse direction σ_r (now negative) is

$$-\sigma_r = -\sigma_y - \sigma_d + \langle \sigma_b \rangle \tag{4.8}$$

Combination of equations (4.7) and (4.8) leads to

$$\langle \sigma_b \rangle = \frac{\sigma_f + \sigma_r}{2} = \frac{\sigma_f - |\sigma_r|}{2} \tag{4.9}$$

$|\sigma_r|$ and $\langle\sigma_b\rangle$ have often been determined with a "permanent softening" method in which the flow curves in both forward and reverse directions become parallel and a consistent decrease of flow stress can be observed [131]. Despite the experimental difficulties on achieving a large reverse strain without structural instabilities, not all tempering conditions show parallelism between forward and reverse curves at large strains. In this case, a reverse strain offset ε^r_{off} needs to be specified in order to use Eq. 4.9 and the measured $|\sigma_r|$ in the tensile directions represents the offset reverse yield strength of the material. If a material shows no Bauschinger effect, the value of σ_f and $|\sigma_r|$ should be the same and a zero $\langle\sigma_b\rangle$ should be found. Figure 4.8b shows the determination of $|\sigma_r|$ on the converted tension-compression curve and figure 4.8c shows the magnitude of $\langle\sigma_b\rangle$ as a function of ε^f_p and its dependence on ε^r_{off}. Regardless of the selection of the ε^r_{off}, $\langle\sigma_b\rangle$ increases quickly until ~2% forward plastic strain and then gradually saturates. In this work, the 0.2% offset was used most of the time which is commonly used in the literature. To compare with materials with different flow stresses, the back stress is often normalised by the forward flow stress, resulting in a dimensionless parameter called the Bauschinger stress parameter ($\beta_\sigma = \langle\sigma_b\rangle / \sigma_f$, shown in figure 4.8d).

Besides the decrease in reverse yield strength, another feature of the Bauschinger effect is the long transient required to regain σ_f in the reverse direction. Quantitatively, the transient can be measured as the plastic reverse strain required to reach σ_f which is often termed as the Bauschinger strain parameter β_ε. Since not all samples can recover σ_f fully due to sample buckling, 85%σ_f was selected as a the target in this work and was termed as $\beta_{0.85}$ (Figure 4.9a). As the forward plastic strain increases, the transient gets larger and the measured $\beta_{0.85}$ values may be described well with a linear regression and the slope of the line is a determination of the magnitude of the Bauschinger effect (Figure 4.9b). For a material that shows a large Bauschinger effect, the strain hardening is mainly kinematic and the transient develops faster as a function of forward plastic strain. The evolution of β_σ and $\beta_{0.85}$ will be shown in Appendix A.

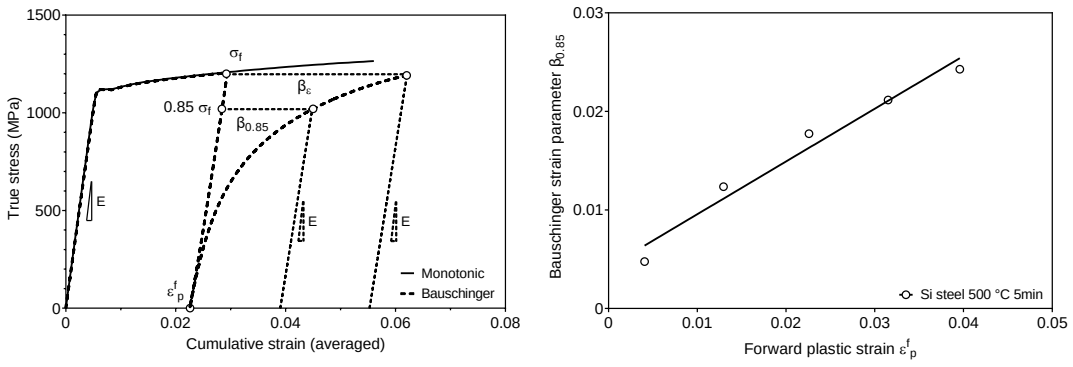

Figure 4.9: *Analysis of the Bauschinger effect using the strain based parameter. (a) Determination of β_ε and $\beta_{0.85}$ using the converted tension-compression curve. (b) Evolution of $\beta_{0.85}$ as a function of forward plastic strains and its linear regression.*

4.2.4 Strength differences between cold rolled and hot rolled materials

As indicated in Section 4.1, materials with different initial states were used in this study and experimental results were obtained from both cold rolled and hot rolled initial rolled states. To ensure the mechanical properties can be compared fairly, Figure 4.10 a1 - c1 show the comparison of tensile curves between materials with different initial states. It can be seen that the HR state shows constantly higher flow strength than the CR state regardless of compositions. This may be attributed to the larger thermal mass of HR samples during tempering, which results in a heating rate effect and higher residual strength. The maximum difference can be seen in the case of the Al steel where the difference between the flow stresses in the as-quenched condition is around 150 MPa, which is about ∼10% of the total flow stress. For the other two compositions, the maximum difference is always around or under 5%. Therefore, it should be appropriate to use the results from both materials states interchangeably with special care for the Al steel. Another noticeable difference is the constantly lower flow stress in the Al steel compared to the other two compositions regardless of the initial states. This could be explained by the larger prior grain size of the Al steel (Figure 4.10 a2 - c2), which reduces the hardening from grain refinement. While it affects the magnitude of the strength of the Al steel, the chemistry effect can still be revealed by normalised parameters shown in later chapters.

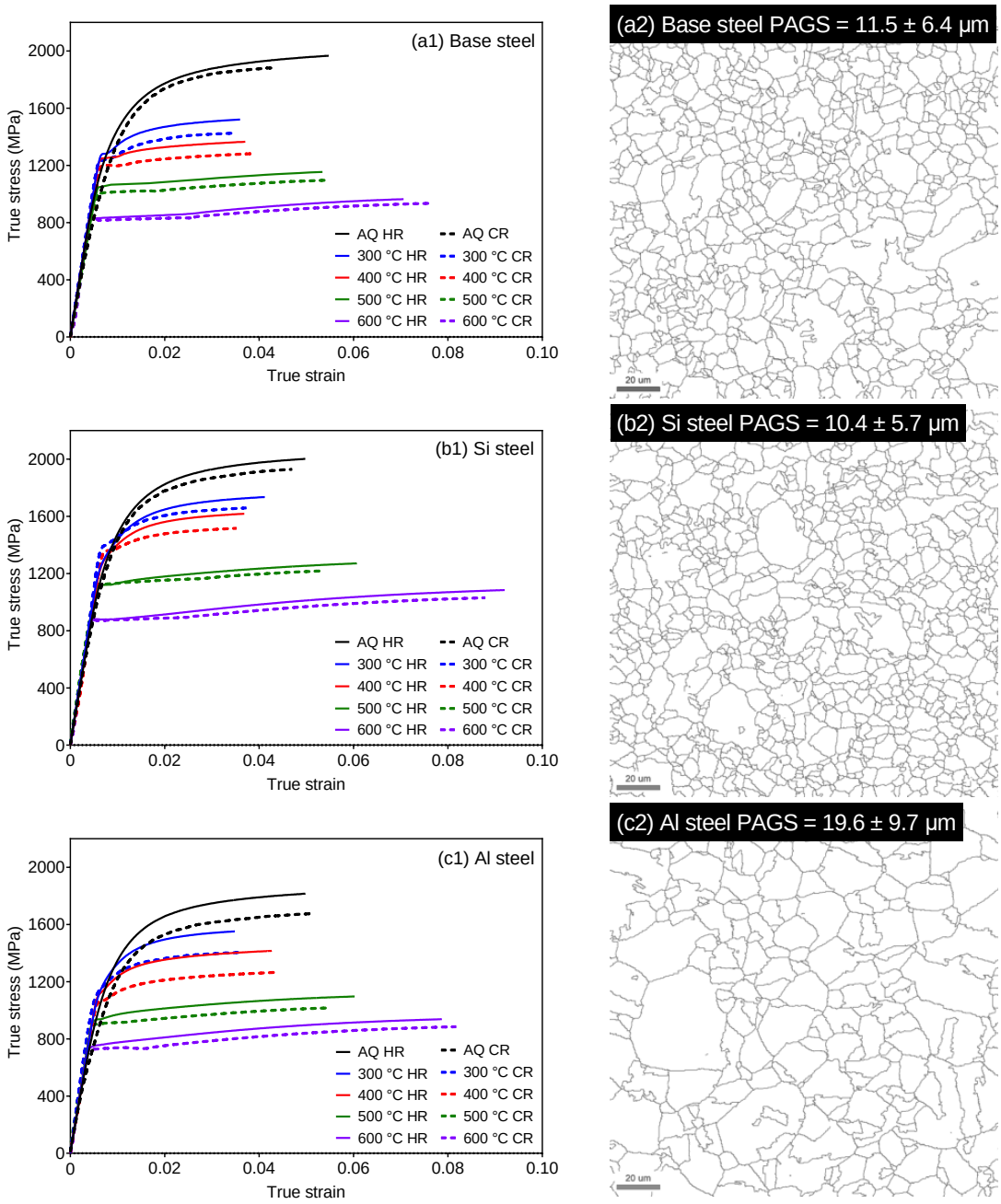

Figure 4.10: *(a1) - (c1) Comparison of tensile curves between materials with a cold rolled or a hot rolled initial state. For tempered samples, the samples were heat treated at the specified temperature for 5 minutes. (a2) - (c2) High angle boundary maps showing the sizes of reconstructed prior austenite grains in each steel (maps obtained from the CR materials, the reconstruction method can be found in the work of Nyyssönen[137]). Average grain sizes were estimated by the equivalent circular diameter and the area fraction weighted average method, errors shown in the micrographs represent one standard deviation of the measurement.*

4.3 Microstructural characterisation

4.3.1 Sample sectioning

Most microstructural characterisations were carried out on CR samples unless specified otherwise. Figure 4.11 shows how samples were cut from the undeformed grip section of the tensile test specimens. The surface perpendicular to the rolling direction was examined in SEM/EBSD tests using a cross-sectional sample holder to minimise drifting of the sample at high tilting angles. At least 1/3 of the sheet thickness was ground off the samples for x-ray diffraction and nanoindentation experiments to eliminate any effect of decarburisation.

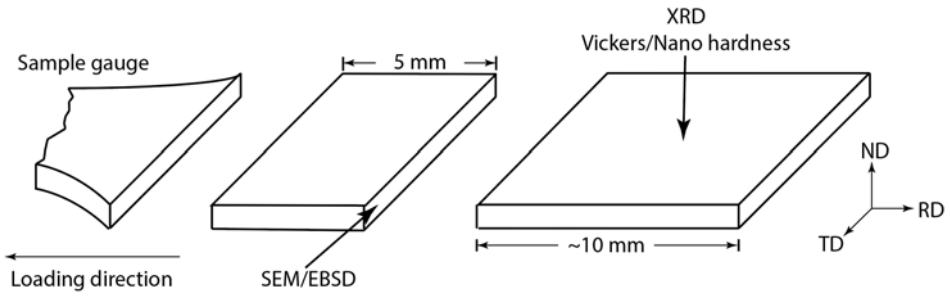

Figure 4.11: *Schematics showing the sample cutting procedure and examined surfaces in microstructural experiments for undeformed samples. Dimensions are not drawn to scale.*

4.3.2 Nanoindentation

The changes in mechanical heterogeneities as a function of tempering were examined using nanoindentation. The nanoindentation experiments were conducted with a Hysitron TriboLab machine equipped with a Berkovich indenter. The indenter tip area function was calibrated using a fused silica standard sample.

Load controlled tests were defined so that a peak load of 2 mN is applied in 10 seconds followed by a 2-second dwell time to accommodate any deformation creep and the load is finally unloaded in 10 seconds (Figure 4.12a). At a peak load of 2 mN, the indentation depth in the as-quenched samples and tempered samples ranged from 0.1 μm to 0.15 μm (Figure 4.12b). A 15 × 15 indentation matrix with an indent spacing of 2 μm (as-quenched samples) or 3 μm (tempered samples) was performed on each sample polished to a 0.05 μm surface finish. Each tested area covered a square of 40 μm to 50 μm in size which should be able to include several prior austenite grains. After each test, data points with a drift rate above ±0.05 nm/s were discarded and the total number of valid measurements for each specimen was 200 to 210. Data analysis was based on the Oliver-Pharr method [138] embodied in the Hysitron TriboScan software (version 9.4). The obtained nanohardness values show a good agreement with the experiments performed by Ohmura and co-workers in Fe-C steels [139–141].

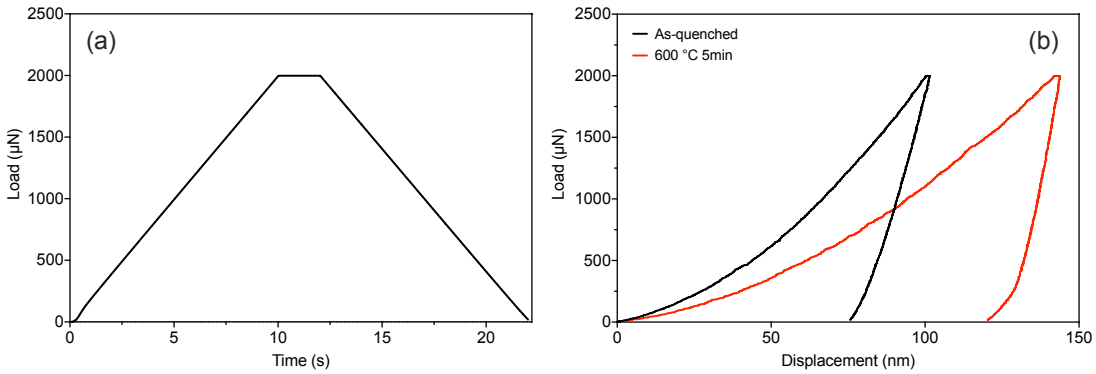

Figure 4.12: *Typical load-time (a) and load-displacement (b) curves obtained from nanoindentation tests conducted on Si steel samples.*

Generally, it is difficult to compare directly the strength results obtained by nanoindentation and monotonic tensile tests since the samples experience different stress states during deformation (i.e. a 3-D stress field in the case of nanoindentation and uniaxial deformation in the case of monotonic tensile test). However, our experimental campaign allows us to construct empirical correlations between the nanohardness and strength values (Figure 4.13). While the correlation between the nanohardness and the yield stress is poor (Figure 4.13a), the one for the ultimate tensile stress is much better (Figure 4.13b). Since the indentation strain associated with a Berkovich tip is about 8% [142], it is not surprising to see that the nanoindentation test is better correlated the ultimate tensile stress which is a result of strain hardening. The UTS-nanohardness correlation will be used in later chapters to compare with modelled results.

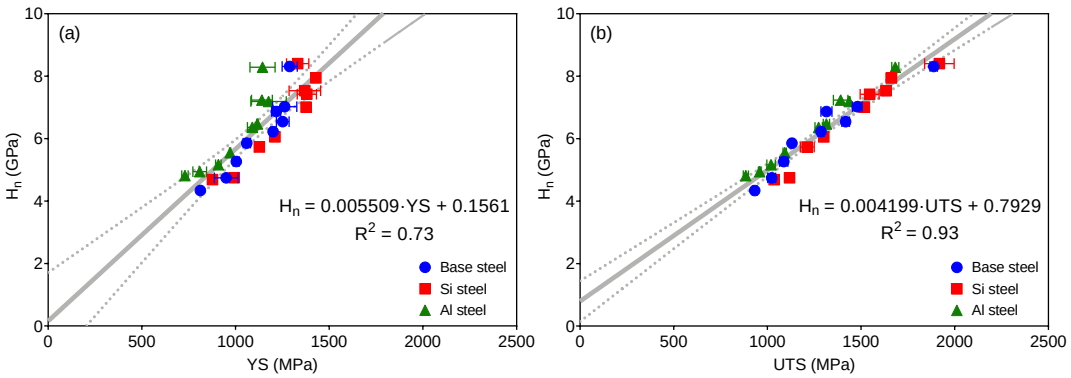

Figure 4.13: *Correlation between the yield stress (a) and the ultimate tensile stress (b) from monotonic tensile tests and the nanohadness values.*

4.3.3 X-ray diffraction (XRD) and line profile analyses

X-ray diffraction (XRD) was used to investigate the recovery kinetics and deformation mechanisms of as-quenched and tempered martensite. For recovery kinetics, the same square samples for the nano-hardness measurement were examined before the indentation tests were performed. For deformation mechanisms, tensile tests were interrupted at different forward strains and the deformed gauge section was cut from the sample and examined. The XRD experiments were conducted on a Bruker D8 Advance diffractometer with a Co tube (operated at 40 kV and 25 mA) under the Bragg-Brentano reflection geometry. Co source emission profiles, zero error and instrument profiles were assessed from the scan of the NIST LaB_6 specimen. X-ray scans were performed over the $38° \sim 132°$ 2θ range at a step size of 0.03° to capture four BCC peaks.

Line profile analyses of XRD patterns were performed in the Bruker-TOPAS (version 5) software using the whole-pattern Pawley method. Peak broadening of BCC reflections was modelled using Balzar's double-Voigt approach [143] embodied in TOPAS that considers convoluted Voigt functions of the Gaussian and the Lorentzian components that can be refined to describe the domain size broadening and the microstrain broadening respectively. In this study, the microstrain broadening is the more dominant factor that controls peak broadening and the fitted microstrain showed good correlations with FWHM of different reflections for various heat treatment conditions (Figure 4.14) since the measured FWHM for each reflection ($FWHM^{hkl}_{2\theta}$) can be related to the peak broadening due to modelled microstrain ($FWHM^{hkl}_{\langle\varepsilon_0\rangle}$) by:

$$FWHM^{hkl}_{2\theta} = 2 \cdot FWHM^{hkl}_{\langle\varepsilon_0\rangle} \cdot \tan\theta^{hkl}_0 \tag{4.10}$$

where θ^{hkl}_0 is the angle at which the hkl reflection was observed. Therefore, the microstrain is used to describe the magnitude of peak broadening instead of FWHM of individual peaks for brevity.

4.3.4 Scanning electron microscopy (SEM) and electron backscattered diffraction (EBSD)

Scanning electron microscopy (SEM) experiments were conducted with a JEOL JSM-7001F field emission gun (FEG) SEM under the secondary electron imaging (SEI) mode with a 10 kV accelerating voltage to reveal cementite precipitates. All samples examined by SEM were polished to 1μm surface finish and etched with either 4% Picral (4 g picric acid, 2 ml hydrochloride acid and 100 ml ethanol) for cementite precipitates or 2% Nital (2ml nitric acid and 100 ml ethanol) for grain boundary contrast.

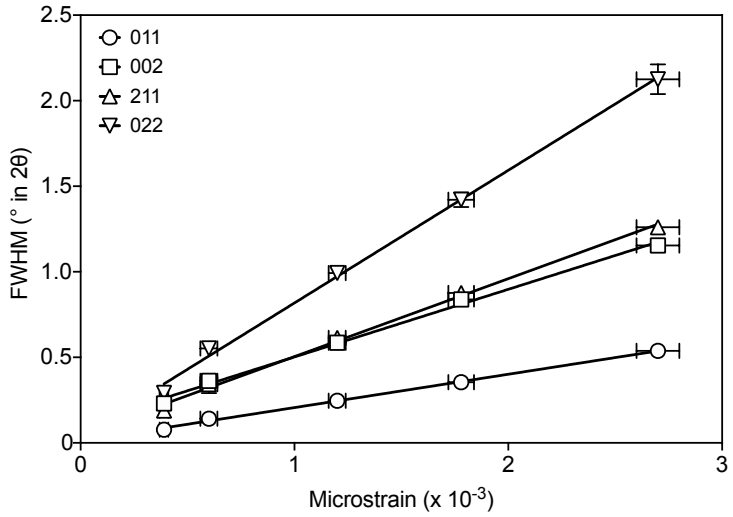

Figure 4.14: *Correlation between FWHM of individual reflections and the fitted microstrain. Data points were collected from XRD scans of one as-quenched base steel sample, and four base steel samples tempered at different temperatures for 5 minutes.*

Electron backscattered diffraction (EBSD) was used to reveal the evolution of martensite substructures. The accelerating voltage in the EBSD mode was 15 kV and the probe current was 18 nA, a Nordlys–II EBSD detector and the Oxford Instruments AZtec software suite were used as the acquisition system. The post-processing of EBSD data was conducted using the TSL-OIM 8 software. The overall indexing rates were above 85% for all samples with a 0.05 μm surface finish and most non-indexed points were found at high angle grain boundaries. One iteration of neighbour misorientation correlation was conducted to clean the data.

Two scanning step sizes were used in this study. Scans with a smaller size (60 μm × 60 μm) were conducted using a step size of 0.1 μm to resolve the fine martensitic substructures. Due to the spatial and the angular resolution of EBSD systems, it is difficult to resolve laths with typical dimensions of 200 nm to 400 nm [89] but it should be sufficient to monitor the size evolution of sub-blocks, blocks and possible recrystallised grains. Scans with a larger size (180 μm × 180 μm) were performed on as-quenched samples with a step size of 0.3 μm to measure the prior austenite grain size. Reconstruction of prior austenite grains were achieved using the open-source MATLAB code developed by Nyyssönen which is embedded in the MTEX package [137, 144]. During post-processing in the TSL-OIM software, grains were defined as pixels that are separated by a misorientation angle (θ_{mis}) greater than 15° and the smallest grain should consist of at least three pixels. The size of a grain was defined as its equivalent circular diameter (ECD). Therefore, the smallest grain size is ∼0.2 μm and ∼1 μm in the case of small scans and large scans respectively.

To estimate the average grain size ($\bar{D}_g$) in each scan, two averaging methods were used. The first method is the arithmetic average:

$$\bar{D}_g^N = \frac{\sum_{i=1}^{N} D_g^i}{N} \tag{4.11}$$

where N is the total number of grains and D_g^i is the grain size for grain i. The value obtained using Eq. 4.11 will be skewed to small values if the scan has a large fraction of grains with small grain sizes. As shown in Chapter 2, both coarse and fine laths/blocks exist in martensite and the arithmetic average can be used to monitor the evolution of fine laths/blocks. The second method is the area weighted average:

$$\bar{D}_g^A = \frac{\sum_{i=1}^{N} A_i D_g^i}{\sum_{i=1}^{N} A_i} \tag{4.12}$$

where A_i is the area for grain i. By using Eq. 4.12, the effect of small grains is reduced and the evolution of coarse laths/blocks may be investigated.

4.3.5 Transmission electron microscopy (TEM)

Transmission electron microscopy (TEM) experiments were performed to quantify the number of Orowan loops stored around cementite precipitates. To allow easy sample preparation and accurate correlation with Bauschinger test results, all TEM specimens were prepared from the HR plate. All studied samples were quenched and tempered at 600 °C for 1 hour. Monotonic tests were interrupted at different total strains and slices with a thickness of ~350 μm were cut from the gauge section of the tensile sample. The slices were then mechanically ground to ~100 μm before 3 mm diameter discs were punched out of the slices. The discs were electropolished with the Struers Tenupol-5 twin-jet polishing system in a 3.5% (vol. %) perchloric acid in methanol at a temperature of -25 °C and a voltage of 50 V. The samples were then examined on an FEI Tecnai G^2 T20 TEM operated at 200 kV.

4.3.6 Differential scanning calorimetry (DSC)

Differential scanning calorimetry was used to study the effect of Si and Al addition on the precipitation kinetics of cementite. Samples were taken from the undeformed grip section and mechanically ground to a dimension of ~4 mm × 4 mm × 0.1 mm, which correspond to a typical sample weight of ~100 - 120 mg. The grips were left at room temperature in a temperature controlled laboratory before the DSC tests. DSC was performed using the Perkin Elmer Pyris 1 with a heating rate of 25 °C/min between 20 °C to 500 °C. Before the tests, calibration of the equipment was performed by testing In and Zn standards. During data acquisition, the baseline is automatically subtracted by the system.

Chapter 5

A unified framework for modelling martensite as a composite - a critical comparison of existing composite models

5.1 Introduction

In Section 2.2.3, four theories on the strain hardening of as-quenched martensite were reviewed. Among them, both the mobile dislocation hypothesis and the retained austenite hypothesis can explain the low elastic limit of as-quenched martensite but it is hard to qualitatively describe the large strain hardening response when the plastic strain becomes large (Section 2.2.3.1 and 2.2.3.2). The other two models treat the martensite as a composite and consider the gradual yielding of as-quenched martensite as a result of transformation induced heterogeneities. These "composite" models both show promising results compared with experimental stress-strain curves. However, limitations of these models were also discussed in Section 2.2.3 and further modelling and experimental works are needed to investigate the capabilities of these models. In this chapter, a unified framework is constructed to compare the simulated flow behaviours using the two composite models available in the literature. Comparison between modelled results and experimental observations enables the quantitative evaluation of the composite strengthening hypotheses. Attempts are also made to experimentally quantify the magnitude of forest dislocation based strengthening and other hardening contributions.

5.2 Comparison of existing composite models under a unified modelling framework

5.2.1 Introduction to the unified modelling framework

In the following sections, the model proposed by Allain *et al*. will be termed the yield stress spectrum model (Section 2.2.3.3 and Ref [5]) and the model proposed by Hutchinson *et al.* will be termed the residual stress spectrum model (Section 2.2.3.4 and Ref [6, 70]). In essence, both models consider as-quenched martensite as a composite but the gradual yielding of composite constituents are related to different initial states (Section 2.2.3): the yield stress spectrum model assumes that as-quenched martensite comprises constituents with different yield stresses that may be described by a continuous yield stress spectrum [5]; the residual stress spectrum model considers that the constituents in martensite share a similar yield stress but each constituent is affected by a initial residual stress that may vary locally as a result of martensitic transformation [6, 70]. The two models also differ in the implementation of incremental straining and strain partitioning. Therefore, it is difficult to compare the two models on the same basis although they share the same fundamental hypothesis (i.e as-quenched martensite may be described as a composite). In this section, we have developed a framework which includes initialisation schemes for both composite models and a unified incremental straining scheme that is able to simulate both monotonic tension and tension-compression tests. This allows the two composite models to be compared quantitatively and to be implemented in combination (Section 7.1). When the composite effect becomes less dominant, the framework can also be simplified to a model that considers proper isotropic and kinematic hardening, which will be used to model high temperature tempered martensite (Section 7.2).

In principle, the macroscopic stress-strain response of the composite-like martensite during straining is obtained by averaging over the response of its individual constituents as:

$$\bar{\varepsilon} = \sum_{i=1}^{n_c} V^i \varepsilon^i \tag{5.1}$$

$$\bar{\sigma} = \sum_{i=1}^{n_c} V^i \sigma^i \tag{5.2}$$

where n_c is the total number of constituents, $\bar{\varepsilon}$ and $\bar{\sigma}$ are the average strain and stress values of the composite, ε^i and σ^i are the strain and stress values of the i^{th} constituent with a volume fraction V^i. At this stage, we do not seek to identify a constituent to a specific microstructural feature, such as martensite lath or block. The stress-strain response of each constituent will be assumed to obey J_2 elasto-plasticity theory with the following parameters [145]:

1. A Young's modulus E^i and a Poisson's ratio v^i(set as constants for constituents, $E^i = 205$ GPa, $v^i = 0.3$).

2. An initial yield stress σ^i_{y0} beyond which the constituent deforms plastically. The instantaneous yield stress σ^i_y evolves with the accumulated plastic strain p^i according to a hardening law.

3. An isotropic hardening law $R^i\left(p^i\right) = \sigma^i_y - \sigma^i_{y0}$.

4. An interaction law that describes the strain partitioning between soft and hard constituents.

While both the yield stress spectrum and residual stress spectrum models can share the same parameter sets 1, 3 and 4, the models differ in their assumptions in parameter sets 2 which also affect the determination of V^i. As a consequence, the unified framework is divided into two main parts. The first part is related to the initialisation of constituents and the initialisation routine is model dependent. The second part is related to the incremental straining of the composite constituents, which is model independent. While detailed discussions on the two parts will be shown in later sections, Table 5.1 summarises the key hypotheses used in the framework and highlights the differences and similarities of the two models.

Table 5.1: *Key hypotheses in the unified framework and composite models.*

		Yield stress spectrum	Residual stress spectrum
Constituent initialisation	Initial stress state	Zero stress state	**Different pre-stress states for each constituent**
	Initial yield stress	**Different yield stresses for each constituent**	Same yield stress for each constituent
	Volume fraction	Found in the discretised yield stress spectrum	Same volume fraction for each constituent
Incremental straining	Young's modulus	Same for all constituents	
	Poisson's ratio	Same for all constituents	
	Stress state during straining	Increments of stress in z-direction only	
	Hardening	No hardening at constituent level	
	Interaction law	$\beta = -\frac{\Delta\bar{\sigma}_{zz} - \Delta\sigma^i_{zz}}{\Delta\bar{\varepsilon}_{zz} - \Delta\varepsilon^i_{zz}}$, β is the same for all constituents	

5.2.2 Constituent initialisation in composite models

5.2.2.1 Yield stress spectrum model

In the yield stress spectrum model, the onset of plasticity in each constituent is governed solely by its initial yield stress σ^i_{y0}. From the continuum mechanics perspective, constituents in the yield stress spectrum model all start from a zero stress state and they reach their unique yield surfaces at different forward strains, which results in the continuous yielding behaviour (Figure 5.1a).

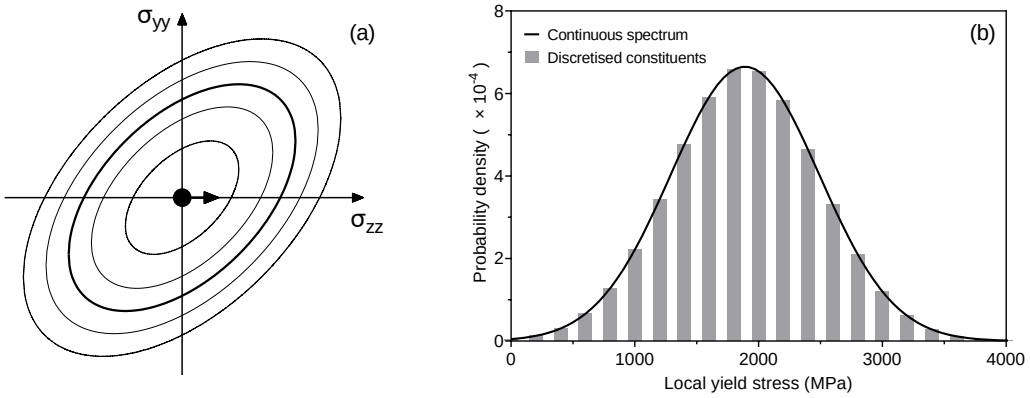

Figure 5.1: *Constituent initialisation for the yield stress spectrum model. (a) Continuum mechanics representation of the yield stress spectrum model. The solid dot represents the common initial stress state for all constituents and the arrow represents the loading direction. (b) Discretisation of a continuous normal distribution with a finite number of bins, the current plot shows 25 bins for clarity.*

In a continuous yield stress spectrum, the probability of finding a constituent with a particular yield stress can be found using a probability density function. In the work of Allain *et al.*, a Weibull distribution was used [5]:

$$f(\sigma^i_{y0}) = \begin{cases} 0 & \sigma_{y0} < \sigma_{min} \\ \frac{n}{\sigma_0}\left(\frac{\sigma^i_{y0}-\sigma_{min}}{\sigma_0}\right)^{n-1} & \sigma_{y0} \geq \sigma_{min} \end{cases} \tag{5.3}$$

σ_{min} is the yield stress of the softest constituent in the composite, σ_0 is the width of the yield stress distribution and n governs the shape of the distribution. While the existence of σ_{min} allows Allain *et al.* to assign a physically reasonable value (300 MPa) to the softest constituent, the shape factor was set arbitrarily and it could be highly correlated with the width factor σ_0. In this chapter, we use a normal distribution which defines the mean (σ_μ) and the standard deviation (σ_{sd}) of the yield stress spectrum and omit the use of σ_{min}:

$$f\left(\sigma^i_{y0}\right) = \frac{1}{\sqrt{2\pi\sigma^2_{sd}}} \exp\left(-\frac{\sigma^i_{y0}-\sigma_\mu}{2\sigma^2_{sd}}\right) \tag{5.4}$$

Of course, a symmetrical distribution without a lower bound may lead to overestimation of the contribution from soft constituents but it also allows this model to be compared fairly with the residual stress spectrum model and the nanoindentation results shown later. In this model, σ_{sd} and σ_{μ} are the two free variables required to describe the flow behaviour of the material.

In the initialisation step, the continuous normal distribution is discretised with a finite number of bins and a schematic of the binning routine is shown in Figure 5.1b. The volume fraction of each constituent is defined as the area under the probability density function within each binning interval and can be approximated with the cumulative density function $F\left(\sigma^i_{y0}\right)$ if the interval size is sufficiently small:

$$V^i = F\left(\sigma^i_{end}\right) - F\left(\sigma^i_{start}\right) \tag{5.5}$$

V^i is the volume fraction of the constituent, $F\left(\sigma^i_{end}\right)$ is the value of the cumulative density function at the end of the interval and $F\left(\sigma^i_{start}\right)$ is the value of the cumulative density function at the start of the interval. In accordance with the volume fraction calculation, the yield stress of each constituent is approximated as the mid-point of the interval as:

$$\sigma^i_{y0} = \left(\sigma^i_{end} + \sigma^i_{start}\right)/2 \tag{5.6}$$

5.2.2.2 Residual stress spectrum model

In the residual stress spectrum model, the onset of plasticity in each constituent is not solely governed by its yield stress but also influenced by its initial residual stress state [6, 70]. If the residual stress is aligned towards the loading direction, it will facilitate the yielding of the constituent and if the residual stress is aligned against the loading direction, it will resist the yielding of the constituent. From the continuum mechanics perspective, it is equivalent to assigning each constituent a non-zero, elastic stress/strain state along the loading direction before straining but the constituents share the same yield surface (Figure 5.2a). The constituent with a positive pre-stress will yield earlier than the constituent with a negative pre-stress.

Based on this principle, the model is constructed to consider the equivalent residual stress along the loading direction only and reduce the 3-D stress state in the original model to a 1-D case [6, 70]. Of course, this simplified implementation lacks considerations of the effect of grain orientation and 3-D strain partitioning compared with the CPFEM model shown in the work of Hutchinson *et al.* [70], it should still be sufficient to capture the key ingredients of the residual stress hypothesis. The number of constituents is determined by the number of residual stress states n_c and each constituent has the same volume fraction as $V^i = 1/n_c$ and shares the same yield stress $\sigma^i_{y0} = \bar{\sigma}_{y0}$. The maximum magnitude

of the residual stress (RS_{max}) can be calculated as a fraction of $\bar{\sigma}_{y0}$. The RS_{max} to $\bar{\sigma}_{y0}$ ratio is the only free variable required in this model. In this way, the descritised distribution of constituents can be described by the flat spectrum shown in Figure 5.2b. As will be shown in later sections, the exact volume fractions of the constituents should not significantly affect the simulated flow behaviour of the bulk material as long as the residual stress spectrum is symmetrical and the macroscopic stress averages to zero. Therefore, we do not seek to refine the flat spectrum with more sophisticated distributions at this stage. However, it must be stressed again that this simplification is highly idealised and does not reflect the full complexity of the residual stress states in martensite.

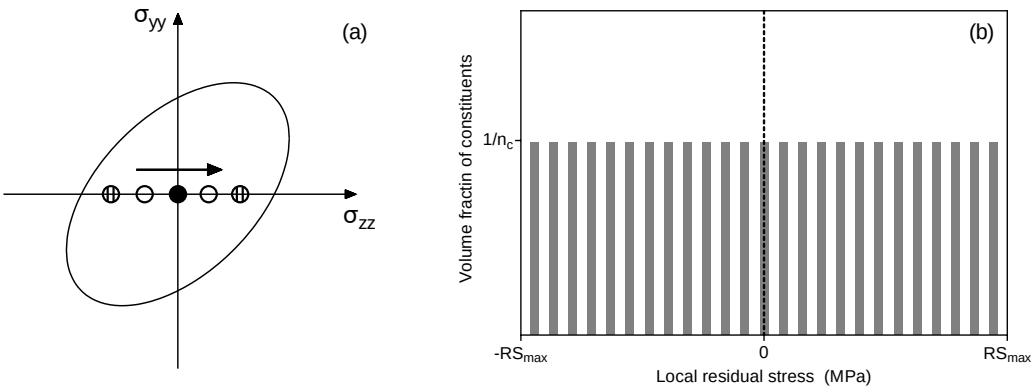

Figure 5.2: *Constituents initialisation for the residual stress spectrum model. (a) Continuum mechanics representation of the residual stress spectrum model. The dots represent the different residual stress states of the constituents and the arrow represents the loading direction. (b) Flat spectrum of a ranges of residual stresses, 25 constituents are presented in the current plot for clarity.*

In the initialisation step, each constituent is assigned with a unique residual stress (σ^i_{rs}) found in the flat spectrum and its initial stress state can be described as:

$$\boldsymbol{\sigma}^i_0 = \begin{pmatrix} 0 & 0 & 0 \\ 0 & 0 & 0 \\ 0 & 0 & \sigma^i_{rs} \end{pmatrix} \tag{5.7}$$

In the current implementation, we focused on the uniaxial loading condition so σ_{zz} is the only non-zero stress component of the stress tensor. Therefore, the initial stress tensor is effectively a scalar. In the three-dimensional case, the initial residual stress should be deviatoric (i.e. trace of the tensor is zero), which is implemented in the original work of Hutchinson *et al.* [6]. The initial strain state can then be calculated using the compliance tensor $\boldsymbol{S}^i$:

$$\boldsymbol{\varepsilon}^i_0 = \boldsymbol{S}^i : \boldsymbol{\sigma}^i_0 \tag{5.8}$$

5.2.3 Incremental straining

After the constituents are initialised according to the selected model, the incremental straining of the constituents and the composite-like martensite can commence. A schematic diagram summarising the work flow of the incremental scheme is shown in Figure 5.4. To simulate an uniaxial tension experiment, a macroscopic strain increment $\Delta\bar{\varepsilon}_{zz}$ is applied to the z-direction. Each constituent is strained by a strain increment $\Delta\varepsilon^i_{zz}$ according to the interaction law discussed below. Strain increments in the other two directions are *a priori* unknown but can be estimated by the Poisson's ratio ν: $\Delta\varepsilon^i_{xx} = \Delta\varepsilon^i_{yy} = -\nu\Delta\varepsilon^i_{zz}$. The microscopic stress increment $\Delta\boldsymbol{\sigma}^i$ can then be calculated using the stiffness matrix $\boldsymbol{C}^i$ and the classic return-mapping algorithm assuming the constituents obey J_2 the elasto-plasticity theory with no strain hardening after yielding [145]:

$$\Delta\boldsymbol{\sigma}^i = \boldsymbol{C}^i : \Delta\boldsymbol{\varepsilon}^i \tag{5.9}$$

$$R^i(p) = 0,\ \sigma^i_y(p) = \sigma^i_{y0} \tag{5.10}$$

The large area EBSD results showed that the magnitude of $\boldsymbol{C}^i$ may be estimated with E and ν assuming the material is elastically isotropic (i.e. no crystallographic texture). In uniaxial tension, we should have ($\sigma^i_{xx} = \sigma^i_{yy} = 0$) at all times. While this holds true when a constituent is under elastic loading, it starts to deviate from uniaxial tension at the onset of plasticity when $\Delta\varepsilon^i_{xx} = \Delta\varepsilon^i_{yy} = -\nu\Delta\varepsilon^i_{zz}$ is no longer valid. In this case, the uniaxial tension condition is maintained by calculating the appropriate $\Delta\varepsilon^i_{xx}$ and $\Delta\varepsilon^i_{yy}$ values using an iterative Newton-Raphson method.

The strain increments $\Delta\varepsilon^i_{zz}$ should be such that the following incremental interaction law is satisfied [5]:

$$\beta = -\frac{\Delta\bar{\sigma}_{zz} - \Delta\sigma^i_{zz}}{\Delta\bar{\varepsilon}_{zz} - \Delta\varepsilon^i_{zz}} \tag{5.11}$$

where $\Delta\bar{\varepsilon}_{zz}$ is the input, $\Delta\sigma^i_{zz}$ is calculated using $\Delta\varepsilon^i_{zz}$, and $\Delta\bar{\sigma}_{zz}$ is determined using the volume average of $\Delta\sigma^i_{zz}$ (Eq. 5.2). The value of β can be varied to consider multiple strain partitioning conditions from iso-strain ($\beta = \infty$) to iso-stress ($\beta = 0$). Figure 5.3 shows the effect of β on the magnitude of σ_μ and σ_{sd} in the yield stress spectrum model. It can be seen that σ_μ decreases as β approaches to the iso-strain condition (Figure 5.3a) whereas σ_{sd} increases (Figure 5.3b). Since we assume that the yield stress spectrum is symmetrical and the constituents are elastic perfectly plastic, the mean of the yield stress spectrum should not deviate much from the experimental tensile strength. If this is not the case, the modelled tensile strength would be found far from the experimental value as the constituents closer to the mean account for most of the total volume fraction and contribute significantly to the modelled

tensile curve. Therefore, β is fixed as $E/4$ and it is the same for all constituents in the yield stress spectrum model. To be consistent with the yield stress spectrum model, the constituents in the residual stress spectrum model are also defined to follow the same interaction law. Eq. 5.11 for all constituents and the macroscopic response can be again solved iteratively using Newton-Raphson method.

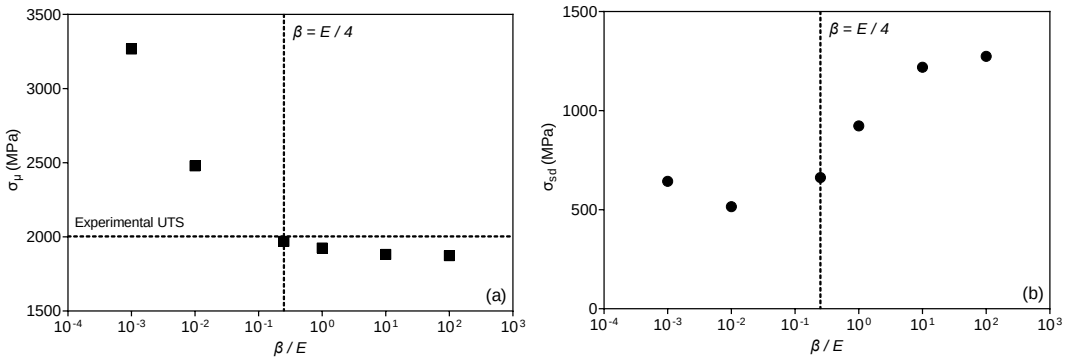

Figure 5.3: *The effect of β on the magnitudes of σ_μ and σ_{sd}. The parameters optimised to best describe the monotonic tensile behaviour of the as-quenched Si steel.*

Once the interaction law is satisfied, the macroscopic response can be calculated using Eq. 5.1 and Eq. 5.2. The simulation continues at the next time step until the termination criterion is met. The termination criterion is usually set as a particular macroscopic strain but other criteria can also be implemented (e.g. Considere's necking criterion). For simulations of the tension-compression test, the sign of $\Delta\bar{\varepsilon}_{zz}$ is changed once a particular $\bar{\varepsilon}_{zz}$ is reached and the termination criteria is also changed to reflect the end point of the compression test.

It is worthy noting that there are potential limitations with the current implementation. By assuming the constituents obey the J_2 yield criterion, it is implied that the constituents should yield at the same stress in both tension and compression. This is not true in the case of martensitic steels. Previous literature has demonstrated that martensitic steels display higher flow stress in compression and the difference between the compressive and tensile flow stresses decreases as a function of tempering [68, 146–148]. For a model that simulates the strain reversal behaviour of martensite, this strength differential (S-D) effect should be considered. However, due to the large aspect ratio of the tension-compression sample and issues with sample buckling, it was difficult to obtain compression and compression-tension test results with compressive strains larger than 1%. This is the main reason that the S-D effect was not included in the current modelling framework. Nevertheless, as will be shown in Chapter 7, this omission should not lead to significant flaws in the model prediction.

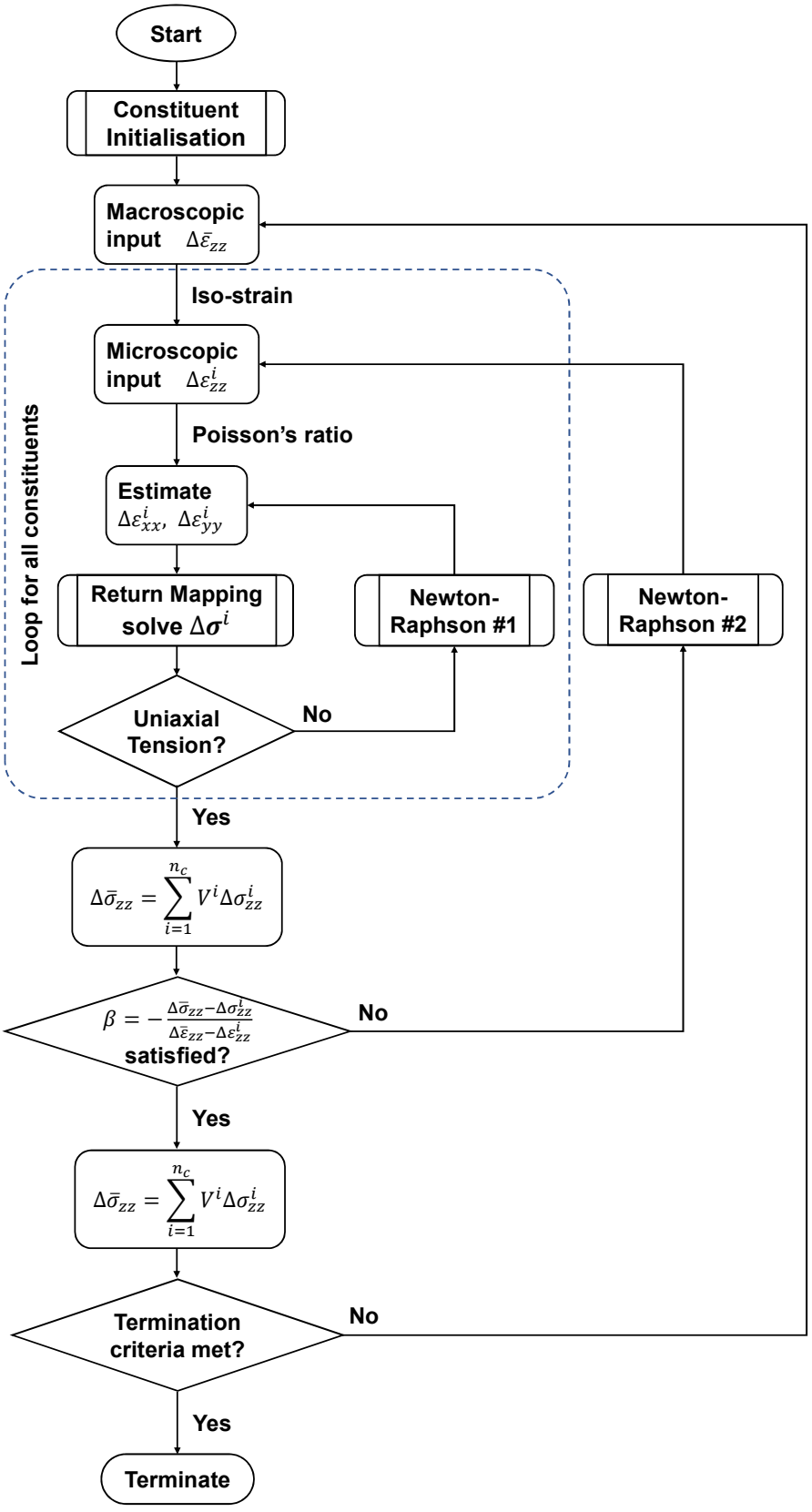

Figure 5.4: *Schematic diagram illustrating the workflow of the incremental scheme.*

The second limitation of the current modelling framework is the lack of strain hardening of constituents. It has been reviewed in Section 2.5 that both isotropic and kinematic hardening may be used to model the flow behaviour of martensite. Our preliminary results have also showed that the inclusion of strain hardening terms would reduce the variation in the yield stress spectrum and the residual stress spectrum and improve the agreement between the experimental and modelled results. However, the modelling parameters used in the hardening models are difficult to quantify and need to be adjusted arbitrarily. Since it is our intention to compare the two existing composite models and avoid adding more free variables, the constituents in the current implementation are assumed to be elastic perfectly plastic.

5.3 Comparison between modelled and experimental results

In the following subsections, the performance of each model is evaluated by comparing model predictions with experimental results. For the macroscopic flow behaviour, the focus is not only on the capabilities of the models to reproduce the monotonic tensile curve but also on their abilities to describe the Bauschinger effect. Besides, by looking at the evolution of stress and strain in individual constituents, the models should be able to predict the evolution of the diffraction peak during monotonic straining.

5.3.1 Yield stress spectrum model

Figure 5.5 shows the experimental and modelled monotonic tension (a1 - c1) and tension-compression (a2 - c2) curves using the yield stress spectrum model. The experimental results are obtained from the HR alloys described in Chapter 4. With optimised yield stress distributions, the monotonic curves can be well reproduced by the model for all compositions. The model is also capable of producing a large Bauschinger effect since individual constituents have different stress states than the bulk which results in back stresses and kinematic hardening. However, discrepancies can be seen when the same yield stress that well describe the forward loading distributions are used to simulate the tension-compression test. Regardless of the alloy composition, the model predicts a larger Bauschinger effect than experimental measurements.

These discrepancies have been also mentioned in the original work of Allain *et al*. [5] and recent work of Badinier [74], which demonstrated that the model tends to overestimate the Bauschinger effect when the yield stress spectrum is optimised based on the monotonic tensile curve. Badinier argued that if the constituents have initial residual stresses, the flow behaviour in the forward direction can be affected by the relaxation of residual stresses and the reverse flow behaviour is more likely to demonstrate the intrinsic flow behaviour of the material. As a consequence, the yield stress spectrum should be optimised based on the reverse portion of the tension-compression curve instead of the monotonic

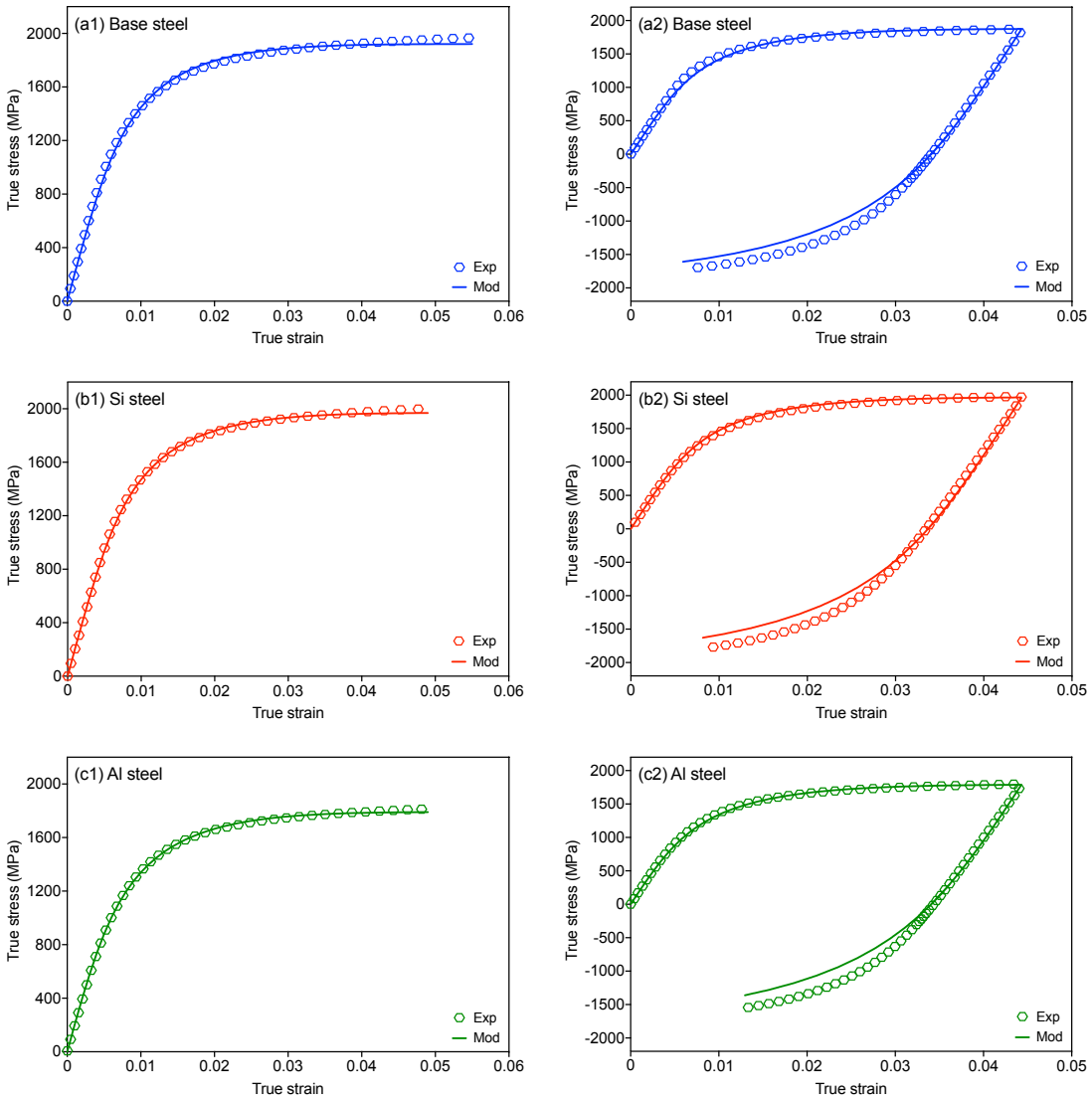

Figure 5.5: *Experimental and modelled tension and tension-compression curves for as-quenched samples using the yield stress spectrum model. (a1) - (c1) Monotonic tension curves. (a2) - (c2) Tension-compression curves. All modelled curves are simulated with parameters optimised based on the monotonic tension curve.*

tensile curve. The spread of the yield stress spectrum optimised based on the reverse portion of the tension-compression curve is usually smaller (Figure 5.6a), which results in a narrower elastic-plastic transition and a smaller Bauschinger effect during tension-compression simulations. While it does make the simulated curves agree better with the experimental tension-compression results (Figure 5.6b), this modified method does not provide a treatment for residual stress relaxation during the forward loading and relies on the robustness of the optimisation routine. Therefore, we will still use the spectrum optimised based on the monotonic tension curve in the following discussions.

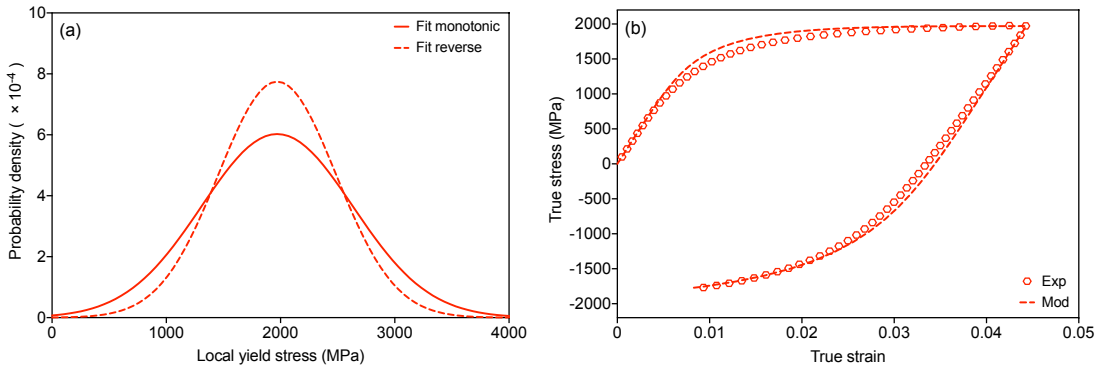

Figure 5.6: *(b) Comparison between the distributions optimised based on different flow curves, the mean of the distributions is fixed to reduce the number of freedom during fitting. (b) Experimental and modelled tension-compression curves for the Si steel simulated with parameters optimised based on the reverse portion of the tension-compression curve.*

Thanks to the discretised nature of the evaluation framework, it is possible to extract the strain and stress states of each constituent during straining. Figure 5.7 shows the extracted strain and stress states of each constituent along the loading direction at different macroscopic forward strains as a function of their initial yield stresses. In Figure 5.7a, it can be seen that the constituents with smaller initial yield stresses will yield first and bear larger strains whereas the constituents with larger initial yield stresses will still be elastic and bear a minimum strain. If we assume each constituent represents an aggregation of grains with a random texture, the strain partitioning phenomenon can lead to anisotropic elastic strains within the grains, which results in anisotropic shifts of the diffraction peaks when the sample is probed by X-ray diffraction. Indeed, in-situ X-ray and neutron experiments do show that the diffractions peaks of as-quenched martensite become asymmetric during deformation [66, 70, 71, 73]. However, the predicted stress evolution shown in Figure 5.7b does not respect another important feature found in the in-situ X-ray and neutron experiments which is the narrowing of diffraction peaks during straining. In the basic assumptions of the yield stress spectrum model, each constituent is elastic-perfect plastic

and its initial yield stress does not change as a function of straining. As a consequence, there is no mechanical homogenisation of the stress states in the material and straining should always lead to plastic incompatibilities between soft and hard constituents which can only lead to diffraction peak broadening. This is not consistent with experimental observations (Figure 2.19).

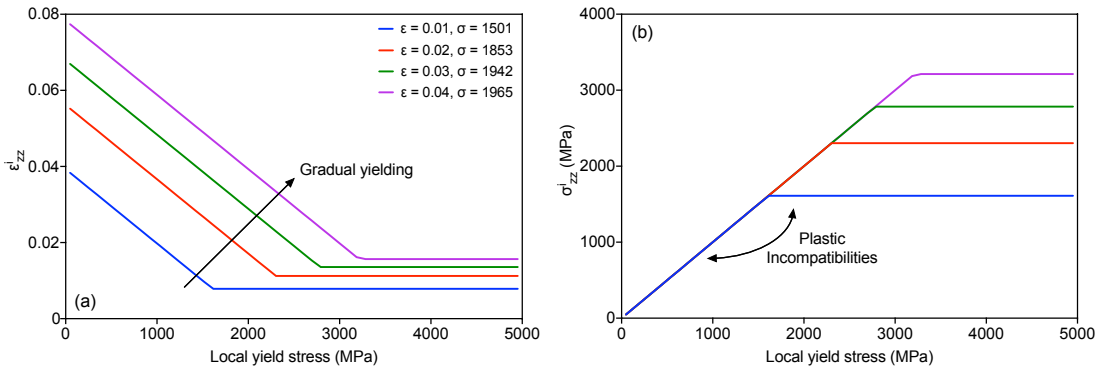

Figure 5.7: *Strain (a) and stress (b) states of constituents as a function of their initial yield stress states. Different colours represent different macroscopic strain and stress levels. Simulated results from the Si steel.*

While some authors have used the yield stress spectrum model to describe the flow behaviours of as-quenched and tempered martensite, limited studies were conducted to quantitatively validate the width of the yield stress spectrum required to describe the flow behaviour. Figure 5.8a - c shows the comparison between the experimentally measured and the optimised stress spectrum for each composition. Nanohardness values are converted to stress values using the empirical linear correlation between the nanohardness values (Figure 4.13). Since the constituents are assumed to be elastic-perfectly plastic, the conversion to UTS values should be appropriate.

It can be seen that the experimentally measured nanohardness values can be fitted well with a normal distribution which allows direct comparison with the spectra optimised based on monotonic tension curves. The mean values of the measured distributions are generally smaller than the modelled ones, which could be attributed to the accuracy of the linear correlation used. Here, the emphasis is not on the exact magnitude of the mean values of the distribution but on the variation of the distribution. For all compositions, the yield stress spectra required to reproduce the macroscopic flow behaviours are much larger than the ones measured experimentally. Quantitatively, the model requires a spectrum that is approximately 4 times the variation measured using nanoindentation regardless of composition (Figure 5.8d), which corresponds well with the nanohardness and EELS measurements from Scott *et al.* in one of their DP steel samples [65] (Figure 2.18). Therefore, the modelled spectra seem hard to justify considering the consistent nanohardness measurements in all compositions.

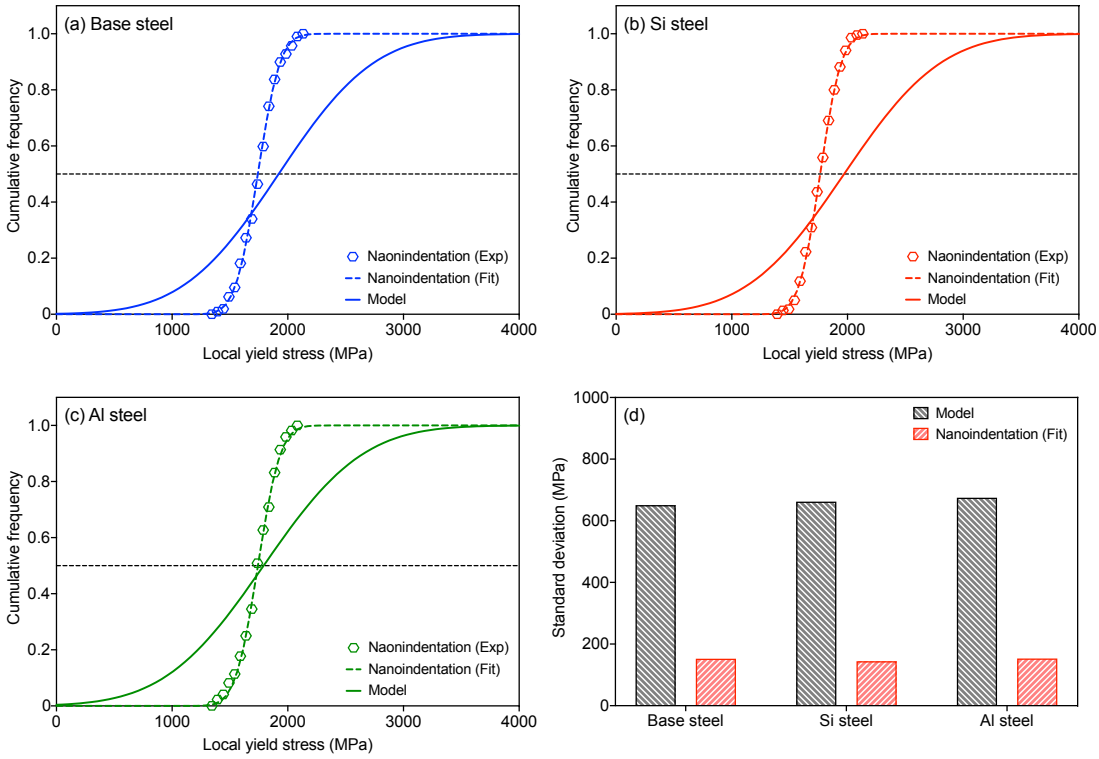

Figure 5.8: *Comparison of modelled and experimentally measured yield stress spectra. (a) - (c) Comparison for each composition, all modelled spectra are optimised based on monotonic tension curves. (d) Quantitative comparison of standard deviations.*

Although the nanoindentation test certainly provides a more localised mechanical response of the material compared to conventional microhardness tests, the hierarchical substructures of martensite may still lead to difficulties in probing the true strength variations of martensite. Figure 5.9a - c show the EBSD image quality (IQ) maps of samples after nanoindentation tests, nanoindents can be seen as triangular impressions that cannot be indexed. It is clear that many indents are located near or on grain boundaries, only a small portion of the indents can be found free of interactions with grain boundaries due to the fine substructure size. In the current study, a maximum force of 2 mN was used, resulting in an average contact depth of ~100 nm. As a consequence, the length of the side of the triangular impression should be around 750 nm (Figure 5.9d), which is much larger than the average lath width (~150 nm) reported in an Fe-0.2C (wt.%) steel [149]. To produce an indent with size less than the average lath width, a contact depth of ~20 nm and a maximum load of ~0.3 mN is required. The nanoindentation results obtained using such a small contact depth are proved to be heavily influenced by the indentation size effect and cannot be regarded as a true reflection of the strength of a specific region [150]. Therefore, the plasticity around a nanohardness indent in martensite will always be affected by interactions with substructure boundaries and the obtained nanohardness value reflects the averaged response around the indent instead of a true localised strength. Results obtained in the current work and the work of Scott *et al.* can both be influenced by this averaging effect and may not demonstrate

the true variation in the local strength of martensite. Factors such as Type II residual stresses could lead to softening or hardening of martensite constituents locally but their contributions will be shielded by the large interaction volume of the indents, which may lead to underestimation of the true variation in local strength.

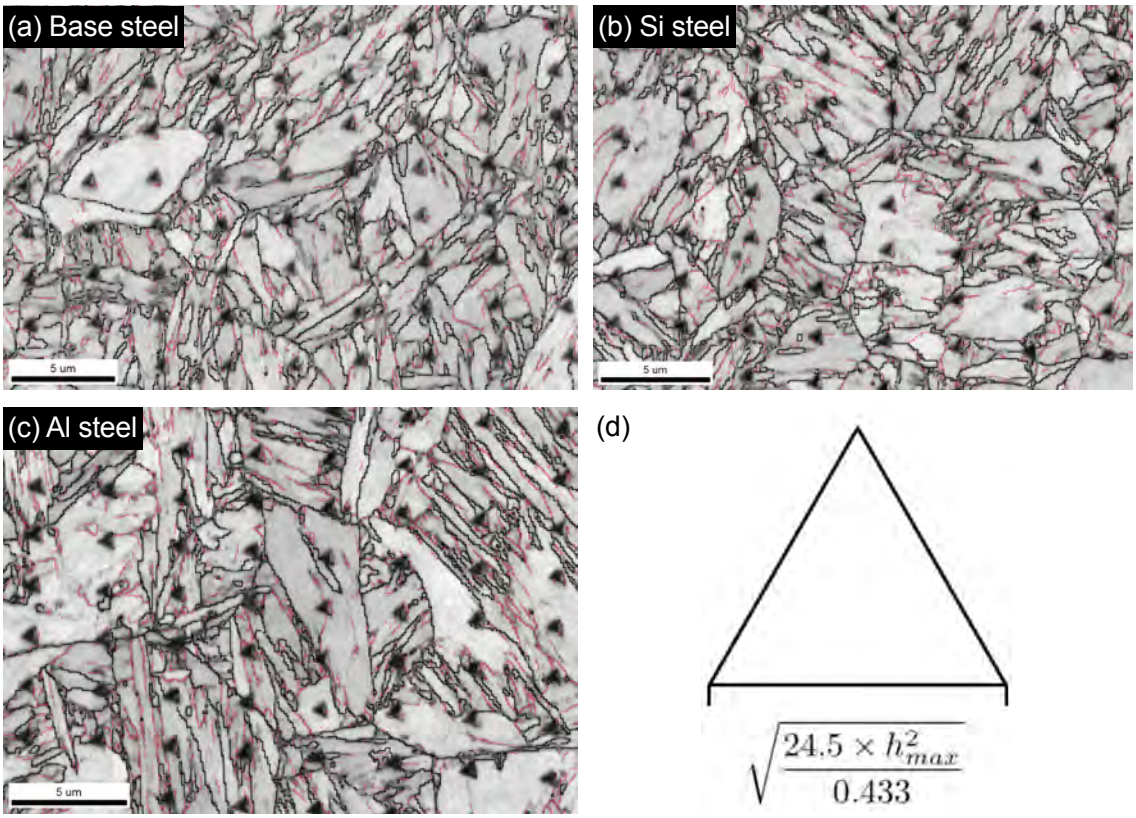

Figure 5.9: *EBSD IQ maps of samples after the nanoindentation test. Red lines represent boundaries with* $2° < \theta_{min} < 15°$ *and black lines represent boundaries with* $\theta_{min} > 15°$. *(a) - (c) Maps for each composition. (d) Schematics showing the estimation of the side length of the triangular impression using the maximum indentation depth* h_{max}.

Whilst we cannot be definitive about the disagreement regarding the experimental width of the spectrum and that we need to use in the simulation, for the reasons discussed above. It remains an issue that the yield strength spectrum model cannot reproduce diffraction peak narrowing during straining. It is clear that additional ingredients are required.

5.3.2 Residual stress spectrum model

Figure 5.10 shows the experimental and modelled monotonic tension (a1 - c1) and tension-compression (a2 - c2) curves using the residual stress spectrum model. For all compositions, the common yield stress for the constituents (σ_{y0}^{i}) is set to be the same as the mean of the normal distribution obtained in the yield stress spectrum to allow a better comparison between the models. The best agreement with the monotonic tension curves can be achieved when the maximum residual stress magnitude is set

as $RS_{max} = \sigma^{i}_{y0}/\sqrt{3}$, which corresponds to ~57% of the common yield stress of the material. While the monotonic tension curves can be well explained by the gradual yielding of constituents with pre-stresses, the model produces no Bauschinger effect during tension-compression test simulations when the material behaves like a single piece of elastic-perfectly plastic element during reverse loading.

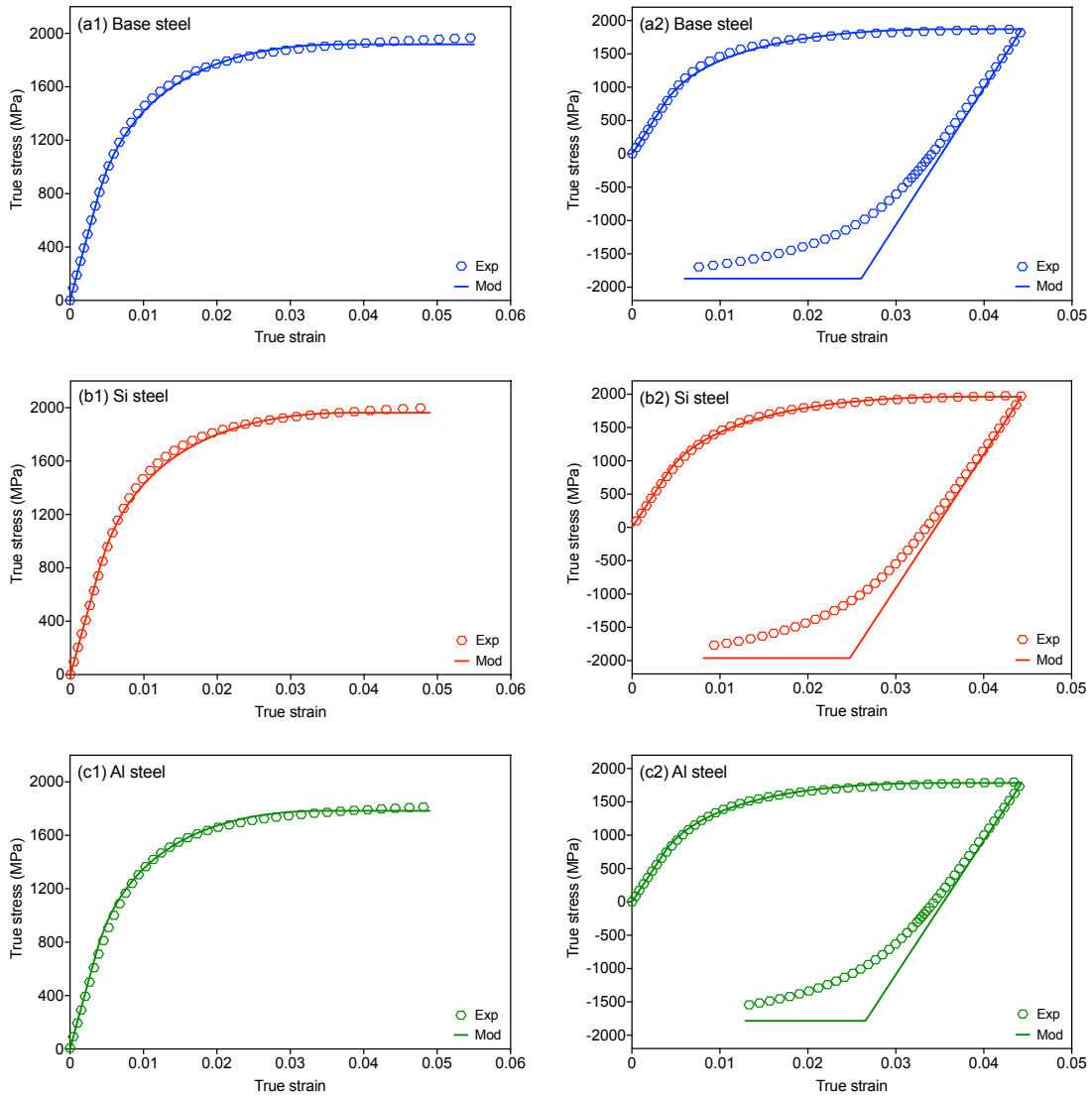

Figure 5.10: *Experimental and modelled tension and tension-compression curves for as-quenched samples using the residual stress spectrum model. (a1) - (c1) Monotonic tension curves. (a2) - (c2) Tension-compression curves.*

The disappearance of the Bauschigner effect is due to the evolution of strain and stress states during straining. As shown in Figure 5.11a, constituents with positive pre-stresses yield first and bear larger strains while constituents with negative pre-stresses do not yield and bear smaller strains as a result of strain partitioning. The heterogeneity in strain at the constituent level leads to the same diffraction peak asymmetry as discussed in the previous section. The stress states in individual constituents, on the other hand, becomes more homogeneous during straining since all constituents share the same initial

yield stress (Figure 5.11b). When all constituents have their axial stress equal to the yield stress, the material is fully yielded and homogenised by plastic straining. Furthermore, this mechanical homogenisation process also eliminates the plastic incompatibilities generated between early and late yield constituents. As a consequence, not only does the diffraction peak get narrower as a result of residual stress relaxation, the material also loses its composite-like behaviour at large forward plastic strains and as a result a significant Bauschinger effect is not observed (Figure 5.10 a2 - c2). Therefore, the residual stress spectrum model alone cannot self-consistently explain both the monotonic tension and the tension-compression flow behaviour of as-quenched martensite. Nevertheless, the residual stress hypothesis does provide a reasonable treatment for the diffraction peak narrowing problem and should be considered in further model developments. In principle, both the yield stress spectrum and the residual stress spectrum should co-exist in as-quenched martensite as a result of the transformation sequence effect (Section 2.1.2.1, Figure 2.4). The framework developed in this chapter provides a means of implementing a model that considers both spectra simultaneously, which will be shown in a later chapter.

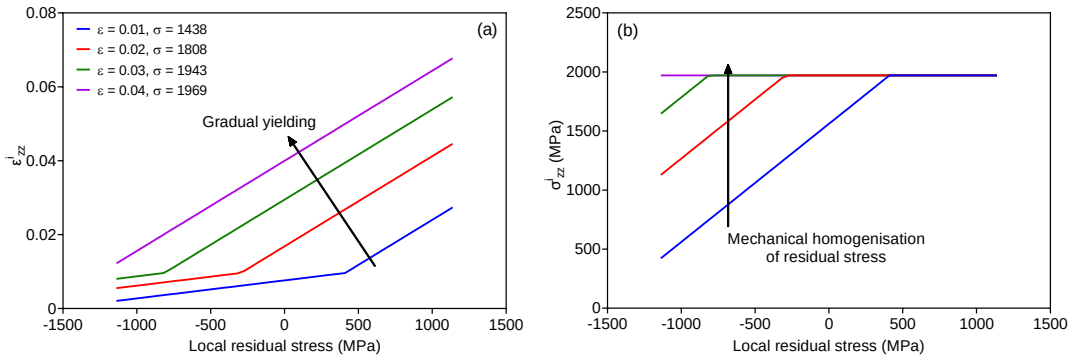

Figure 5.11: *Strain (a) and stress (b) states of constituents as a function of their initial residual stress states. Different colours represent different macroscopic strain and stress levels. Simulated results from the Si steel.*

5.4 Athermal and kinematic hardening of as-quenched martensite

Both models presented in the previous sections consider as-quenched martensite as a composite material since its extremely high strain hardening rate cannot be explained by the classic dislocation storage mechanism (Section 2.2.1, Figure 2.9) and other strain hardening mechanisms need to be considered. If dislocation based strain hardening is not the dominant hardening contribution, one should expect a large athermal contribution to the flow stress which is insensitive to thermally activated dislocation motion (i.e. temperature and strain rate insensitive).

To test this hypothesis in detail, strain-rate sensitivity tests were performed on as-quenched martensite samples and the results are shown in Figure 5.12a. While the first few data points on the Haasen plot do not obey the Cottrell-Stokes law, the points obtained close to the UTS values can be fitted well by a linear regression. Regardless of the alloy composition, a single slope can be used for the linear regressions and the fitted lines have large intercepts with the stress axis. As discussed in Section 4.2.2.2, the x-intercept on the Haasen plot can be regarded as an estimation of the athermal contribution (σ_{ath}) to the flow stress. If we assume the flow stress consists of only thermal and athermal contributions (i.e. $\sigma_f = \sigma_{th} + \sigma_{ath}$), the thermal contribution σ_{th} can be estimated by subtracting σ_{ath} from the UTS and the results can be seen in Figure 5.12b. Since the steels have different UTS', the magnitude of the athermal contribution also varies. However, despite the differences in the UTS' and athermal contributions, the thermal contribution to the flow stress show a remarkable independence on compositions (all around 500 MPa). According to the physical construction of the Haasen plot (Figure 4.5b), the thermal contribution should only come from forest dislocations [135, 136]. Current results suggests that the thermal contribution to the flow strength of as-quenched martensite is relatively insensitive to alloying additions and accounts for ~25% of the UTS of the material. This is in agreement with the hypothesis made in the composite strengthening models that the dislocation storage based mechanism is not the dominant strengthening mechanism in as-quenched martensite. Since both the yield stress spectrum model and the residual stress spectrum model suggest that the constituents yield at different stages of loading, plastic incompatibility can be developed between the elastic and plastic constituents and results in athermal hardening. Although the origin of the plastic incompatibility is different in the two composite models, the resulted athermal contribution should shift the Haasen plot to the right along the stress axis regardless of which hypothesis is considered.

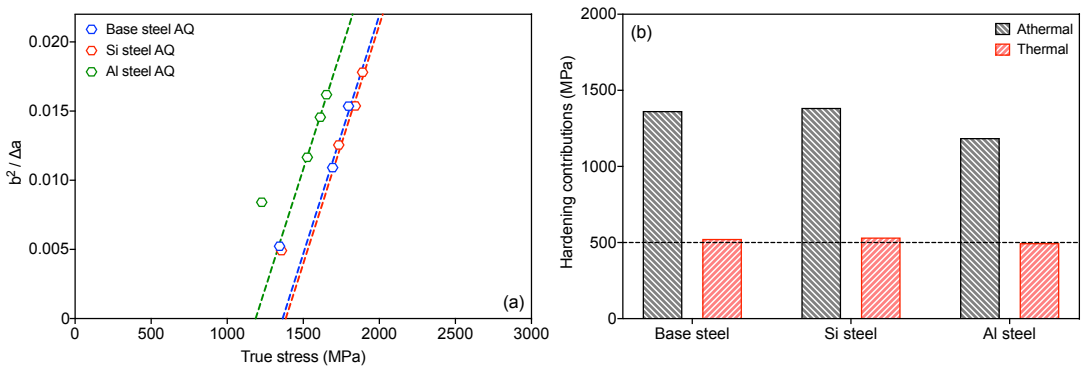

Figure 5.12: *Athermal hardening in as-quenched martensite. (a) Haasen plot for as-quenched martensite, the same slope is used for the linear regressions for all steels. (b) Magnitudes of different hardening contributions in different steels.*

Athermal contributions to the flow stress arise from dislocation interactions with obstacles that are less susceptible to thermal activation than forest dislocations. In the case of as-quenched martensite, plastic incompatibilities and dislocation-grain boundary interactions should be the dominant contributions as a result of its heterogeneous and hierarchical microstructure. These two mechanisms can also have complex interactions with each other since plastic incompatibilities are often seen to develop at grain boundaries which may consequently affect the generation of geometrically necessary dislocations around the grain boundary. Theoretically, both mechanisms should lead to the continuous development of athermal hardening during straining and contribute to the strain hardening of the material. While the strain-rate sensitivity test gives an estimation of the total contribution from athermal hardening, tension-compression Bauschinger tests can be used to monitor the development of the athermal, kinematic hardening contribution. It can be seen from Figure 5.13a that the back stress (quantified by Eq. 4.9) starts small and quickly develops during straining and the maximum back stress obtained near the UTS accounts for ~27% of the total flow stress and ~40% of the total athermal hardening contribution regardless of alloy composition (Figure 5.13b). Therefore, kinematic hardening developed during straining has a non-trivial contribution to the strength of as-quenched martensite.

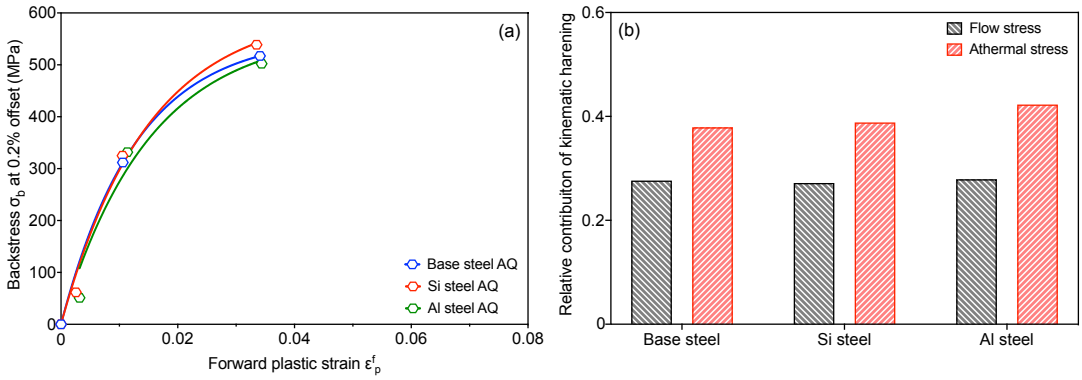

Figure 5.13: *Kinematic hardening in as-quenched martensite. (a) Evolution of back stress as a function of forward plastic strain. The open hexagons are calculated using Eq. 4.9 and the solid lines are fitted with Eq. 2.12. (b) Relative contribution of kinematic hardening to the total flow stress and the total athermal hardening contribution.*

Although it remains difficult to determine which mechanism, plastic incompatibilities or dislocation-grain boundary interactions, dominates the development of kinematic hardening, tempering experiments may be designed to help the investigation since the sources of the two strengthening mechanisms should behave differently upon tempering. More specifically, it is known that the substructures of martensite are very stable up to 700 °C (Section 2.3.4), especially the ones separated by high angle grain boundaries (e.g. sub-blocks, blocks and packets). As a consequence, the kinematic hardening contribution from grain boundaries should be relatively insensitive to low and medium temperature tempering. In contrast, the origin of plastic incompatibilities (due to heterogeneities in intrinsic strengths and/or

residual stress states) should evolve more quickly during tempering since the heterogeneities originate from a much smaller scale and may be more susceptible to thermal activations. Therefore, one may expect that the decrease in the kinematic hardening at low temperatures comes predominantly from the reduction of plastic incompatibilities as a result of homogenisation of microstructural heterogeneities. Detailed experimental results will be shown in the next chapter.

5.5 Summary

A unified platform was constructed to evaluate if the composite strengthening models are capable of describing the strain hardening of as-quenched martensite as well as related microstructural evolutions. In the case of the yield stress spectrum model, it is able to describe both the monotonic tension and the tension-compression flow behaviour of as-quenched martensite. However, it fails to address the diffraction line narrowing phenomenon and requires a much larger variation in the intrinsic yield strengths of constituents than observed experimentally in order to reproduce the flow curves. In contrast, although the residual stress spectrum model can describe the monotonic tension curve and provide feasible explanations for the diffraction line narrowing problem, it cannot reproduce a large Bauschinger effect as a result of relaxation of residual stresses at large forward strains. While both models have their limitations, their fundamental hypotheses: the strain hardening of as-quenched martensite does not come from dislocation storage based mechanisms, is supported by experimental evidence.

Strain-rate sensitivity tests and tension-compression Basuchinger tests were conducted to quantify the magnitude of the athermal hardening contribution to the total flow stress of as-quenched martensite. It is found that most of the hardening in as-quenched martensite comes from the athermal contribution and a portion of the athermal contribution is developed during plastic straining and in the nature of kinematic hardening. Although the dominant mechanism that contributes to the kinematic hardening is not clear, it is believed that carefully designed tempering experiments will help develop further understanding on this issue.

Chapter 6

Evolution of mechanical properties and microstructural features during tempering of martensite

6.1 Introduction

The mechanical properties of tempered martensite have always been a topic of scientific and industrial importance. This chapter focuses on the evolution of mechanical properties of tempered martensite as a function of tempering temperatures and times and the emphasises are on the changes of both strength and strain hardening behaviours. The relationship between mechanical properties and microstructures is investigated using a series of multi-scale characterisation techniques. By comparing the tempering kinetics of the base steel, with steels having Si and Al additions, the chemistry dependence of the tempering response can also be revealed. To compare the tempering effect at different temperatures and times and to facilitate the identification of the alloying element effect, the Hollomon-Jaffe plot will be shown in some sections. The constant A in Eq. 2.9 is set to be 13 (i.e. $TP = T(K) \times [A + \log(t(sec))]$), which is in accordance with the parameter used in tempering research conducted at ArcelorMittal [151].

6.2 Microstructural evolution of tempered martensite

6.2.1 Evolution of precipitates

As discussed in Chapter 2, the addition of Si and Al affects predominantly the precipitation kinetics of cementite in martensite during tempering. DSC results in Figure 6.1a further demonstrates the alloying element effect in the present study. Three distinct exothermic events can be found in all steels with different peak temperatures. Positions of the second and the third peaks in the Si steel and the Al steel match closely with the results of De Moor *et al.* on steels with similar compositions (Figure 6.1b [152]). De Moor *et al.* proposed that the second peak corresponds to the decomposition of retained austenite and the third peak represents the precipitation of cementite. The first peak, in this case, should correspond to the precipitation of transition carbides since the DSC samples were cut from as-quenched samples that were left at room temperature for one year. This could also explain the much earlier onset of the transition carbide peak in the current study as the segregation of carbon may promote the nucleation of transition carbides [153]. Nevertheless, it is clear that the addition of Si and Al postpones cementite precipitation to higher temperatures (~450 °C cf. 350 °C in the base steel).

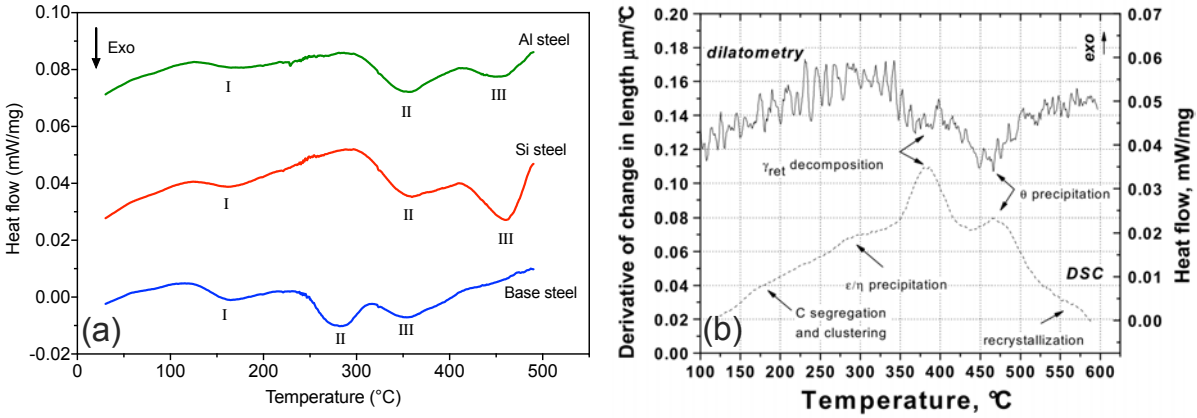

Figure 6.1: *(a) DSC heat flow results for the base steel, the Si steel and the Al steel heated at a heating rate of 25 °C/min, the three major exothermic peaks were represented by Roman letters. (b) Derivative of change in length (left axis) and DSC heat flow (right axis) results for an as-quenched Fe-0.18C-1.56Mn-1.73Al (wt%) steel heated at heating rate of 20 °C/min.*

Figure 6.2, 6.3 and 6.4 show high magnification SEM images of precipitates in the base steel, the Si steel and the Al steel tempered at 300 °C - 600 °C for 5 minutes. For the base steel, a high density of plate shaped carbides can be readily found after tempering at 300 °C. Further tempering at 400 °C does not seem to affect the plate morphology of carbides (Figure 6.2b). At 500 °C and 600 °C, on the other hand, spheroidisation of carbides can be observed as the precipitation kinetics are much promoted at high temperatures (Figure 6.2c and d). In the case of the Si steel and the Al steel, tempering at 300 °C and 400 °C results in much more sparsely spaced, thin plate-shaped carbides (Figure 6.3 - 6.4 a and

b). Since the DSC results show that the onset austenite decomposition and cementite precipitation are postponed to ~450 °C in the Si steel and the Al steel, the carbides found here should be transition carbides instead of cementite. As the tempering temperatures rise to 500 °C and 600 °C, the same spheroidisation behaviour can be found in the Si steel and the Al steel (Figure 6.3 - 6.4 c and d) and the alloying elements are less effective in influencing the tempering kinetics at higher temperatures.

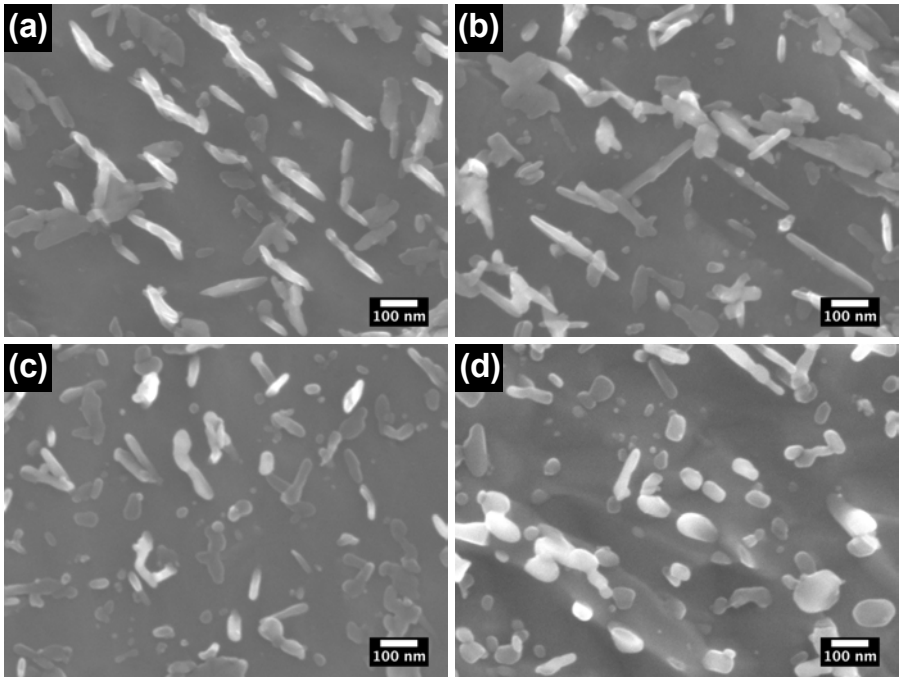

Figure 6.2: *SEM images of the precipitates found in the base steel tempered at different temperatures for 5 minutes (a) 300 °C, (b) 400 °C, (c) 500 °C and (d) 600 °C. Etched with Picral.*

6.2.2 Evolution of microstrain

The evolution of microstrain as measured by X-ray diffraction is used here to monitor the recovery kinetics in martensite, which may include both residual stress relaxation and dislocation recovery. Figure 6.5 shows the evolution of the (011) peak in the base steel samples as a function of tempering temperatures and the Rietveld refinement result. It shows that peak width decreases as a function of tempering and the peak shape can be well captured by the whole pattern fitting function considering only the existence of the BCC phase. The volume fraction of retained austenite in the as-quenched state is below the sensitivity of the Rietveld method (~1 vol. %) and no distinct FCC peaks can be observed. Therefore, the change in the peak shape is not a result of decomposition of retained austenite. The microstrain is a parameter that describes the width of the BCC diffraction peaks and can be extracted from the Rietveld refinement (Section 4.3.3, Figure 4.14).

Figure 6.6 shows the evolution of microstrain during tempering and the effect of alloying elements. In the as-quenched state, all steels have a similar level of microstrain and it is likely this is due to the similar carbon content of the steels. Upon tempering, the drop in the magnitude of the microstrain is readily visible when the tempering time is short (i.e. $<$ 1 minute). The magnitude of the initial drop

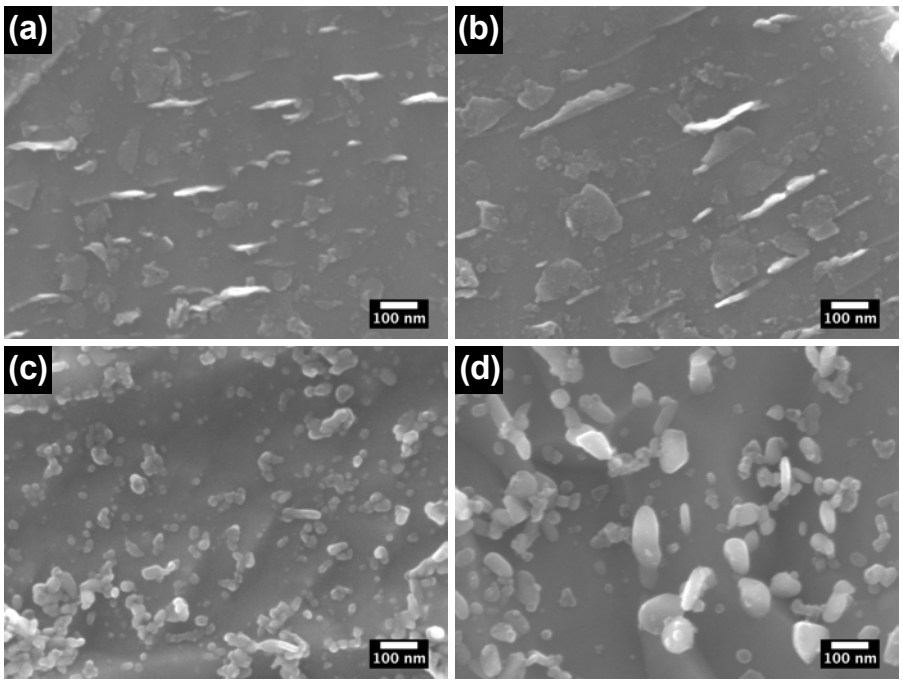

Figure 6.3: *SEM images of the precipitates found in the Si steel tempered at different temperatures for 5 minutes (a) 300 °C, (b) 400 °C, (c) 500 °C and (d) 600 °C. Etched with Picral.*

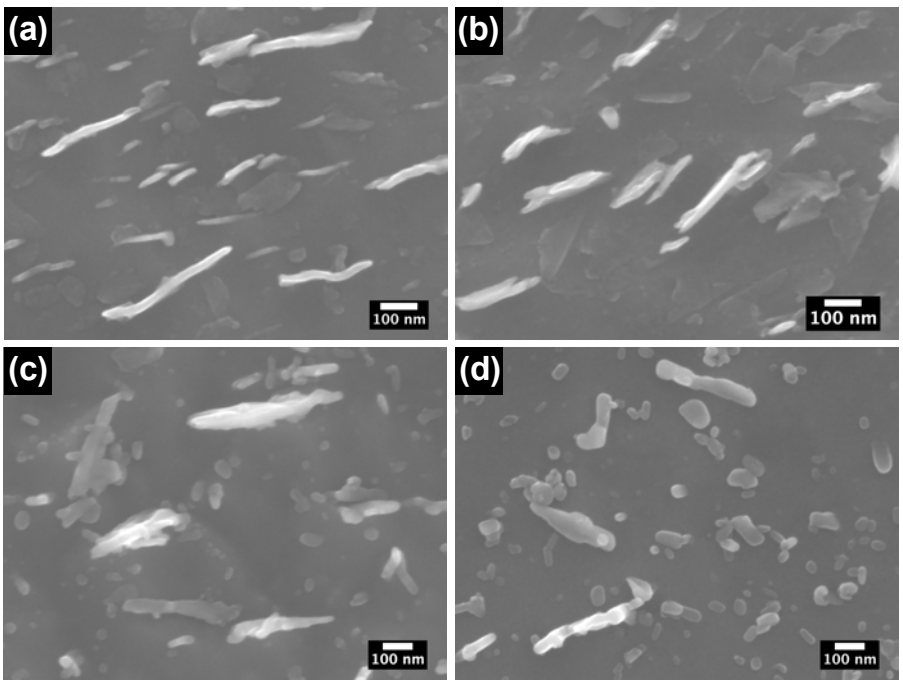

Figure 6.4: *SEM images of the precipitates found in the Al steel tempered at different temperatures for 5 minutes (a) 300 °C, (b) 400 °C, (c) 500 °C and (d) 600 °C. Etched with Picral.*

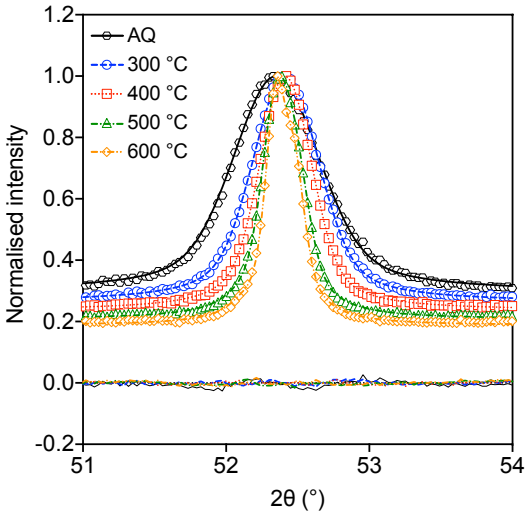

Figure 6.5: *The evolution of the (011) ferrite peak as function of tempering temperatures for the base steel. Each tempered sample is tempered at the specified temperature for 5 minutes. The open symbols show the experimental curves and the lines show the results of Rietveld refinement.*

increases as the tempering temperature increases. For the same tempering temperature, the microstrain also decreases gradually with time but the kinetics of microstrain reduction at longer times is much slower compared to the initial drop. This fast-to-slow transition in recovery kinetics is true for all steels regardless of alloy composition. Similar findings can be found in the work of Wu and the slower kinetics occurring at longer tempering times may be reasonably described using a dislocation recovery mechanism (Section 2.4.4 and Ref. [2]). The faster kinetics at shorter times, however, cannot be described by the dislocation recovery theory and may be related to the relaxation of residual stresses. Further discussions on the relaxation of residual stresses will be shown in a later section.

The addition of Si and Al reduces the magnitude of the initial drop and slows down the kinetics of microstrain reduction at 300 °C and 400 °C. The relative potency of Si and Al can be more clearly shown when the differences between the as-quenched states and the tempered states are normalised by the magnitude of the as-quenched states (i.e. $\frac{\langle\varepsilon_0\rangle_{AQ}-\langle\varepsilon_0\rangle_{Temper}}{\langle\varepsilon_0\rangle_{AQ}}$, denoted as the *softening parameter* in the following text, Figure 6.6d). It is obvious that Si is more capable in resisting microstrain reduction compared to Al. The plot also shows that while the addition of Si and Al does affect the recovery kinetics at lower temperatures, this effect disappears when the temperature is raised above 500 °C. The chemistry dependence of the microstrain evolution may be interpreted as a consequence of the slower precipitation kinetics in the Si and Al steels. If the cementite precipitation is retarded by the addition of Si and Al at lower temperatures, supersaturated carbon atoms can segregate to dislocations and reduce their mobility. At higher temperatures, all steels show the same precipitation response which results in similar recovery kinetics of the microstrain.

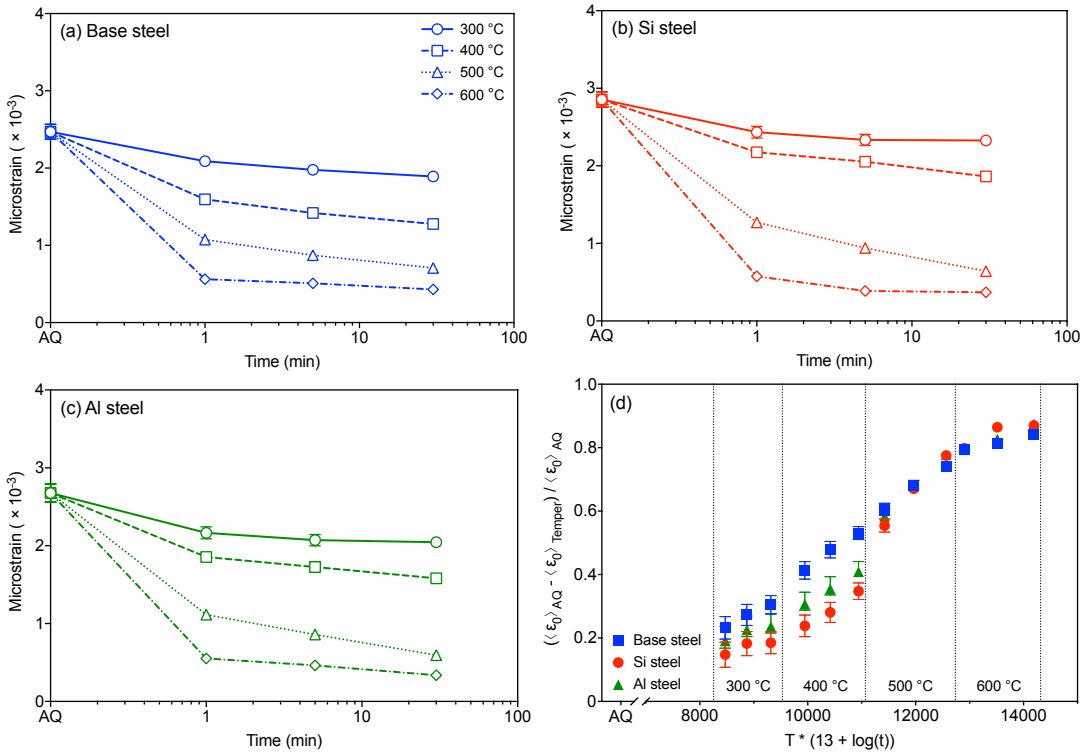

Figure 6.6: *Evolution of microstrain during tempering in the case of the base steel (a), the Si steel (b) and the Al steel (c). Error bars represent two times the Rietveld error which include most of uncertainties associated with sample to sample variation. (d) Hollomon-Jaffe plot showing the evolution of softening parameters for the microstrain as a function of tempering parameters. At each temperature, three tempering times are shown (i.e. 1 minute, 5 minutes and 30 minutes). Error bars are calculated using the error propagation function.*

6.2.3 Evolution of martensitic substructures

Besides recovery of dislocations and residual stresses, tempering can also lead to coarsening and/or recrystallisation of martensitic substructures. Figure 6.7 shows EBSD image quality (IQ) maps of the base steel samples tempered at 300 °C to 600 °C for 30 minutes. The lath morphology of martensite crystals can be retained at high temperatures and no signs of recrystallisation can be observed even at 600 °C. However, it can be seen that fewer low angle grain boundaries can be found in the 600 °C tempered sample which may be caused by recovery and coarsening of laths. Similar findings can be found in the work of Caron and Krauss shown in Section 2.3.4 [103].

While EBSD is not suitable to estimate the lath size due to its limited spatial resolution, it is possible to gain information on a larger scale and monitor the evolution of martensite blocks. Figure 6.8 shows the evolution of the average grain size of martensite crystals that are separated by high angle grain boundaries ($\theta_{mis} > 15°$). Since the martensite crystals can have a range of sizes as a result of the transformation sequence effect, two averaging methods are used to highlight the evolutions of small and large blocks. For small blocks whose sizes may be estimated by the arithmetic average (Figure

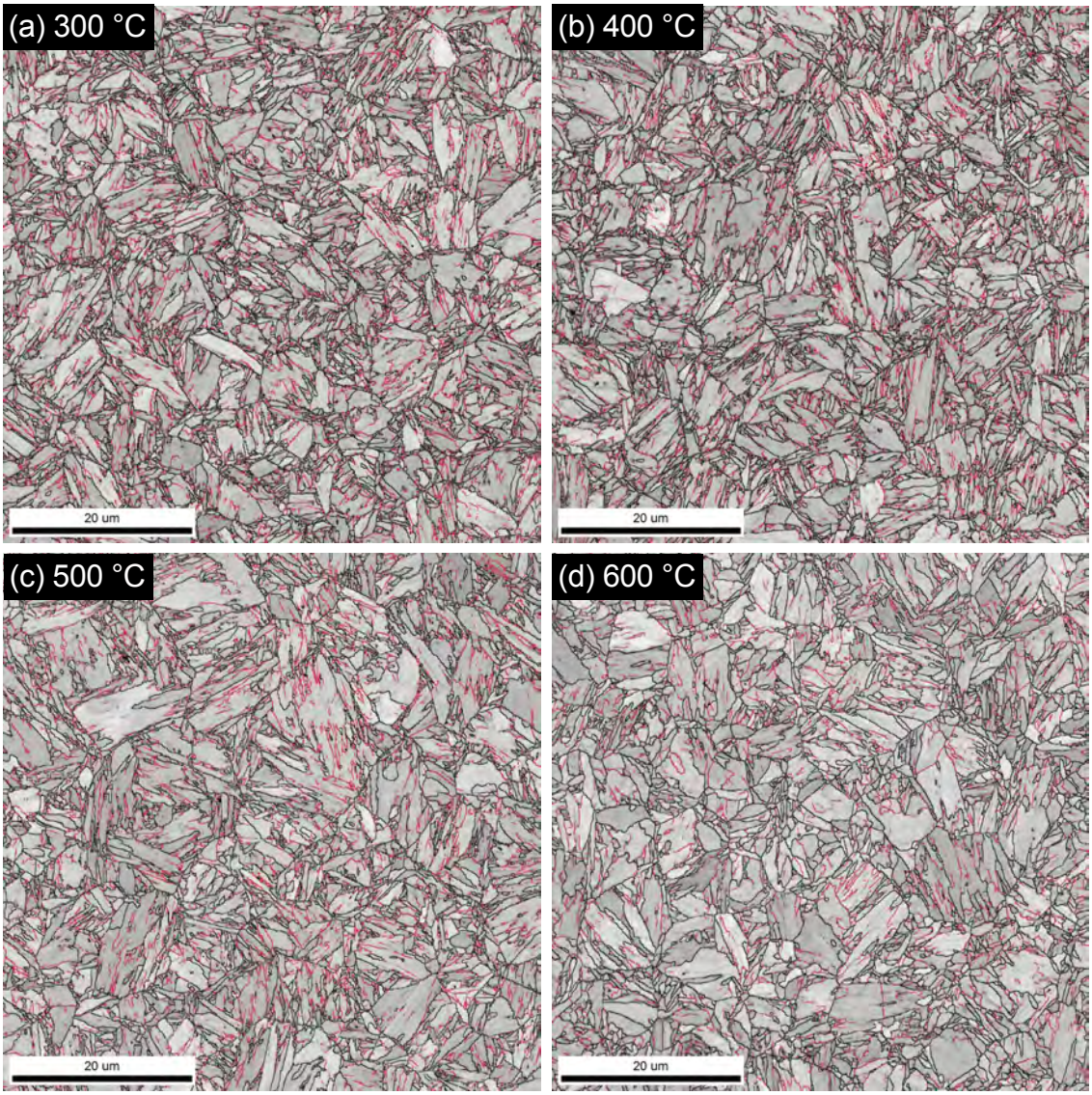

Figure 6.7: *IQ maps of base steel samples tempered at 300 °C (a), 400 °C (b), 500 °C (c) and 600 °C (d) for 30 minutes. High angle grain boundaries ($\theta_{mis} > 15°$) are marked in black and low angle grain boundaries ($2° < \theta_{mis} < 15°$) are marked in red.*

6.8a), all steels show similar average grain sizes and tempering below 600 °C does not have a significant effect on the average grain size. When the tempering temperature is raised above 600 °C, there is an increase in the arithmetic average regardless of the alloy composition, suggesting coarsening of small blocks. For large blocks whose sizes may be estimated by the area weighted average (Figure 6.8b), the Al steel shows a markedly larger average grain size than the other compositions due to its coarser prior austenite grains (Figure 4.10). Fluctuation of the area weighted average is found during tempering and no significant increase of the average grain size can be observed.

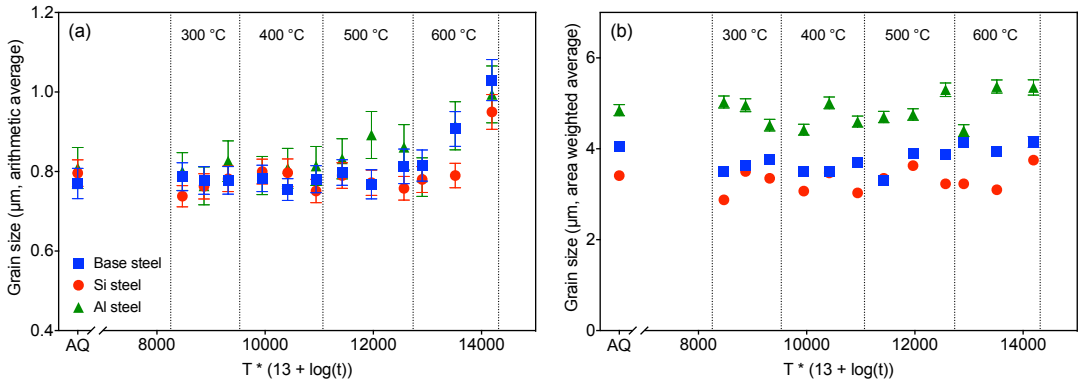

Figure 6.8: *Hollomon-Jaffe plots showing the evolution of the effective grain size as a function of tempering parameters. (a) Evolution of the arithmetic average representing the change in small blocks. (b) Evolution of the area weighted average representing the change in large blocks. At each temperature, three tempering times are shown (i.e. 1 minute, 5 minutes and 30 minutes). Error bars represent the 95% confidence interval of the calculated averages.*

The changes in both arithmetic and area weighted averages may be further explained if we consider the Zener pinning effect from cementite particles. The average grain size during grain coarsening is constrained by the presence of secondary particles by [154]:

$$R_c = \frac{4r_p}{3V_f} \tag{6.1}$$

where R_c is the critical radius of the grain, r_p and V_f are the size and the volume fraction of secondary particles. In the context of the present study, the equilibrium volume fraction of cementite particles is around 3.75% for all steels and the average size of cementite particles can be measured using the SEM images and the size distribution of cementite particles can be estimated using the correlation found in the work of Wu [2]. Figure 6.9 shows the evolution of the critical diameter of the average grain size as a function of precipitate sizes assuming the equilibrium volume fraction is reached. The shaded area represents the possible sizes of cementite precipitates when tempering is conducted at 600 °C (around 20 nm to 40 nm). It can be seen that the small blocks are free to grow once the precipitate size is larger than 10 nm while the large blocks can still be pinned by particles unless an average particle size of 70 nm is reached. Therefore, the growth of small blocks at 600 °C can likely be attributed to the coarsening of cementite particles. Combination of the SEM studies (Figure 6.2 - 6.4) and Figure 6.9 also suggests that the smaller substructures (laths and blocks) in martensite may also be free to grow at lower temperatures since the average precipitate sizes are clearly larger than 10 nm. The growing trend is not reflected in Figure 6.8a and it is possible that the grain boundary mobility is still low at low temperatures and the magnitude of grain growth is smaller than the resolution limit of the EBSD technique. Nevertheless, coarsening of smaller substructures is inevitable in tempered martensite and it can contribute to further softening of the material.

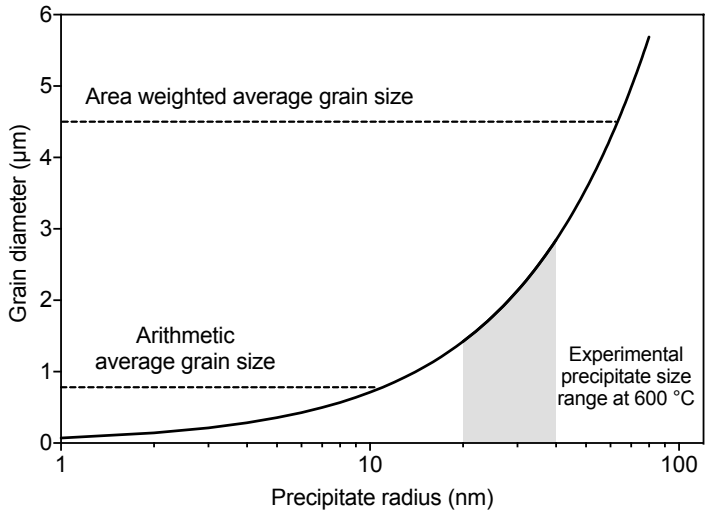

Figure 6.9: *Precipitate size effect on the critical diameter of the grain.*

6.3 Evolution of monotonic tension properties

6.3.1 General evolution of tensile and strain hardening curves

Figure 6.10 shows the true stress - true strain curves for the base, Si and Al steels in both the as-quenched state and as a function of tempering. Overall, the Si steel shows a higher strength than the base steel due to the solid solution strengthening effect of Si. The lower strength of the Al steel at all heat treatment conditions can be largely attributed to its larger prior austenite grain size (Figure 4.10 a2 - c2). For all alloy compositions, tensile curves for the as-quenched condition start to deviate from linearity at around 400 MPa to 500 MPa, which is in good agreement with the trend found in the literature [5]. After tempering, the elastic-plastic transition becomes much narrower and yield points are clearly visible.

The ultimate tensile strengths of tempered samples witness a significant drop after tempering. Tempering temperatures seem to play a more significant role in martensite softening than tempering times as tensile curves for the same tempering temperature usually cluster together (as shown in Figure 6.10a by the brackets). The uniform elongations first decrease due to the temper induced embrittlement effect at 300 °C to 400 °C and then increase at higher tempering temperatures [18]. Yield discontinuities can be seen in the tensile curve for the base steel and the Si steel tempered above 300 °C (Figure 6.10a, b) and for the Al steel tempered above 400 °C (Figure 6.10c). The discontinuities then develop into yield point elongations (YPEs) resembling the Lüders band found in the tensile behaviour of low carbon ferritic steels. The presence of yield discontinuities and YPE upon tempering implies that dislocations

are pinned by carbon atmospheres and the degree of pinning increases with increasing temperatures. The details of this change in yielding behaviour have not been studied in depth but it is suspected that the decrease in the dislocation density during tempering could be the cause of this phenomenon [109, 155].

The strain hardening behaviour of tempered martensite can be more clearly shown when plotting the strain hardening rate against the true stress (i.e. the Kocks-Mecking (K-M) plot, Figure 6.11). The strain hardening rates of the as-quenched states are much larger than the tempered states and are always higher than the E/50 limit for dislocation storage based mechanisms. The strain hardening rates decrease as a function of annealing temperatures and times. Yield discontinuities and YPEs appear as inflection points on the K-M plots and a recovery of strain hardening rates can be found beyond the YPE region, resembling the behaviours of TRIP steels. Since the as-quenched microstructures do not have detectable retained austenite and the fraction of retained austenite can only decrease when tempering at high temperatures, the recovery of strain hardening rates should not be a result of the TRIP effect but from the unpinning of locked dislocations.

Generally, when the tempering temperature is below 500 °C, the strain hardening rates after the yield discontinuities share a similar slope with the as-quenched condition and a significant portion of the curve is above the E/50 limit, suggesting that the same strain hardening mechanism for as-quenched martensite may still be effective when the tempering temperature is low. For the base steel and the Si steel tempered above 500 °C, the maximum strain hardening rates after YPEs are always around or below the E/50 limits (Figure 6.11a, b), which indicates that the classical dislocation storage strengthening mechanisms may be more suitable in describing the strain hardening of martensitic steels tempered at high temperatures. On the other hand, this value in the Al steel only drops below the theoretical limit after tempering at 500 °C for 5 minutes and at 600 °C (Figure 6.11c). This could imply that the Al steel has a better resistance to microstructural changes leading to the reduction of strain hardening capabilities but the effects of larger prior austenite grain sizes need to be justified.

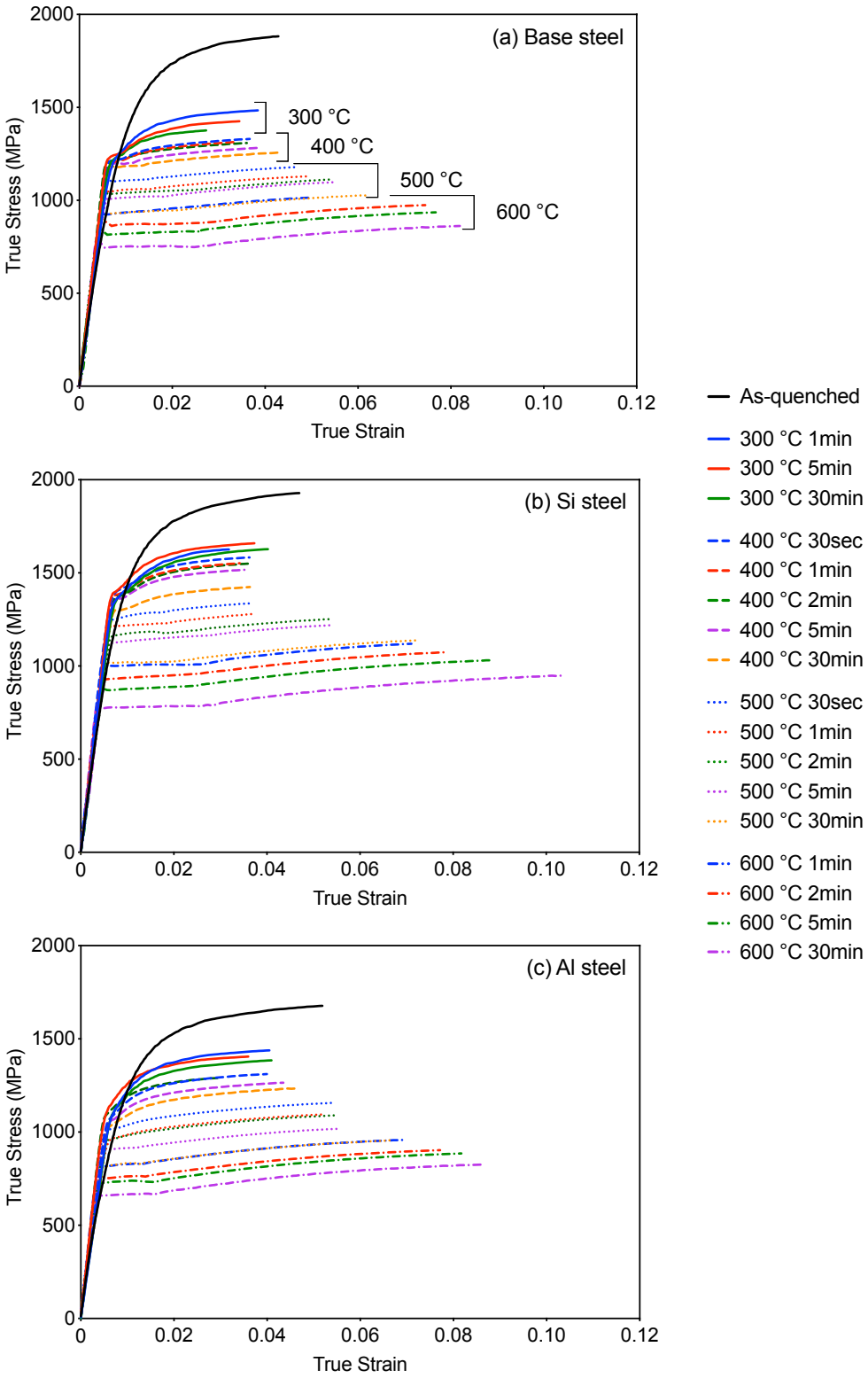

Figure 6.10: *True stress - true strain curves of the base steel (a), the Si steel (b) and the Al steel (c) with different heat treatment conditions.*

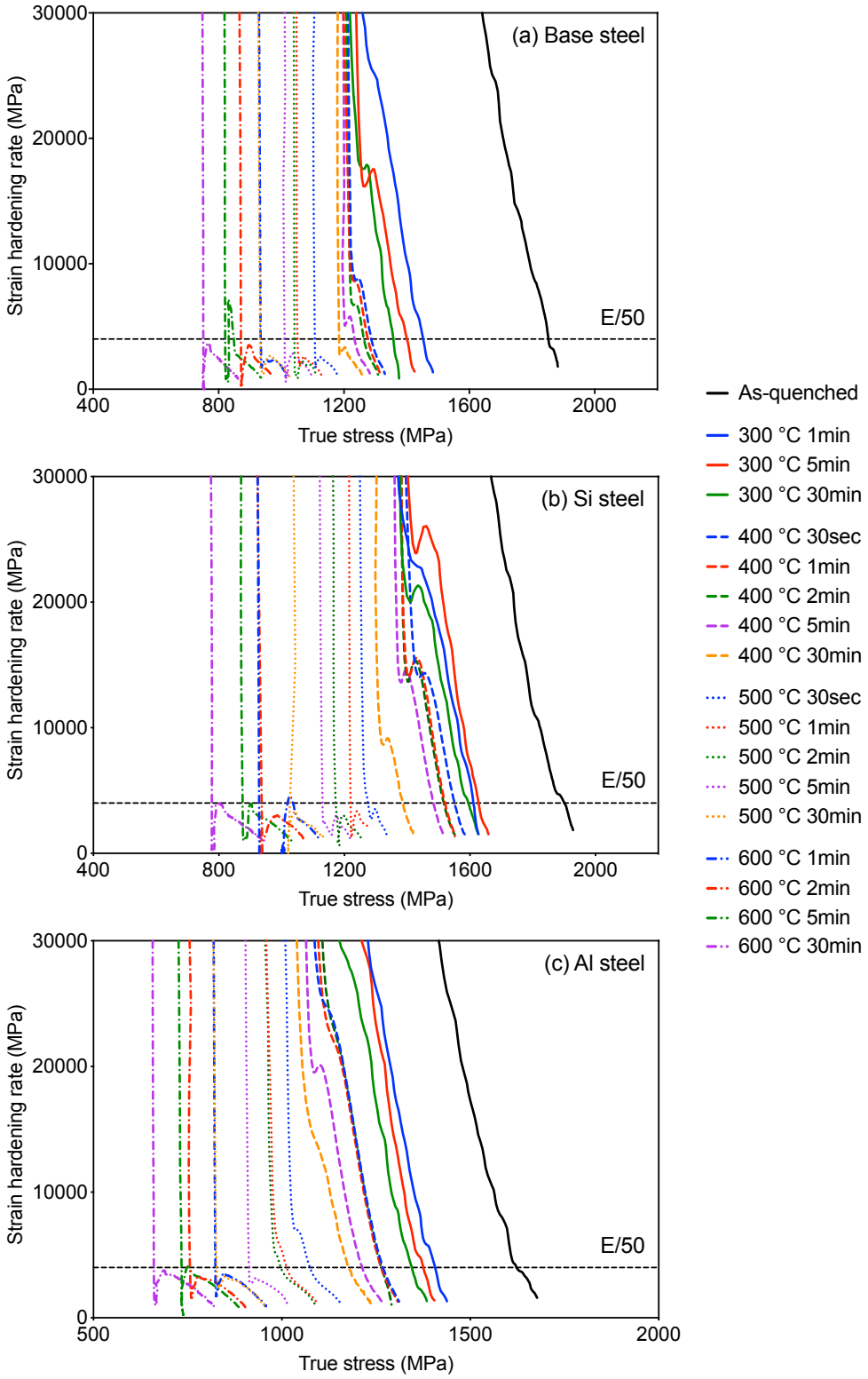

Figure 6.11: *Strain hardening rate - true stress curves of the base steel (a), the Si steel (b) and the Al steel (c) with different heat treatment conditions.*

6.3.2 Evolution of mechanical properties

Figure 6.12 shows the evolution of yield strength and ultimate tensile strength during tempering. Compared to the as-quenched state, the YS of all steels remain relatively constant at 300 °C and 400 °C while the UTS decreases dramatically during tempering. This implies that softening of martensite at lower temperatures may be attributed to the decrease in the strain hardening response. This hypothesis can be supported by the results in Figure 6.13 where the evolution of the strain hardening exponent (n in Eq. 4.1) is plotted as a function of tempering parameters. The strain hardening exponents of all steels first witness a drop to a minimum value ~0.04 when tempered at 300 °C and 400 °C and then gradually increase when tempered above 500 °C for longer times. Therefore, the significant decrease in UTS' of martensite tempered at 300 °C and 400 °C is indeed caused by the reduction in strain hardening compared to the as-quenched state. In the case of samples tempered at 500 °C and 600 °C, while the strain hardening capabilities may be recovered by high temperature and long time tempering, both YS' and UTS' decrease significantly. Hence, the softening of martensite tempered at high temperature is most likely related to a loss of base strength of the material. This assumption can be supported by the microstructural evolutions occurring at high temperatures (e.g. coarsening of precipitates and substructures).

The alloying element effect of Si and Al can be assessed using the evolution of the softening parameters for YS and UTS (Figure 6.14). While the addition of Si and Al does have an effect on retarding the temper softening of martensite at all temperatures, it is interesting to see that the alloying elements have a more significant effect on UTS compared to YS, especially at 300 °C and 400 °C. This may also be linked to the different evolution in strain hardening exponent seen in Figure 6.13 where the addition of Si and Al helps maintain higher strain hardening capabilities at 300 °C and 400 °C and postpones the minimal strain hardening exponent to higher TPs. Together with the microstrain evolution discussed previously, the high strain hardening capabilities of the Si and Al steels may be attributed to the slower relaxation kinetics of microstrain during tempering. Further experimental works will be shown later to support this hypothesis.

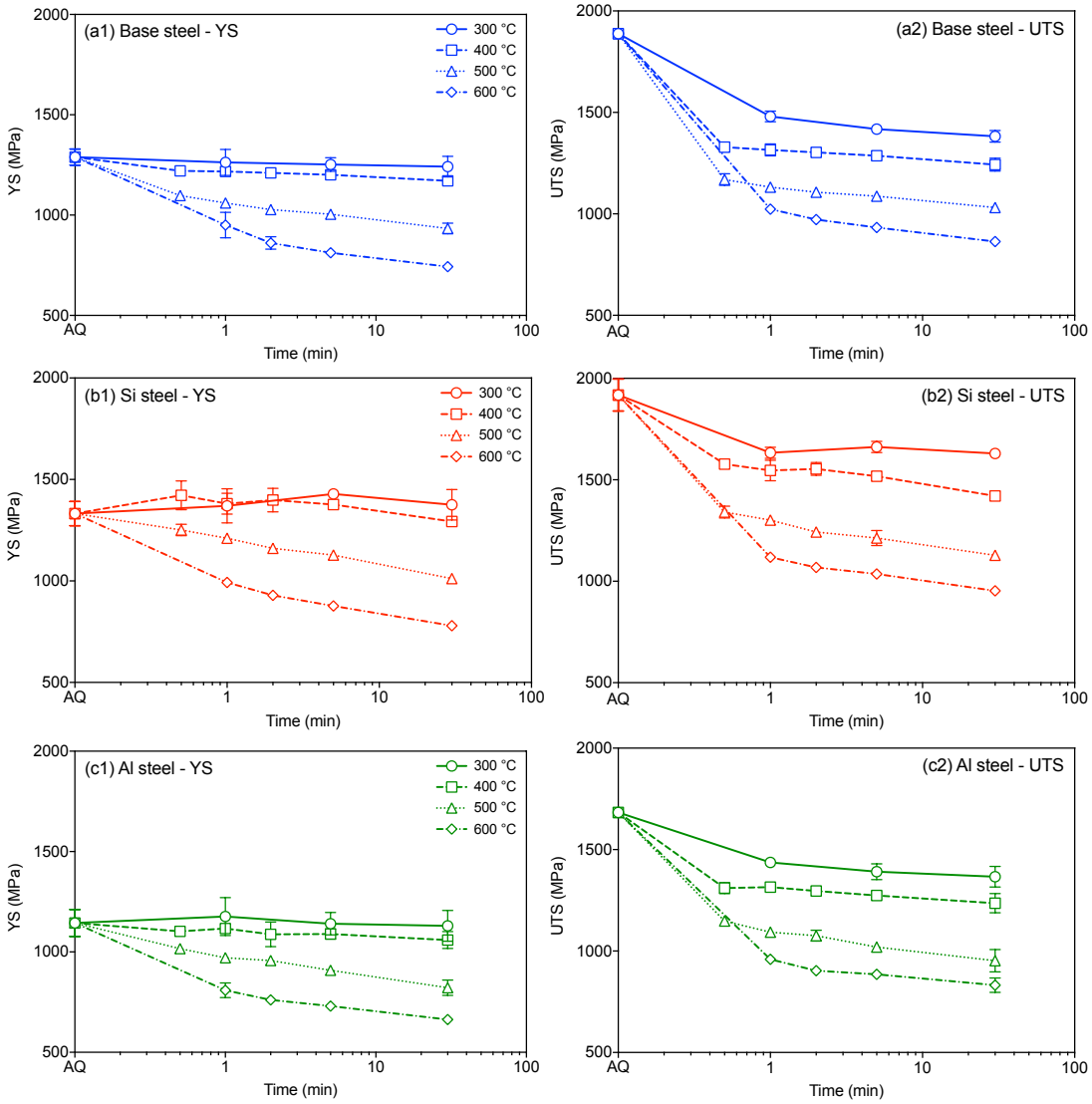

Figure 6.12: *Evolution of yield strength (a1) - (c1) and ultimate tensile strength (a2) - (c2) for all compositions. Error bars represent 95% confidence intervals calculated from three samples. Note that no 30-second samples were tested for 300 °C and 600 °C tempered conditions*

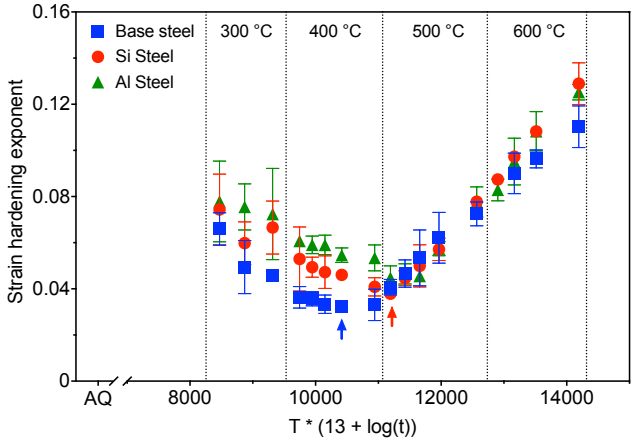

Figure 6.13: *Hollomon-Jaffe plot showing the evolution of the strain hardening exponent as a function of tempering parameters. At each temperature, tempering times vary from 30 seconds to 30 minutes. Error bars represent the 95% confidence intervals calculated from three samples. Example fits for strain hardening exponents can be found in Figure 4.3b.*

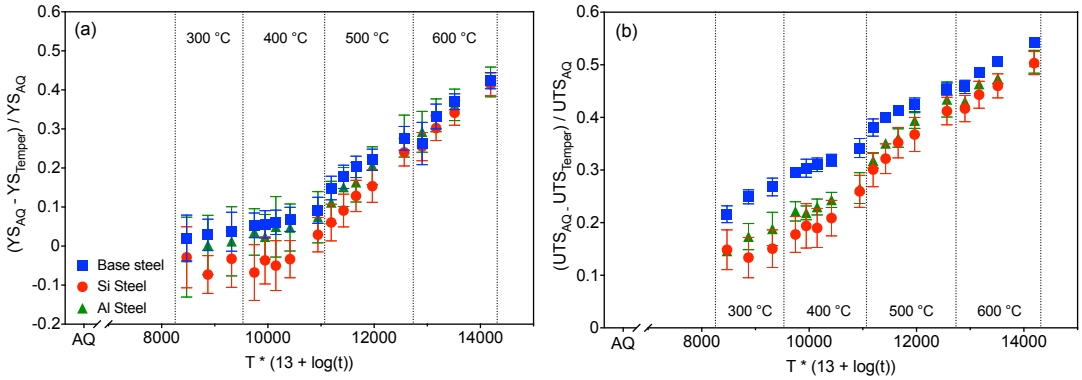

Figure 6.14: *Hollomon-Jaffe plots showing the evolution of softening parameters for YS (a) and UTS (b) as a function of tempering parameters. At each temperature, tempering times vary from 30 seconds to 30 minutes. Error bars are calculated using the error propagation function.*

6.4 Evolution of composite strengthening parameters

6.4.1 Evolution of nanohardness and its variation

It has been demonstrated in Chapter 5 that although the experimentally measured variation in nanohardness is smaller than the one needed in the yield stress spectrum model, there is indeed a distribution of strength in as-quenched martensite. In one application of the yield stress spectrum model, Mahlheiros *et al.* demonstrated that it is possible to describe the mechanical behaviour of tempered martensite if the distribution in intrinsic strengths decreases during tempering [112] (Figure 2.33). Figure 6.15a shows the evolution of the nanohardness during tempering. The evolution of the nanohardness shows a similar trend to the evolution of macroscopic mechanical properties: the average nanohardness values decrease during tempering and the tempering temperature has a much larger impact on the reduction of nanohardness compared to the tempering time. The addition of Si slows down the softening kinetics and the effect of Al is less obvious.

The main focus of this set of experiments is the evolution of the variation in the nanohardness shown in Figure 6.15b - d. The error bars shown in the figures represent the 95% confidence intervals of the standard deviations. The confidence intervals were calculated using Eq. 6.2 which assumes the measured data can be described by a normal distribution (an example of normality can be seen in Figure 5.8):

$$\begin{aligned} \text{Upper limit} &= s\sqrt{\frac{n-1}{\chi^2_{(1-\alpha/2,n-1)}}} \\ \text{Lower limit} &= s\sqrt{\frac{n-1}{\chi^2_{(\alpha/2,n-1)}}} \end{aligned} \tag{6.2}$$

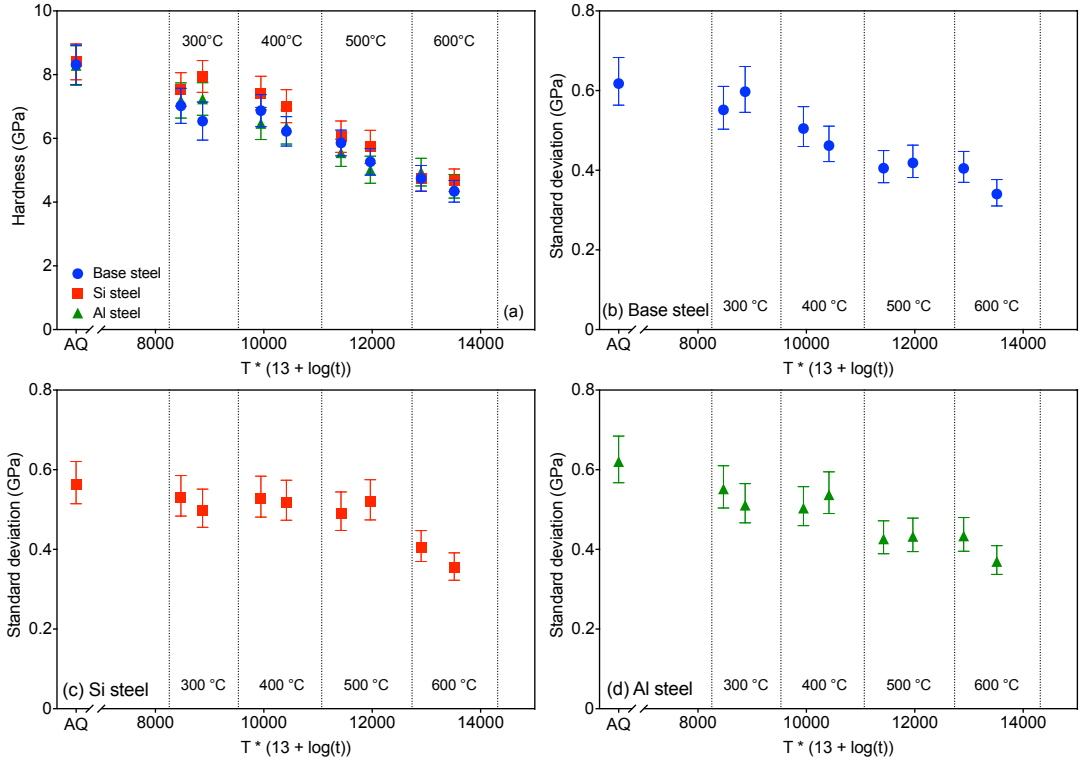

Figure 6.15: *Hollomon-Jaffe plots showing the evolution of nanohardness (a) and standard deviations (b - d) as a function of tempering parameters. At each temperature, two tempering times are shown (i.e. 1 minute and 5 minutes). Error bars in (a) represent one standard deviation of the mean and the error bars in (b - d) represent the 95% confidence interval of the measured standard deviations.*

where s is the measured standard deviation, n is the number of measurements and $\alpha = 0.05$. Generally, the standard deviations decrease as a function of tempering (Figure 6.15b - d). In the case of the base steel, a large decrease in the standard deviation can be found after tempering at temperatures above 400 °C. With the addition of Si and Al, the onset of this large decrease is postponed to higher temperatures. This is consistent with the evolution of microstrain (Section 6.2.2) and macroscopic mechanical properties (Section 6.3) and may be again attributed to the alloying element effect on the recovery and precipitation kinetics. At 600 °C, all steels share a similar level of standard deviation in nanohardness and its magnitude is roughly one half of the initial standard deviation in the as-quenched state. The change in the magnitude of standard deviation supports the findings of Mahlheiros *et al.* that tempering leads to a homogenisation of the mechanical heterogeneities. However, it is worth noting that the average nanohardness also changes dramatically during tempering and the nanohardness values in the 600 °C tempered conditions are also approximately one half of the as-quenched nanohardness. As a result, the coefficient of variation (the standard deviation normalised by the mean) only show small changes throughout tempering considering the scatter in the confidence intervals (Figure 6.16a). It suggests that the variation scales with the average strength and there is indeed a weak correlation between the mean nanohardness values and the measured standard deviations (Figure 6.16b). Although this

empirical correlation may predict a much smaller variation in strength as required in the yield stress spectrum model, it implies that any models that use the concept of the yield stress spectrum should be able to reproduce such a correlation between the mean of the spectrum and the width of the spectrum.

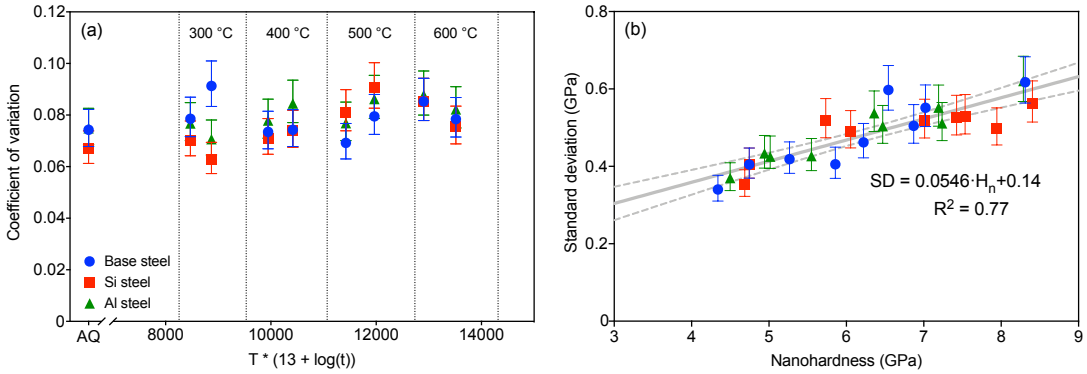

Figure 6.16: *(a) Hollomon-Jaffe plot showing the evolution of the coefficient of variation as a function of tempering parameters. At each temperature, two tempering times are shown (i.e. 1 minute and 5 minutes). Error bars represent the upper and lower limits of the coefficients calculated from the 95% confidence intervals of the standard deviations. The confidence interval for the nanohardness values are very small due to the large number of measurements. (b) Correlation between experimentally measured standard deviations and nanohardness values, the solid grey line is fitted to the experimental data from all compositions and the dashed grey lines represent the 95% confidence bands.*

6.4.2 Evolution of microstrain during deformation after tempering

A key characteristic of the deformation behaviour of as-quenched martensite is the narrowing of diffraction lines during straining (Section 2.2.3.4). The residual stress spectrum model regards this phenomenon as a result of relaxation of Type II residual stresses, which leads to the high strain hardening rate in the as-quenched state. It is shown in Section 6.3.2 that the strain hardening rates for 300 °C and 400 °C tempered samples show values comparable to the as-quenched state. This suggests that the line narrowing phenomenon may still be visible if interrupted X-ray diffraction experiments are performed. In the case of high temperature tempered samples, all samples show strain hardening rates below the dislocation storage limit, which implies that the classic peak broadening behaviour should resume.

Figure 6.17 shows the effect of tempering and straining on the evolution of microstrain derived from diffraction experiments. To the left of the vertical dashed line, the figures show the effect of tempering temperatures and reinforce the findings of Figure 6.6 that tempering leads to a decrease in microstrain (i.e. diffraction peak narrowing). To the right of the dashed line, the figures show the effect

of monotonic straining. For each tempering condition, several interrupted tests were performed and the maximum forward strain was set approximately 0.5% to 1% below the uniform elongation of each condition. This ensures that strain localisation as result of necking does not affect the measurement of microstrain.

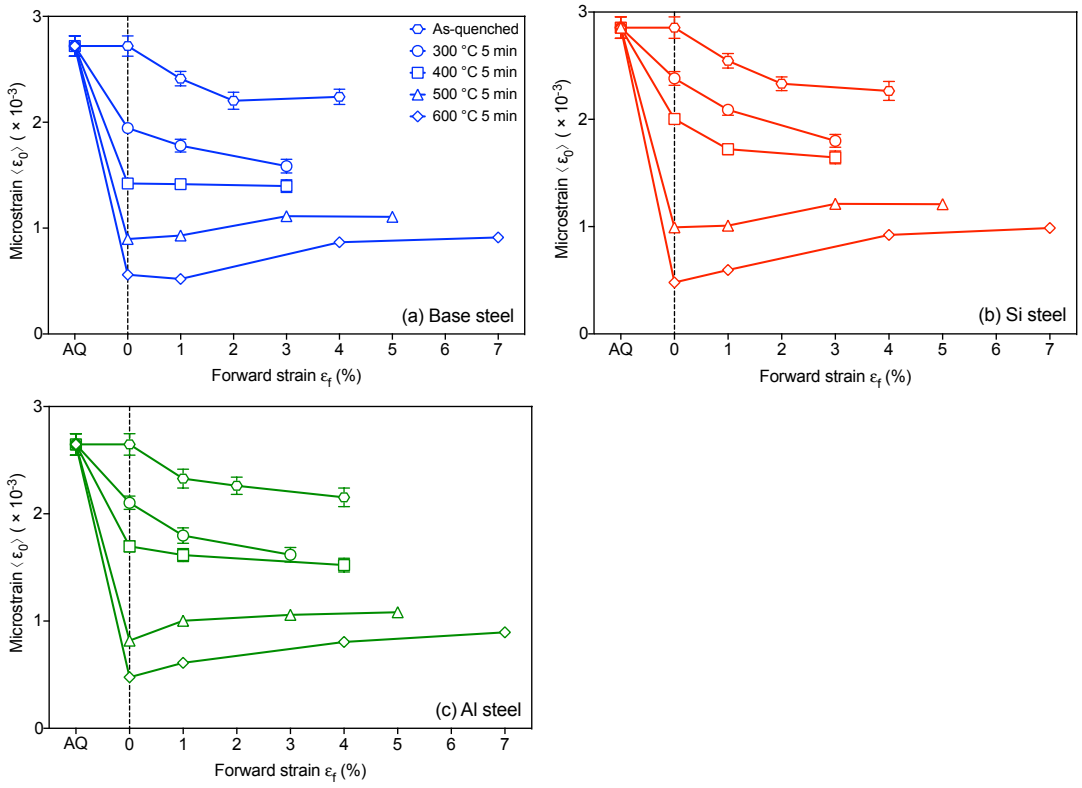

Figure 6.17: *Evolution of microstrain as a function of tempering temperature and straining for the base steel (a), the Si steel (b) and the Al steel (c). All samples were tempered at different temperatures for 5 minutes. Error bars represent two times the Rietveld error.*

Depending on the tempering temperatures, two microstrain evolution kinetics can be observed. For samples in the as-quenched state and tempered at 300 °C, decrease of microstrain during straining is clearly observed regardless of composition. For samples tempered at 500 °C and 600 °C, increase of microstrain (i.e. diffraction peak broadening) is found. In the case of 400 °C tempered samples, the Si and the Al steels both show a decrease in microstrain while the value of the base steel witnesses limited evolution. This could be a result of competition between peak narrowing and peak broadening contributions. Together with the strain hardening rate results in Figure 6.11, we will still consider the 400 °C tempered samples to be largely affected by peak narrowing. In general, the results from interrupted diffraction experiments agree well with the hypotheses made previously: the high strain hardening rate observed in the 300 °C and 400 °C tempered samples is accompanied by peak narrowing; and the low strain hardening rate observed in the 500 °C and 600 °C tempered samples is a result of dislocation storage shown by peak broadening.

According to the residual stress spectrum model, peak narrowing is a result of residual stress relaxation. The fact that 300 °C and 400 °C tempered samples still show peak narrowing implies that residual stresses cannot be fully relaxed by thermal treatments at low temperatures and some of the residual stresses remain to be relaxed by plastic straining. Moreover, prolonged tempering at 300 °C and 400 °C does not influence much the peak narrowing behaviour during deformation (Figure 6.18a - c) but it does reduce the magnitude of the peak narrowing (expressed as the difference between the microstrain before deformation $\langle\varepsilon_0\rangle_{Undeform}$ and the microstrain after deformation to strains close to UTS $\langle\varepsilon_0\rangle_{Deform}$, Figure 6.18d). This suggests that the long time tempering at low temperatures leads to further relaxation of residual stresses. Similar to the evolution of other properties, the addition of Si and Al affects the relaxation process and their effect is most clearly seen in samples tempered at 400 °C. While the base steel displays limited relaxation and even peak broadening during deformation after tempering at 400 °C, a considerable amount of residual stresses remain in the alloyed samples even after tempering at 400 °C for 1 hour.

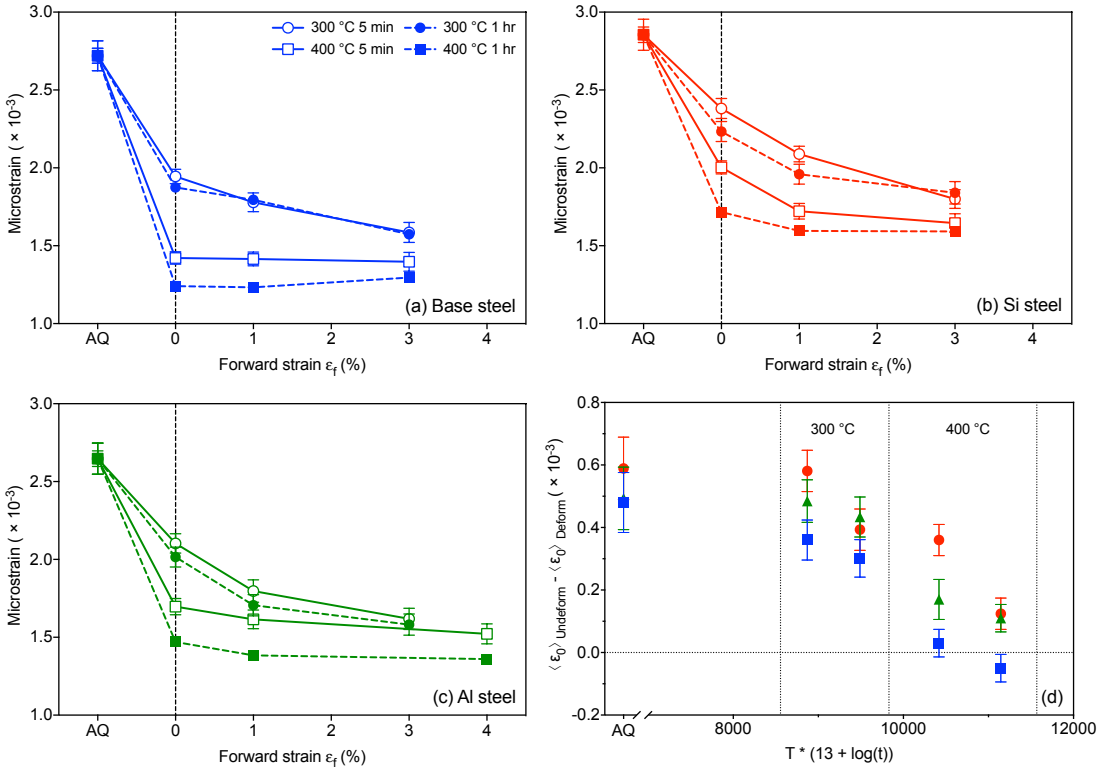

Figure 6.18: *Evolution of microstrain as a function of straining for the base steel (a), the Si steel (b) and the Al steel (c) tempered at 300 °C and 400 °C for 5 minutes and 1 hour. (d) Hollomon-Jaffe plot showing the evolution of the magnitude of the microstrain reduction after deformation. At each temperature, two tempering times are shown (i.e. 5 minutes and 1 hour). Error bars in all plots represent two times the Rietveld error.*

6.5 Evolution of athermal and kinematic contributions

In the as-quenched condition, it was found using strain-rate sensitivity tests that the dominant contribution to the high flow stress comes from athermal hardening (Section 5.4). Figure 6.19 shows the strain-rate sensitivity test results for tempered conditions. The same slope used in the as-quenched state (Figure 5.12) was used to describe the evolution of the inversely normalised activation area ($b^2/\Delta a$) in tempered samples. Although some discrepancies may be found in the 600 °C tempered samples, the overall fit between the linear regression and the experimental data show good agreement regardless of chemical composition and tempering state. This indicates that the addition of Si and Al, as well as tempering, has a relatively small effect on the dislocation storage in martensite until reaching the heavily tempered states. Discrepancies observed at high temperatures may be attributed to the recovery of strain hardening capabilities (Figure 6.13) that are predominantly dislocation related. Further evidence will be shown in the analyses of kinematic hardening contributions.

The evolution of athermal and thermal hardening contributions can be more clearly seen if they are plotted against the tempering parameters (Figure 6.20). The athermal hardening contributions decrease continuously as a function of tempering but the thermal hardening contributions remain relatively constant and the reduction from the as-quenched state is approximately 200 MPa for all compositions after tempering at 300 °C. This suggests that while the decrease in dislocation based thermal stresses contribute to the softening of martensite, a large proportion of softening can still be attributed to the reduction of athermal hardening contributions. The evolution of softening parameters based on the athermal stress is shown in Figure 6.21 to demonstrate the chemistry effect. At low tempering temperatures, softening is related to the decrease in mechanical heterogeneities and relaxation of residual stresses shown in Section 6.4. The addition of Si and Al slows down the softening kinetics of athermal stresses which also agrees with the microstructural evolutions observed previously. Once the heterogeneities are homogenised by tempering, the chemistry effect is less obvious at high tempering temperatures and the further softening may come from the coarsening of precipitates and substructures shown in Section 6.2.1 and 6.2.3.

If the evolution of microstructural features affects the magnitude of athermal hardening contributions, it should also influence the change in the kinematic hardening contributions since the kinematic hardening should be less susceptible to thermal activations than dislocation based forest strengthening. Figure 6.22 shows the tension-compression test results of the 300 °C and 500 °C tempered samples for the Si steel. It can be seen that the reproducibility of the forward behaviour is very good which allows us to confidently compare the evolution of the back stress during tempering. The complete set of tension-compression data can be found in Appendix A and the overall sample-to-sample variation is estimated

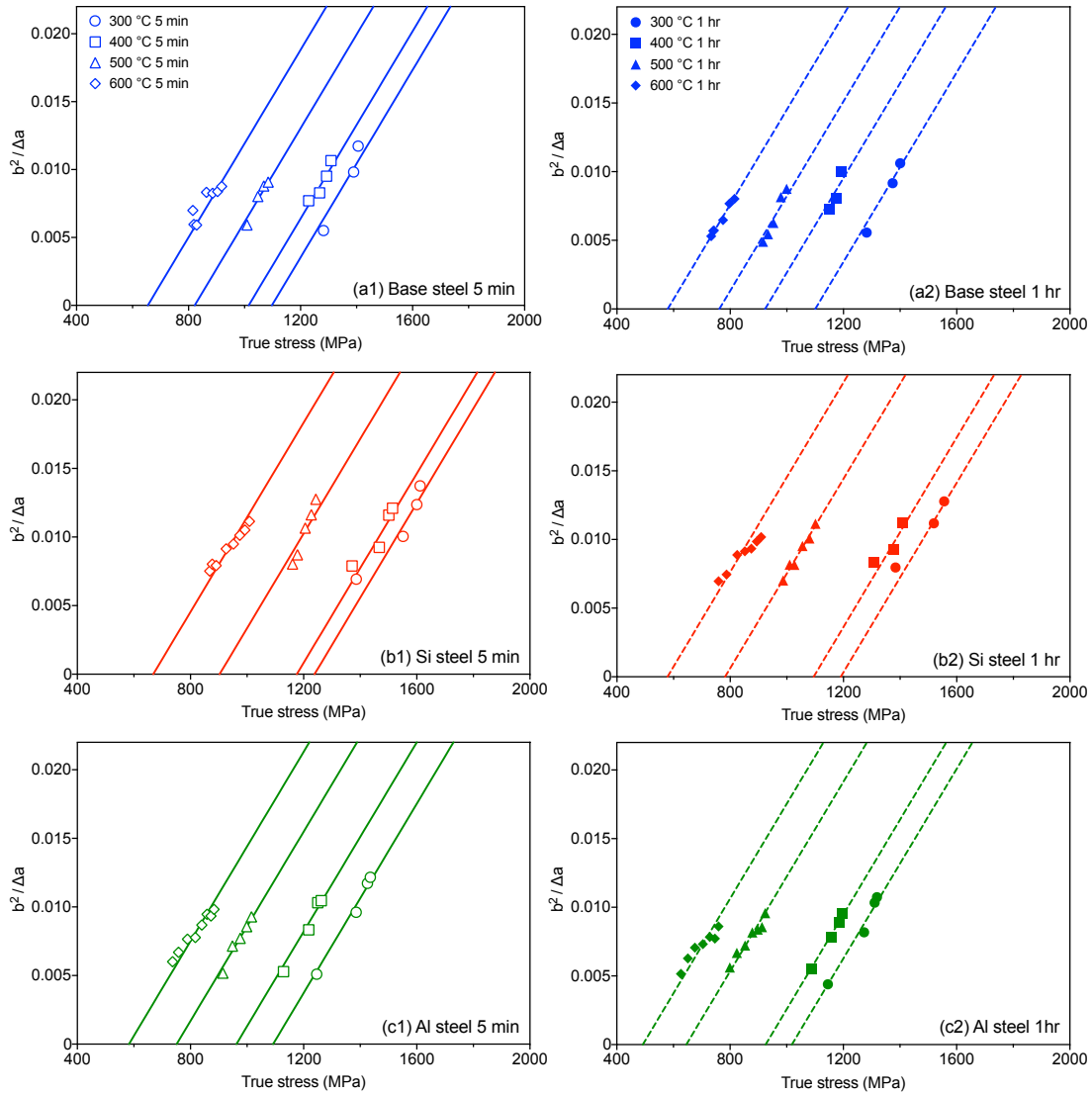

Figure 6.19: *Haasen plots for the tempered conditions. (a1) - (c1) Samples tempered at different temperatures for 5 minutes. (a2) - (c2) Samples tempered at different temperatures for 1 hour. The same slope is used for the linear regressions for all steels.*

to be less than 5% using the forward loading curves. Figure 6.22 also shows that the forward flow stress (σ_f, solid symbols) and the reverse yield stress ($|\sigma_r|$, open symbols) evolve with different trends during deformation (i.e. an increasing trend for σ_f and a decreasing trend for $|\sigma_r|$), which results in the increase in the back stress as $\langle\sigma_b\rangle = \left(\sigma_f - |\sigma_r|\right)/2$.

Figure 6.23 shows the evolution of the back stress during plastic straining for the tempered conditions. The solid and dashed lines are obtained by fitting the experimental back stress data with the phenomenological non-linear kinematic hardening model (Eq. 2.12). In general, the fitted lines can describe well the evolution of the back stress as a function of plastic strain. It can be seen that tempering does not only reduce the magnitude of the back stress but also affects the development of the back stress. As tempering proceeds, the kinematic strain hardening rates at high plastic strains decrease and eventu-

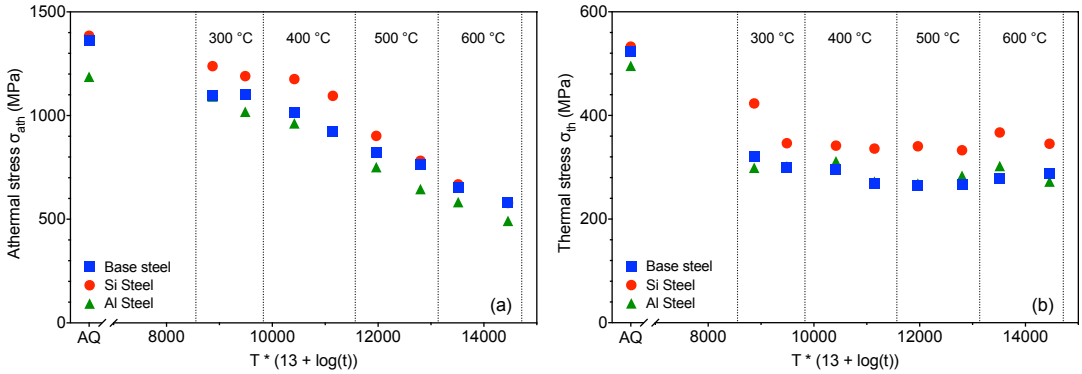

Figure 6.20: *Hollomon-Jaffe plots showing the evolution of athermal (a) and thermal (b) hardening contributions. The thermal contribution is derived by the subtraction between the UTS in the strain-rate sensitivity test and the athermal hardening contribution. At each temperature, two tempering times are shown (i.e. 5 minutes and 1 hour). Typical uncertainties can be estimated by the sample to sample difference observed in monotonic tests and should be around 20 - 30 MPa.*

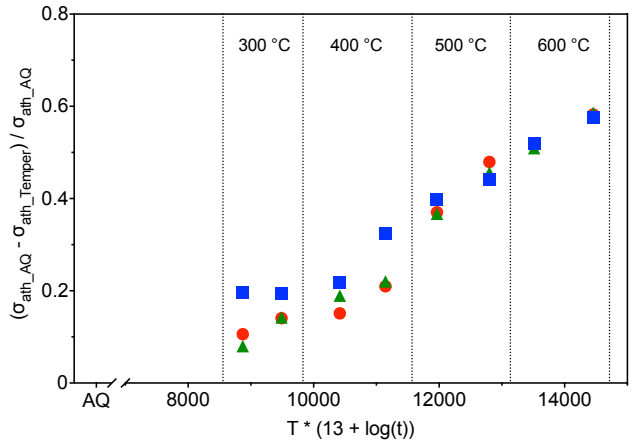

Figure 6.21: *Hollomon-Jaffe plot showing the evolution of softening parameters for the athermal stress as a function of tempering parameters. At each temperature, two tempering times are shown (i.e. 5 minutes and 1 hour).*

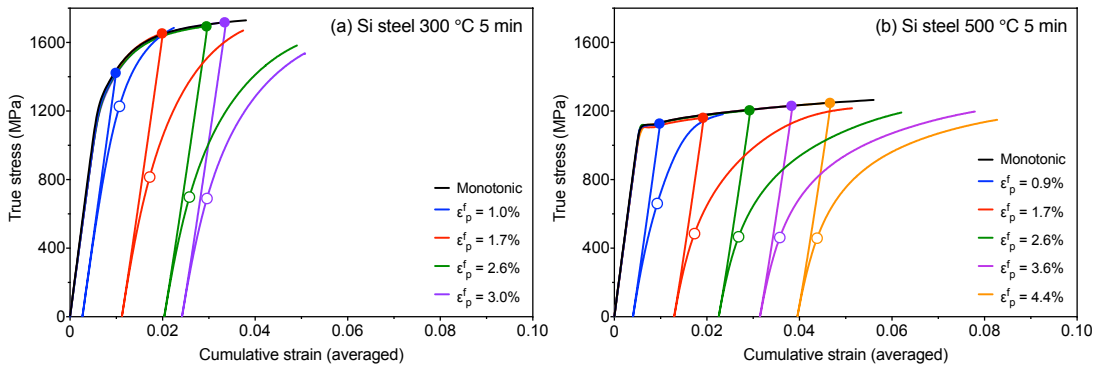

Figure 6.22: *Tension-compression test results for the Si steel tempered at 300 °C (a) and 500 °C (b) for 5 minutes. The solid symbols represent the forward flow stress and the open symbols represent the reverse yield stress determined using the 0.2% offset strain.*

ally become relatively flat after high temperature tempering. This indicates that the decrease in strain hardening rates and strain hardening exponents at lower temperatures (Figure 6.13) may be related to the reduction in kinematic hardening. The microstructural origin of this again comes from the homogenisation of microstructural heterogeneities. At high tempering temperatures, kinematic hardening does not contribute much to the strain hardening at large plastic strains so the increase in the strain hardening exponent (Figure 6.13) should be related to the increase in the dislocation based, isotropic hardening contributions.

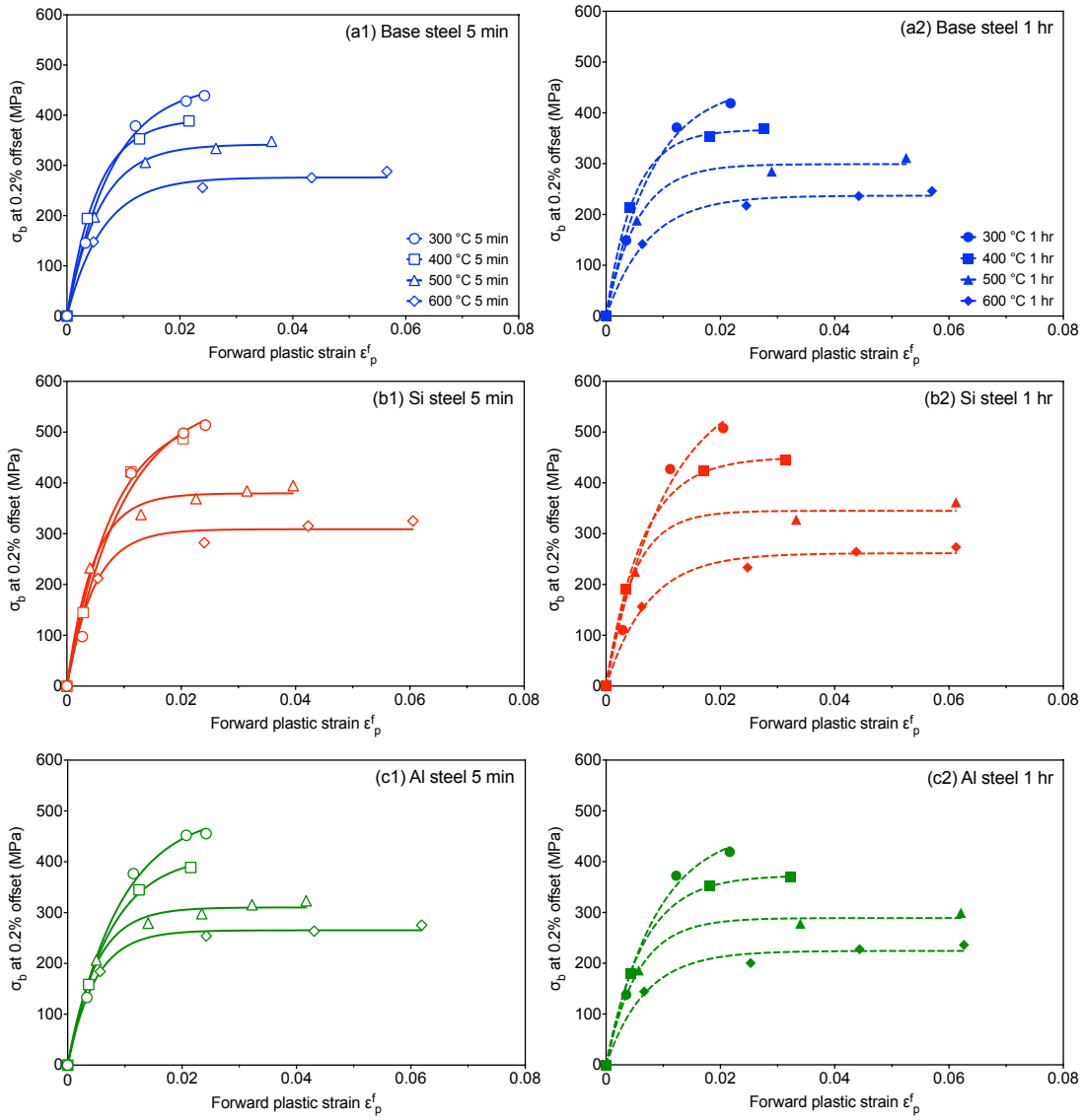

Figure 6.23: *Evolution of back stresses as a function of forward plastic strain. (a1) - (c1) Samples tempered at different temperatures for 5 minutes. (a2) - (c2) Samples tempered at different temperatures for 1 hour. The solid and dashed lines are fitted with Eq. 2.12.*

The chemistry effect can be demonstrated when the maximum back stresses (Figure 6.24a) and the associated softening parameters (Figure 6.24b) are plotted as a function of tempering parameters. It can be found that the addition of Si can significantly reduce the reduction of kinematic hardening, especially at 400 °C. The addition of Al, on the other hand, has a limited effect. This is again in agreement with the evolution of the athermal stress (Figure 6.20a) and microstructural evolutions (Section 6.1).

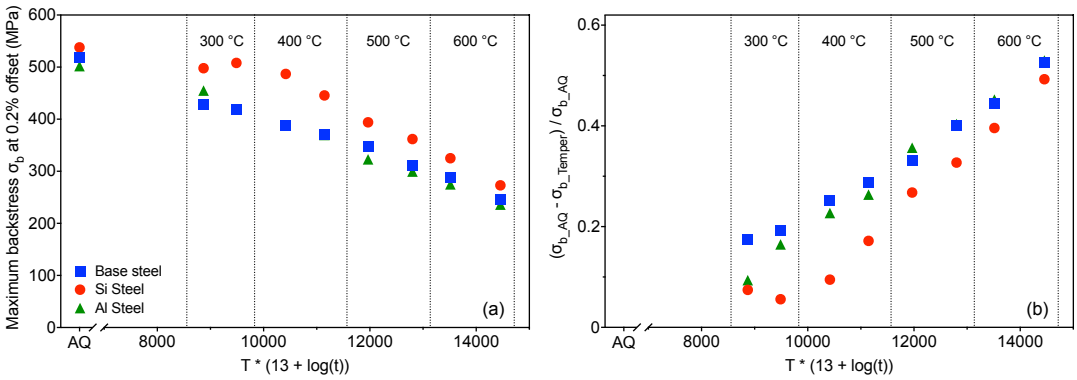

Figure 6.24: *Hollomon-Jaffe plots showing the evolution of maximum back stresses (a) and softening parameters for the back stress (b) as a function of tempering parameters. At each temperature, two tempering times are shown (i.e. 5 minutes and 1 hour).*

Since both the athermal hardening and the kinematic hardening contributions originate from long-range internal stresses developed during straining, it is worth exploring if they are correlated in the martensite system. Figure 6.25a - c shows the correlation between the back stress measured from tension-compression tests and the athermal stress estimated using the strain-rate jump tests and the Haasen plot in the studied compositions. A linear correlation is found for all compositions. The slope of the linear correlation depends on the offset strain used in the back stress estimation but the magnitude of the slope does not become one even if a small offset (0.1%) is chosen. It implies that the magnitude of kinematic hardening is always smaller than the magnitude of athermal hardening and kinematic hardening accounts for approximately the same fraction of athermal hardening throughout tempering. Moreover, it is found that a master line can be fitted to all compositions for all tempering conditions (Figure 6.25d), which suggests that the correlation is not strongly altered by the addition of Si and Al regardless of their effects on the tempering kinetics. Therefore, it is possible to use the athermal stress found using the strain-rate sensitivity tests to estimate the magnitude of the kinematic hardening contribution, which may significantly reduce the complexity of further experimental designs.

Another interesting finding of this master curve is that it has a non-zero intercept with the back stress axis and the magnitude of the intercept is not sensitive to the selection of the offset strain (~60 - 70 MPa). This implies that if the material is predominantly strengthened by forest dislocations, the kinematic hardening contribution does not necessarily go to zero. One example to support this implication

may be found in the test results of IF steels. Bouaziz *et al.* performed shear reversal tests on sheet IF steel samples and found that the maximum magnitude of the back stress is ~30 MPa and it could be attributed to the development of dislocation cell structures during plastic straining [156, 157]. It agrees reasonably well with the intercept found in this work considering the vast differences between martensite and IF steel microstructures.

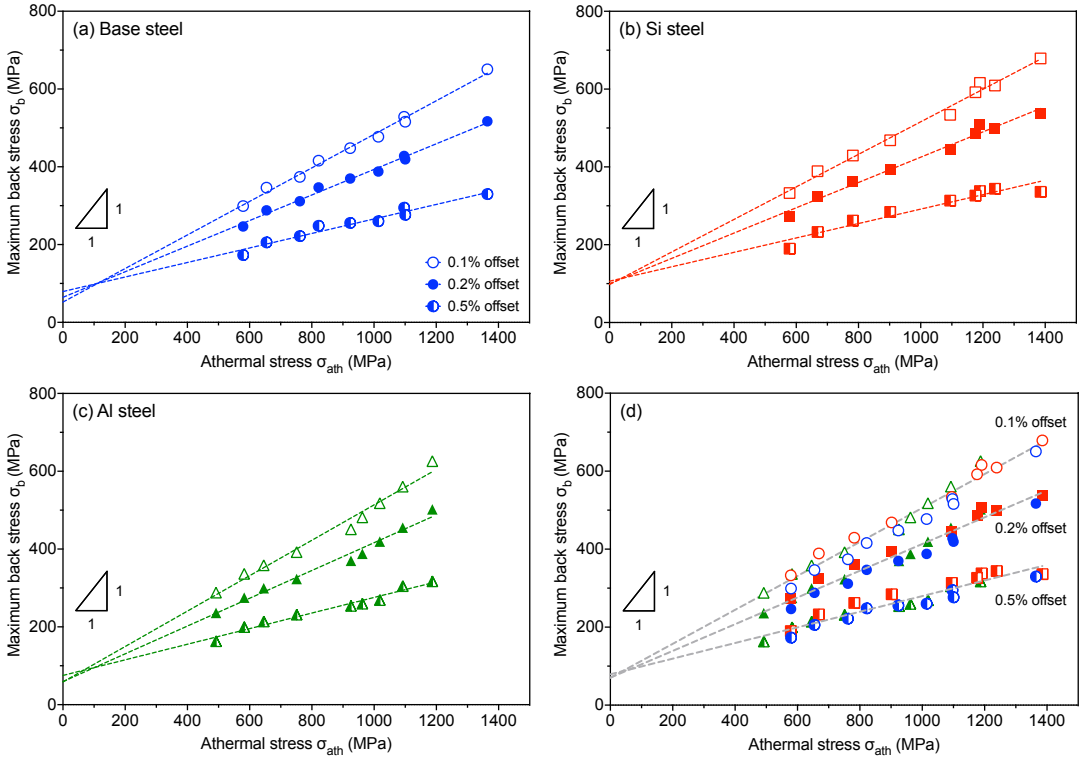

Figure 6.25: *Plots showing the correlation between the maximum back stress obtained from Bauschinger tests and the athermal stress obtained from strain rate jump tests. (a) Base steel. (b) Si steel. (c) Al steel. (d) All steels combined. Dashed lines are fitted with linear regressions with different slopes. The triangles in the plots represent the slope for a one-to-one ratio.*

6.6 Summary

Tempering behaviour observed in this study can be separated into two parts depending on the tempering temperatures. At lower tempering temperatures (300 °C and 400 °C), the strain hardening response of tempered martensite resembles the one observed in the as-quenched state (i.e. greater than the E/50 limit). However, a continuous loss of strain hardening capabilities can be also observed during tempering. This can be attributed to the homogenisation of microstructural heterogeneities including the reduction in intrinsic strength variations and the relaxation of residual stresses, which results in less strain hardening from athermal and kinematic hardening contributions. The addition of Si and Al has a significant impact on the softening kinetics at this stage and it can be related to their effects on retarding cementite precipitation.

At higher tempering temperatures (500 °C and 600 °C), the strain hardening rates of all samples are below the E/50 limit, suggesting that dislocation storage mechanisms are the dominant contribution. It is further proved by interrupted X-ray diffraction experiments that there is limited influence from residual stresses and diffraction peak broadening is observed. Softening of martensite is caused by the reduction in athermal contributions that arise from the hierarchical microstructures (i.e. grain boundaries and precipitates). Moreover, the recovery of strain hardening capabilities at high temperatures can be largely attributed to the increase in dislocation based isotropic hardening contributions. Chemistry effects on martensite softening are less obvious in this temperature range since the microstructural evolutions are not strongly affected by the addition of Si and Al at high tempering temperatures.

Chapter 7

Modelling the mechanical response of martensite

7.1 Introduction

As demonstrated in Chapter 6, the flow behaviour of tempered martensite can be separated into two categories depending on the magnitude of the strain hardening rate, which is correlated to tempering temperatures. Therefore, two different modelling approaches are presented to rationalise the mechanical response of martensite depending on the tempering conditions. For the as-quenched and low temperature (300 °C and 400 °C) tempered conditions, the two composite models discussed in Chapter 5 are integrated to consider both the variation in intrinsic yield stresses and the relaxation of residual stresses during straining. For high temperature tempered conditions where the strain hardening capability of martensite is recovered ($T \geq 600$ °C) , a combined isotropic and kinematic hardening model is developed. In both cases, the modelled results are compared with the tension-compression results to demonstrates the capabilities of the models in describing both the forward and reverse flow behaviours of martensite. Limitations of the models and future work required will also be addressed at the end of each section.

7.2 A modified composite model for as-quenched and low temperature tempered martensite

While both the yield stress spectrum model and the residual stress spectrum model are promising candidates in describing the flow behaviour of as-quenched martensite (Chapter 5), they have limitations in explaining certain features: the yield stress spectrum model does not reflect the diffraction line narrowing phenomenon observed during straining of as-quenched martensite; the residual stress spectrum model does not result in a Bauschinger effect as all residual stresses are relaxed and the composite effect is eliminated after forward straining. It is, however, interesting to explore if the two models could be integrated into a new framework that simultaneously considers the variation in local yield stresses and relaxation of residual stresses.

7.2.1 A composite model incorporating both yield stress spectrum and residual stress spectrum hypotheses

In the first instance, we investigated the possibility to include the relaxation of residual stresses into the yield stress spectrum model. As mentioned in the work of Scott *et al.* [65] and Badinier [74], the variation in yield stresses can come not only from the heterogeneous carbon contents in martensite crystals or lath size variations, but also from the residual stress states within different constituents. Since we assume the constituents are elastic perfectly plastic, the variation in intrinsic yield stresses should not change during deformation but the residual stresses should be able to relax as a result of mechanical homogenisation. Therefore, if the initial yield stress spectrum is affected by the existence of residual stresses, the spectrum should become narrower after deformation since the residual stresses are, to some extent, relaxed by the forward loading and exert less influence on the variation in yield stresses.

For the purpose of illustration, consider Figure 7.1. The black solid line in Figure 7.1a represents the initial yield stress spectrum of the material which comes from the convolution of the intrinsic yield stress spectrum and the residual stress spectrum. Constituents that reside on the left-hand side of the distribution have smaller yield stresses compared to the mean of the distribution. Besides the lower intrinsic yield stresses, they are also likely to be affected by residual stresses that are aligned with the loading direction which result in the lower apparent yield stresses. As a result, these constituents will have smaller yield surfaces (dotted black line in Figure 7.1b) than the mean (solid black line). In contrast, constituents that are found on the right-hand side of the distribution are likely to be affected by higher intrinsic yield stresses and residual stresses that are opposite to the loading direction. These constituents can be represented by the larger yield surfaces shown as dashed black lines in Figure 7.1b.

Upon straining, constituents with lower apparent yield stresses (i.e. left to the mean) will yield first and relax their residual stresses. Since they are affected by residual stresses that facilitate yielding in the forward direction, relaxation of these stresses should lead to an increase in the apparent yield stresses so their yield surfaces should expand (dotted red line in Figure 7.1b). On the other hand, when the forward strain is large enough to deform constituents with higher apparent yield stresses (i.e. right to the mean), the relaxation of residual stresses should lead to a loss of resistance to forward plasticity so the apparent yield stresses should decrease. Therefore, their yield surfaces should shrink (dashed red line in Figure 7.1b). As plasticity develops in all constituents, the influence of residual stresses become less and the width of the spectrum decreases, which can be represented by the red dashed spectrum in Figure 7.1a.

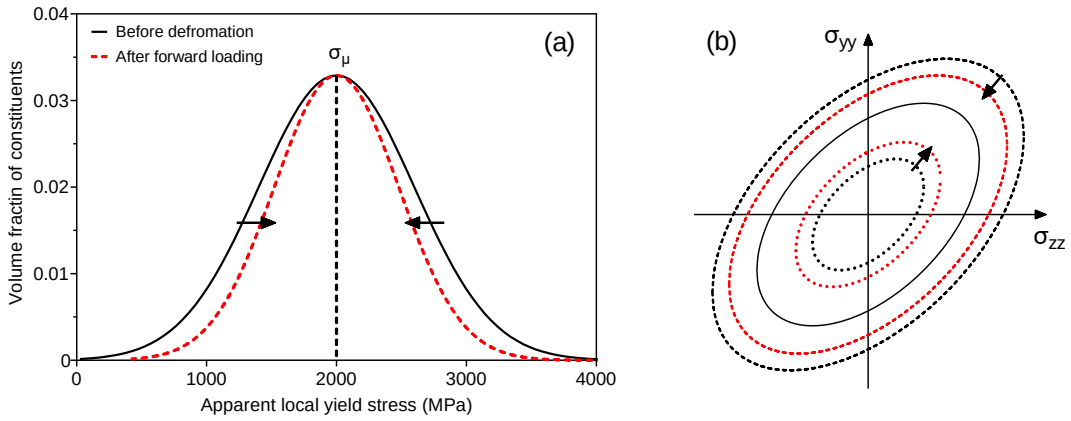

Figure 7.1: *(a) Apparent local yield stress spectra before and after forward loading. (b) Yield surfaces of constituents with lower (dotted lines) and higher (dashed lines) apparent local yield stress than the mean (solid black line). The red lines represent the size of the yield surface after relaxation of residual stresses.*

In our implementation of this modified model, the initialisation scheme for the yield stress spectrum model is used assuming a mean σ_μ and an initial spread σ^0_{sd} (Section 5.2.2.1). Each constituent is then assigned with an initial apparent yield stress σ^i_{y0}. During straining, if the stress at the constituent level exceeds σ^i_{y0}, the apparent yield stress is allowed to evolve to reflect a reduction in the residual stress contribution in the following way:

$$\sigma^i_{yr} = \sigma^i_{y0}\left[1-\alpha_r\left(\frac{\sigma^i_{y0}-\sigma_\mu}{\sigma^i_{y0}}\right)\right] \tag{7.1}$$

where σ^i_{yr} is the apparent yield stress of the constituent after relaxation of residual stresses and α_r is the relaxation parameter ranging from 0 to 1. In the first instance, we assume this relaxation process occurs instantaneously when the constituent yields and no further hardening is allowed after the relaxation (i.e. constituents are still elastically-perfect plastic). The $\left(\sigma^i_{y0}-\sigma_\mu\right)/\sigma^i_{y0}$ term allows Eq. 7.1 to locate the position of the constituent relative to the mean: if the constituent has a yield stress smaller than

the mean, this term will be negative and vice versa. Together with the relaxation parameter α_r, Eq. 7.1 is able to describe the magnitude of the change in the apparent yield stress for each constituent. Eq. 7.1 also regulates the maximum/minimum σ^i_{yr} after residual stress relaxation: for a constituent with a smaller yield stress than the mean, $\sigma^i_{yr} = \sigma_\mu$ is the maximum value it can reach; for a constituent with a larger yield stress than the mean, $\sigma^i_{yr} = \sigma_\mu$ is the minimum value it can reach.

Figure 7.2a shows an example of the modelled tensile curve assuming $\sigma_\mu = 2000\,\text{MPa}$, $\sigma^0_{sd} = 600\,\text{MPa}$, and $\alpha_r = 0.2$. When the strain is low, only the constituents with lower apparent yield stresses are plastically deformed and the relaxation process leads to an asymmetric yield stress spectrum (Figure 7.2b). As plasticity develops, constituents with higher apparent yield stresses start to relax their residual stresses and the spectrum starts to become symmetrical again (Figure 7.2c - d). Figure 7.2d shows that if the constituents are heavily influenced by the convolution of large intrinsic yield stress and negative residual stresses, they may not yield even at large strains. However, these constituents only account for a small fraction of the total number constituents and should not affect greatly the overall flow behaviour. This statement can be supported by the slope of the modelled tensile curve after point d where little strain hardening is observed. If the elastic constituents do contribute to the strain hardening of the bulk sample, the slope after point d should still be significantly large.

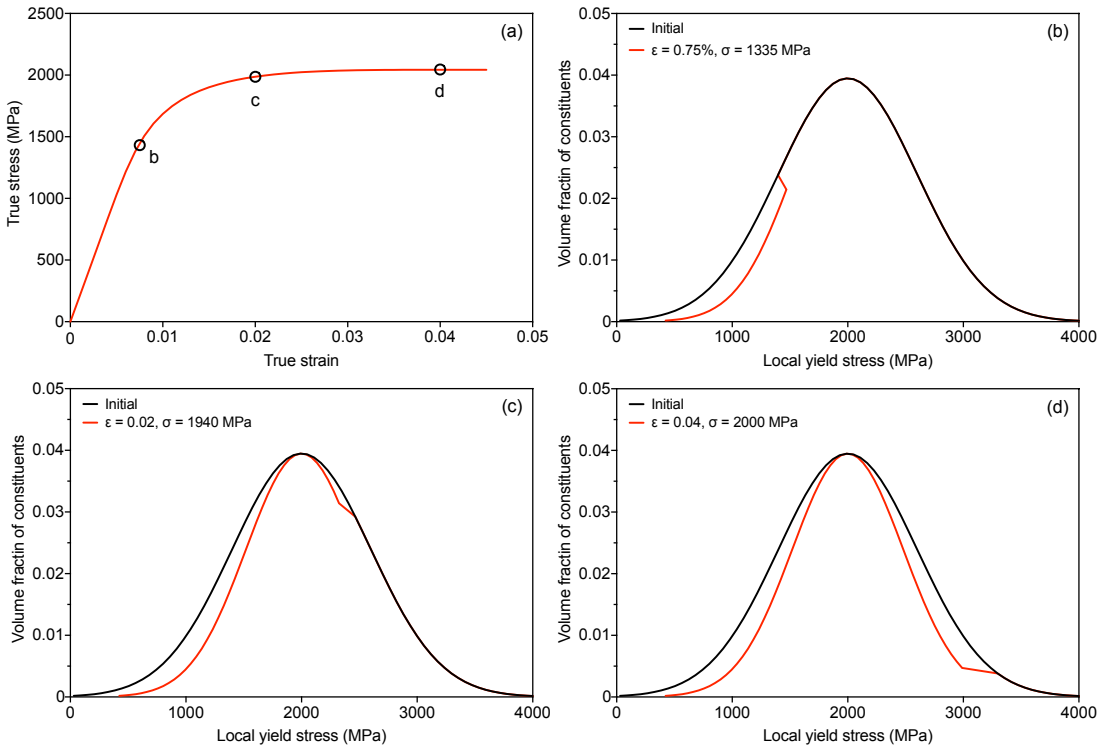

Figure 7.2: *Modelled macroscopic and microscopic behaviour of a sample with $\sigma_\mu = 2000\,MPa$, $\sigma_{sd} = 600\,MPa$, and $\alpha_r = 0.2$. (a) Modelled tensile behaviour, black circles represent the strain and stress levels for the other plots. (b) - (d) Evolution of the apparent yield stress spectrum as a function of strain. The black curves represent the initial spectrum and the red curves represent the spectrum after relaxation of residual stresses.*

7.2.2 Interpretation and determination of the relaxation parameter α_r

At this stage, σ_μ, σ_{sd}^0 and α_r are the three free variables needed to fully describe the flow behaviour of martensite. While σ_μ and σ_{sd}^0 can be inferred from the yield stress spectrum model, the key issue with the modified composite model is the physical origin of the relaxation parameter α_r. Figure 7.3 shows the effect of α_r on the relaxed spectrum (Figure 7.3a) and the tensile curve (Figure 7.3b) assuming the same set of σ_μ and σ_{sd} is used. If $\alpha_r = 0$, there is no plastic relaxation of residual stresses during the forward straining and the apparent yield stress spectrum is maintained (i.e. equivalent to the yield stress spectrum model). If $\alpha_r = 1$, the spectrum becomes a line located at σ_μ, suggesting that all constituents share the same yield stress after complete relaxation (i.e. equivalent to the residual stress spectrum model). Therefore, α_r can be regarded as a parameter that describes the convolution of the yield stress spectrum model and the residual stress spectrum model. The width of the yield stress spectrum after relaxation σ_{sd}^r can then be calculated as the fraction of the width of the initial apparent yield stress spectrum:

$$\sigma_{sd}^r = \sigma_{sd}^0 \times (1 - \alpha_r) \tag{7.2}$$

As α_r increases, a larger fraction of the initial apparent yield stress spectrum will be influenced by the existence of residual stresses.

However, the spread of the initial apparent yield stress spectrum needs to be optimised for a given α_r in order to describe a reasonable flow behaviour. It can be seen in Figure 7.3b that if a fixed set of σ_μ and σ_{sd} is used, α_r values larger than 0.4 lead to a peculiarly large Young's modulus at low strains and strain softening at large strains. This can be attributed to the large hardening/softening of the constituents as a result of residual stress relaxation. To eliminate this problem, σ_{sd}^0 needs to be adjusted according to the magnitude of α_r. Therefore, σ_{sd}^0 and α_r may be highly correlated and result in large uncertainties in the modelled results.

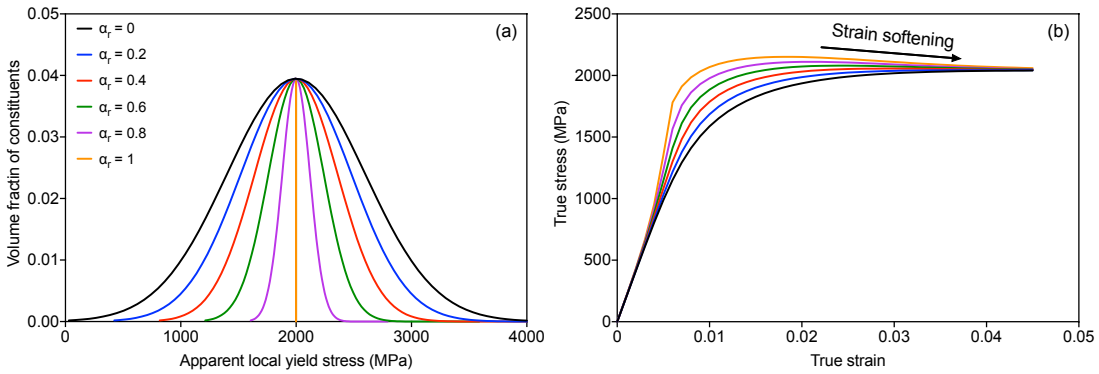

Figure 7.3: *Effect of α_r on the evolution of the final yield stress spectrum (a) and the modelled tensile curve (b). σ_μ is set to be 2000 MPa and σ_{sd} is set to be 600 MPa.*

Since α_r is a parameter that describes the influence of residual stresses, it should evolve as a function of tempering as residual stresses can be relaxed by thermal treatments. Moreover, if the diffraction peak narrowing as a function of strain is also a result of residual stress relaxation, the magnitude of this relaxation may be a suitable quantity to estimate α_r. Figure 7.4 shows the evolution of the experimentally measured relaxation parameter from the interrupted X-ray diffraction experiments. In this case, the experimentally measured relaxation parameter is expressed as the magnitude of the microstrain reduction normalised by the microstrain before deformation (i.e. $\frac{\langle\varepsilon_0\rangle_{Undeform}-\langle\varepsilon_0\rangle_{Deform}}{\langle\varepsilon_0\rangle_{Undeform}}$). This normalised parameter represents the fraction of microstrain that can be relaxed by forward plasticity, which is the physical basis for α_r. It can be seen that the experimentally measured relaxation parameter remains relatively constant in the as-quenched and 300 °C tempered conditions. When tempered at 400 °C, only the steels with Si and Al additions still show a considerable relaxation whereas the base steel shows no or negative relaxation. It should also be noted that the experimental relaxation parameters may underestimate the true relaxation behaviour since dislocation based mechanisms can contribute to diffraction peak broadening and reduce the measurable reduction in microstrain. This is especially true for the as-quenched samples since they have relatively large thermal hardening contributions (Figure 6.20).

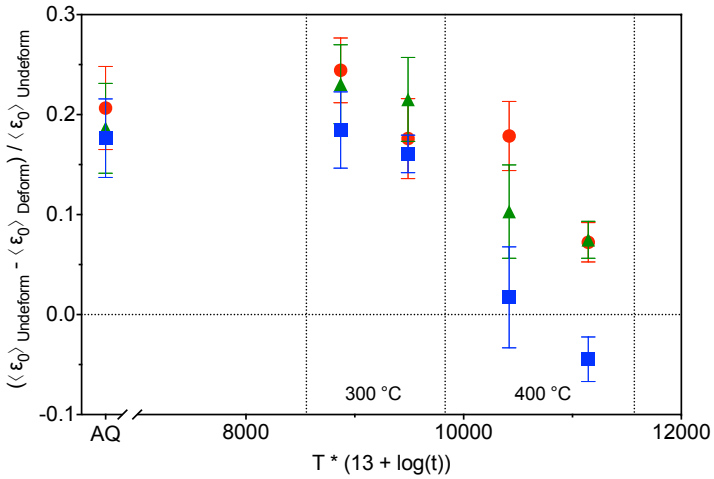

Figure 7.4: *Hollomon-Jaffe plot showing the evolution of the experimentally measured relaxation parameters from interrupted X-ray diffraction experiments. Error bars are calculated using the error propagation function considering the errors in microstrain measurements shown in Figure 6.17 and Figure 6.18. At each temperature, two tempering times are shown (i.e. 5 minutes and 1 hour).*

Considering the contribution of dislocation based mechanisms and the scatter in experimental measurements, the estimated α_r values used in the model are shown in the first three rows of Table 7.1. It can be seen that most as-quenched and 300 °C tempered samples share the same α_r value of 0.25 but the value for the base steel tempered at 300 °C is dropped to 0.2. This is to address the chemistry effect of Si and Al seen in the previous sections. In the case of 400 °C tempered samples, α_r for the base steel

is set to be zero since it shows limited or negative relaxation. For Si and Al steels tempered at 400 °C, the α_r values are obtained by slightly increasing the values in Figure 7.4. Although these estimated relaxation parameters may not reveal the true convolution mechanism of the two composite models, they should provide reasonable estimation for α_r. To further reduce the degrees of freedom in the model, the mean of the initial apparent yield stress spectrum is set to be the experimentally measured UTS (Table 7.1). This constraint is similar to the one used in the original work of Hutchinson *et al.* and restricts the magnitude of the residual stress relaxation [6]. As a consequence, the width of the initial apparent yield stress spectrum σ_{sd}^0 is the only parameter that needs to be optimised in order to describe the flow behaviour of the material.

Table 7.1: *Magnitude of α_r, σ_μ and σ_{sd}^0 used in the as-quenched and low temperature tempered conditions. α_r values are informed from diffraction peak narrowing experiments and σ_μ values are measured from the UTS of the tensile curve.*

Parameter	Steel grade	As-quenched	300 °C 5 min	300 °C 1 hr	400 °C 5 min	400 °C 1 hr
	Base steel	0.25	0.2	0.2	0	0
α_r	Si steel	0.25	0.25	0.25	0.2	0.1
	Al steel	0.25	0.25	0.25	0.1	0.1
	Base steel	1900	1521	1487	1365	1271
σ_μ (MPa)	Si steel	2003	1734	1726	1619	1459
	Al steel	1815	1552	1482	1416	1262
	Base steel	560	486	468	434	455
σ_{sd}^0 (MPa)	Si steel	591	541	537	502	516
	Al steel	563	499	466	462	452

7.2.3 Modelling results and discussions

Figure 7.5 - Figure 7.7 show the comparison between the experimental and modelled tension-compression curves for the as-quenched and low temperature tempered states. The modelled curves are simulated using σ_{sd}^{0} values that best reproduce the experimental curves. In the as-quenched and 300 °C tempered conditions, the modelled curves show good agreement with the experimental data and demonstrate better capabilities than the original composite models. The underestimation of the Bauschinger effect in the reverse direction for the as-quenched samples is eliminated since the relaxation of residual stresses is properly treated (see discussions in Section 5.3.1 and Figure 5.5). Discrepancies between experimental and modelled curves start to appear when samples are tempered at 400 °C as a result of accelerated microstructural homogenisation. This can be demonstrated by the underestimation around the elastic-plastic transitions during forward loading and the overestimation in the reverse direction, which is especially obvious in the samples tempered at 400 °C for 1 hour (Figure 7.7 a2 - c2). It indicates that the modified composite model starts to become less capable in describing the flow behaviour of high temperature tempered samples.

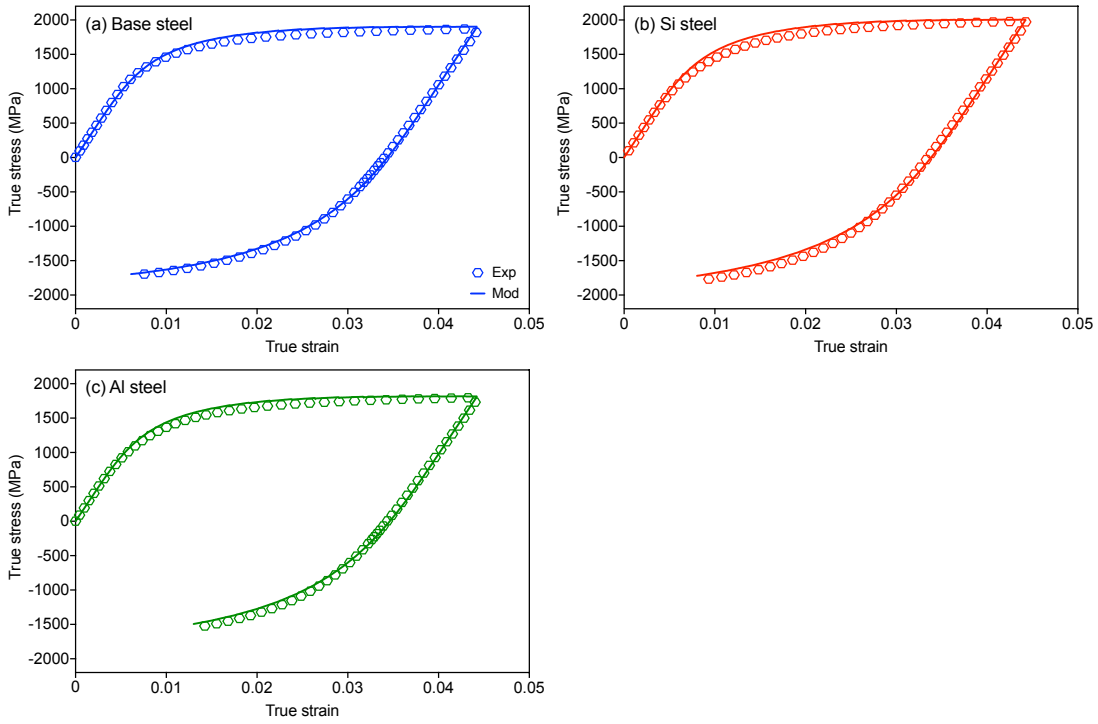

Figure 7.5: *Experimental and modelled tension-compression curves for the as-quenched samples. (a) the base steel, (b) the Si steel and (c) the Al steel.*

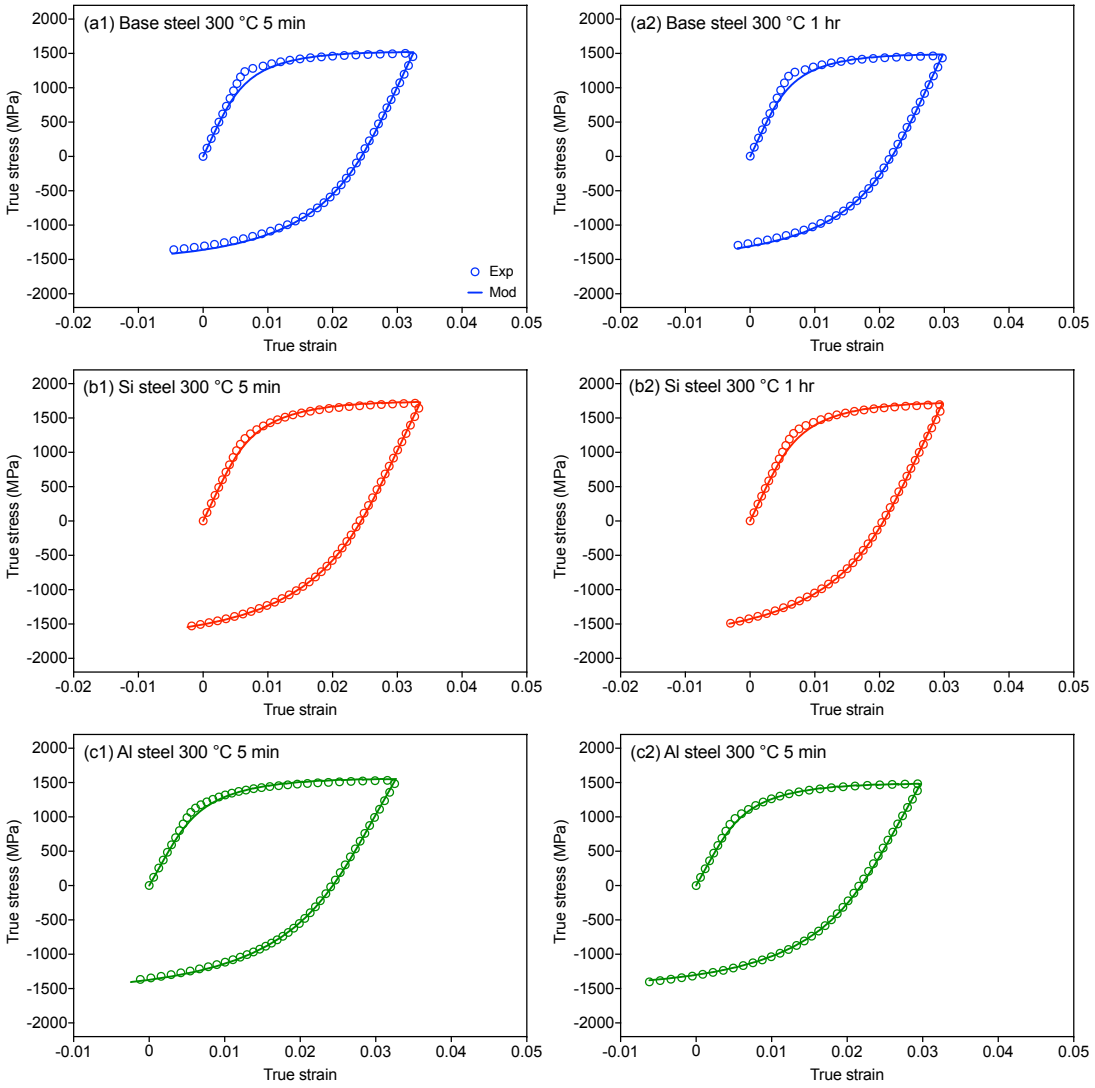

Figure 7.6: *Experimental and modelled tension-compression curves for 300 °C tempered samples. (a1) - (c1) samples tempered for 5 minutes. (a2) - (c2) samples tempered for 1 hour.*

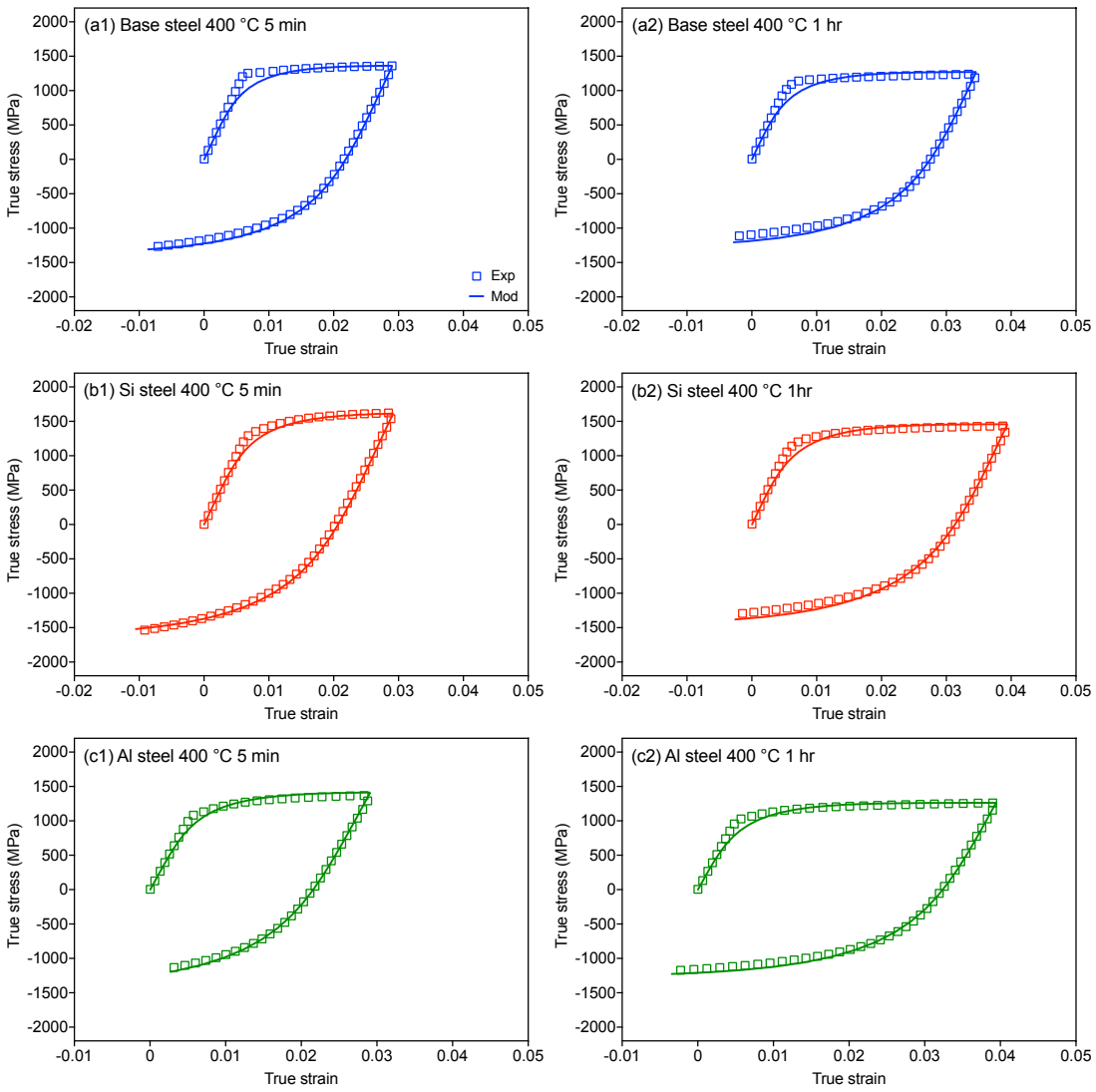

Figure 7.7: *Experimental and modelled tension-compression curves for 400 °C tempered samples. (a1) - (c1) samples tempered for 5 minutes. (a2) - (c2) samples tempered for 1 hour.*

Nanoindentation results shown in Section 6.4.1 and Figure 6.16b suggest that the variation in the intrinsic yield stresses should scale with the average strength of the material. To check if the modelling parameters follow this finding, the width of the spectrum after relaxation σ_{sd}^{r} is plotted against the experimentally measured UTS (Figure 7.8). Unlike the initial width of the spectrum σ_{sd}^{0}, σ_{sd}^{r} represents a spectrum that is less influenced by residual stresses. As shown in Figure 5.9, the size of the nanoindent is larger than the typical width of fine lath/blocks in as-quenched martensite so the nanoindentation experiment gives an average mechanical response of the region underneath the hardness impression. Moreover, the plasticity associated with the Berkovich tip is about 8% [142], which means the measurement of nanohardness may also include the relaxation of residual stresses. Therefore, it is more suitable to use the correlation between σ_{sd}^{r} and UTS to compare with the relationship found in the nanohardness measurements (Figure 6.16b). While most data points can be described by a master line regardless of alloy compositions, three points are located well away from the master line. These data points come from samples that are tempered at 400 °C for 1 hour. It suggests that although we can obtain reasonably good agreement with experimental data for this tempering condition, the modelling parameters may not reflect the true variation in the intrinsic yield stress and could be caused by fitting uncertainties. Again, this implies that the modified composite model may not be suitable to explain the strain hardening of high temperature tempered samples.

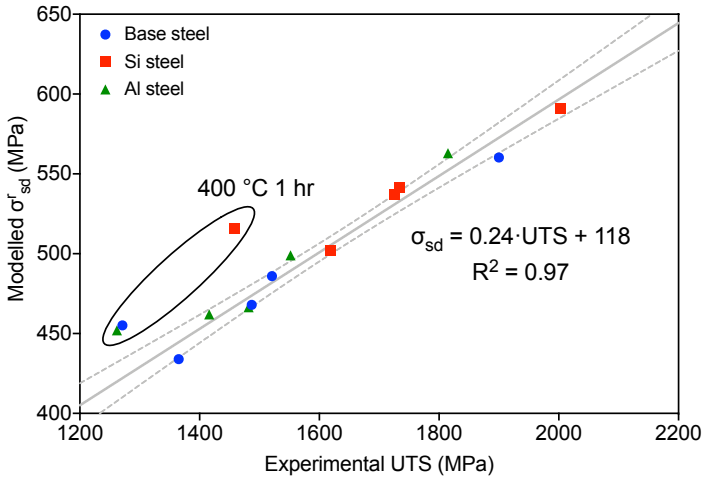

Figure 7.8: *Correlation between the modelled σ_{sd}^{r} and the experimentally measured UTS. The solid line is fitted with a linear regression and the dashed curves represent the 95% confidence band of the fit.*

Besides the uncertainties at high tempering temperatures, the existence of a master line that is chemistry insensitive (Figure 7.8) suggests that it is possible to use the master line to predict the flow behaviour of as-quenched and low temperature tempered martensite. Figure 7.9 shows the performance of the model in predicting the strain reversal behaviours of two as-quenched steels taken from the literature. In both cases, the mean of the spectrum σ_{μ} is determined as the stress at the strain reversal (assuming close to UTS) since no monotonic results are available. As both samples were tested to relatively large

strains, the stress at the reversal should be close to the UTS of the material. σ_{sd}^{r} values are calculated using the equation shown in Figure 7.8. Since the steels to be predicted have similar carbon contents compared with the steels used in the current study, the same α_r of 0.25 is used and the initial width of the spectrum is calculated as $\sigma_{sd}^{0} = \sigma_{sd}/(1-\alpha_r)$ (i.e. the reciprocal of Eq. 7.2). For steels with higher carbon contents, a larger α_r may be required since the developed residual stress could be larger as suggested by Hutchinson and co-workers [6, 76]. It can be seen that the predicted curves have very good agreement with the experimental results without additional optimisation of the modelling parameters. It indicates that the modified composite model may still be proposed here as a good candidate in predicting the flow behaviour of as-quenched and low temperature tempered martensite. The fact that the prediction for the shear reversal test is reasonably good suggests that the strength differential effect does not affect the validity of the current model.

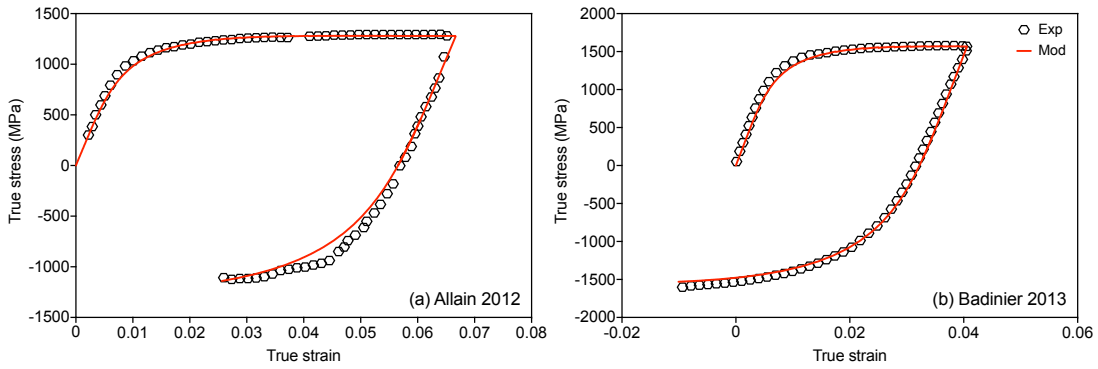

Figure 7.9: *Experimental and modelled strain reversal behaviours of two steels found in the literature. (a) Fe-0.1C-2.3Mn-0.3Si-0.8Cr (wt.%) as-quenched steel modelled with* $\sigma_\mu = 1280\,MPa$, $\sigma_{sd}^{0} = 566\,MPa$, *and* $\alpha_r = 0.25$. *Experimental results are from the shear reversal test. The Young's modulus is adjusted to 140 GPa to better describe the elastic behaviour. More explanation on this can be found in the work of Allain et al. [5]. (b) Fe-0.24C (wt.%) as-quenched steel modelled with* $\sigma_\mu = 1568\,MPa$, $\sigma_{sd}^{0} = 659\,MPa$, *and* $\alpha_r = 0.25$. *Experimental results are from the uniaxial tensions-compression test [74].*

7.2.4 Limitations of the modified composite model

Although the modified composite model is able to describe well the experimental data, it has some limitations that need to be improved in future development. The first issue is related to the spread of the spectrum. After the amendment of the relaxation parameter, the magnitude of σ_{sd}^{r} is ~75% of the σ_{sd}^{0} in the case of as-quenched martensite. This value is still roughly three times the standard deviation measured by nanoindentation. If we assume that the intrinsic variation in local yield stresses is indeed very large then discrepancy between the modelled results and experimental measurements may be attributed to the uncertainties in quantifying the local yield strength using nanoindentation. As discussed previously (Section 5.3.1), the nanoindentation experiments performed in this experiment can only give an average response of the material under the hardness impression and the interaction

volume of the hardness indents is larger than the dimension of fine laths/blocks. Therefore, a lot of information regarding the true variation in local yield stress may be shielded by the large size of the indent. A more systematic study of the effect of indentation size on the spread of the local hardness should be conducted to rationalise this hypothesis. To reduce the uncertainties associated with indentation size effect [150] and substructure boundaries, samples with large prior austenite grain sizes may be explored to allow large indents to be placed away from grain boundaries.

The second issue is the simplicity of the implicit convolution of the yield stress spectrum and the residual stress spectrum. In the modified composite model, the initialisation scheme assumes that the apparent initial yield stress spectrum is affected by both yield stress and residual stress spectra and the convolution is loosely defined by the relaxation parameter α_r. According to the definition of α_r and the relaxation function Eq. 7.1, if a constituent has a smaller initial apparent yield stress than the mean, the maximum intrinsic yield stress it can reach after residual stress relaxation is the mean of the spectrum σ_μ (Section 7.2.1 and Figure 7.3a). In reality, it is also possible that a constituent has an intrinsic yield stress larger than σ_μ to be influenced by a large positive residual stress which results in it having a smaller initial apparent yield stress than σ_μ. This is also true for constituents with small yield stresses but large negative residual stresses that results in constituents to be found on the right-hand side of the mean. These scenarios are not considered by the current model and requires further development. One approach to solve this problem is to construct a large-scale CPFEM model that considers both the variation in yield stresses and residual stresses explicitly in its initialisation step. The initial stress/strain states of the model can be calibrated by comparing the simulated flow behaviour and the diffraction peak narrowing behaviour using in-situ X-ray diffraction experiments shown in the work of Hutchinson *et al.* [70].

7.3 A combined isotropic and kinematic hardening model for high temperature tempered martensite

As discussed in Chapter 2 and Chapter 6, the flow behaviour of high temperature tempered martensite is similar to that observed in ferrite-cementite steels and the material is predominantly strengthened by dislocation based strengthening mechanisms. As a result, we attempt to model the strain hardening behaviour of high temperature tempered martensite with a combined isotropic and kinematic hardening model. While the isotropic hardening comes from dislocation storage and Taylor hardening (Eq. 2.8), the kinematic hardening is attributed to the presence of cementite precipitates (Eq. 2.17, Section 2.5.3). Although the fine grain size in tempered martensite can also lead to kinematic hardening due to dislocation pile-ups at grain boundaries, quantification of modelling parameters used in this model

require more theoretical and experimental justifications. Moreover, the spacing between precipitates is generally smaller than the spacing of lath/blocks boundaries, which means the dislocations are more likely to first interact with precipitates and form dislocation loops. Therefore, one of the objectives of the present model is to demonstrate the capability of the combined hardening model in the case of tempered martensite which may be further improved by incorporating more complexities.

7.3.1 Kinematic hardening

Let us first revisit the description of the kinematic hardening from secondary particles which is first proposed by Brown and Stobbs [127] and further developed by Proudhon *et al.* and da Costa Teixera *et al.* [121, 132]. In cases where the particles are shear-resistant and able to support dislocation loops, the generated back stress may be described by:

$$\langle\sigma\rangle_{ppt} = M^2 g D \mu V_f \varepsilon_p^{*max} \left[1 - \exp\left(-\frac{\varepsilon_p}{\varepsilon_p^{*max}}\right)\right], \quad \varepsilon_p^{*max} = \frac{n_{ppt}^* b}{2Mr} \tag{7.3}$$

where M is the Taylor factor, g is the accomodation factor, D is the modulus correction factor, μ is the shear modulus of the matrix, V_f is the volume fraction of secondary particles, ε_p^* is the unrelaxed plastic strain, n_{ppt}^* is the maximum number of loops that can be supported by one particle, b is the Burgers vector and r is the particle radius. In the case of spherical particles under multi-slip conditions [127]:

$$g = \frac{7 - 5\nu}{20(1-\nu)} \tag{7.4}$$

where ν is the Poisson's ratio (~0.3 in steel). The modulus correction factor can be also calculated using the shear moduli of cementite (μ_θ) and ferrite (μ) [127]:

$$D = \frac{\mu_\theta}{\mu_\theta - g\,(\mu_\theta - \mu)} \tag{7.5}$$

μ_θ is set to be 74 GPa according to first principle calculations by Jiang *et al.* [158] and the experimental work by Laszlo and Nolle [159]. μ is calculated as

$$\mu = \frac{E}{2\,(1+\nu)} \tag{7.6}$$

where the Young's modulus $E = 205$ GPa is obtained from the flow behaviour.

For high temperature tempered martensite, it can be assumed that the equilibrium volume fraction is achieved soon after the tempering starts [2, 95]. As a result, the total volume fraction is set to be 0.0375 for all steels since they share similar carbon contents and the addition of Si and Al only affects slightly the equilibrium volume fraction. Therefore, n^*_{ppt} is the only parameter that needs to be quantified in Eq. 7.3. Following the work of Laird and co-workers [133, 160] and da Costa Teixeira *et al.* [121], we used TEM to estimate the spacing of Orowan loops on cementite particles (i.e. the $2r/n^*_{ppt}$ ratio in Eq. 7.3). Figure 7.10 shows the TEM micrographs of a deformed Base steel sample under the two-beam condition. Cementite particles are highlighted with white arrows in Figure 7.10a and alternating bright and dark contrasts can be observed on the particles (Figure 7.10b). These patterns may be identified as closely packed dislocations since they have ragged edges compared to the sharp interfaces found in the case of Moiré fringes. Figure 7.10b shows an enlarged area of Figure 7.10a and the spacing between bright and dark contrasts is ~3 - 4 nm.

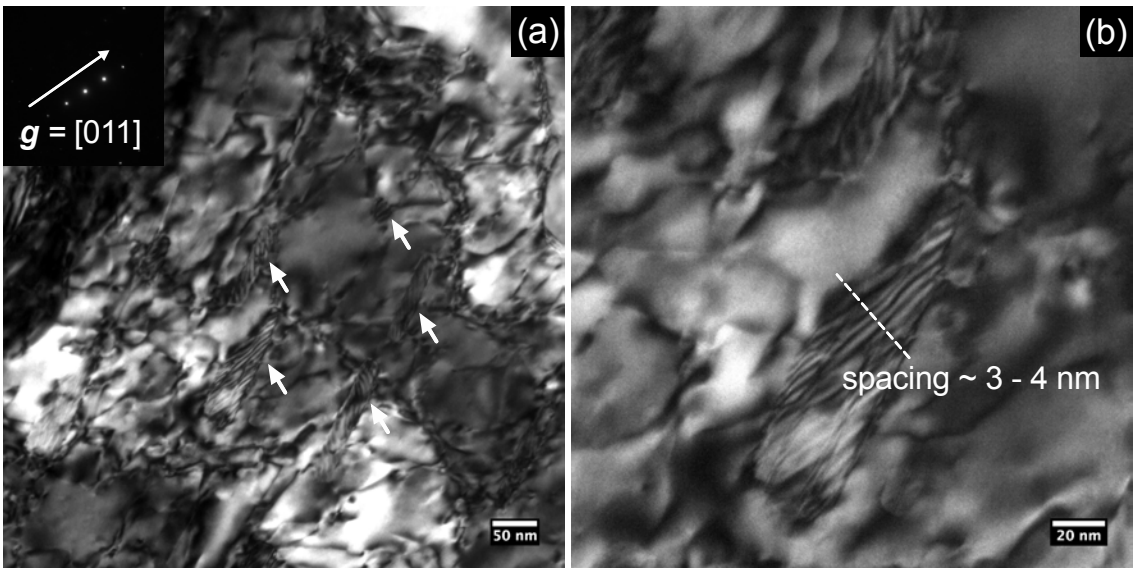

Figure 7.10: *TEM micrographs of Orowan loops deposited on cementite particles. The sample was deformed to ~7% plastic strain after being tempered at 600 °C for 1 hour. (a) Large area micrograph showing multiple particles (highlighted by white arrows) with Orowan loops. The operating* $\boldsymbol{g}$ *vector is shown in the inset. (b) An enlarged area of (a) showing a single particle and how the spacing is measured. The electron beam direction is close to the* $\left[1\bar{2}2\right]$ *zone axis.*

To ensure that the contrasts are indeed from Orowan loops, TEM was also performed on tempered samples before straining. It can be seen that the particles do not show the same contrast as the deformed samples (Figure 7.11a). While some alternating bright and dark contrasts can be found at the edge of the particles (Figure 7.11b), they only appear at the edge of particles and the interface between the

bright and dark regions are much sharper compared to the ones observed in Figure 7.10. Therefore, these contrasts may be associated with surface defects or Moiré fringes at the particle-matrix interface. The contrasts found in Figure 7.10 should be indeed attributed to the existence of Orowan loops as suggested by Laird and co-workers [133, 160].

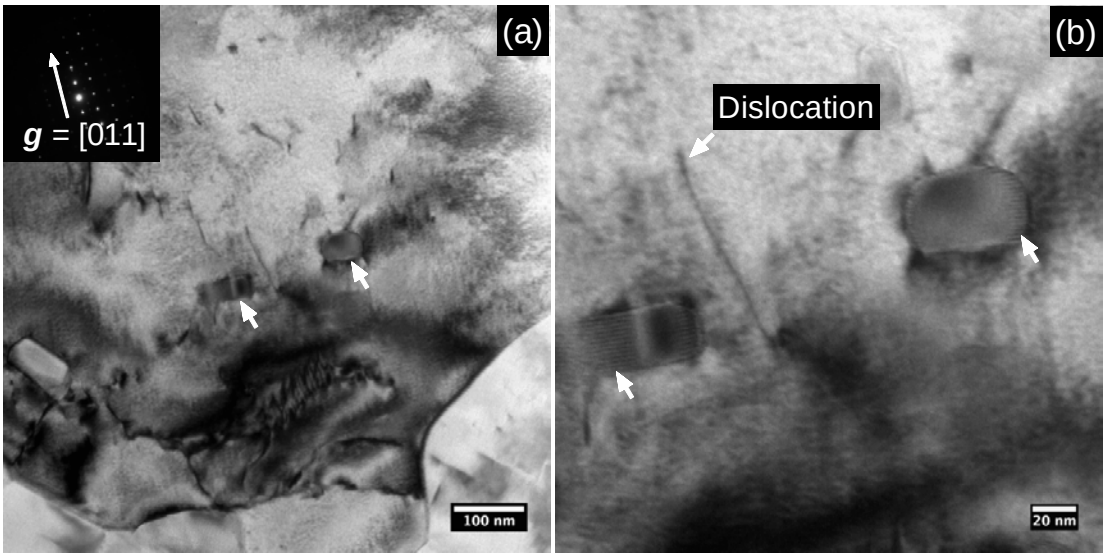

Figure 7.11: *TEM micrographs showing cementite particles in the ferrite matrix. The sample was tempered at 600 °C for 1 hour and cut from the non-deformed head of the tension-compression sample. (a) Large area micrograph showing multiple particles (highlighted by white arrows). The operating* $\boldsymbol{g}$ *vector is shown in the inset. (b) An enlarged area of (a) showing two particles with Moiré fringes at the particle-matrix interface. The electron beam direction is close to the* [100] *zone axis.*

The same characterisation procedures were also performed on samples with Si and Al additions after deforming to different plastic strains (Figure 7.12). The loop spacing is relatively constant at plastic strains greater than 2%, which agrees with the model by Brown and Stobbs that the the number of dislocation loops on the precipitates reaches a maximum value n^*_{ppt} at large plastic strains. This leads to a saturation value in the evolution of back stress which is also consistent with the experimental results in Figure 6.23 that saturate at plastic strains of ~2%. Due to the presence of yield point elongations in high temperature tempered samples, TEM experiments were not performed on samples interrupted inside the Lüders band. However, we should expect that the loop spacing decreases at low plastic strains as predicted by the back stress evolution. This has been demonstrated in the Al-Cu system by da Costa Teixeira *et al.* [121]. In the current model, a minimum loop spacing of 3 nm is used, which is around the lower limit of the experimentally measured values. It is also assumed that the $2r/n^*_{ppt}$ ratio is independent of the particle radius so the same spacing is used for all tempering conditions.

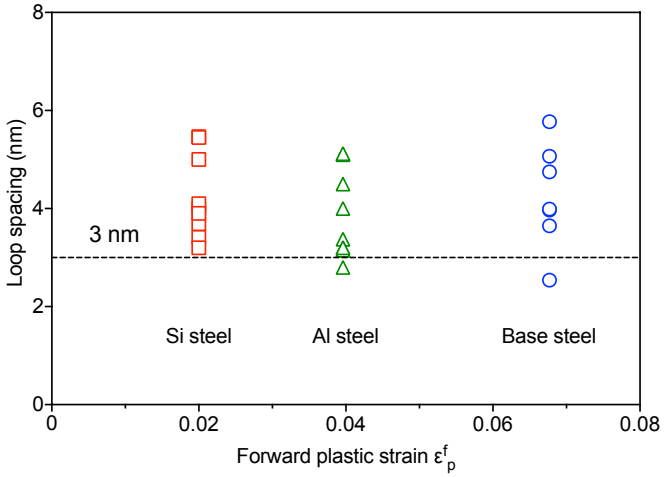

Figure 7.12: *Evolution of the spacing of Orowan loops during plastic deformation. All samples were tempered at 600 °C for 1 hour. The dashed line represents the* $2r/n^*_{ppt}$ *ratio used in the model.*

Another consideration with the cementite particles in high temperature tempered martensite is their heterogeneous distribution in tempered martensite. Figure 7.13 shows the SEM micrographs of the Si steel after tempering at 600 °C for different times. It can be seen that an increasing number of particles can be found on the martensite grain boundaries instead of inside the martensite laths as the tempering time increases. The precipitates on the grain boundaries should be less effective in storing dislocation loops compared with the precipitates within the grain due to the large defect density at grain boundaries. In the current model, two physical parameters are used to estimate the fraction of precipitates within grains (V_f^g) and the loop spacing for precipitates on the grain boundaries (expressed as $\eta \cdot 2r/n^*_{ppt}$). While the value of V_f^g should decrease as a function of tempering, the enhancement factor η is kept constant ($\eta = 2.5$) for all tempering conditions since the potency of grain boundary precipitates in storing Orowan loops should not be affected by thermal treatments. This modification to the Brown-Stobbs model also allows the particles with large loops spacing to be considered and reduce the uncertainties in the estimation of n^*_{ppt}.

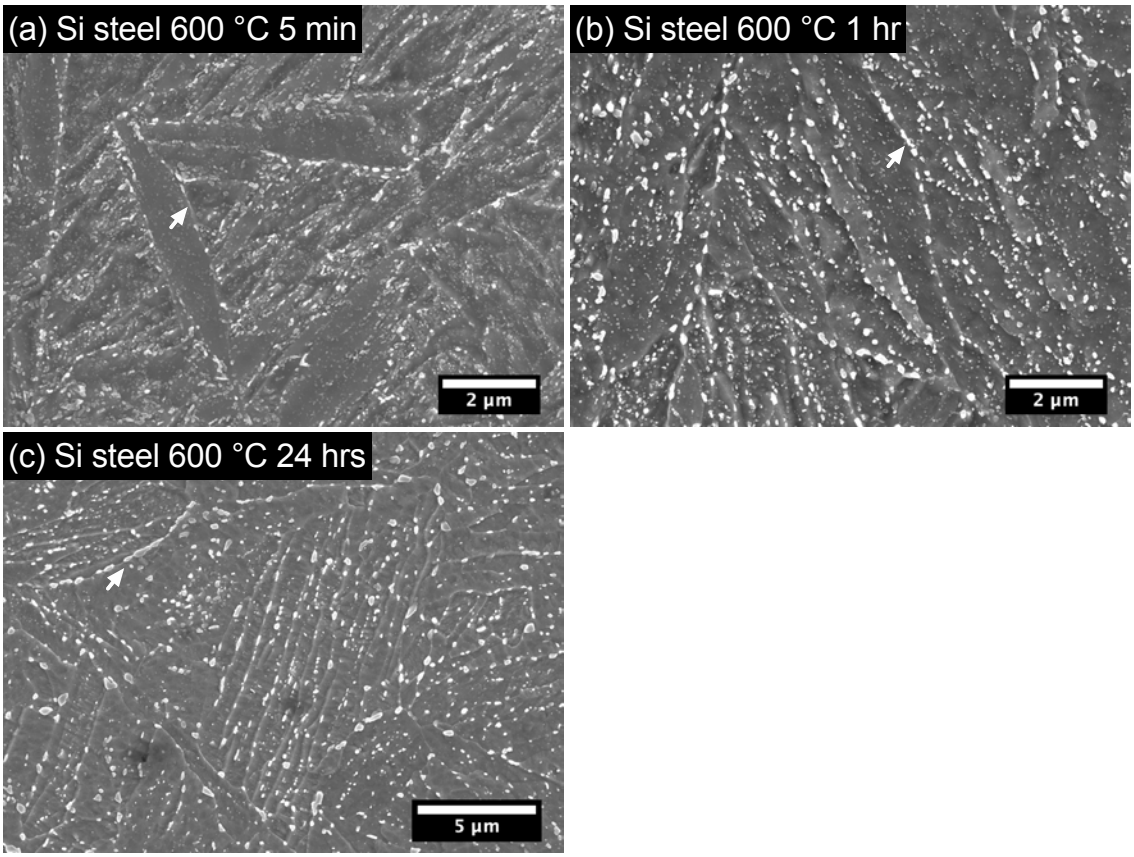

Figure 7.13: *SEM micrographs showing the cementite particles within grains and on grain boundaries. All samples were from the Si steel and were tempered at 600 °C for 5 minutes (a), 1 hour (b) and 24 hours (c). Typical grain boundaries are highlighted with arrows. Etched with Picral.*

7.3.2 Isotropic hardening

In the current model, we use the Kocks-Mecking model and the derived Voce law to describe the isotropic hardening of the material [34]:

$$\sigma_{iso} = \frac{\theta_0}{\beta_0}\left[1 - \exp\left(\beta_0 \varepsilon_p\right)\right] \tag{7.7}$$

where $\theta_0 = \alpha M^2 \mu b k_1/2$ and $\beta_0 = k_2 M/2$. k_1 is a constant that considers the self-trapping efficiency of dislocations and k_2 accounts for the annihilation of dislocations due to dynamic recovery. The values of k_1 and k_2 are often treated as fitting parameters in the literature. In this case, we attempt to fix the k_1 value for all tempering conditions and only allow k_2 to be changed. According to Kocks and Mecking the maximum θ_0 value can be estimated by $E/50$ [34], which results in a maximum k_1 value of $\sim 1.5 \times 10^8$ MPa. A varying k_2 would suggest that the annihilation rate of dislocation changes as a function of tempering. This could be attributed to the change in the grain boundary spacing during high temperature tempering since grain boundaries are found to be effective sinks for dislocations [161, 162].

7.3.3 Implementation of the model

The combined isotropic and kinematic hardening model is implemented in a 3-D continuum mechanics framework considering uniaxial loading along one dimension (i.e. the same modelling framework developed in Chapter 5). Most of the incremental straining steps are the same as those discussed in Section 5.2.3. However, this model differs from the composite model in the initialisation schemes and the hardening laws. In this case, the material is considered to be homogeneous and only one constituent is modelled. In the initialisation scheme, the initial strain and stress tensors are set to be zero. During straining, the yield function of the material is written as:

$$f = J_2\left(\boldsymbol{\sigma} - \langle\boldsymbol{\sigma}\rangle_{ppt}\right) - \sigma_{iso} - \sigma_{y0} \leq 0 \tag{7.8}$$

where J_2 is the second invariant of the stress tensor $\boldsymbol{\sigma}$, $\langle\boldsymbol{\sigma}\rangle_{ppt}$ is the deviatoric tensor that represents the kinematic hardening, σ_{iso} and σ_y are the scalars that describe the isotropic hardening and the yield strength. Since precipitates within grains and precipitates on grain boundaries contribute differently to kinematic hardening, $\langle\boldsymbol{\sigma}\rangle_{ppt}$ can be further written as:

$$\langle\boldsymbol{\sigma}\rangle_{ppt} = \langle\boldsymbol{\sigma}\rangle^{g}_{ppt} + \langle\boldsymbol{\sigma}\rangle^{gb}_{ppt} \tag{7.9}$$

where $\langle\boldsymbol{\sigma}\rangle^{g}_{ppt}$ represents precipitates within grains and $\langle\boldsymbol{\sigma}\rangle^{gb}_{ppt}$ represents precipitate on grain boundaries. In each case, the evolution of the back stress can be expressed in the tensor form by combining the Brown-Stobbs model and the Armstrong-Frederick type kinematic hardening law [124]:

$$\dot{\langle\boldsymbol{\sigma}\rangle}^{g}_{ppt} = \frac{2}{3}C^{g}_{\xi}\dot{\boldsymbol{\varepsilon}}_{\boldsymbol{p}} - \xi^{g}\langle\boldsymbol{\sigma}\rangle^{g}_{ppt}\dot{p} \tag{7.10}$$

$$\dot{\langle\boldsymbol{\sigma}\rangle}^{gb}_{ppt} = \frac{2}{3}C^{gb}_{\xi}\dot{\boldsymbol{\varepsilon}}_{\boldsymbol{p}} - \xi^{gb}\langle\boldsymbol{\sigma}\rangle^{gb}_{ppt}\dot{p} \tag{7.11}$$

where $\dot{\boldsymbol{\varepsilon}}_{\boldsymbol{p}}$ and $\dot{p}$ are the strain-rate for the plastic strain and the accumulative plastic strain respectively. $C^{g}_{\xi} = M^2 g D \mu V^{g}_{f}$ and $C^{gb}_{\xi} = M^2 g D \mu \left(V^{tot}_{f} - V^{g}_{f}\right)$ are the hardening parameters and $\xi^{g} = \frac{2Mr}{n^{*}_{ppt} b}$ and $\xi^{gb} = \eta \cdot \frac{2Mr}{n^{*}_{ppt} b}$ are the recovery parameters in the kinematic hardening equation. In the current model, we consider the material is strain-rate independent and the magnitudes of $\dot{\boldsymbol{\varepsilon}}_{\boldsymbol{p}}$ and $\dot{p}$ are estimated by the incremental $\Delta\boldsymbol{\varepsilon}_{\boldsymbol{p}}$ and Δp, both of which can be determined by the macroscopic strain increment $\Delta\boldsymbol{\varepsilon}$ using appropriate integration schemes.

Due to the presence of yield point elongations in the high temperature tempered samples, the yield strength is estimated by assuming the material follows the Hollomon hardening law ($\sigma = K\varepsilon^n$) and finding the interception between $\sigma = E\varepsilon$ and $\sigma = K\varepsilon^n$, which is the same method used in the work of Chang and Asaro [118]:

$$\sigma_{y0} = \left(\frac{K}{E^n}\right)^{1/(1-n)} \tag{7.12}$$

At each time step, a strain increment $\Delta\boldsymbol{\varepsilon}$ is applied along the z-direction of the material and the stress increment $\Delta\boldsymbol{\sigma}$ can be calculated using the return-mapping algorithm proposed by Sawyer *et al.* which considers the combined isotropic and kinematic hardening [163]. Modelling parameters that are set to be constant in all tempering conditions are summarised in Table 7.2.

Table 7.2: *Fixed parameters used in the combined isotropic and kinematic hardening model.*

Parameter	Description	Value	Comment/Reference
E	Young's modulus of ferrite	205 GPa	Measured
ν	Poisson's ratio	0.3	Estimated
μ	Shear modulus of ferrite	79 GPa	Calculated
μ_θ	Shear modulus of θ	74 GPa	[158, 159]
g	Accommodation factor	0.39	Calculated
D	Modulus correction factor	0.97	Calculated
M	Taylor factor	2.75	[164]
V_f^{tot}	Total volume fraction of θ	0.0375	Calculated, Thermo-Calc
r	Precipitate radius	20 nm (5 min) 25 nm (1 hr) 40 nm (24 hrs)	Measured
$2r/n^*_{ppt}$	Orowan loop spacing	3 nm	Measured
η	Enhancement factor for grain boundary precipitates	2.5	Estimated
α	Dislocation-dislocation junction strength	0.38	[165]
b	Burgers vector	0.248 nm	
k_1	Coefficient of dislocation self-trapping efficiency	1.5×10^8 MPa	Estimated

7.3.4 Modelling results and discussion

Figure 7.14 shows the modelled and experimental results for all steels tempered at 600 °C for 5 minutes, 1 hour and 24 hours. Figure 7.14 a1 - c1 shows the comparison of monotonic tensile curves and Figure 7.14 a2 - c2 shows the comparison of tension-compression curves plotted as a function of cumulative strain. The monotonic curves are shown here since the 24-hour tempered samples show larger uniform elongations than the maximum forward strain used in the tension-compression test. Table 7.3 shows the values of optimised parameters (V_f^g and k_2) used in the model.

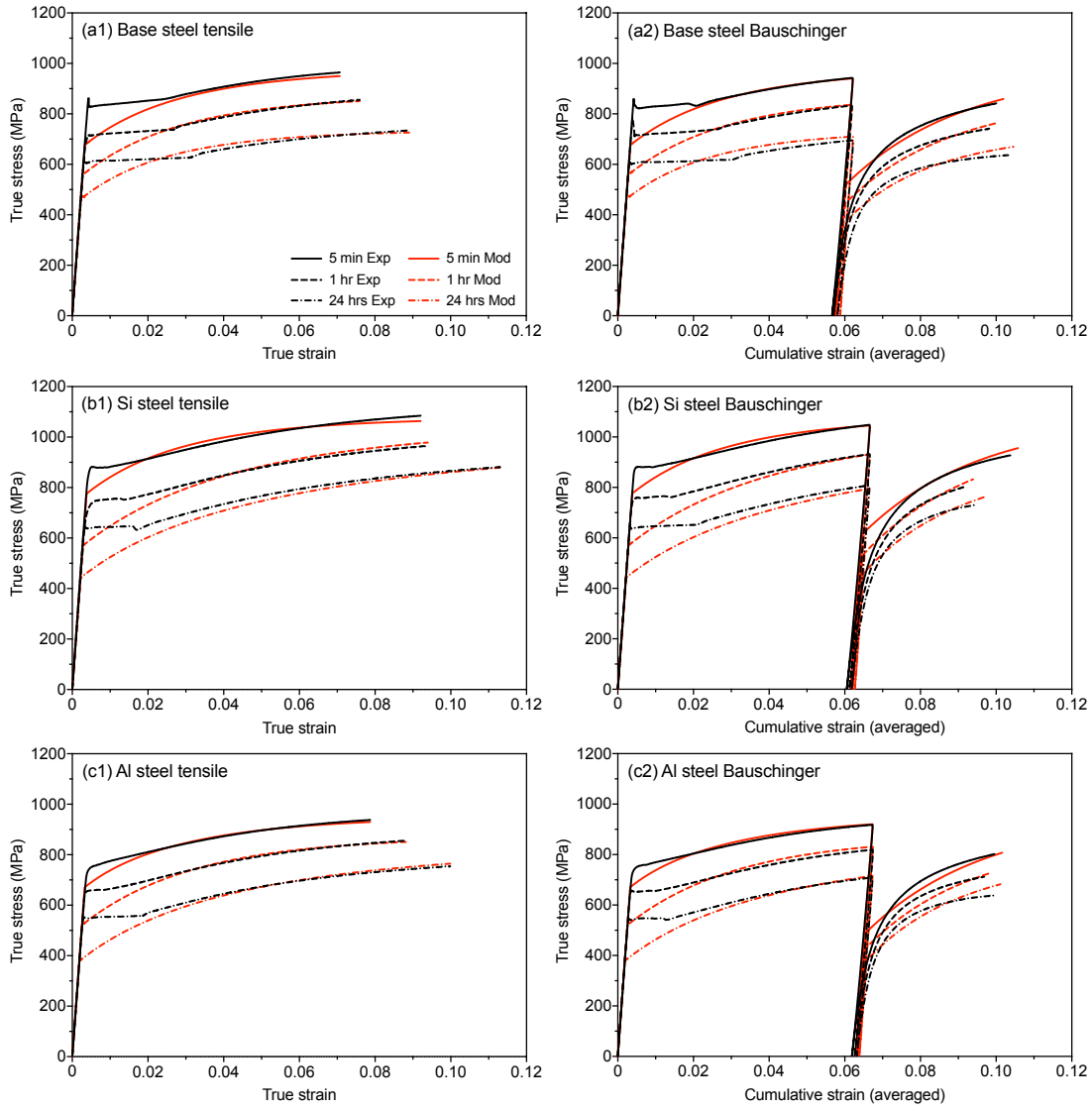

Figure 7.14: *Experimental and modelled tensile (a1 - c1) and tension-compression (a2 - c2) curves for the 600 °C degree tempered samples.*

Table 7.3: *V_f^g and k_2 values used in the modelled curves.*

Parameter	Steel grade	600 °C 5 min	600 °C 1 hr	600 °C 24 hrs
V_f^g	Base steel	0.035	0.03	0.02
	Si steel	0.035	0.03	0.02
	Al steel	0.035	0.03	0.02
k_2	Base steel	57	35	35
	Si steel	56	12	9
	Al steel	94	25	12

It can be seen that the existence of yield point elongations leads to a much lower apparent yield stresses compared to the conventional 0.2% proof stresses (i.e. the sharp yield points), which may lead to uncertainties in the description of the yielding behaviour of the material. However, these estimated yield stress values and the proposed model allows both the monotonic and the tension-compression behaviour of the samples to be modelled simultaneously and show reasonably good agreement with the experimental results. Generally, the modelled strain reversal behaviour shows worse agreement compared with the monotonic behaviour. In all cases, the model demonstrates that the reverse curves can strengthen at the same rate as the forward curves but the experimental results show much smaller hardening rate and permanent softening at large reverse strains. This is especially obvious in the 24-hour tempered conditions. It can be attributed to the simplicity of the non-linear hardening law and the lack of permanent softening descriptions in the model. The model can be improved by incorporating permanent softening theories such as the Yoshida-Uemori law in continuum mechanics [166, 167] and the Rauch-Gracio-Barlat-Vincze (RGBV) law in the materials science community [157, 168]. However, both models have fitting parameters that are difficult to quantify experimentally which can only introduce more uncertainties to the current model.

To best describe the experimental results, the volume fraction of the precipitates within grains for all steels is set to be 0.035, 0.03 and 0.02 for the 5-minute, 1-hour, 24-hour tempered conditions respectively. Qualitatively, it agrees with the findings the in the SEM investigation (Figure 7.13) where the precipitates are disappearing inside the martensite grains. One way to justify the values used here is to use metallography method to estimate the volume fraction of precipitates on grain boundaries V_f^{gb} and back calculated the value of V_f^g. This reduces some uncertainties in highlighting small precipitates within grains. Figure 7.15a shows a low magnification SEM image in a base steel sample tempered at 600 °C for 24 hours etched with Nital which highlights both ferrite grain boundaries and cementite particles. Particles on the grain boundaries can be highlighted and analysed to estimate the average particles size r_{gb} and the areal number density N_s^{gb} (Figure 7.15b). The volumetric number density

and volume fraction can be estimated as $N_v^{gb} = 2r_{gb}$ and $V_f^{gb} = N_v^{gb} \cdot \frac{4}{3}\pi r_{gb}^3$ [169]. Several field views in samples tempered at 600 °C for 24 hours were analysed and the estimated volume fraction at grain boundaries is ~0.022, which results in a V_f^g of 0.0155. Considering the uncertainties in estimating volume fraction using 2-D images, this is in relatively good agreement with the value used in the model. In the case of 5-minute and 1-hour tempered samples, the number density of precipitates is relatively large and precipitates often show great overlapping, which makes the quantification of V_f^{gb} difficult. Further metallography methods need to be explored to justify the values used in the model.

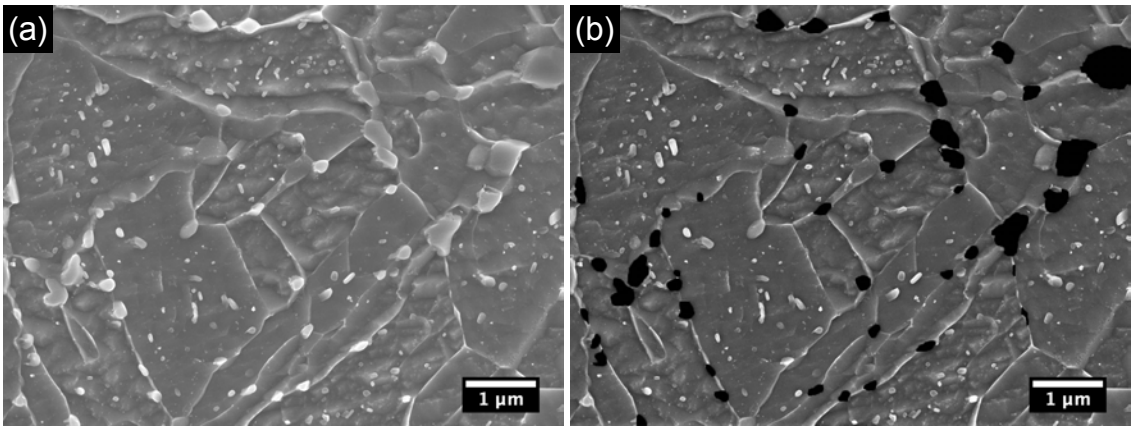

Figure 7.15: *Estimation of volume fraction precipitates on grain boundaries. (a) Original SEM image from a base steel sample tempered at 600 °C for 24 hours. (b) Particles on grain boundaries highlighted for image analysis in ImageJ. Etched with Nital.*

Another way to quantitatively assess the validity of the estimation is to compare the modelled and experimentally measured back stress (Figure 7.16). In this case, a reverse strain offset of 0.6% is chosen to lower the experimental measurements to the same level of the modelled ones. Although the selection of this reverse strain offset is still arbitrary, both the evolution and the magnitude of the offset back stress can be well reproduced by the kinematic hardening model using the estimated volume fractions for all tempering times.

Finally, we come back to the only parameter that needs to be optimised for each tempering condition, k_2 (Table 7.3). It can be seen that the values start very high in the 5-minute tempered states and decrease as a function of tempering time. Typical values of k_2 in coarse grain ferritic steels are around 7 - 22 [170], which correspond well with the values in 1-hour and 24-hours tempered samples. This agreement can be explained by the coarsening of grains at high temperatures shown in Figure 6.8. The high values in 5-minute tempered samples can be again attributed to the small spacing between grain boundaries which increases the probability of dislocation annihilation at grain boundaries [162].

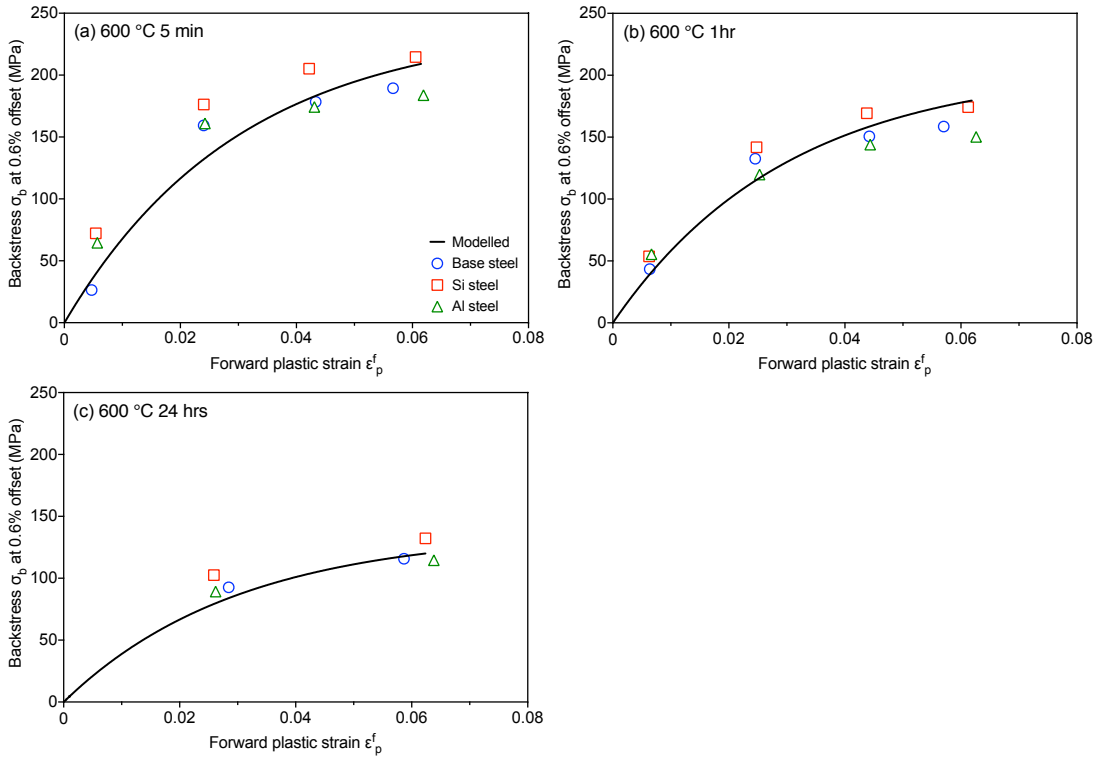

Figure 7.16: *The evolution of the back stress at 0.6% offset and the modelled back stress as a function of forward plastic strain for the 600 °C tempered samples.*

7.3.5 Limitation of the combined hardening model in tempering state with low strain hardening

As the combined hardening model works reasonably well in the 600 °C tempered conditions, we have attempted to implement the same model for the 500 °C tempered conditions. However, the model is not able to describe fully the tension-compression behaviour of the material. Figure 7.17a shows the comparison between the experimental and modelled curves for samples tempered at 500 °C for 5 minutes considering only the kinematic hardening contribution ($V_f = 0.0375$, $k_1 = 0$). Although the forward loading can be reproduced, the modelled curve significantly underestimates the Bauschinger effect in the reverse direction. This can be attributed to the underestimated back stress shown in Figure 7.17b. It indicates that the kinematic hardening contribution from precipitates alone cannot reproduce the reduction in reverse yield strength and more kinematic hardening contributions need to be included. This could be achieved by incorporating the kinematic hardening contribution from grain boundaries as suggested in the work of Kim *et al.* (Section 2.4.4, [126]). However, if we are to consider kinematic hardening contributions from both precipitates and grain boundaries, we may greatly overestimate the

hardening in the forward direction since the measurable strain hardening is only ~150 MPa, which is much smaller than the measured kinematic hardening ~250 MPa. The low strain hardening and large Bauschinger effect observed in the 500 °C and 400 °C tempered samples are the major obstacles for the future improvement of the model.

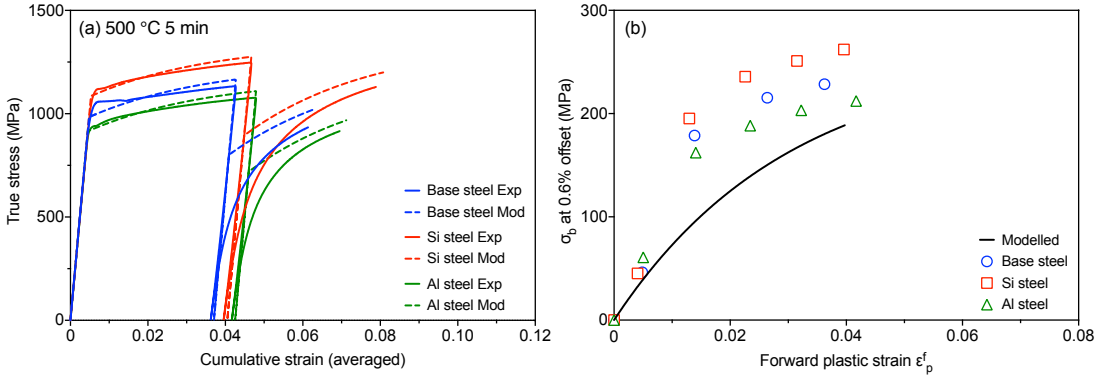

Figure 7.17: *(a) Experimental and modelled tension-compression curve for the Si steel tempered at 500 °C for 5 minutes. (b) The evolution of the back stress at 0.6% offset and the modelled back stress as a function of forward plastic strain for the samples tempered at 500 °C for 5 minutes.*

7.4 Summary

This chapter shows two modelling frameworks that focus on the strain hardening behaviours of as-quenched and tempered martensite. For the as-quenched and low temperature (300 °C and 400 °C) tempered conditions, the yield stress spectrum model and the residual stress spectrum model are combined by the introduction of a residual stress relaxation parameter α_r that describes the implicit convolution of the two models. α_r can be estimated using interrupted X-ray diffraction tests and the diffraction peak narrowing phenomenon that is unique to martensite with unrelaxed residual stresses. The modified model is capable of describing the tension-compression flow behaviour of the material and a correlation is found between the experimentally measured UTS and the width of the apparent yield stress spectrum after residual stress relaxation. Using this correlation, it is possible to extend the current model to martensite with similar carbon contents without additional optimisation of modelling parameters.

For samples tempered at 600 °C, a combined isotropic and kinematic hardening model is successfully used. This model is borrowed from approaches for other particle containing alloys such as ferrite-pearlite steels and Al-Cu alloys. The combined hardening model is implemented in a continuum mechanics framework but uses microstructural based parameters that enables the rigorous simulation of

tension-compression curves. With reasonable estimation of isotropic and kinematic hardening parameters, the model is able to describe the strain hardening and strain reversal behaviours of the material simultaneously. Although the current model lacks the capability to reproduce the permanent softening behaviour in the reverse loading, more complexities can be incorporated in the future.

While the two models perform reasonably well at high (600 °C) and low (400 °C) tempering temperatures, discrepancies can be seen at intermediate tempering temperatures (especially 500 °C). This temperature range corresponds to the region where small strain hardening capabilities are measured (Figure 6.13). Although the samples cannot be significantly strain hardened, they show large Bauschinger effects which cannot be described by classic kinematic hardening models. Further investigations into the origin of this phenomenon need to be conducted before a quantitative model can be developed.

Chapter 8

Conclusions and future work

8.1 Conclusions

In this thesis, a systematic study of the flow behaviour and microstructural evolution of as-quenched and tempered martensite is conducted, the main conclusions of the thesis can be summarised as follows:

1. A unified modelling platform is developed to evaluate if the composite models considering a yield stress spectrum (proposed by Allain *et al.* [5]) and a residual stress spectrum (proposed by Hutchinson *et al.* [6, 70]) are capable of describing the strain hardening of as-quenched martensite as well as related microstructural evolutions. While the yield stress spectrum model is able to describe both the monotonic tension and the tensions-compression flow behaviour of as-quenched martensite, it fails to address the diffraction line narrowing phenomenon observed in *in-situ* Neutron and X-ray diffraction. In contrast, the residual stress spectrum model can describe the monotonic tension curve and provide feasible explanations to the diffraction line narrowing problem but it cannot reproduce a large Bauschinger effect. While both models have their limitations, their fundamental hypotheses: the strain hardening of as-quenched martensite does not predominantly come from dislocation storage based mechanisms, is supported by the estimation of athermal and kinematic hardening contributions using strain-rate sensitivity and tension-compression tests.

2. A systematic study on the effect of tempering has been conducted which includes both mechanical testing and microstructural characterisations. Depending on the tempering temperatures, the tempering behaviour of martensite may be separated into two categories:

- At lower tempering temperatures (300 °C and 400 °C), the strain hardening response of tempered martensite resembles the one observed in the as-quenched state (i.e. greater than the E/50 limit) but the strain hardening capability of the material (characterised by the strain hardening exponent) decreases continuously as a function of tempering. At the same time, the diffraction peak narrowing phenomenon persists in samples tempered at 300 °C and disappears gradually when the tempering temperature is raised to 400 °C. These observations suggest that the same composite strengthening hypotheses may be used for low temperature tempered martensite.

  Based on the unified modelling platform developed in this work, the yield stress spectrum model and the residual stress spectrum model are combined and a relaxation parameter is identified to describe the convolution of the two models. The modified composite model is capable of describing the tension-compression flow behaviour of the studied as-quenched and low temperature tempered samples. The systematic experimental and modelling results also allows an empirical correlation to be found which may be used to predict the flow behaviour of other as-quenched and low temperature tempered martensitic steels.

- At higher tempering temperatures (500 °C and 600 °C), the strain hardening rates of all samples are below the E/50 limit and interrupted X-ray diffraction experiments show diffraction peak broadening. Moreover, the strain hardening capabilities also increase at high tempering temperatures. This suggests that it is possible to model the flow behaviour of high temperature tempered martensite using dislocation based models.

  In this case, the unified modelling platform is simplified to the case that no mechanical heterogeneity exists in the microstructure and the constituents are allowed to hardening through a combination of isotropic hardening and kinematic hardening mechanisms. Using modelling parameters obtained from the literature and experimental works done in this study, the combined hardening model is capable of describing the tension-compression flow behaviour of 600 °C tempered samples, but not the 500 °C ones.

3. The effect of Si and Al additions on martensite tempering is also studied in this thesis. While the addition of Si and Al retards the cementite precipitates and slows down the relaxation kinetics of martensite at lower tempering temperatures, it becomes less effective at higher tempering temperatures when cementite particles start to precipitate out of the matrix. Furthermore, these alloying elements do not seem to affect the main softening mechanism during martensite tempering, which is the reduction of the athermal and directional hardening contributions.

8.2 Future work

The future work of this thesis can be divided into two parts. The first part stems from the suggestions and limitations of the newly developed models:

1. A large-scale CPFEM model with an explicit initialisation scheme that considers both the yield stress spectrum and the residual stress spectrum.

   As discussed in Section 7.2.4, the modified composite model considers the implicit convolution of the yield stress spectrum and the residual stress spectrum. The relaxation process in this model is constrained by the initial location of the constituent and the magnitude of the relaxation parameter. In reality, the residual stress states are much more complex than that assumed in the current model. A more general form of this model should have an explicit initialisation scheme that considers the two spectra simultaneously. Both the yield stress and the residual stress states for a particular constituent should be able to vary freely during the initialisation step. This could be implemented in a CPFEM framework suggested by Hutchinson *et al.* [70], which allows the simulation of both the flow behaviour and the diffraction peak evolution at the same time.

2. Experimental measurement of the yield stress spectrum and the residual stress spectrum.

   As an important part of the initialisation step, it is essential to estimate the magnitude of the variation in the local yield stress and residual stress states. In the case of the local yield stress, we may still use nanoindentation but we need to conduct a more systematic study on the effect of the indent size since the large indent size used in this work results in nanohardness values that are affected by the residual stress relaxation process. Smaller indentation sizes (< 200 nm) may be used to get around this problem but the indentation size effect should also be considered. In the case of the local residual stress, the microscopic ring-core milling method may be used (Figure 2.21 [77]). If we can mill an $n \times n$ matrix on the surface of the sample, we should be able to estimate the magnitude of the residual stresses and their spatial distributions.

3. Validation of the model using *in-situ* high energy synchrotron X-ray diffraction.

   Once we construct the model with the estimated yield stress spectrum and residual stress spectrum, we may further validate this hypothesis and the modelling parameters using the macroscopic and microscopic response. On one hand, the loading of the modelled structure should reproduce the macroscopic tension-compression response. On the other hand, the loading process should also relax some of the residual stresses and result in the diffraction peak narrowing phenomenon. An advantage of the CPFEM framework is that both the macroscopic and the microscopic behaviours can be obtained simultaneously. The characterisation method that is suitable

to probe these behaviours is the *in-situ* high energy synchrotron X-ray diffraction. By using a high energy light source, we should be able to test a relatively thick sample *in-situ* which can be deformed in both forward and reverse diffractions and reduce the probability of buckling. The *in-situ* method also allows us to monitor the evolution of the diffraction peaks in real time and enable the comparison of the experimental and modelled results.

4. Generality of the high temperature tempering model in simple systems.

   In the model developed for the high temperature tempered conditions, we assume that both isotropic and kinematic hardening contribute to the strengthening of the materials. Due to the complexity of the microstructure, it is difficult to determine if it is indeed the precipitates that is contributing to the kinematic hardening. One way to test this hypothesis is to implement this model in a much simpler system such as silica strengthened copper. This is a classic model alloy that forms the basis of the Brown-Stobbs model [129, 130]. In this case, we can easily manipulate the grain size of copper by deformation and annealing and keep the volume fraction and the size of silica constant. The comparison between the experimental tension-compression data and the modelled results will demonstrate if additional ingredients (e.g. kinematic hardening due to grain boundaries) are needed in order to improve the model.

5. Development of a unified model that describes the flow behaviour of as-quenched and tempered martensite.

   In this study, we developed two models that separately describe the two extremes in martensite tempering as the strain hardening behaviours evolve drastically during tempering. For the as-quenched and low temperature tempered conditions, no true strain hardening is allowed and the entire strain hardening of the material is attributed to the composite effect. In reality, this is not strictly true since we do observe hardening from dislocations throughout tempering (i.e. the thermal stresses shown in Figure 6.20b). Therefore, the ultimate goal would be the development of a unified model that considers both the composite effect and the true strain hardening of martensite simultaneously. This could be achieved by incorporating microscopic constitutive laws found in the high temperature tempered conditions into the CPFEM model developed for the as-quenched and low temperature tempered states. A major difficulty for the development of this model will be the identification of the constitutive laws for the intermediate temperatures where low strain hardening and large Bauschinger effects are observed.

The second part of the future work originates from the implications of experimental results:

1. Diffraction peak narrowing in other systems and its relationship with residual stresses.

   A key microscopic characteristic of the deformation behaviour of as-quenched martensite is the narrowing of diffraction peaks as a function of plastic straining. It is considered as a result of relaxation of residual stresses generated during the martensitic transformation. Another system that may have such residual stresses is the 3-D printed materials. During printing, there could also be a built-up of residual stresses due to the rapid solidification process [171]. If the hypothesis of Hutchinson *et al.* is true [6, 70], we should also be able to observe the diffraction peak narrowing phenomenon in these materials and model their deformation behaviours using the residual stress spectrum model.

2. Generality of the master curve found in the comparison of the athermal stress and the back stress.

   In Figure 6.25, we have demonstrated that there is a linear correlation between the athermal stress measured using strain-rate jump tests and the back stress measured using Bauschinger tests. While more tempered martensite samples should be tested to validate this master curve, it also interesting to explore if this correlation exists in other alloy systems that show significant Bauschinger effects. This may include alloys strengthened by secondary particles (e.g. Copper-silica and precipitation hardened Fe/Al/Ni alloys). If this correlation is indeed valid for a broad range of alloy systems, it can greatly reduce the experimental complexity in estimating the magnitude of the Bauschinger effect. This would be particularly beneficial for the sheet metal community since thin sheet samples are naturally prone to buckling when tested in uniaxial tension-compression experiments [172].

Bibliography

[1] WorldAutoSteels. Automotive Steel Definitions, 2016.

[2] Y. X. Wu. *Phase Transformations during the Processing of Third Generation Advanced High Strength Steels*. PhD thesis, Monash University, 2019.

[3] D. W. Suh and S. J. Kim. Medium Mn transformation-induced plasticity steels: Recent progress and challenges. *Scripta Materialia*, 126:63–67, 2017.

[4] E. De Moor, S. Lacroix, A. J. Clarke, J. Penning, and J. G. Speer. Effect of retained austenite stabilized via quench and partitioning on the strain hardening of martensitic steels. *Metallurgical and Materials Transactions A: Physical Metallurgy and Materials Science*, 39(11):2586–2595, 2008.

[5] S. Allain, O. Bouaziz, and M. Takahashi. Toward a New Interpretation of the Mechanical Behaviour of As-quenched Low Alloyed Martensitic Steels. *ISIJ International*, 52(4):717–722, 2012.

[6] B. Hutchinson, D. Lindell, and M. Barnett. Yielding Behaviour of Martensite in Steel. *ISIJ International*, 55(5):1114–1122, 2015.

[7] A. Arlazarov, O. Bouaziz, A. Hazotte, M. Goune, and S. Allain. Characterization and Modeling of Manganese Effect on Strength and Strain Hardening of Martensitic Carbon Steels. *ISIJ International*, 53(6):1076–1080, 2013.

[8] T. Maki, K. Tsuzaki, and I. Tamura. The Morphology of Microstructure Composed of Lath Martenistes in Steels. *Transactions of Iron and Steel Institute of Japan*, 20:207–214, 1980.

[9] C. L. Magee and R. G. Davies. The structure, deformation and strength of ferrous martensites. *Acta Metallurgica*, 19(4):345–354, 1971.

[10] A. M. Sherman, G. T. Eldis, and M. Cohen. The Aging and Tempering of Iron-Nickel-Carbon Martensites. *Metallurgical Transactions A*, 14(5):995–1005, 1983.

[11] G. B. Olson. Introduction: Martensite in Perspective. In *Martensite: A Tribute to Morris Cohen*, page 1. 1992.

[12] L. Kaufman and M. Hillert. Thermodynamics of Martensitic Transformations. In *Martensite: A Tribute to Morris Cohen*, pages 41–58. 1992.

[13] S. M. C. Van Bohemen. Bainite and martensite start temperature calculated with exponential carbon dependence. *Materials Science and Technology*, 28(4):487–495, 2012.

[14] D. P. Koistinen and R. E. Marburger. A general equation prescribing the extent of the austenite-martensite transformation in pure iron-carbon alloys and plain carbon steels. *Acta Metallurgica*, 7:59–60, 1959.

[15] E. C. Bain. The Nature of Matensite, 1924.

[16] Z. Nishiyama, M. E. Fine, M. Meshii, and C. M. Wayman. Martensitic transformation. 1978.

[17] C. S. Roberts. Effect of carbon on the volume fractions and lattice parameters of retained austenite and martensite, 1953.

[18] G. Krauss. *Steels: processing, structure, and performance*. ASM International, 2015.

[19] G. Kurdjumov and G. Sachs. Over the Mechanisms of Steel Hardening. *Zeitschrift für Phys.*, 64(5-6):325–343, 1930.

[20] Z. Nishiyama. X-ray Investigation of the Mechanism of the Transformation from Face-centered Cubic Lattice to Body-centered Cubic. *Sci. Rep.*, 23:637–664, 1934.

[21] G. Wassermann and K. Mitt. About the Mechanism of α-γ Transformation of the Iron. *Wilh.-Inst. Eisenforsch*, 17(149), 1935.

[22] A. B. Greninger and A. R. Troiano. The Mechanism of Martensite Formation. *Trans. AIME*, 185:590–598, 1949.

[23] S. Morito, H. Tanaka, R. Konishi, T. Furuhara, and T. Maki. The morphology and crystallography of lath martensite in Fe-C alloys. *Acta Materialia*, 51(6):1789–1799, 2003.

[24] L. Morsdorf, C. C. Tasan, D. Ponge, and D. Raabe. 3D structural and atomic-scale analysis of lath martensite : Effect of the transformation sequence. *Acta Materialia*, 95:366–377, 2015.

[25] L. Morsdorf, O. Jeannin, D. Barbier, M. Mitsuhara, D. Raabe, and C. C. Tasan. Multiple mechanisms of lath martensite plasticity. *Acta Materialia*, 121:202–214, 2016.

[26] K. Y. Zhu, H. Shi, H. Chen, and C. Jung. Effect of Al on martensite tempering: comparison with Si. *Journal of Materials Science*, 53(9):6951–6967, may 2018.

[27] S. Morito, K. Oh-ishi, K. Hono, and T. Ohba. Carbon Enrichment in Retained Austenite Films in Low Carbon Lath Martensite Steel. *ISIJ International*, 51(7):1200–1202, 2011.

[28] J. D. Baird. Strain Aging of Steels-A Critical Review. *Iron Steel Institute*, 36(June):186–192, 326–334, 368–374, 400–405, 1963.

[29] G. R. Speich. Tempering of Low-Carbon Martensite. *Transactions of the Metallurgical Society of AIME*, 245(December):2553–2564, 1969.

[30] B. Hutchinson, J. Hagström, O. Karlsson, D. Lindell, M. Tornberg, F. Lindberg, and M. Thuvander. Microstructures and hardness of as-quenched martensites (0.1-0.5%C). *Acta Materialia*, 59(14):5845–5858, 2011.

[31] S. Takaki, D. Akama, N. Nakada, T. Tsuchiyama, R. Uemori, M. Murakami, K. Iwanaga, and S. Mizoguchi. Possibility of Auto-Tempering In Martensitic Steels. In *Proceedings of the International Conference on Solid-Solid Phase Transformations in Inorganic Materials 2015*, pages 79–80, 2015.

[32] G. Krauss. Martensite in steel: strength and structure. *Materials Science and Engineering: A*, 273-275:40–57, 1999.

[33] H. Muir, B. L. Averbach, and M. Cohen. The elastic limit and yield behavior of hardened steels. *Transaction of American Society for Metals*, 47:380–407, 1955.

[34] U. F. Kocks and H. Mecking. Physics and phenomenology of strain hardening: The FCC case. *Progress in Materials Science*, 48(3):171–273, 2003.

[35] T. Swarr and G. Krauss. The effect of structure on the deformation of as-quenched and tempered martensite in an Fe-0.2 pct C alloy. *Metallurgical Transactions A*, 7(1):41–48, 1976.

[36] F. B. Pickering and T. Gladman. Metallurgial Developments in Carbon Steels. Technical report, Iron and Steel Institute, London, 1963.

[37] G. R. Speich and H. Warlimont. Yield Strength and transformation substructure of low-carbon martensite. *Iron and Steel Institute*, 206:385–392, 1968.

[38] R. L. Fleischer. Substitutional solution hardening. *Acta Metallurgica*, 11(3):203–209, 1963.

[39] L. Å. Norström. On the Yield Strength of Quenched Low-Carbon Lath Martensite. *Scandinavian Journal of Metallurgy*, 5:159–165, 1976.

[40] E. O. Hall. The Deformation and Ageing of Mild Steel: III Discussion of Results. *Proceedings of the Physical Society. Section B*, 64(9):747–753, 1951.

[41] N. J. Petch. The cleavage strength of polycrystals. *Journal of the Iron and Steel Institute*, 174:25–28, 1953.

[42] S. Morito, H. Yoshida, T. Maki, and X. Huang. Effect of block size on the strength of lath martensite in low carbon steels. *Materials Science and Engineering A*, 438-440(SPEC. ISS.):237–240, 2006.

[43] M. J. Roberts. Effect of transformation substructure on the strength and toughness of Fe-Mn alloys. *Metallurgical Transactions*, 1(12):3287–3294, 1970.

[44] G. Krauss and A. R. Marder. The morphology of martensite in iron alloys. *Metallurgical Transactions*, 2(9):2343–2357, 1971.

[45] J. W. Christian. The Strength of martensite. In *Strengthening Methods in Crystals*, pages 261–328. 1971.

[46] S. Kennett. *Strengthening and Toughnening Mechanisms in Low-C Microalloyed Steel as Influenced by Austenite Conditioning*. PhD thesis, Colorado School of Mines, 2014.

[47] A. Shibata, T. Nagoshi, M. Sone, S. Morito, and Y. Higo. Evaluation of the block boundary and sub-block boundary strengths of ferrous lath martensite using a micro-bending test. *Materials Science and Engineering A*, 527(29-30):7538–7544, 2010.

[48] C. Du, J. P. M. Hoefnagels, R. Vaes, and M. G. D. Geers. Block and sub-block boundary strengthening in lath martensite. *Scripta Materialia*, 116:117–121, 2016.

[49] S. Morito, J. Nishikawa, and T. Maki. Dislocation Density within Lath Martensite in Fe-C and Fe-Ni Alloys. *ISIJ International*, 43(9):1475–1477, 2003.

[50] M. Kehoe and P. M. Kelly. The role of carbon in the strenght of ferrous martensite. *Scripta Metallurgica*, 4:473–476, 1970.

[51] G. I. Taylor. The Mechanism of Plastic Deformation of Crystals. Part I. Theoretical. *Proceedings of the Royal Society of London A: Mathematical, Physical and Engineering Sciences*, 145(855):362–387, 1934.

[52] A. J. Mcevily, R. C. Ku, and T. L. Johnston. The Source of Martensite Strength. *Transactions of the Metallurgical Society of AIME*, 236(1):108–114, 1962.

[53] S. Takaki, K. L. Ngo-Huynh, N. Nakada, and T. Tsuchiyama. Strengthening Mechanism in Ultra Low Carbon Martensitic Steel. *ISIJ International*, 52(4):710–716, 2012.

[54] D. Akama, T. Tsuchiyama, and S. Takaki. Change in Dislocation Characteristics with Cold Working in Ultralow-carbon Martensitic Steel. *ISIJ International*, 56(9):1675–1680, 2016.

[55] S. Takaki, S. Iizuka, K. Tomimura, and Y. Tokunaga. Influence of cold working on recovery and recrystallization of lath martensite in 0.2% C steels. *Materials Transactions, JIM*, 33(6):577–584, 1992.

[56] C. L. Magee and H. W. Paxton. The Microplastic Response of Partially Transformed Fe-31Ni. *Transactions of the Metallurgical Society of AIME*, 242(August):1741–1749, 1968.

[57] M. A. Zaccone and G. Krauss. Elastic limits and microplastic response in ultrahigh strength carbon steels. *Metallurgical Transactions A*, 20(1):188–191, 1989.

[58] F. Maresca, V. G. Kouznetsova, and M. G. D. Geers. On the role of interlath retained austenite in the deformation of lath martensite. *Modelling and Simulation in Materials Science and Engineering*, 22(4):045011, 2014.

[59] C. Du, J. P. M. Hoefnagels, R. Vaes, and M. G. D. Geers. Plasticity of lath martensite by sliding of substructure boundaries. *Scripta Materialia*, 120:37–40, 2016.

[60] G. S. Ansell and A. Arrot. The Strengthening Mechanism of Ferrous Martensite. Technical report, 1963.

[61] G. Masing. Zur Heyn'schen Theorie der Verfestigung der Metalle durch verborgen elastische Spannungen. In S.B. Heidelberg, editor, *Wissenschaftliche Veröffentlichungen aus dem Siemens-Konzern*, pages 231–239. Springer Berlin Heidelberg, Berlin, Heidelberg, 1923.

[62] R. J. Asaro. Elastic-Plastic Memory and Kinematic Type Hardening. *Acta Metallurgica*, 23:1255–1265, 1975.

[63] B. B. He and M. X. Huang. Revealing the Intrinsic Nanohardness of Lath Martensite in Low Carbon Steel. *Metallurgical and Materials Transactions A: Physical Metallurgy and Materials Science*, 46(2):688–694, 2014.

[64] L. Zhang, T. Ohmura, and K. Tsuzaki. Application of Nanoindentation Technique in Martensitic Structures. In *Nanoindentation in Materials Science*, chapter 5, pages 109–130. InTech, Rijeka, 2012.

[65] C. P. Scott, B. Shalchi Amirkhiz, I. Pushkareva, F. Fazeli, S. Y. P. Allain, and H. Azizi. New insights into martensite strength and the damage behaviour of dual phase steels. *Acta Materialia*, 159:112–122, 2018.

[66] T. Ungár, S. Harjo, T. Kawasaki, Y. Tomota, G. Ribárik, and Z. M. Shi. Composite Behavior of Lath Martensite Steels Induced by Plastic Strain, a New Paradigm for the Elastic-Plastic Response of Martensitic Steels. *Metallurgical and Materials Transactions A*, 48(1):159–167, 2017.

[67] S. Y. Zhang, S. Morito, and Y. I. Komizo. Variant Selection of Low Carbon High Alloy Steel in an Austenite Grain during Martensite Transformation. *ISIJ International*, 52(3):510–515, 2012.

[68] W. C. Leslie and R. J. Sober. The strength of ferrite and of martensite as functions of composition, temperature and strain rate. *Transactions of the ASM*, 60:459–484, 1967.

[69] C. L. Magee and H. W. Paxton. Experimental Support for Hard Martensite. *Transactions of the Metallurgical Society of Aime*, 242(8):1766–1967, 1968.

[70] B. Hutchinson, P. Bate, D. Lindell, A. Malik, M. Barnett, and P. Lynch. Plastic yielding in lath martensites - An alternative viewpoint. *Acta Materialia*, 152:239–247, jun 2018.

[71] S. Morooka, Y. Tomota, and T. Kamiyama. Heterogeneous Deformation Behavior Studied by in Situ Neutron Diffraction during Tensile Deformation for Ferrite, Martensite and Pearlite Steels. *ISIJ International*, 48(4):525–530, 2008.

[72] S. Harjo, T. Kawasaki, and S. Morooka. Changes of Dislocation Density and Dislocation Arrangement during Tensile Deformation in Lath Martensitic Steels. *Advanced Experimental Mechanics*, 2:112–117, 2017.

[73] S. Harjo, T. Kawasaki, Y. Tomota, W. Gong, K. Aizawa, G. Tichy, Z. G. Shi, and T. Ungár. Work Hardening, Dislocation Structure, and Load Partitioning in Lath Martensite Determined by In Situ Neutron Diffraction Line Profile Analysis. *Metallurgical and Materials Transactions A*, 48(9):4080–4092, sep 2017.

[74] G. Badinier. *Effect of Carbon Segregation and Carbide Precipitation on the Mechanical Response of Martensite*. PhD thesis, The University of British Columbia, 2013.

[75] M. D. Richards, C. J. Van Tyne, and D. K. Matlock. The influence of dynamic strain aging on resistance to strain reversal as assessed through the Bauschinger effect. *Materials Science and Engineering A*, 528(27):7926–7932, 2011.

[76] B. Hutchinson and J. Brask. An Investigation of Short Range Residual Stress Fields in Ferrous Lath Martensite. *Metallurgical and Materials Transactions A*, 50(12):5581–5584, dec 2019.

[77] F. Archie, M. Z. Mughal, M. Sebastiani, E. Bemporad, and S. Zaefferer. Anisotropic distribution of the micro residual stresses in lath martensite revealed by FIB ring-core milling technique. *Acta Materialia*, 150:327–338, 2018.

[78] G. Krauss. Heat Treated Martensitic Steels: Microstructural Systems for Advanced Manufacture. *ISIJ International*, 35(4):349–359, 1995.

[79] K. A. Taylor and M. Cohen. Aging of ferrous martensites. *Progress in Materials Science*, 36(C):151–272, 1992.

[80] K. A. Taylor, L. Chang, G. B. Olson, G. D. W. Smith, M. Cohen, and J. B. Vander Sande. Spinodal decomposition during aging of Fe-Ni-C martensites. *Metallurgical Transactions A*, 20(12):2717–2737, 1989.

[81] G. R. Speich and K. A. Taylor. Tempering of of Ferrous Martensites. In *Martensite: A Tribute to Morris Cohen*, pages 243–276. ASM International, 1992.

[82] G. R. Speich and W. C. Leslie. Tempering of steel. *Metallurgical Transactions*, 3(5):1043–1054, 1972.

[83] G. Krauss. Tempering of martensite in carbon steels. In *Phase Transformations in Steels*, volume 2, pages 126–150. Woodhead Publishing Limited, 2012.

[84] G. Badinier, C. W. Sinclair, S. Allain, F. Danoix, and M. Gouné. The Mechanisms of Transformation and Mechanical Behavior of Ferrous Martensite. In *Reference Module in Materials Science and Materials Engineering*, number January 2016, pages 1–34. Elsevier, 2017.

[85] D. H. Jack. The orientation relationships of interstitial phases in iron. *Materials Science and Engineering*, 13(1):19–27, 1974.

[86] M. G. H. Wells. An electron transmission study of the tempering of martensite in an Fe-Ni-C alloy. *Acta Metallurgica*, 12(4):389–399, 1964.

[87] Y. Hirotsu, Y. Itakura, K. Su, and S. Nagakura. Electron Microscopy and Diffraction Study of the Carbide Precipitated from Martensitic Low and High Nickel Steels at the First Stage of Tempering. *Trans. JIM*, 17:503–513, 1976.

[88] D. L. Williamson, K. Nakazawa, and G. Krauss. A study of the early stages of tempering in an Fe-1.2 Pct alloy. *Metallurgical Transactions A*, 10(9):1351–1363, 1979.

[89] G. Badinier, C. W. Sinclair, X. Sauvage, X. Wang, V. Bylik, M. Gouné, and F. Danoix. Microstructural heterogeneity and its relationship to the strength of martensite. *Materials Science and Engineering: A*, 638:329–339, jun 2015.

[90] D. L. Williamson, R. G. Schupmann, J. P. Materkowski, and G. Krauss. Determination of small amounts of austenite and carbide in hardened medium carbon steels by Mössbauer spectroscopy. *Metallurgical Transactions A*, 10(3):379–382, 1979.

[91] R. M. Horn and R. O. Ritchie. Mechanisms of tempered martensite embrittlement in low alloy steels. *Metallurgical Transactions A*, 9(8):1039–1053, 1978.

[92] E. J. Fasiska and G. A. Jeffrey. On the cementite structure. *Acta Crystallographica*, 19(3):463–471, 1965.

[93] Y. A. Bagaryatsky. Possible Mechanism of Martensite Decomposition. *Dokl. Akas. Nauk SSSR*, 73(6):1161, 1950.

[94] V. Massardier, M. Goune, D. Fabregue, A. Selouane, T. Douillard, and O. Bouaziz. Evolution of microstructure and strength during the ultra-fast tempering of Fe-Mn-C martensitic steels. *Journal of Materials Science*, 49(22):7782–7796, 2014.

[95] Y. X. Wu, W. W. Sun, M. J. Styles, A. Arlazarov, and C. R. Hutchinson. Cementite coarsening during the tempering of Fe-C-Mn martensite. *Acta Materialia*, 159:209–224, 2018.

[96] C. K. Ande and M. H. F. Sluiter. First-principles prediction of partitioning of alloying elements between cementite and ferrite. *Acta Materialia*, 58(19):6276–6281, 2010.

[97] G. Miyamoto, J. C. Oh, K. Hono, T. Furuhara, and T. Maki. Effect of partitioning of Mn and Si on the growth kinetics of cementite in tempered Fe-0.6 mass% C martensite. *Acta Materialia*, 55(15):5027–5038, 2007.

[98] W. C. Leslie and G. C. Rauch. Precipitation of carbides in low-carbon Fe-AI-C alloys. *Metallurgical Transactions A*, 9(3):343–349, 1978.

[99] J. Emo, P. Maugis, and A. Perlade. Austenite growth and stability in medium Mn, medium Al Fe-C-Mn-Al steels. *Computational Materials Science*, 125:206–217, dec 2016.

[100] Z. M. Shi, W. Gong, Y. Tomota, S. Harjo, J. Li, B. Chi, and J. Pu. Study of tempering behavior of lath martensite using in situ neutron diffraction. *Materials Characterization*, 107:29–32, 2015.

[101] F. HajyAkbary, J. Sietsma, A. J. Böttger, and M. J. Santofimia. An improved X-ray diffraction analysis method to characterize dislocation density in lath martensitic structures. *Materials Science and Engineering A*, 639(April 2018):208–218, 2015.

[102] Z. Y. Hou, R. P. Babu, P. Hedström, and J. Odqvist. Microstructure evolution during tempering of martensitic Fe-C-Cr alloys at 700 Â°C. *Journal of Materials Science*, 2018.

[103] R. N. Caron and G. Krauss. The tempering of Fe-C lath martensite. *Metallurgical Transactions*, 3(9):2381–2389, 1972.

[104] T. Tsuchiyama, Y. Miyamoto, and S. Takaki. Recrystallization of Lath martensite with bulge nucleation and growth mechanism. *ISIJ International*, 41(9):1047–1052, 2001.

[105] M. Tokizane, N. Matsumura, K. Tsuzaki, T. Maki, and I. Tamura. Recrystallization and formation of austenite in deformed lath martensitic structure of low carbon steels. *Metallurgical Transactions A*, 13(8):1379–1388, 1982.

[106] M. A. Zaccone and G. Krauss. Elastic limit and microplastic response of hardened steels. *Metallurgical Transactions A*, 24(10):2263–2277, 1993.

[107] M. Saeglitz and G. Krauss. Deformation, fracture, and mechanical properties of low-temperature-tempered martensite in SAE 43xx steels. *Metallurgical and Materials Transactions A*, 28(February):377–387, 1997.

[108] George Krauss. Deformation and fracture in martensitic carbon steels tempered at low temperatures. *Metallurgical and Materials Transactions B*, 32(2):205–221, apr 2001.

[109] G. Krauss. Tempering of Lath Martensite in Low and Medium Carbon Steels: Assessment and Challenges. *Steel Research International*, 87(9999):1700038, 2017.

[110] J. H. Hollomon and L. D. Jaffe. Time-temperature relations in tempering steel. *Transactions of the Metallurgical Society of AIME*, pages 223–249, 1945.

[111] Y.-K. Lee. Unpublished work. 1998.

[112] L. R. Cupertino Malheiros, E. A. Pachon Rodriguez, and A. Arlazarov. Mechanical behavior of tempered martensite: Characterization and modeling. *Materials Science and Engineering: A*, 706(August):38–47, 2017.

[113] N. Tsuchida, H. Masuda, Y. Harada, K. Fukaura, Y. Tomota, and K. Nagai. Effect of ferrite grain size on tensile deformation behavior of a ferrite-cementite low carbon steel. *Materials Science and Engineering A*, 488(1-2):446–452, 2008.

[114] M. Verdier, Y. Brechet, and P. Guyot. Recovery of A1Mg alloys: Flow stress and strain-hardening properties. *Acta Materialia*, 47(1):127–134, 1998.

[115] E. I. Galindo-Nava and P. E. J. Rivera-Diaz-del Castillo. A model for the microstructure behaviour and strength evolution in lath martensite. *Acta Materialia*, 98:81–93, 2015.

[116] L. Malik and J. A. Lund. A study of strengthening mechanisms in tempered martensite from a medium carbon steel. *Metallurgical Transactions*, 3(6):1403–1406, 1972.

[117] L. Zhonghua and G. Haicheng. Bauschinger effect and residual phase stresses in two ductile-phase steels: Part I. The influence of phase stresses on the Bauschinger effect. *Metallurgical Transactions A*, 21(2):717–724, 1990.

[118] Y. W. Chang and R. J. Asaro. Bauschinger effects and work-hardening in spheroidized steels. *Metal Science*, 12(6):277–284, 1978.

[119] M. D. Richards. *The Effects of Deformation Beahviour on the Fatigue Performance of Deep Rolled Medium Carbon Bar Steels*. PhD thesis, Colorado Scool of Mine, 2008.

[120] C. W. Sinclair, W. J. Poole, and Y. Bréchet. A model for the grain size dependent work hardening of copper. *Scripta Materialia*, 55(8):739–742, 2006.

[121] J. da Costa Teixeira, L. Bourgeois, C. W. Sinclair, and C. R. Hutchinson. The effect of shear-resistant, plate-shaped precipitates on the work hardening of Al alloys: Towards a prediction of the strength-elongation correlation. *Acta Materialia*, 57(20):6075–6089, 2009.

[122] D. Bardel, M. Perez, D. Nelias, S. Dancette, P. Chaudet, and V. Massardier. Cyclic behaviour of a 6061 aluminium alloy: Coupling precipitation and elastoplastic modelling. *Acta Materialia*, 83:256–268, 2014.

[123] T. Carvalho Resende, S. Bouvier, F. Abed-Meraim, T. Balan, and S. S. Sablin. Dislocation-based model for the prediction of the behavior of b.c.c. materials - Grain size and strain path effects. *International Journal of Plasticity*, 47:29–48, 2013.

[124] J. L. Chaboche. A review of some plasticity and viscoplasticity constitutive theories. *International Journal of Plasticity*, 24(10):1642–1693, 2008.

[125] S. Cobo and O. Bouaziz. Investigations and Modelling of the Work Hardening of As-Quenched Martensite. In *New Developments on Metallurgy and Applications of High Strength Steels, Buenos Aires 2008 - Proc. Int. Conf. New Developments on Metallurgy and Applications of High Strength Steels*, pages 909–918, 2008.

[126] B. Kim, E. Boucard, T. Sourmail, D. San Martin, N. Gey, and P. E. J. Rivera-Diaz-Del-Castillo. The influence of silicon in tempered martensite: Understanding the microstructure-properties relationship in 0.5-0.6 wt.% C steels. *Acta Materialia*, 68:169–178, 2014.

[127] L. M. Brown and D. R. Clarke. Work hardening due to internal stresses in composite materials. *Acta Metallurgica*, 23(7):821–830, 1975.

[128] J. D. Eshelby. The Determination of the Elastic Field of an Ellipsoidal Inclusion, and Related Problems. *Proceedings of the Royal Society A: Mathematical, Physical and Engineering Sciences*, 241(1226):376–396, 1957.

[129] L. M. Brown and W. M. Stobbs. The work-hardening of copper-silica I. A model based on internal stresses with no plastic relaxation. *Philosophical Magazine*, 23(185):1185–1199, 1971.

[130] L. M. Brown and W. M. Stobbs. The work-hardening of copper-silica II. The role of plastic relaxation. *Philosophical Magazine*, 23(185):1201–1233, 1971.

[131] J. D. Atkinson, L. M. Brown, and W. M. Stobbs. The work-hardening of copper-silica: IV. The Bauschinger effect and plastic relaxation. *Philosophical Magazine*, 30(6):1247–1280, 1974.

[132] H. Proudhon, W. J. Poole, X. Wang, and Y. Bréchet. The role of internal stresses on the plastic deformation of the Al-Mg-Si-Cu alloy AA6111. *Philosophical Magazine*, 88(5):621–640, 2008.

[133] C. Calabrese and C. Laird. Cyclic stress-strain response of two-phase alloys Part I. Microstructures containing particles penetrable by dislocations. *Materials Science and Engineering*, 13(2):141–157, 1974.

[134] G. Fribourg, Y. Bréchet, A. Deschamps, and A. Simar. Microstructure-based modelling of isotropic and kinematic strain hardening in a precipitation-hardened aluminium alloy. *Acta Materialia*, 59(9):3621–3635, 2011.

[135] U. F. Kocks, A. S. Argon, and M. F. Ashby. Thermodynamics and Kinetics of Slip. *Progress in Materials Science*, 19:1, 1975.

[136] R. A. Mulford. Analysis of strengthening mechanisms in alloys by means of thermal-activation theory. *Acta Metallurgica*, 27(7):1115–1124, 1979.

[137] T. Nyyssönen, P. Peura, and V. T. Kuokkala. Crystallography, Morphology, and Martensite Transformation of Prior Austenite in Intercritically Annealed High-Aluminum Steel. *Metallurgical and Materials Transactions A: Physical Metallurgy and Materials Science*, 49(12):6426–6441, 2018.

[138] W. C. Oliver and G. M. Pharr. An improved technique for determining hardness and elastic modulus using load and displacement sensing indentation experiments. *Journal of Materials Research*, 7(06):1564–1583, 1992.

[139] T. Ohmura, K. Tsuzaki, and S. Matsuoka. Nanohardness measurement of high-purity Fe-C martensite. *Scripta Materialia*, 45(8):889–894, 2001.

[140] T. Ohmura, K. Tsuzaki, and S. Matsuoka. Evaluation of the matrix strength of Fe-0.4 wt% C tempered martensite using nanoindentation techniques. *Philosophical Magazine A: Physics of Condensed Matter, Structure, Defects and Mechanical Properties*, 82(10):1903–1910, 2002.

[141] J. X. Li, T. Ohmura, and K. Tsuzaki. Microstructure effect on nanohardness distribution for medium-carbon martensitic steel. *Science in China, Series E: Technological Sciences*, 49(1):10–19, 2006.

[142] A. C. Fischer-Cripps. Nanoindentation Testing. Mechanical Engineering Series, pages 21–38. Springer New York, New York, NY, 2004.

[143] D. Balzar. Voigt-function model in diffraction line-broadening analysis. In R. L. Snyder, H. J. Bunge, and J. Fiala, editors, *Microstructure Analysis from Diffraction*. International Union of Crystallography, 1999.

[144] F. Bachmann, R. Hielscher, and H. Schaeben. Texture Analysis with MTEX - Free and Open Source Software Toolbox. *Solid State Phenomena*, 160(August 2014):63–68, 2010.

[145] I. Doghri. Elasto-plasticity. In *Mechanics of Deformable Solids*, pages 301–327. Springer Berlin Heidelberg, Berlin, Heidelberg, 2000.

[146] J. P. Hirth and M. Cohen. On the strength-differential phenomenon in hardened steel. *Metallurgical Transactions*, 1(1):3–8, 1970.

[147] G. C. Rauch and W. C. Leslie. The extent and nature of the strength differential effect in steel. *Metallurgical Transactions*, 3(February):373–385, 1972.

[148] R. Chait. Factors influencing the strength differential of high strength steels. *Metallurgical Transactions*, 3(2):369–375, 1972.

[149] C. A. Apple, R. N. Caron, and G. Krauss. Packet microstructure in Fe-0.2 pct C martensite. *Metallurgical Transactions*, 5(3):593–599, 1974.

[150] R. Rodríguez and I. Gutierrez. Correlation between nanoindentation and tensile properties influence of the indentation size effect. *Materials Science and Engineering A*, 361(1-2):377–384, 2003.

[151] L. Cupertino, V. Blesse, A. Pachon, and A. Arlazarov. Internal Report. Technical report, ArcelorMittal Mazieres Research SA, 2016.

[152] E. De Moor, S. Lacroix, L. Samek, J. Penning, and J. G. Speer. Dilatometric study of the quench and partitioning process. In *The 3rd International Conference on Advanced Structural Steels, Gyeongju, Korea*, pages 873–878, 2006.

[153] W. Lu, M. Herbig, C. H. Liebscher, L. Morsdorf, R. K.W. Marceau, G. Dehm, and D. Raabe. Formation of eta carbide in ferrous martensite by room temperature aging. *Acta Materialia*, 158:297–312, 2018.

[154] P. A. Manohar, M. Ferry, and T. Chandra. Five Decades of the Zener Equation. *ISIJ International*, 38(9):913–924, 1998.

[155] V. K. Judge. *Effects of Short-Time Tempering on Mechanical Properties and Fracture of 4340 Steel*. PhD thesis, Colorado School of Mines, 2017.

[156] O. Bouaziz, D. Barbier, J. D. Embury, and G. Badinier. An extension of the Kocks-Mecking model of work hardening to include kinematic hardening and its application to solutes in ferrite. *Philosophical Magazine*, 93(1-3):247–255, 2013.

[157] E. F. Rauch, J. J. Gracio, and F. Barlat. Work-hardening model for polycrystalline metals under strain reversal at large strains. *Acta Materialia*, 55(9):2939–2948, 2007.

[158] C. Jiang, S. G. Srinivasan, A. Caro, and S. A. Maloy. Structural, elastic, and electronic properties of Fe3 C from first principles. *Journal of Applied Physics*, 103(4), 2008.

[159] F. Laszlo and H. Nolle. On some physical properties of cementite. *Journal of the Mechanics and Physics of Solids*, 7(3), 1959.

[160] C. Laird and H. I. Aaronson. Structures and Migration Kinetcs of Alpha:Theta Prime Boundaries in Al-4 Pct Cu: Part I - Interfacial Structures. *Transactions of the Metallurgical Society of Aime*, 242(July):1393, 1968.

[161] G. A. Malygin. Strength and plasticity of nanocrystalline materials and nanosized crystals. *Physics-Uspekhi*, 54(11):1091–1116, 2011.

[162] S. H. He, K. Y. Zhu, and M. X. Huang. A unified dislocation-based model for ultrafine- and fine-grained face-centered cubic and body-centered cubic metals. *Computational Materials Science*, 131(November):1–10, 2017.

[163] J. P. G. Sawyer, C. H. Wang, and R. Jones. An implicit algorithm using explicit correctors for the kinematic hardening model with multiple back stresses. *International Journal for Numerical Methods in Engineeringi*, 50(October 1999):2093–2107, 2001.

[164] U. F. Kocks. The relation between polycrystal deformation and single-crystal deformation. *Metallurgical and Materials Transactions*, 1(5):1121–1143, 1970.

[165] E. J. Seo, L. Cho, Y. Estrin, and B. C. De Cooman. Microstructure-mechanical properties relationships for quenching and partitioning (Q&P) processed steel. *Acta Materialia*, 113:124–139, 2016.

[166] F. Yoshida and T. Uemori. A model of large-strain cyclic plasticity describing the Bauschinger effect and workhardening stagnation. *International Journal of Plasticity*, 18(5-6):661–686, 2002.

[167] F. Yoshida, T. Uemori, and K. Fujiwara. Elastic-plastic behavior of steel sheets under in-plane cyclic tension-compression at large strain. *International Journal of Plasticity*, 18(5-6):633–659, 2002.

[168] E. F. Rauch, J. J. Gracio, F. Barlat, and G. Vincze. Modelling the plastic behaviour of metals under complex loading conditions. *Modelling and Simulation in Materials Science and Engineering*, 19(3), 2011.

[169] R. L. Fullman. Measurement of Particle Sizes in Opaque Bodies. *JOM*, 5(3):447–452, 1953.

[170] X. F. Fang and W. Dahl. Strain hardening of steels at large strain deformation. Part I: Relationship between strain hardening and microstructures of b.c.c. steels. *Materials Science and Engineering A*, 203(1-2):14–25, 1995.

[171] D. W. Brown, J. D. Bernardin, J. S. Carpenter, B. Clausen, D. Spernjak, and J. M. Thompson. Neutron diffraction measurements of residual stress in additively manufactured stainless steel. *Materials Science and Engineering A*, 678(September):291–298, 2016.

[172] R. H. Wagoner, H. Lim, and M. G. Lee. Advanced issues in springback. *International Journal of Plasticity*, 45:3–20, 2013.

Appendix A

Bauschinger effect in martensite

This appendix summarises the results from tension-compression experiments and shows the evolution of Bauschinger effect parameters during tempering. Figures A.1 - A.4 show tension-compression curves for as-quenched and tempered conditions. The black solid lines in the plots represent the monotonic tensile curve and the coloured lines represent the tension-compression curves. Generally, the reproducibility of the data is good and the maximum deviation is less than 5%.

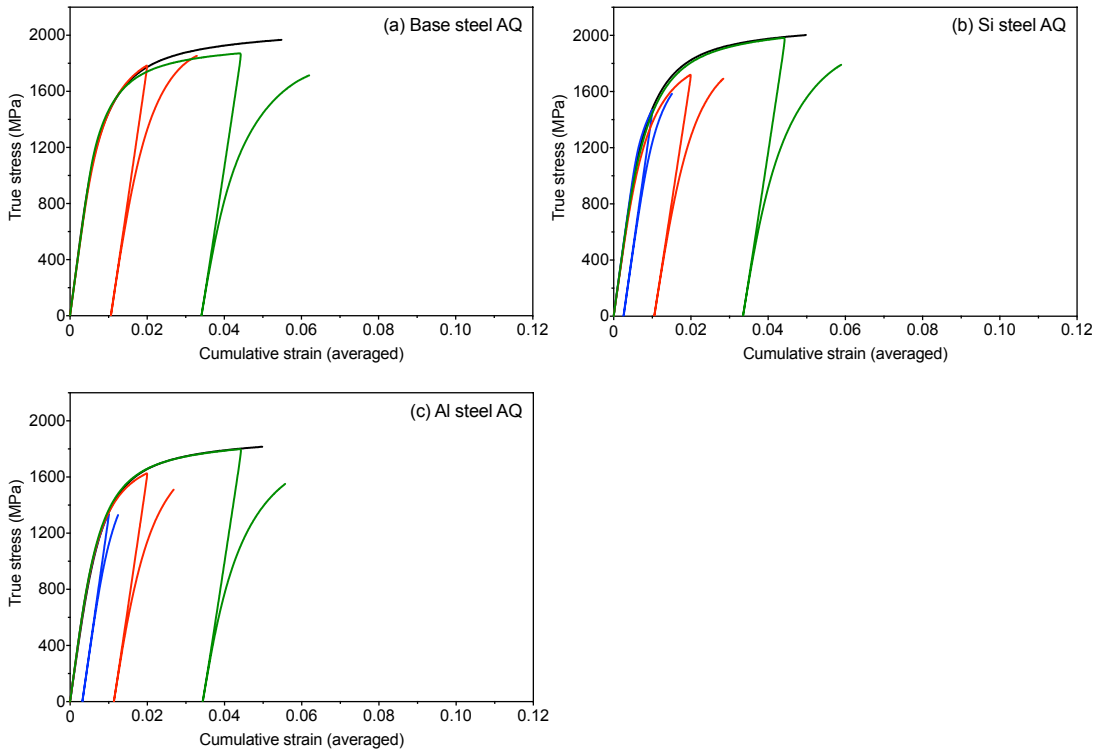

Figure A.1: *Tension-compression curves for as-quenched samples.*

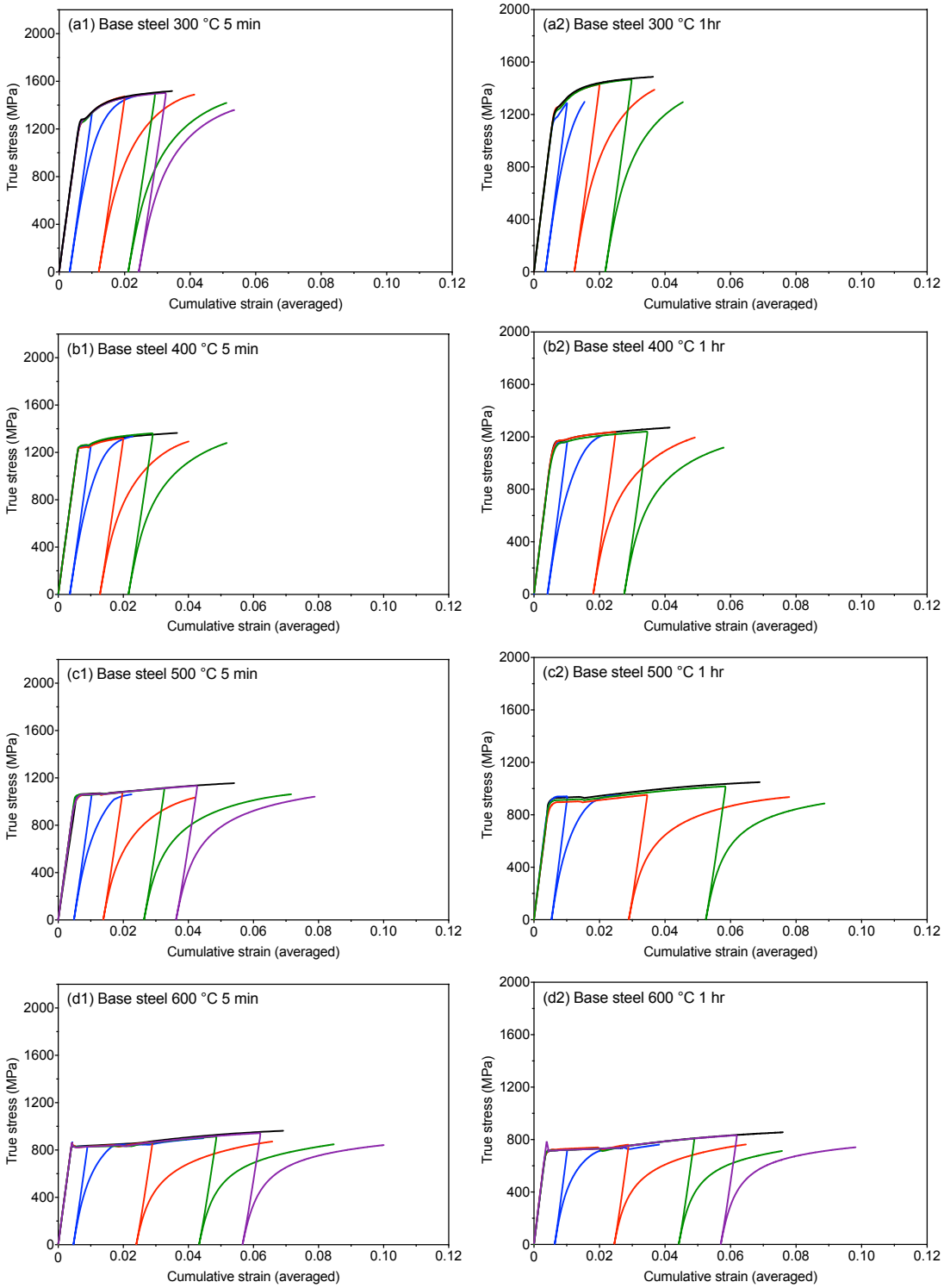

Figure A.2: *Tension-compression curves for tempered base steel samples.*

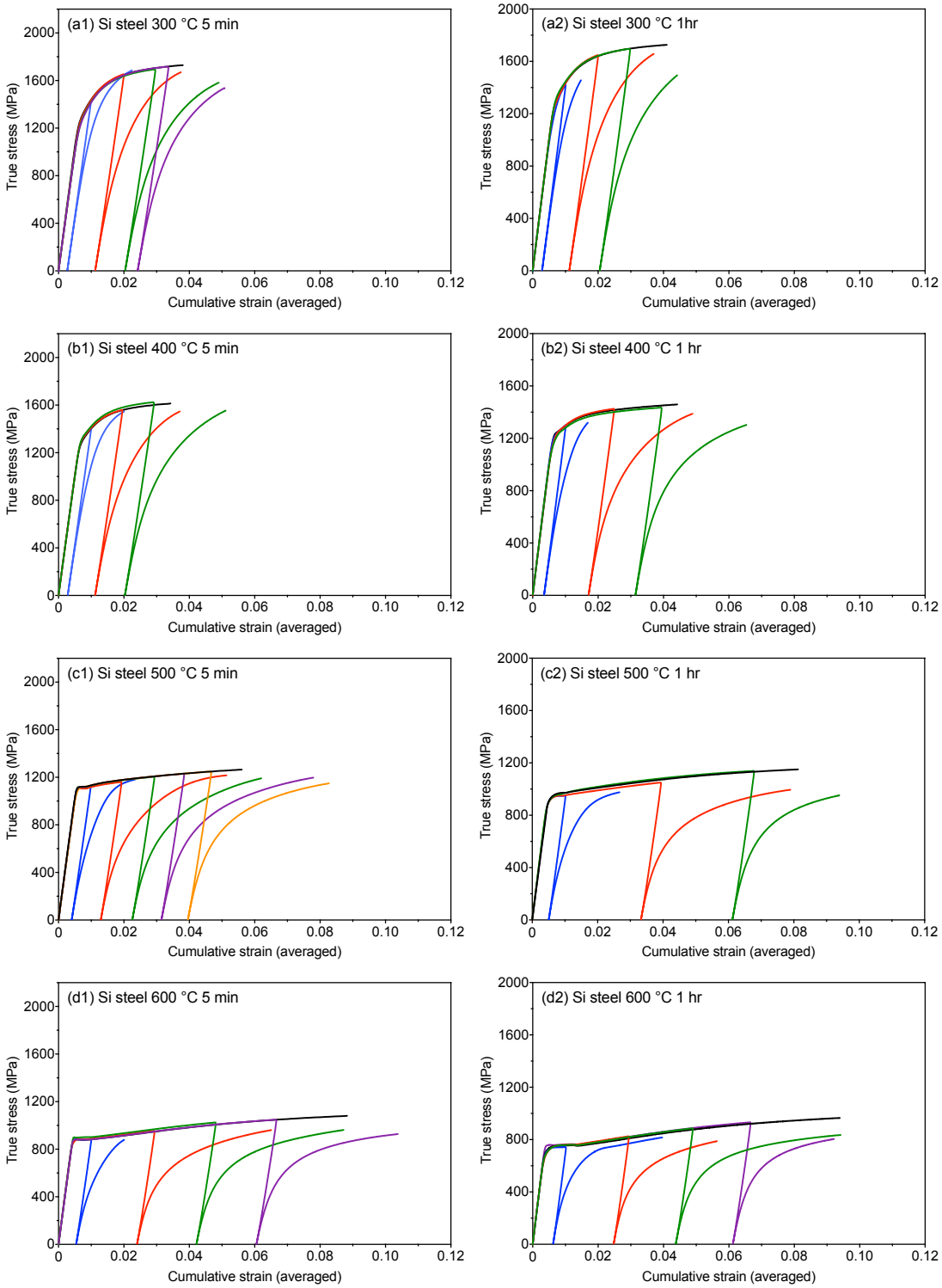

Figure A.3: *Tension-compression curves for tempered Si steel samples.*

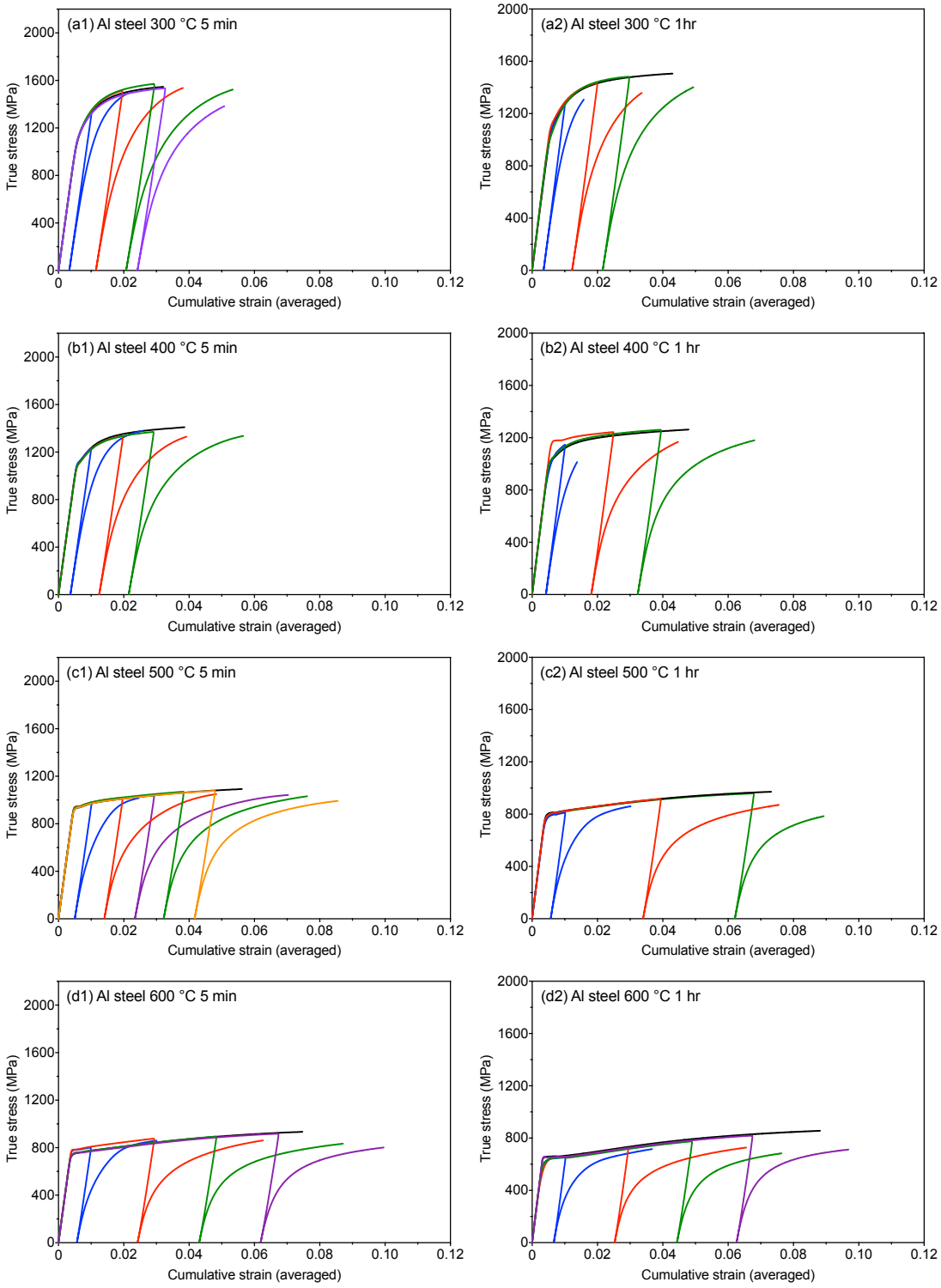

Figure A.4: *Tension-compression curves for tempered Al steel samples.*

Figure A.5 shows the evolution of the Bauschinger stress parameter β_σ using 0.2% reverse offset (Figure A.5a) and the Bauschinger strain parameter $\beta_{0.85}$ (Figure A.5b) as a function of forward plastic strains for samples in the as-quenched state and samples tempered at different temperatures for 5 minutes. Individual plots for each composition are not reproduced here since the Bauschinger effect parameters are not very sensitive to chemistry and tempering temperatures. Although the materials differ in their UTS, the normalised Bauschinger parameters for all steels can be explained by similar descriptors. For the Bauschinger stress parameter, the β_σ values saturate at ~0.3 after ~2% plastic strain for all conditions except the as-quenched state. In the case of the as-quenched martensite, the maximum β_σ for all steels falls below the 0.3 limit. For the Bauschinger strain parameter, data points after ~2% can be well described by a master curve regardless of chemistry and tempering temperatures. Again, the slope for the tempered state is smaller than that found in the as-quenched state, which indicates the as-quenched state shows smaller Bauschinger effect compared to the tempered states. The discrepancy observed in the as-quenched state may be explained by their larger thermal contributions which is relatively less strain path dependent (Figure 6.20b).

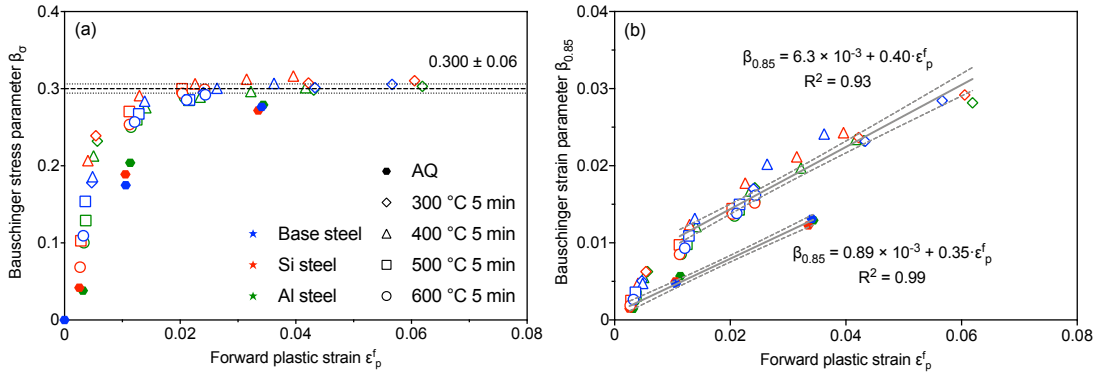

Figure A.5: *Evolution of the Bauschinger stress (a) and the Bauschinger strain (b) parameters as a function of forward plastic strains for the as-quenched and 5-minute tempered states.*

Figure A.6 shows the evolution of β_σ and $\beta_{0.85}$ for the 1-hour tempered samples. It can be seen that the data points also follow the master curves found in the 5-minute tempered samples except for the $\beta_{0.85}$ values found in samples tempered at 600 for 1 hour. At large strains, the samples display smaller $\beta_{0.85}$ values compared to the prediction of the master curve. This indicates that the Bauschinger effect starts to decrease when the material is tempered at high temperatures for long times, which agrees with the modelled results shown in Chapter 7.3.4. Nevertheless, the master curves found in this contribution may serve as a useful empirical law to predict the Bauschinger effect of tempered martensite in other alloy systems.

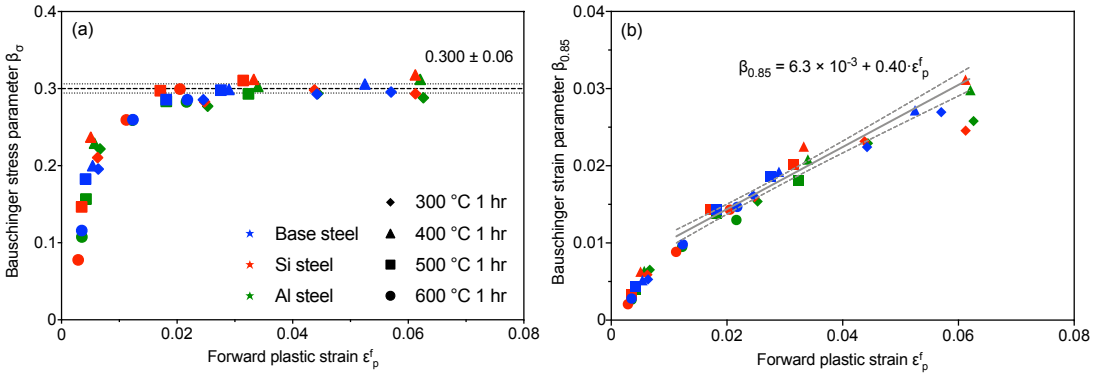

Figure A.6: *Evolution of the Bauschinger stress (a) and the Bauschinger strain (b) parameters as a function of forward plastic strains for the as-quenched and 1-hour tempered states.*